

Spin Structure of Exchange Biased Heterostructures: Fe/MnF₂ and Fe/FeF₂

Vom Fachbereich Physik der
Universität Duisburg-Essen
zur Erlangung des akademischen Grades eines
Doktors der Naturwissenschaften
genehmigte Dissertation

von
Balaram Sahoo
aus
Nayagarh, Indien

Referent: Prof. Dr. Werner Keune
Korreferent: Prof. Dr. Günter Dumpich
Tag der mündlichen Prüfung: 18 Dezember 2006

Abstract

In this work, the ^{57}Fe probe layer technique is used in order to investigate the depth- and temperature-dependent Fe-layer spin structure of exchange biased Fe/MnF₂ and Fe/FeF₂ (pseudo-twinned) antiferromagnetic (AFM) systems by conversion electron Mössbauer spectroscopy (CEMS) and nuclear resonant scattering (NRS) of synchrotron radiation.

Two kinds of samples with a 10 Å ^{57}Fe probe layer directly at or 35 Å away from the interface, labeled as interface and center sample, respectively, were studied in this work. The spin structure was explained by considering two different models, unidirectional and step-shaped distribution (fanning) model. The results obtained by CEMS for Fe/MnF₂ suggests that, at 80 K, i.e., above $T_N = 67$ K of MnF₂, the remanent state Fe-layer spin structure of the two studied samples are slightly different due to their different microstructure. In the temperature range from 300 K to 80 K, the Fe-layer spin structure does not change just by zero-field cooling the sample in remanence. By zero-field cooling the samples in remanence to 18 K, i.e., below T_N , the Fe spins rotate towards the ($\pm 45^\circ$)- easy axes of MnF₂ twins. This rotation results in the same spin structure for both the interface and center samples at 18 K. By field cooling the interface sample in a field of 0.35 T to 18 K and measuring in remanence, a smaller rotation (or fanning angle) of the Fe-spins in comparison to the case of zero-field cooling in remanence from 300 K to 18 K was observed. When the interface sample was zero-field cooled or field cooled to 18 K, and subsequently zero-field heated to 80 K ($T > T_N$), the CEMS results indicate that the Fe-layer keeps the memory of its low temperature spin structure.

For Fe/FeF₂, a continuous non-monotonic change of the remanent-state Fe spin structure was observed by cooling from 300 K to 18 K. This effect can be related to the peculiar T-dependence of magnetic anisotropy of FeF₂ and short-range-ordered magnetic correlations in the AFM induced by Fe above $T_N = 78$ K. The high temperature Fe spin structure of the two different samples (interface and center) is different due to their different microstructure, but at 18 K ($T < T_N$) the spin structures of both samples are the same, and the Fe spins are oriented close to the easy axes of the FeF₂ twins, similar to the case of Fe/MnF₂ at 18 K.

NRS of synchrotron radiation was used to investigate the temperature- and depth-dependent Fe - layer spin structure during magnetization reversal in pseudo-twinned Fe/MnF₂. A ^{57}Fe -probe layer was embedded in the ^{56}Fe layer in a wedge-type manner, so that the distance of the ^{57}Fe layer from the Fe/MnF₂ interface varies when the synchrotron beam is scanned from one end of the sample to the other end. A depth-dependent Fe spin structure in an applied magnetic field (applied along the bisector of the twin domains) was observed at 10 K, where the Fe spins closer to the interface are not aligned along the field direction. During magnetization reversal the spins of the top Fe layer rotate at a smaller field than the Fe spins closer to the interface. Upon decreasing the field from the fully aligned state in a strong positive magnetic field, the Fe spins coherently rotate up to the easy direction of MnF₂ (at $\pm 45^\circ$ from the applied field), then "jump" to the opposite direction of the easy axes (i.e., $\mp 45^\circ$), and then further rotate towards the negative applied field direction. The depth-dependence of the spin structure in an applied field and the rotation via the jump disappear at 150 K, i.e., above T_N of MnF₂.

Contents

1	Introduction	1
2	Basics of experimental techniques	5
2.1	Introduction	5
2.2	Mössbauer spectroscopy	5
2.2.1	The Mössbauer effect	5
2.2.2	Basics of Mössbauer spectroscopy	6
2.3	Conversion electron Mössbauer spectroscopy	8
2.4	Mössbauer spectroscopical parameters	11
2.4.1	Mössbauer linewidth and recoil-free events	11
2.4.2	Chemical or isomer shift (δ)	14
2.4.3	Second-order Doppler shift	15
2.4.4	Quadrupole splitting	16
2.4.5	Magnetic hyperfine field	20
2.4.6	Combined hyperfine interactions	22
2.4.7	Calibration and least-squares fitting of the Mössbauer spectra	23
2.5	X-ray Diffraction	23
2.6	SQUID Magnetometry	25
3	Nuclear resonant scattering of synchrotron radiation	27
3.1	Synchrotron radiation: production and control	27
3.2	Introduction to scattering techniques	31
3.3	NRS experimental setup	31
3.4	Nuclear resonant scattering: beat pattern	33
3.5	Simulation of the NRS time spectrum	34
4	Introduction to exchange bias	43
4.1	Introduction	43
4.1.1	Experimental observations of exchange bias	44
4.1.2	Theoretical Models explaining the observed Exchange Bias Effects	47
4.2	Exchange bias and spin structure	54
5	Magnetic Anisotropy and Hyperfine Interactions in MnF_2 and FeF_2	57
5.1	Introduction	57
5.1.1	Crystallographic and magnetic structure of MnF_2 and FeF_2	57
5.1.2	Anisotropies in MnF_2 and FeF_2	58
5.2	Sample preparation and characterization	62
5.3	Hyperfine interaction in FeF_2	66

6	Fe Spin Structure in Exchange Biased Fe/MnF₂ Bilayers	71
6.1	Introduction	71
6.2	Sample preparation and characterization	73
6.3	SQUID magnetometry: results	77
6.4	Conversion electron Mössbauer spectroscopy of Fe/MnF ₂ bilayers	79
6.4.1	CEMS measurement geometry	79
6.4.2	In-plane spin distribution models	81
6.4.3	Experimental details and CEMS results	83
6.5	CEMS results: discussion	89
6.5.1	Depth-dependent Fe spin structure at remanence	89
6.5.2	Influence of the cooling field on the Fe spin structure	93
6.5.3	Temperature dependence of the Fe spin structure	94
6.5.4	Memory effect of the Fe spin structure	96
6.6	Modeled angular Fe spin distributions in Fe/MnF ₂	97
6.6.1	Angular Fe spin distribution in remanence	97
6.6.2	Angular Fe spin distribution after field cooling	101
6.6.3	Memory of the angular Fe spin distribution	102
6.7	Supplementary vector SQUID magnetometry: results and discussion	103
6.8	Conclusions for the Fe spin structure in Fe/MnF ₂	106
7	Fe and FeF₂ Spin Structure in Exchange Biased Fe/FeF₂ Bilayers	109
7.1	Introduction	109
7.2	Sample Preparation and Characterization	111
7.3	CEMS Results	115
7.3.1	Experimental details and the hyperfine parameters	115
7.3.2	Temperature and depth dependent Fe spin structure	126
7.3.3	FeF ₂ -layer spin structure and the EFG components	131
7.4	SQUID magnetometry results	131
7.5	Conclusions for the Fe spin structure in Fe/FeF ₂	135
8	Nuclear Resonant Scattering: Fe Spin Structure in Fe/MnF₂	137
8.1	Introduction	137
8.2	Sample preparation and characterization	138
8.3	NRS experimental procedure	142
8.4	NRS results and discussion	143
8.4.1	Field dependent Fe spin rotation during magnetization reversal	143
8.4.2	Depth dependent Fe layer spin structure during magnetization reversal	148
8.4.3	Temperature dependence of the Fe spin rotation during magnetization reversal	150
8.4.4	Virgin and conventional remanent state spin structure	151
8.4.5	Fe spin rotation: H is perpendicular to cooling field H _{FC}	152
8.5	Conclusions: NRS results for Fe spin structure in Fe/MnF ₂	153
9	Summary	155
	Bibliography	157
10	Appendix	171

Chapter 1

Introduction

Exchange anisotropy is caused by the exchange coupling between two magnetic layers, namely one ferromagnetic (FM) layer adjacent to an antiferromagnetic (AFM) layer. The exchange anisotropy is established when the FM/AFM bilayer is cooled below the Néel temperature (T_N) of the AFM in the presence of an applied field. As a result, the ferromagnetic hysteresis loop shifts from its origin along the field axis which is known as the exchange bias effect. Even after fifty years of discovery of this effect by Meiklejohn and Bean [1], details of this phenomenon are not yet fully understood. Phenomenologically, the interfacial ferromagnetic spins are exchange coupled to the spins of the antiferromagnetic interface layer and, hence, the ferromagnetic spins favor to align in one direction due to strong exchange interaction. Hence, the exchange anisotropy is also known as unidirectional anisotropy. This property of the exchange biased bilayer is used in the read-write heads of magnetic storage devices such as computer hard discs, and also for various spin valve devices [2]. However, a full understanding of the exchange bias effect is necessary. For the basic understanding of exchange bias effect, a complete understanding of the temperature and depth dependent spin structure (at and away from the interface) is necessary.

In this work, we have used conversion electron Mössbauer spectroscopy (CEMS), and nuclear resonant scattering (NRS) of synchrotron radiation (synchrotron Mössbauer spectroscopy), supported by vector SQUID (Superconducting QUantum Interferences Device) magnetometry to investigate the depth and temperature dependent Fe spin structure in remanence and in an applied field during spin reversal in exchange biased Fe/MnF₂ and Fe/FeF₂ bilayers. These systems are among the most studied exchange bias systems and, hence, we have used Fe/MnF₂ and Fe/FeF₂ bilayers as model systems for our investigation.

Conversion electron Mössbauer spectroscopy is a powerful technique for the direct measurement of the spin structure at surfaces or buried interfaces, because CEMS is sensitive only to the Mössbauer nuclei, e.g., ⁵⁷Fe in our case. CEMS provides direct atomistic information about the direction of the Fe magnetic moment of the Mössbauer atom. As CEMS can also provide information about all the metallurgical and magnetic phases present in the sample, the information about intermixing at the interface can also be obtained. NRS of synchrotron radiation is a technique similar to CEMS, however, the main advantage of NRS over CEMS is that it provides a short measurement times and spatial resolution.

In this thesis, a short introduction to CEMS and NRS techniques are given in Chapter 2 and Chapter 3, respectively. A short introduction to the exchange bias effect; the models, the techniques and the materials used to study exchange bias; and a short review of the spin structure of the ferromagnetic layer studied up to now, is given in Chapter 4. As a better understanding of the antiferromagnet used is necessary to study the exchange bias effect and the spin structure of the ferromagnet. A detailed X-ray diffraction (XRD) and CEMS study of the antiferromagnetic MnF_2 and FeF_2 is given in Chapter 5, along with a description on the uniaxial anisotropy as studied in the literature.

By depositing a ^{57}Fe probe layer just at the Fe/MnF_2 interface or away from the interface, we have obtained the remanent-state Fe spin structure both above and below T_N of the antiferromagnet. We have also studied a possible memory effect of the low- or high- temperature spin structure during field cooling(FC) - zero-field heating (ZFH), or zero-field cooling (ZFC)-ZFH in remanence. This will be describe in Chapters 6 and 7.

All the existing exchange bias models, except the model by Kiwi et al. [3–5], assume a homogenous spin structure throughout the whole depth of the ferromagnetic layer. By using X-ray magnetic circular dichroism (XMCD), Ohldag et al. [6] have observed that at the interface a fraction of ferromagnetic spins is pinned along the AFM spin directions. However, this alignment changes when the film becomes thicker and this does not directly provide the depth dependent spin structure as the induced anisotropy of the whole layer is not the same for smaller and larger thicknesses. Exchange bias is the well known interfacial effect, but there are a few methods available to directly probe the sample in order to get depth dependent information. Nuclear resonant scattering (NRS) of synchrotron radiation is among the most suitable methods for obtaining depth dependent information. We have used NRS for obtaining the depth dependent Fe layer spin structure on the same sample and at the same magnetic field, during magnetization reversal in Fe/MnF_2 , both above and below T_N ($= 67 \text{ K}$) of MnF_2 . This is the subject of Chapter 8.

The ferromagnetic reversal mode (whether coherent rotation or nucleation and domain propagation) during magnetization reversal in exchange biased Fe/MnF_2 and Fe/FeF_2 still remains a debate. By using polarized neutron reflectometry on twinned Fe/FeF_2 system Fitzsimmons et al. [7] have observed that: (1) when the sample was field cooled from above T_N of the antiferromagnet to below T_N , with the field applied exactly between the two twin directions, the ferromagnet reverses by coherent rotation during the first reversal (i.e., for the left branch of the hysteresis loop) and by nucleation and domain propagation for the right branch of the hysteresis loop. (2) When the sample was field cooled with the cooling field applied along one of the twin directions, Fitzsimmons et al. have observed a coherent rotation type of reversal mode for both branches of the hysteresis loop. By using the method of magnetoresistance measurement, Krivorotov et al. [8] have concluded that in Fe/MnF_2 for the left branch of the hysteresis loop, the magnetization reverses via coherent rotation, while for the right branch of the hysteresis loop, the magnetization reverses via domain nucleation and propagation. In exchange biased Co/CoO , Radu et al. [9] have observed that the domain nucleation and propagation type of magnetization reversal occurs only on the asymmetric branch of the hysteresis loop (left branch in their case) and is also associated with training effect. Theoretically, it has been calculated by Beckmann et al.[10] that the asymmetry in the

hysteresis loop is observed when the cooling field direction is (even slightly) different from the exact bisector direction of the two antiferromagnetic FeF_2 twin directions. By using nuclear resonant scattering of synchrotron radiation, we have also determined the reversal modes in Fe/MnF_2 , both above and below T_N , of the antiferromagnet MnF_2 . This will be described in Chapter 8.

The work presented in this thesis will provide a better understanding of the Fe spin structure in exchange-biased Fe/MnF_2 and Fe/FeF_2 bilayers.

Chapter 2

Basics of experimental techniques

2.1 Introduction

In the last decades, Mössbauer spectroscopy has gained increasing interest for the analysis of structural, chemical and magnetic properties of many crystalline and amorphous substances including chemical, biological and magnetic materials. Because of sharp nuclear energy level transitions, Mössbauer effect provides an extremely high energy resolution in the range of neV (with the γ -ray photon energy in the keV range) and, hence, Mössbauer effect can be used to probe the electronic environment of a nucleus via the hyperfine interactions. In solids, the property of the individual atoms are affected by the other atoms present in its close surrounding. Mössbauer spectroscopy may be used to probe the change in the hyperfine interaction parameters to characterize the probing atom and its surroundings. Due to its importance in characterizing materials, Mössbauer spectroscopy is widely used in many branches of science, including physics, chemistry, materials science, biology, medical sciences and geology etc. Recently, Mössbauer spectroscopy is used for exploring the surface of the planet Mars. In this chapter, the basics of Mössbauer spectroscopy and other experimental techniques used in this work will be briefly described (except the experimental technique "nuclear resonant scattering" of synchrotron radiation, which will be described in Chapter 3).

2.2 Mössbauer spectroscopy

2.2.1 The Mössbauer effect

Nuclei in atoms undergo a variety of energy level transitions. These transitions are often associated with the emission or absorption of one or more photons (γ -ray) and may also involve the processes of absorption of quasi-particles like phonons (lattice vibrational excitations), if the nucleus is embedded in a solid. During the absorption or emission process of a free atom the nucleus recoils, due to conservation of momentum. Thus, for the free atom the emitted γ -ray has lower energy than the nuclear transition energy. This can also be observed in a γ -ray emission and absorption process of atoms bound to a solid, where the emitting and absorbing nuclei recoil. In these circumstances, resonant emission or absorption does not occur, meaning that the energy of the resonantly absorbed photon has to be greater than that of the transition energy in order to compensate the

recoil energy of the atom. However, in 1957, Rudolph Ludwig Mössbauer discovered the phenomenon of recoil-less emission and absorption of γ -rays (nuclear resonance), later, widely known as the “Mössbauer effect” [11–13], for which R. L. Mössbauer received the nobel prize for physics in 1961.

2.2.2 Basics of Mössbauer spectroscopy

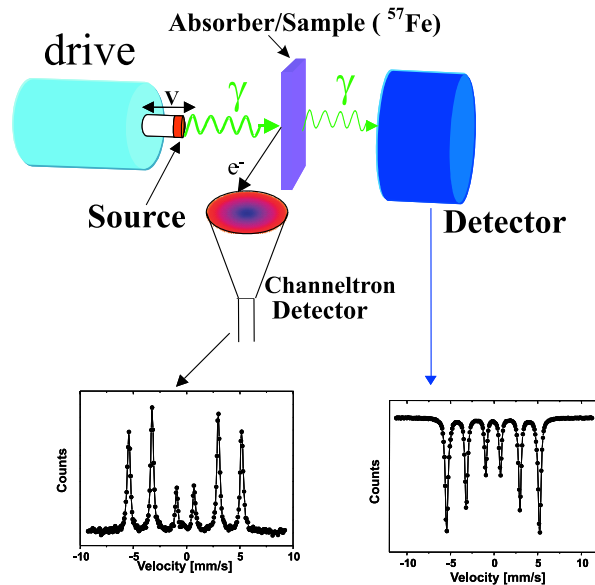


Figure 2.1: Schematic diagram of the experimental set-up for Mössbauer spectroscopy. The spectrum measured by CEMS (scattering) looks inverted in comparison to the transmission (absorption) spectrum, but both spectra provide the same physical information.

A spectrum, in general, means a plot of the number of counts versus a range of energies. The technique of Mössbauer spectroscopy uses the γ rays emitted from the nuclei of a radioactive source to probe the properties of the sensitive nuclei in the sample to be studied. In order to probe the energy levels of nuclei in different sample environments the energy of the Mössbauer γ -ray must be scanned. This is achieved by moving the source relative to the absorber. The source contains the parent nucleus of the Mössbauer isotope, embedded, generally, in a rigid matrix. The source is generally mounted on a Mössbauer drive, where the Doppler effect produces an energy shift in the gamma ray energy, allowing us to match the resonant energy level(s) in the absorber. The γ -rays emitted from the source pass through the material (absorber) being investigated and are detected and counted by a detector. If the nuclei in the source and absorber are in exactly the same environment (i. e. the energy of the nuclear transitions is equal for both nuclei) the gamma rays will be resonantly absorbed and an absorption peak will be observed. During scanning of the energy of the γ -ray, the energy of the emitted γ -ray will match with the energy difference of nuclear levels in the absorber, and the γ -quantum is absorbed, while the rest of the γ -quanta (without energy matching) pass through the sample and are then detected by a detector. Fig. 2.1 shows the simplest experimental arrangement for a Mössbauer experiment. To measure a Mössbauer spectrum one needs

three different equipments: (a) the Mössbauer source, (b) the detector for the transmitted photons (or for emitted conversion electrons in a backscattering experiment), and (c) the sample (absorber) and the equipment necessary to produce the necessary sample environment (temperature, magnetic field, high pressure, etc.).

Mössbauer source

Mössbauer sources generally employ a metallic host matrix in order to minimize the possible chemical effects of the precursor nuclear transition. The matrix is cleverly chosen by using the knowledge on Chemistry, metallurgy and nuclear physics. Inside the matrix, Mössbauer sources are formed by exciting the atoms or isotopes to their Mössbauer levels. This is done in nuclear reactors or accelerators according to proper nuclear reaction. Details on preparation and the influence of the matrix can be referred from ref. [14]. ^{57}Co (for ^{57}Fe), ^{119}Sn (for ^{119}Sn), ^{149}Eu (for ^{151}Eu), ^{161}Tb (for ^{161}Dy) and ^{197}Pt (for ^{197}Au) are a few among the many different Mössbauer sources generally used for the study of condensed matter physics. The radiations coming from a Mössbauer source is rather complex. It consists of (a) the resonant γ -rays from the excited to a ground state, (b) non-resonant γ -rays from the same transitions, (c) radiation from all other transitions in the nucleus, and (d) secondary radiation produced in the matrix. Except the resonant γ -rays produced by the transition from the excited state to the ground state, which produces the Mössbauer effect, all other type of radiations contribute to the background. In this thesis only ^{57}Co source is used for performing Mössbauer spectroscopy. This nuclide is produced by the (d, p) reaction on ^{56}Fe at a cyclotron. The strength of the sources used in the work is generally ~ 100 mCi ($1 \text{ Ci} = 3.7 \times 10^{10}$ disintegrations per second $= 3.7 \times 10^{10}$ Bq). The source is mounted on a constant-acceleration Mössbauer drive, which is in principle similar to the the transducer of a loudspeaker and offers the possibility to generate triangular, sinusoidal or square-like wave forms of the velocity of the source. Because of this back-and-forth motion of the source, the energy of the emitted photon, as seen by the sample (which is at rest in the laboratory) changes due to the Doppler effect. For a ^{57}Co source (with the γ -ray energy E_γ of 14.4125 KeV) mounted on a Mössbauer drive, which is vibrating with a velocity v of about ± 10 mm/s, the energy of the γ -rays changes by about $\delta E = \pm 500$ neV (according to the equation $\delta E = (v/c) \cdot E_0$, $c =$ velocity of light) [15].

Detectors

After the Mössbauer nucleus has been excited by recoilless absorption of γ -ray it decays to the ground state by emitting either γ -rays or internal conversion electrons (which may also lead to secondary emission of X-rays). The nuclear level and decay scheme of ^{57}Fe is shown in Fig. 2.2. There are three different types of detectors [14] used to detect these emitted γ -rays or X-rays; (a) NaI(Tl) scintillation counters, (b) proportional counters, and (c) Ge(Li) solid state counters. In this work, only proportional counters were used for counting the transmitted γ -rays from the sample. (The channeltron detectors used to detect the emitted electrons will be discussed in the next section 1.3.) The proportional counters are generally filled (~ 1 atm pressure) with either argon, xenon, krypton, or neon (about 95 %) and methane or nitrogen (quenching gas, about 5%). The counters are directly connected to a (low capacitance) preamplifier and the high voltage (~ 3 keV) power supply. The signal from the preamplifier is then amplified by a main

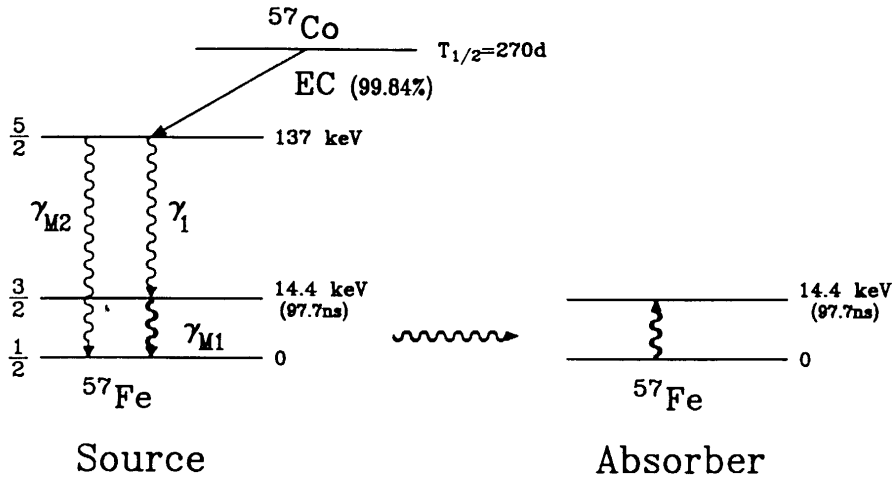


Figure 2.2: Nuclear transition scheme of ^{57}Fe (^{57}Co source)(left). γ_{M1} is the widely used 14.4125 keV Mössbauer transition. EC = electron capture. Absorption process for the 14.4125 keV γ -ray in the ^{57}Fe absorber (right) [16].

amplifier and counted by a multichannel analyzer. The counts in each channel are added for a large number of energy scans of the source until one gets a good statistics of the spectrum, which leads to the Mössbauer spectrum.

Sample and sample environment

Mössbauer effect is sensitive only to the material containing the Mössbauer isotope, which uses the nuclear transition of the Mössbauer nucleus as the probe. The intensity of a Mössbauer spectrum is limited by the recoilless fraction f . Because of the recoil it is impossible to measure a Mössbauer spectrum of a liquid or a gas. The recoilless fraction of γ -rays varies from solid to solid depending on the strength of the chemical binding of the Mössbauer atom to the solid or its Debye temperature. In this work, thin film samples containing ^{57}Fe as the probing nucleus are used, namely thin films and bulk materials of ^{57}Fe and $^{nat}\text{FeF}_2$. As ^{nat}Fe (natural Fe) contains 2.14 % of ^{57}Fe , ^{nat}Fe containing bulk materials are generally used for the study by Mössbauer spectroscopy. For the measurement of the Mössbauer spectrum at various sample environments various equipments can be used. For example, bath cryostat containing a superconducting (solenoid) magnet may be used for measurements at various temperatures and with applied magnetic fields. For changing and detecting temperature of the sample, electrical heaters and temperature sensors (such as carbon-glass or Pt resistance thermometers or diodes) may be used. In this work, Mössbauer measurements were performed in the temperature range from 4.2 K to 300 K, and without applied magnetic field. In some cases, the sample was field-cooled in an applied field by using an electromagnet.

2.3 Conversion electron Mössbauer spectroscopy

After the absorption of the γ quantum, the excited ^{57}Fe Mössbauer nucleus may decay after a mean lifetime τ of 1.41×10^{-7} s via reemission of a 14.4125 keV γ -quantum or, alternatively, via the transfer of its energy to its own electron shells, preferentially

to the K-shell, being closest to the nucleus. In this way a K-conversion electron is emitted from the ^{57}Fe atom with a kinetic energy of $E_{kin} = E_{\gamma} - E_{K-binding} \approx 14.4 - 7.1 = 7.3$ keV, where E_{γ} = energy of the γ -quantum and $E_{K-binding}$ = binding energy of the electron in the K-shell. In a similar process L- and M-conversion electrons are also emitted, but their probability is smaller, because their average distance from the nucleus is higher and the difference in energy between E_{γ} and $E_{binding}$ becomes larger for these shells. After the conversion electron is emitted, electrons from higher shells jump to the hole in the shell from which the conversion electron was emitted. As a result a variety of Auger electrons and X-rays of different energies are produced. The schematic diagram of the decay channels of various conversion and Auger electrons and the X-rays is shown in Fig. 2.3. The method of obtaining a Mössbauer spectrum by measuring these conversion electrons and the secondary electrons (after emission of the conversion electron) is known as conversion electron Mössbauer spectroscopy (CEMS). Because of the limitation in energy of the conversion electrons (maximum 7.3 keV for K-conversion electron), CEMS is sensitive to a limited depth of the probing material (about 100 nm in iron). The emitted electrons lose their energy by scattering with other electrons and nuclei during their path to the surface of the sample. Due to the isotope-selective nature of the Mössbauer effect and monolayer sensitivity of CEMS, CEMS is suitable for the study of various properties at the surfaces, subsurface regions and interfaces of nanoscale materials including thin films and heterostructures. In CEMS one counts the number of electrons originating from Mössbauer events versus the source velocity v ; the method is sensitive even to a coverage of 0.1 monolayer of ^{57}Fe .

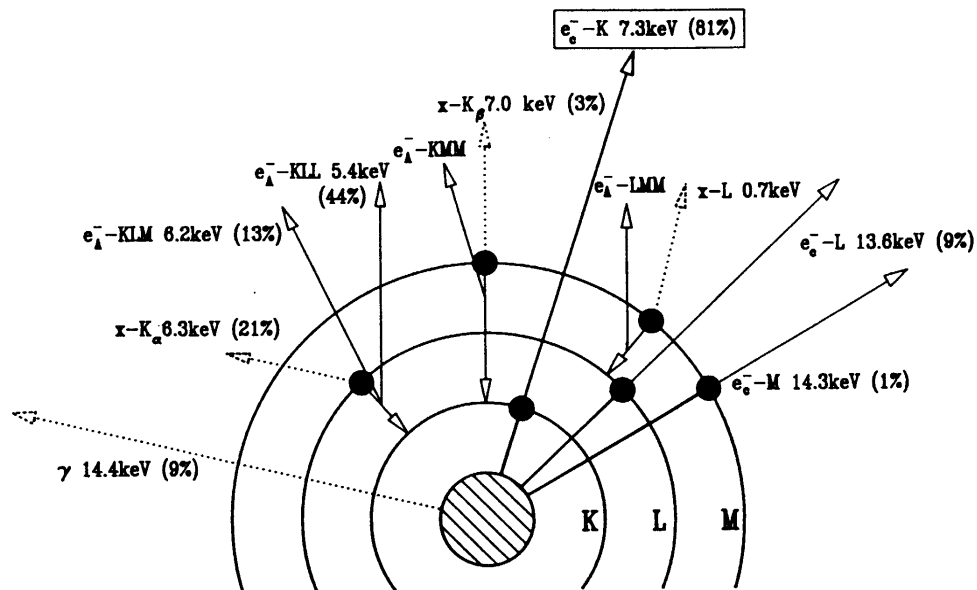


Figure 2.3: Decay channels of the 14.4125 keV excited state of ^{57}Fe . The ^{57}Fe nucleus decays by emission of a photon or a conversion electron. The conversion electron emission is followed by emission of various secondary low energy electrons or X-rays [16].

The schematic diagram of the measurement setup is shown in Fig. 2.1, where the channeltron is the detector for the electrons. The efficiency of a channeltron is low at 7.3 keV. Many other supportive arrangement should be done in order to increase the

efficiency of a channeltron. In order to avoid the scattering of the electrons by various gas molecules during its path to the channeltron, the channeltron and the sample are kept in high or ultrahigh vacuum. To collect more electrons from the sample surface the channeltron has a conical shape with a long tail. To increase the detection efficiency of the channeltron, the cone of the channeltron and the sample are generally surrounded by a MgO-coated aluminum foil, which serves as a secondary electron emitter. The conversion and Auger electrons from the sample are accelerated and directed towards the channeltron by applying a small positive voltage ($\sim +100$ Volts) at the collecting end (cone) of the channeltron. A high voltage ($\sim +3000$ Volts) is applied to the other end (tail) of the channeltron. Hence, a voltage gradient is created from one to the other end of the channeltron, which functions as an electron multiplier. A preamplifier is connected to the high voltage end (tail) of the channeltron, which is then connected to the main amplifier and multichannel analyzer for the measurement of the Mössbauer spectrum. As high vacuum is the requirement for the detection of electrons, the channeltrons are very useful for the measurement of the Mössbauer spectrum at low temperatures.

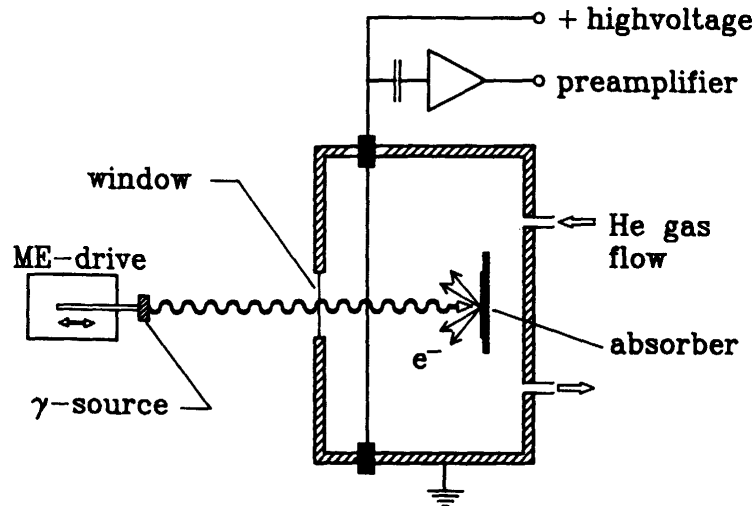


Figure 2.4: Schematic diagram of a CEMS gas flow proportional counter [16].

For the measurement of conversion electrons at room temperature (RT) a different kind of counter is used. The sample is mounted inside of a proportional counter. Fig. 2.4 shows the schematic view of the room temperature gas flow proportional counter used for CEMS. A continuous flow of high purity He + 4% CH₄ gas mixture is supplied. Here, CH₄ acts as the quenching gas. The conversion electrons take part in an ionization and re-ionization process producing a cloud of negative charges which travel towards the high (+) voltage wire which serves as cathode. The number of events in this process is counted, which gives rise to the Mössbauer spectrum. In this work, along with this gas flow proportional counter (at room temperature), a home-made proportional counter filled with He+ 4% CH₄ gas (constant pressure of about 500 mbar) is used for the CEMS measurement. In this case, this counter works down to 40 K. Here, the impurities inside the He gas seems to work as the quenching gas at low temperatures (when CH₄ is condensed), and, when liquid He is used for cooling the sample with

the detector further down below 40 K, the quenching gas condenses at the inner walls of the proportional counter and, hence, no ionization process could be detected below 40 K.

2.4 Mössbauer spectroscopical parameters

The number of lines and the position of the lines of a Mössbauer spectrum is determined by the contributions of two effects: (i) hyperfine interaction and (ii) relativistic effects. Hyperfine interaction is the interaction of the nucleus with the surrounding electrons. The important hyperfine parameters (such as isomer shift, quadrupole splitting and magnetic hyperfine field) and relativistic parameters (such as second-order Doppler shift) are described below. The intensity of a Mössbauer line also provides important information about the material under investigation.

2.4.1 Mössbauer linewidth and recoil-free events

Heisenberg's uncertainty relation, $(\Delta E) \cdot (\Delta t) \geq \hbar$, can be used to determine the linewidth of a Mössbauer spectrum. A Mössbauer transition has a mean lifetime τ of the excited state or a half lifetime $t_{1/2} = \tau \cdot \ln 2$, while the ground state is stable and has an infinitely long lifetime, i.e. its energy level is well defined. Hence, the uncertainty principle suggests a natural linewidth [17]:

$$\Delta E = \Gamma = \frac{\hbar}{\tau} = \frac{0.693\hbar}{t_{1/2}} \quad (2.1)$$

For instance, the half life of the excited state of ^{57}Fe ($E_\gamma = 14.4$ keV) is $t_{1/2} = 0.977 \times 10^{-7}$ s. Thus the natural linewidth $\Gamma = 4.7 \times 10^{-9}$ eV. The energy distribution of the emission and absorption process can be derived from the Breit-Wigner formula, which results in a Lorentzian shape for a Mössbauer line. The intensity of the Mössbauer line, combined to its shape, can be expressed by the total cross section ($\sigma(E)$) [18]:

$$\sigma(E) = \sigma_0 \frac{\Gamma^2}{\Gamma^2 + 4(E - E_\gamma)^2} \quad (2.2)$$

with the maximum crosssection

$$\sigma_0 = \frac{\lambda^2}{2\pi} \frac{2I_e + 1}{2I_g + 1} \frac{1}{\alpha_t + 1}, \quad (2.3)$$

where I_e and I_g are the nuclear spins of the excited and ground state, respectively. λ is the wave length of the γ -ray and α_t is the total internal conversion coefficient which takes into account the competing modes of transition. For ^{57}Fe , α_t is in the order of 10.

The intensity of the Mössbauer lines, depends on the recoil energy of the emitting and absorbing atom. The typical energy required for the displacement of an atom to another position in a solid is in the range of 15-30 eV. Thus, the emitting or absorbing atom in a solid is relatively strongly bound. The recoil energy (e.g., 2×10^{-3} eV for ^{57}Fe) following emission (or absorption) of a Mössbauer γ -ray is insufficient to displace the Mössbauer atom, but the atom may change its vibrational motion. If the vibrational motion is not changed as a result of the emission (or absorption) of the γ -ray, the recoil energy must

be absorbed by the solid as a whole. Since the mass M_{tot} of the crystal is about 10^{23} times larger than the mass M of a single atom, the recoil energy $E_R = (\hbar^2 k^2)/(2M_{tot})$ becomes infinitely small. This results in an unbroadened, unshifted "zero-phonon" line or Mössbauer line in the γ -spectrum. The fraction of emitted (or absorbed) unshifted γ -ray emissions (or absorptions) (relative to the total number of events) is the recoilless fraction. This recoilless fraction is known as Debye-Waller factor or Lamb-Mössbauer factor or f -factor.

Considering the atoms in a solid as having harmonic interaction forces, the mean kinetic energy $(1/2)Mv^2$ per degree of freedom is the same as that for an ideal gas $((1/2)k_B T)$ and is also equal to the mean potential energy $(1/2)M\omega^2 \langle x^2 \rangle$. Using quantum theory, the mean-square vibrational amplitude for the lowest Einstein oscillator level can be expressed as [18]:

$$\langle x^2 \rangle = \frac{\hbar}{2M\omega} \quad (2.4)$$

where M = mass of the Mössbauer atom, \hbar = Planck's constant = $h/2\pi$ and ω = frequency of the oscillator level spacing. Considering only one-phonon excitations and multiphonon processes being infrequent, the recoil energy can be expressed as [18]:

$$E_R = (1 - f)\hbar\omega \quad (2.5)$$

$$\Rightarrow f = 1 - \frac{E_R}{\hbar\omega} = 1 - \frac{2\hbar\omega M}{\hbar^2 k^2} \quad (2.6)$$

The above equation can be expressed in terms of the mean vibrational amplitude of the oscillator [19]:

$$f = e^{-k^2 \langle x^2 \rangle} \quad (2.7)$$

where k = wave number of the photon.

By using the Debye model for the vibration of the atoms in a solid, i.e. there exists a continuum of oscillator levels in the solid and a frequency distribution quadratic in ω , $\langle x^2 \rangle$ may be expressed as [19]:

$$\langle x^2 \rangle = \frac{3\hbar^2}{4Mk_B\theta_D} \left[1 + 4 \left(\frac{T}{\theta_D} \right)^2 \int_0^{\theta/T} \frac{y}{e^y - 1} dy \right] \quad (2.8)$$

where $y = \frac{\hbar\omega}{k_B T}$ and θ_D = Debye temperature, k_B = Boltzmann constant and the integral in eq. (2.8) is the Debye integral. The Debye temperature can be visualized as an approximate limit, which separates the high temperature region, where the oscillators or the solid can be treated in a classical fashion, from the low temperature region, where quantum mechanical effects are significant.

The above equation (eq. (2.8)) explains that the Debye-Waller factor is temperature dependent. The temperature dependence of $\langle x^2 \rangle$ and of the Debye-Waller factor, $f = f(T)$, considering different temperature regimes are given below.

When $T \gg \theta_D$,

$$\begin{aligned} \langle x^2 \rangle &= \frac{3\hbar^2}{Mk_B\theta_D} \left(\frac{T}{\theta_D} \right) \\ &\Rightarrow \langle x^2 \rangle \propto T. \end{aligned} \quad (2.9)$$

Hence, at high temperatures, $\langle x^2 \rangle$ of $\ln f$ is linear in T , and the slope depends on θ_D .

For $T \ll \theta_D$,

$$\begin{aligned} \langle x^2 \rangle &= \frac{3\hbar^2}{Mk_B\theta_D} \left[\frac{1}{4} + \frac{\pi^2}{6} \left(\frac{T}{\theta} \right)^2 \right] \\ &\Rightarrow \langle x^2 \rangle \propto T^2, \end{aligned} \quad (2.10)$$

i.e., at low temperatures, $\langle x^2 \rangle$ is proportional to T^2 , and the curvature depends on θ_D .

For $T = 0$ K,

$$\langle x^2 \rangle = \frac{3\hbar^2}{4Mk_B\theta_D} \Rightarrow f(T = 0) = \exp\left(-\frac{3\hbar^2 k^2}{4Mk_B\theta_D}\right) \quad (2.11)$$

Classically, at $T = 0$, no oscillations are excited, i.e., $\langle x^2 \rangle = 0$ and eq. (2.7) implies $f = 1$. However, quantum mechanically, f has the highest value at absolute zero, but is always less than one ($f < 1$), due to the quantum-mechanical zero-point vibrations, where $\langle x^2 \rangle \neq 0$ and $f < 1$.

From the above discussions it is clear that the intensity of the Mössbauer lines will be changed by varying the Debye-Waller factor f (e.g., by changing temperature, pressure, lattice structures, environment (i.e., introducing atoms close to defects, at surfaces or interfaces, etc.)), because this changes the mean-square displacement $\langle x^2 \rangle$ of the Mössbauer atoms. The integrated intensity (area) under the spectrum is proportional to the recoilless fraction f of the Mössbauer atom. If the recoilless fraction is higher, the Mössbauer line intensity and the spectral area will be higher. Hence, under proper experimental conditions, the Debye-Waller factor and the intensity of the Mössbauer spectra may be employed to derive the components of phase mixtures in a material and also to study phase transformations. In Chapter 6 it will be discussed that we have obtained the thickness of a Fe/FeF₂ bilayer film from consideration of the f -factor. The Debye-Waller factor f has following important behaviors:

1. The Debye Waller factor decreases with increasing recoil energy.
2. The Debye Waller factor is higher at low temperatures, and hence, low temperatures ($T < \theta_D$) are favorable for the observation of large Mössbauer effect.
3. As the Debye-Waller factor depends on the mean-square vibrational amplitude of the atoms, one can obtain integral (indirect) information about the phonon frequency spectrum $g(\omega)$ by measuring the Debye-Waller factor.

2.4.2 Chemical or isomer shift (δ)

The isomer shift (δ) arises due to the non-zero volume of the nucleus in, both, the excited and ground state and due to the different s -electron charge density at the nucleus in source and absorber. (The electron charge density due to other electrons (p - and d -electrons) at the nuclear site is negligible or zero.) This causes an electric monopole (Coulomb) interaction which alters the nuclear energy levels. The volumes of the nucleus in its ground and excited state are different (for instance, the nuclear radius of ^{57}Fe in the first excited state is smaller than that of the ground state) and, the s -electron densities are affected by the local chemical environment. A change of the nuclear size and/or the chemical environment changes the nuclear energy levels and this is observed by a shift of the Mössbauer spectrum which is known as the chemical or isomer shift. The isomer shift may be expressed by the following relationship [17]:

$$\delta = C \frac{\Delta R}{R} (|\Psi_A(0)|^2 - |\Psi_S(0)|^2) \quad (2.12)$$

where $C = (4\pi/5)Ze^2R^2$ is a constant for a given isotope containing nuclear parameters (where Z = atomic number of the Mössbauer atom and e = electronic charge, R = mean nuclear radius). $\Delta R/R = (R_{ex} - R_{gr})/R$, is the relative change of the mean nuclear radius between the excited and the ground state. The term inside the parenthesis represents the difference in the total electron density (evaluated at the nucleus) between the absorber and the source. In a typical Mössbauer experiment the position of this resonant Mössbauer line at the Doppler velocity v is given by

$$v = (c/E_\gamma) C \frac{\Delta R}{R} (|\Psi_A(0)|^2 - |\Psi_S(0)|^2) \quad (2.13)$$

in velocity units, where E_γ is the energy of the resonant γ -ray.

The above discussion shows that any difference in the electronic environment between source and absorber produces a shift in the resonance energy of the transition. However, this is a relative shift, and a suitable reference is necessary, such as a specific source or absorber. In a Mössbauer experiment usually one uses a standard source, e.g., ^{57}Co in a Rh matrix, and, hence, $|\Psi_S(0)|^2$ is a constant in eq. (1.12). In this case, the isomer shift can be positive or negative depending on whether the value $\Delta R/R$ is positive or negative, i.e. the radius of the excited state is larger or smaller than that of the ground state. As the nuclear radius of ^{57}Fe in the excited state is smaller than that of the ground state, the combination of a ^{57}Co (Rh matrix) source and an α -Fe absorber produces a negative isomer shift (in velocity units) of $\delta = -0.106$ mm/s at RT. In all of the results presented in this thesis, the isomer shifts are given relative to an α -Fe foil at room temperature as a standard reference absorber, while the source was always ^{57}Co in Rh matrix.

In all of the following Chapters (except Chapter 3), it will be noticed that the isomer shifts of ^{57}Fe in different chemical environments are different. In addition to the change of the nuclear radius of the excited state, a change of the valence state of Fe, e.g., Fe in a divalent Fe^{2+} state or in a trivalent Fe^{3+} state (with the electronic configurations $1s^22s^22p^63s^23p^63d^6$ or $1s^22s^22p^63s^23p^63d^5$, respectively) also changes the isomer shift appreciably, although the number of s -electrons is the same. The only difference is the number of electrons in the d -orbital. This difference in the isomer shift of the above two states of Fe arises indirectly due to the screening of the $3s$ electrons by the

3d electrons. By adding one electron to the 3d-orbital of Fe, the attractive Coulomb potential for the 3s-electrons is reduced, which and causes the wave function to expand and also to reduce its charge density at the nucleus. In this way, the removal of the 6th 3d-electron by going from Fe^{2+} to Fe^{3+} increases the charge density at the nucleus and produces a sizable isomer shift towards smaller values. The isomer shift observed for FeF_2 (a divalent iron compound that will be discussed in Chapters 4 and 6) is different from that observed for metallic bcc-Fe.

2.4.3 Second-order Doppler shift

The atoms in a solid are vibrating, in 3 dimensions, about their mean position with many different frequencies (ω). The frequency distribution is different for different materials, and is given by the vibrational (or phonon) density of states $g(\omega)$. The Doppler effect equation can be applied to the case of random thermal motion of atoms in a solid [14, 20, 21]. The relativistic expression for the Doppler effect is:

$$\nu_{source} = \nu_{obs} \left[\left(1 - \frac{\vec{V} \cdot \vec{r}}{c} \right) / \left(\sqrt{1 - \frac{V^2}{c^2}} \right) \right] \quad (2.14)$$

where \vec{r} are the unit vector in the direction of motion of the source, ν_{source} and ν_{obs} are the frequencies of the source and observer, respectively, and \vec{V} is the velocity of the observer.

Expanding the denominator and neglecting the higher order terms lead to,

$$\nu_{source} \approx \nu_{obs} \left(1 - \frac{\vec{V} \cdot \vec{r}}{c} \right) \left(1 + \frac{V^2}{2c^2} \right) = \nu_{obs} \left(1 - \frac{\vec{V} \cdot \vec{r}}{c} + \frac{V^2}{2c^2} - \frac{\vec{V} \cdot \vec{r}}{c} \cdot \frac{V^2}{2c^2} \right) \quad (2.15)$$

Neglecting the 3rd order term, one obtains:

$$\nu_{source} \approx \nu_{obs} \left(1 - \frac{\vec{V} \cdot \vec{r}}{c} + \frac{V^2}{2c^2} \right) \quad (2.16)$$

$$\Rightarrow \frac{\nu_{obs} - \nu_{source}}{\nu_{obs}} = \frac{\delta\nu}{\nu} = \frac{\vec{V} \cdot \vec{r}}{c} - \frac{V^2}{2c^2} \quad (2.17)$$

The first term is a linear component of velocity and is the linear Doppler effect. The linear Doppler effect is related to the motion of the radiating or absorbing atoms or nuclei, which results in broadening of the gamma rays, and hence, of the Mössbauer line, for a gas or liquid, where diffusive motion of the atoms occur. However, because of thermal motion of atoms in a solid, the velocity changes in direction at frequencies characteristic of lattice vibrations ($10^{12} - 10^{13} \text{ s}^{-1}$), i.e., many oscillations take place within the lifetime of the nuclear levels $10^{-7} - 10^{-8} \text{ s}$. Since positive and negative velocity occurs with equal probability, the time average of the term $\frac{\vec{V} \cdot \vec{r}}{c}$ vanishes. However, the second order term will not average to zero, because it only depends on the square of the magnitude of velocity, but not on its direction. Hence, equation (2.17) reduces to the term of second order in the velocity:

$$\frac{\delta\nu}{\nu} = -\frac{\langle V^2 \rangle}{2c^2} \quad (2.18)$$

where $\langle V^2 \rangle$ is the mean square velocity of the atoms in the solid. Notice the negative sign in eq. (1.18), which leads to a “red shift”.

The above equation (2.18) suggests that there is a shift of the Mössbauer line known as second-order Doppler (SOD) shift. The SOD shift can be evaluated by taking the value of the mean-square thermal velocity, for instance, of the ^{57}Fe atoms in the material. The mean-square thermal velocity is obtained by averaging over all the modes of the lattice vibrations.

$$\langle V^2 \rangle = \int V^2 g(\omega) d\omega,$$

where $g(\omega)$ is the frequency distribution function or the vibrational density of states. The SOD shift depends on the phonon density of states $g(\omega)$. Using the Debye model of lattice vibrations and assuming atoms as isotropic harmonic oscillators one obtains

$$\frac{\delta\nu}{\nu} = -\frac{9k_B\theta_D}{2Mc^2} \left[\frac{1}{8} + \left(\frac{T}{\theta_D} \right)^4 \int_0^{\frac{\theta_D}{T}} \frac{y^3}{e^y - 1} dy \right] \quad (2.19)$$

For the comparison of the chemical shifts at low temperature, it is useful to consider eq.(2.19) when $T \rightarrow 0$ K. For very low temperatures, $T \ll \theta_D$, eq. (2.19) reduces to

$$\frac{\delta\nu}{\nu} = -\frac{9k_B\theta_D}{2Mc^2} \left[\frac{1}{8} + \frac{\pi^4}{15} \left(\frac{T}{\theta_D} \right)^4 \right] \approx -\frac{9k_B\theta_D}{16Mc^2} \quad (2.20)$$

This equation implies that the zero-point vibrational term is a function of the Debye temperature θ_D .

On the other hand, for high temperatures $T \gg \theta_D$, one obtains from eq. (1.19):

$$\frac{\delta\nu}{\nu} = -\frac{3k_B T}{2Mc^2} \left[1 + \frac{1}{20} \left(\frac{\theta_D}{T} \right)^2 - \frac{1}{1680} \left(\frac{\theta_D}{T} \right)^4 + \dots \right] \approx -\frac{3k_B T}{2Mc^2} \quad (2.21)$$

According to the equation (2.21) the second-order Doppler shift is independent of Debye temperature θ_D and has a linear temperature dependence at high temperatures.

The second-order Doppler shift ($\delta_{SOD}(T)$) adds to the chemical (isomer) shift of the material (δ_{chem} , a constant of temperature) to give the measured total isomer shift (“center” line shift), δ_{total} , of the center of gravity of a Mössbauer spectrum [26]:

$$\delta_{total}(T) = \delta_{chem} + \delta_{SOD}(T) \quad (2.22)$$

In Chapters 6 and 7, the Debye model is used for the fitting of the observed total isomer shift (center shift) (chemical plus second order Doppler shift) of the Mössbauer spectra measured at various temperatures.

2.4.4 Quadrupole splitting

The interaction of the nuclear electric quadrupole moment eQ with the principal component of the diagonalized electric-field gradient (EFG) tensor at the site of the

nucleus splits the nuclear states into sublevels known as quadrupole splitting. The nuclear quadrupole moment reflects the deviation of the nucleus from spherical symmetry. An oblate (flattened) nucleus has a negative quadrupole moment, while a prolate (elongated) one has a positive quadrupole moment. Nuclei with spin zero or $\frac{1}{2}$ are spherically symmetric and have zero quadrupole splitting. Hence, ^{57}Fe with $I = \frac{1}{2}$, the ground state, exhibits no quadrupole splitting. However the excited state with $I = \frac{3}{2}$ has a quadrupole moment and shows quadrupole splitting. There are few exceptions where the cubic lattice environment also produces quadrupole splitting. Some examples are ^{161}Dy Mössbauer spectrum of Dysprosium iron garnet, and ^{169}Tm Mössbauer spectrum of TmFe_2 , where the rare-earth (Dy or Tm) site is cubic but quadrupole splitting is observed. This is caused by the ferrimagnetic nature of the substance, which gives rise to a splitting of the $4f$ electronic levels, resulting in a non-cubic charge distribution.

The quadrupole splitting, ΔE , is temperature dependent and varies from compound to compound. The quadrupole interaction Hamiltonian can be written in terms of the quadrupole moment (Q), the nuclear spin operator (I), and the electric field gradient (EFG) tensor at the position of the nucleus:

$$H = \frac{eQ}{4I(2I-1)} \{V_{zz}[3I_z^2 - I(I+1)] + (V_{xx} - V_{yy})(I_x^2 + I_y^2)\} \quad (2.23)$$

The EFG is obtained by applying the gradient operator on each component of the electric field vector. The EFG is then a 3×3 tensor and can be reduced to the diagonal form in the proper co-ordinate axes giving the three required components ($\partial^2 V / \partial x^2$, $\partial^2 V / \partial y^2$ and $\partial^2 V / \partial z^2$) of EFG. These are generally abbreviated as V_{xx} , V_{yy} and V_{zz} . Again zero total charge density in a region makes these three components to obey the Laplace equation ($V_{xx} + V_{yy} + V_{zz} = 0$). The remaining two independent parameters are chosen to be V_{zz} and the asymmetry parameter η . The asymmetry parameter is defined as below:

$$\eta = \frac{V_{xx} - V_{yy}}{V_{zz}} \quad (2.24)$$

The components are usually chosen so that $V_{yy} \leq V_{xx} < V_{zz}$, which makes the value of the asymmetry parameter between 0 and 1 ($0 \leq \eta \leq 1$).

The electric field gradient originates from the charge distribution of the $3d$ -valence electrons of the Mössbauer atom and the charge distribution of the neighbouring atoms in the lattice. The contribution of the atom's own electrons to the EFG is greatly modified by the distant charges, which modifies the atom's own charge distribution. This modification results in an amplification of the EFG, which is like an antishielding. Hence, an antishielding (also known as Sternheimer correction) factor $(1 - \gamma_\infty)$ is multiplied with the lattice contribution. On the other hand, in ferrous ions the lowest order state $^5D(3d^6)$ has a ferric like core and an unpaired valence electron. The valence electron polarizes the core electrons and this also contributes to the EFG. To include this polarization effect of the valence electron a similar Sternheimer correction factor, $(1 - R)$ has been introduced [22, 23].

The EFG components can be expressed as:

$$V_{zz}/e = q = (1 - R)q_{val} + (1 - \gamma_\infty)q_{lat}$$

and

$$(V_{xx} - V_{yy})/e = \eta q = (1 - R)\eta_{val}q_{val} + (1 - \gamma_{\infty})\eta_{lat}q_{lat}$$

However, the most important contribution arises from the Mössbauer atom's own valence electrons, which has an relative value of $(4/7) \langle r^{-3} \rangle$ for the free ^{57}Fe ion [22, 23].

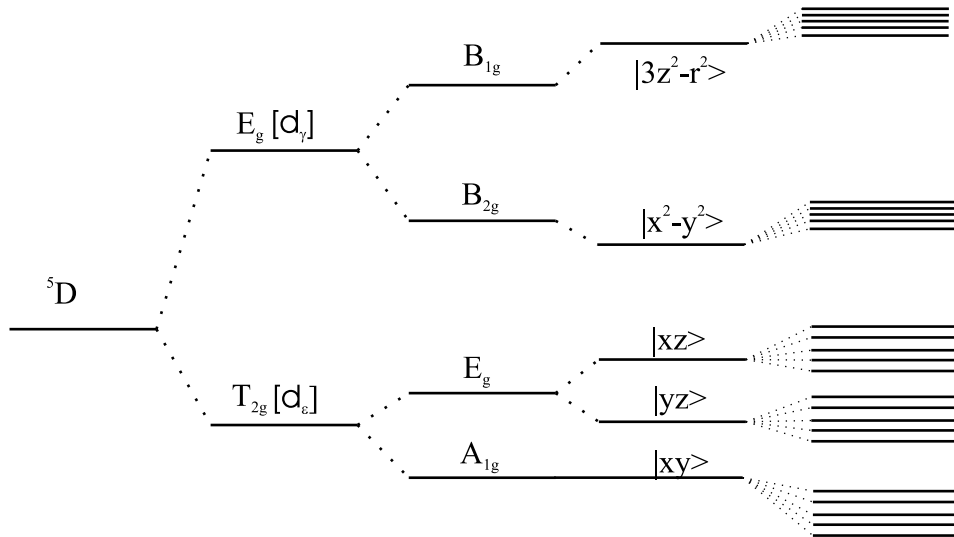
For ^{57}Fe with spin $\frac{3}{2}$, the quadrupole splitting is given by:

$$\Delta E = \frac{1}{2}e^2Qq \left[1 + \frac{1}{3}\eta^2 \right]^{\frac{1}{2}} \quad (2.25)$$

The exact angular dependence of the electron wave functions for the above five different $3d$ -orbitals can be written in terms of the associated Legendre polynomials $P_2^0(u)$, $P_2^1(u)e^{\pm i\phi}$ and $P_2^2(u)e^{\pm i\phi}$, where $u = \cos\theta$ [17]. The presence of the crystal field, which has symmetry lower than cubic, splits the degenerate 5D state of the ferrous ion (Fig. 2.5). The symmetry can be approximated by a distorted octahedron, and the crystal field can then be treated as a sum of cubic, axial and rhombic crystal fields:

$$V = V_{cubic} + V_{axial} + V_{rhombic}$$

The cubic crystal field splits of the degenerate 5D state into two states or groups: (1) The two-fold degenerate higher state, which transforms like $(3z^2 - r^2)$ and $(x^2 - y^2)$, and is called the $d\gamma$ orbital, where $r^2 = x^2 + y^2$. (2) The three-fold degenerate lower state, which transforms like xz , yz and xy , and is called the $d\epsilon$ orbital. In these orbitals the charge density is localized between the co-ordinate axes. This happens in case of an undistorted octahedral symmetric environment, where negative charged ligands lie along the coordinate axes.



Free ion + cubic field + axial field + Rhombic field + Spin-Orbit coupling

Figure 2.5: Electronic energy-level scheme for the ferrous ion under the action of the crystalline field plus spin-orbit coupling [23].

The population of the orbital is determined by the exchange interaction between electrons and the Boltzmann factor $e^{(-E/k_B T)}$, where E is the separation of the levels [18, 26]. The exchange interaction between electrons is important because the sixth electron in the 3d orbital, whose spin aligns antiparallel to the spins of the other five electrons, which are aligned parallel to each other with spin up, obeying Hund's rule. The sixth electron with spin down is spread over the orbitals of lowest energy. This produces the exchange interaction with the other electrons.

The three lower orbitals $d\epsilon$ are equally populated by the sixth electron in case of an octahedral symmetric environment. This makes the energy of the three $d\epsilon$ orbital the same (degenerate). However, when the symmetry is reduced, the population of the sixth electron becomes different and the degeneracy of the $d\epsilon$ orbitals are lifted. However, this nondegeneracy is now determined by the temperature dependent Boltzmann factor $e^{(-E/k_B T)}$ alone. At very low temperatures the Boltzmann factor retains the nondegeneracy. However at higher temperatures close to room temperature the Boltzmann factor approaches unity and all the states are populated equally, making the states degenerate.

The axial crystal field (e.g., trigonal or tetragonal symmetry) lifts the degeneracy of the $d\gamma$ and $d\epsilon$ orbitals. The $d\gamma$ orbital is split into the two states $|3z^2 - r^2\rangle$ and $|x^2 - y^2\rangle$. The $d\epsilon$ orbital also splits into two states, one state is $|xy\rangle$, and the other is a degenerate state of $|xz\rangle$ and $|yz\rangle$. The rhombic crystal field (e.g., orthorhombic symmetry) lifts the degeneracy of $|xz\rangle$ and $|yz\rangle$ states. The energy difference of these two states with respect to the $|xy\rangle$ state can be written as Δ_1 and Δ_2 . These states may become orbitally mixed states in case of spin-orbit interaction.

The spin-orbit interaction is the primary cause of the spread of the low temperature quadrupole splitting. The spin-orbit interaction can be written as: $V_{so} = -\lambda \mathbf{L} \cdot \mathbf{S}$, where λ is the spin-orbit coupling constant. In Fig. 2.5 a schematic of the level splitting due to the crystal fields and the spin-orbit interaction is displayed. Spin-spin interaction is very weak and often can be neglected.

The effective spin-orbit coupling constant is somewhat smaller in the crystal than in the free ion [24]. By using the method of molecular orbital theory it has been shown that the spin-orbit coupling constants of the free ion and the ion inside the lattice are related:

$$\lambda = \alpha^2 \lambda_0 \quad (2.26)$$

Here α^2 is called the 'covalency factor', and its value is between 0.6 and 0.9. Although, the reason for this reduction is not clearly understood, this might occur because of the radial expansion of the ion due to screening [25]. Whatever the cause may be, this reduction of the spin-orbit coupling constant is responsible for the variation of the quadrupole splitting.

The temperature dependent quadrupole splitting (ΔE) can be expressed as

$$\Delta E = (2/7) \langle r^{-3} \rangle_0 \alpha^2 F(\Delta_1, \Delta_2, \alpha^2 \lambda_0, T) \quad (2.27)$$

where $(2/7) \langle r^{-3} \rangle_0$ is the (relative) expectation value of the EFG operator, $(1 - R_0)$ is the Sternheimer correction factor, the covalency factor α^2 takes care of the change of

various parameters from the free ion value to that for the ions inside the lattice, F is the reduction factor which is temperature dependent and also a function of the spin-orbit coupling constant, and the suffix zero stands for free ion values.

2.4.5 Magnetic hyperfine field

The interaction of the nuclear dipole moment μ_N with a magnetic field H at the site of the nucleus splits the nuclear states with spin I into $(2I + 1)$ states with eigenvalues [18]:

$$E_m = -\frac{\mu_N H m_I}{I} = -g_N \beta_N H m_I \quad (2.28)$$

where m_I = magnetic quantum number with values $m_I = I, I - 1, \dots, -I$, g_N = nuclear Landé splitting factor, and β_N = nuclear magneton. The magnetic field at the nuclear site of an atom may be caused by many factors [17]: (1) Fermi contact interaction, (2) orbital magnetic moment of the electrons, (3) magnetic dipolar interaction with electronic spins, (4) contribution from exchange-polarized s -electrons due to the polarization of the conduction electrons of a metal, either in an applied magnetic field or in magnetic field produced by the neighboring atoms.

Further, from eq. (2.28),

$$\mu_N = g_N \beta_N I \quad (2.29)$$

For a purely magnetic interaction at the nuclear site of the isotope ^{57}Fe , which has $I = 1/2$ for the ground state and $I = 3/2$ for the first excited state, the nuclear states split due to the Zeeman effect, as shown in Fig. 2.6. The ordering of the sublevels m_I indicates the fact that the ground state nuclear magnetic moment is positive, while the excited state has a negative magnetic moment. As we have dipolar transition (M1), the nuclear Zeeman effect has the selection rule $\Delta m = 0, \pm 1$. The allowed transitions, which give rise to the six-line Mössbauer spectrum (sextet), is also shown in Fig. 2.6.

A Zeeman-split Mössbauer spectrum of an α -Fe foil with a hyperfine magnetic field B_{hf} of 33 T at RT is shown in Fig. 2.1 (right). This hyperfine field of 33 T corresponds to a local Fe magnetic moment of $2.2 \mu_B$ (μ_B = Bohr magneton). The ratio $33 \text{ T}/2.2 \mu_B \approx 15 \text{ T}/\mu_B$ is the hyperfine interaction constant and provides a means of estimating the local Fe magnetic moment from the measured hyperfine magnetic field. In many materials containing Fe this conversion factor works reasonably well. As the hyperfine magnetic field at the nucleus of ^{57}Fe is created by the electrons of the atom, the direction of the hyperfine field B_{hf} is opposite to the direction of the magnetic moment of the Fe atom.

The angular dependence of the allowed transitions is given in Table 2.1 [18]. From this table one can obtain the relative line intensities of a magnetically (Zeeman) split Mössbauer sextet. The six lines of the ^{57}Fe Mössbauer sextet have the following intensity ratio: $3:R_{23}:1:1:R_{23}:4$, where the intensity $R_{23} = R_{54}$ may vary from 0 to 4 depending on the angle θ between the direction of the magnetic hyperfine field at the nucleus and the γ -ray direction. This has also been schematically shown in Fig. 2.7. As the magnetic

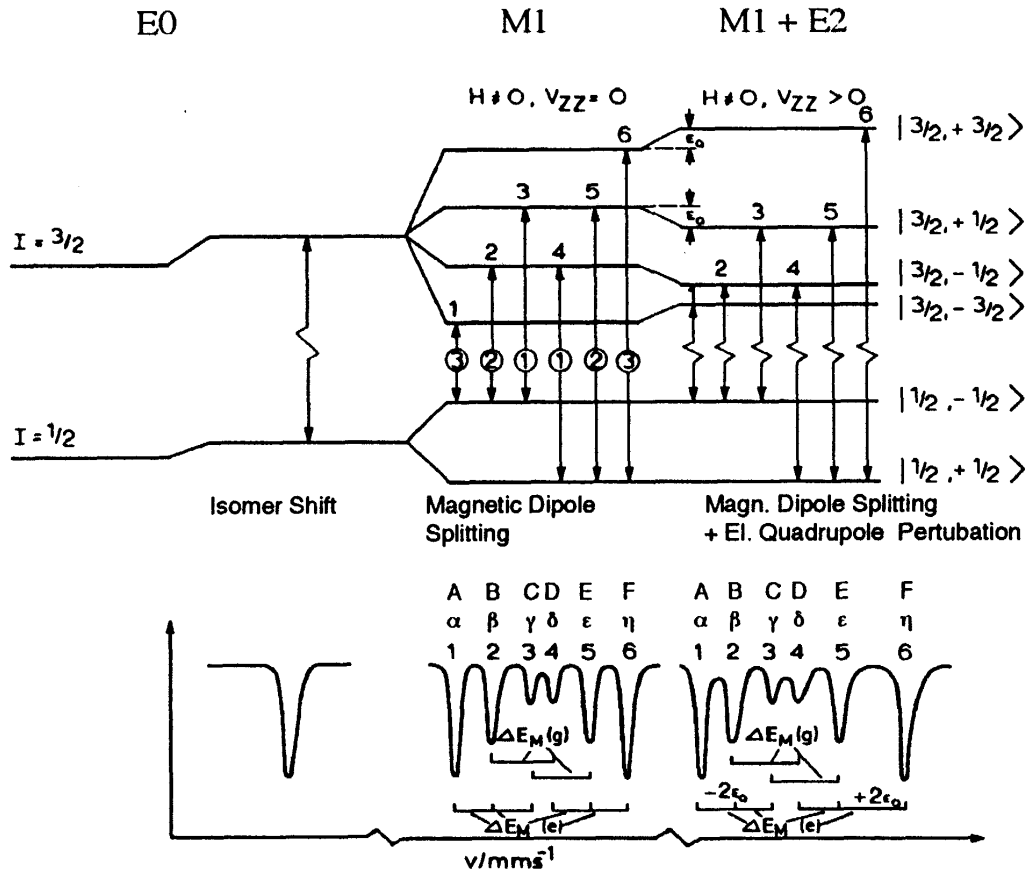


Figure 2.6: Schematic diagram of a nuclear level splitting due to various hyperfine interactions (E0: electric monopole interaction, M1: magnetic dipole interaction, and M1+E2: magnetic dipole and electric quadrupole interaction) and the allowed transition schemes for ^{57}Fe [26].

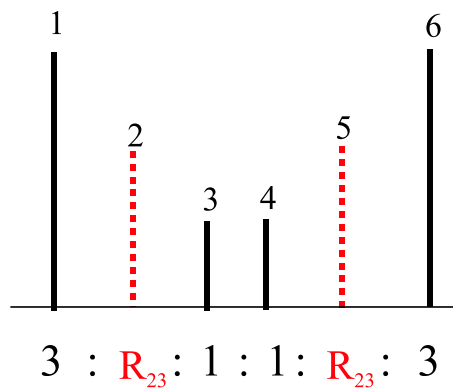


Figure 2.7: Line intensity ratio of a Mössbauer spectrum (schematically) showing line positions (top) and the relative line intensity (bottom).

hyperfine field is opposite to the spin (magnetic moment) direction of the ^{57}Fe atom, Mössbauer spectroscopy may be used to obtain the spin structure of different materials containing the magnetic Mössbauer atom. The details of the obtained spin structure of

various thin films FeF₂, Fe/MnF₂ and Fe/FeF₂ will be described later (Chapters 5, 6, 7 and 8).

Table 2.1 Angular dependence of the allowed transitions in a pure nuclear Zeeman pattern of ⁵⁷Fe [18]. θ represents the angle between the direction of the magnetic hyperfine field at the nucleus and the propagation direction of the γ -ray.

Transition	Δm	Angular dependence
$\pm 3/2 \rightarrow \pm 1/2$	± 1	$3/4(1 + \cos^2\theta)$
$\pm 1/2 \rightarrow \pm 1/2$	0	$\sin^2\theta$
$\mp 1/2 \rightarrow \pm 1/2$	∓ 1	$1/4(1 + \cos^2\theta)$

As the magnetic hyperfine field is created predominantly by the d -electrons via polarization of the core electrons, the temperature dependence of the magnetic hyperfine field ($B_{hf}(T)$) varies approximately like the magnetization i.e. like a Brillouin function [27]. At low temperatures, B_{hf} behaves according to Bloch's spin wave law. According to Bloch's law, the spontaneous magnetization, M , is a function of temperature and, at low T , is given by [27],

$$M = M_0 \left[1 - C \left(\frac{k_B T}{J} \right)^{3/2} \right] \quad (2.30)$$

where J is the exchange interaction and C is a constant. As there is a proportionality between $M(T)$ and $B_{hf}(T)$. Hence, $B_{hf}(T)$ can be expressed as

$$B_{hf}(T) = B_{hf}(0) [1 - bT^{3/2}] \quad (2.31)$$

where $B_{hf}(0)$ is the hyperfine field extrapolated to $T = 0$ K and b is the stiffness constant.

2.4.6 Combined hyperfine interactions

Combined effects of hyperfine interactions are often encountered in different materials. However, the combined effects of magnetic dipole (or Zeeman) and electric quadrupole interactions makes the interpretation of the Mössbauer spectrum more complicated. Normally, when one interaction is small in comparison to the other, either the magnetic hyperfine interaction is perturbed by the electric quadrupole interaction or the quadrupole interaction is perturbed by the magnetic Zeeman interaction, e.g., by applying a magnetic field. Hence, when the electric field gradient is small and collinear with the magnetic hyperfine fields, the quadrupole interaction may be taken as a small perturbation on the magnetic interactions. In this case the Mössbauer spectrum can be explained in a simple manner as shown in Fig. 2.6. However, a strong quadrupole interaction comparable to the Zeeman interaction makes the spectrum complicated. In general, "forbidden" transitions occur in that case. For the case of ⁵⁷Fe, two forbidden transitions appear along with the six line spectrum. It will be seen in Chapters 4 and 6 that an eight line spectrum appears for FeF₂, which has a strong quadrupole interaction.

If the recoil-free fraction f of an anisotropic material depends on the crystal orientation, it will also depend on the orientation of the EFG axes and the spin direction (in a magnetic material). In this case the relative line intensity of the magnetic

and/or quadrupole hyperfine pattern will reflect the vibrational anisotropy in the material. This effect is known as Goldanskii-Karyagin effect. In case of tetragonal FeF_2 , although there is strong quadrupole interaction and magnetic hyperfine splitting, the Goldanskii-Karyagin effect is not observed.

Time-dependent features are often observed in a Mössbauer spectrum. The correlation time (relaxation time of electron spin and nuclear Larmor precession time) characterizing various relaxation processes causes the spectrum to have broadened lines, for example, in the case of paramagnetism or in superparamagnetism of small particles, where the total magnetic moment of the particle fluctuates thermally. In this cases, along with the line broadening, the spectra becomes more complicated.

2.4.7 Calibration and least-squares fitting of the Mössbauer spectra

Before all Mössbauer measurements, a calibration spectrum from an α -Fe foil at RT was taken. The distance between the outer lines of the Mössbauer spectrum of an α -Fe foil corresponds to 10.66 mm/s, which is equivalent to a hyperfine field B_{hf} of 33.16 T at room temperature. The isomer shift of an α -Fe foil at RT relative to a ^{57}Co source in Rh matrix is -0.106 mm/s. All isomer shifts given in this work are relative to the α -Fe foil at RT (unless explicitly mentioned).

All the Mössbauer spectra in this work, have been least-squares fitted by using the computer program "NORMOS" written by R. A. Brand [28, 29]. This program offers also the possibility of taking a hyperfine field distribution $P(B_{hf})$ into account. Most of the spectra are fitted by assuming either a magnetic hyperfine field as a small perturbation with a strong quadrupole interaction, or an electric quadrupole interaction as a small perturbation with a strong magnetic Zeeman interaction. An exception is the Mössbauer spectrum of FeF_2 , where both a strong electric quadrupole and a strong magnetic dipole interaction exists at the nuclear site of ^{57}Fe . In this exceptional case, the spectra were fitted by using the full Hamiltonian fitting procedure of the program.

2.5 X-ray Diffraction

X-rays are scattered by the electrons of a material. Therefore, by using X-ray diffraction (XRD) one can obtain information about the electron density of a material. In a crystalline solids, the atoms (and also the electron density) are arranged in a periodic manner. Hence, in crystalline materials X-rays scatter coherently from the periodic arrangement of electron densities in order to give rise to the diffraction peaks. However, for amorphous materials no sharp diffraction peak can be observed. XRD may provide the information about the structure (crystalline or amorphous) and the existing phases in a material, but also, layer thickness, quality of the interface and epitaxy or texture of a thin film sample may be inferred. Large angle ($> 15^\circ$) XRD is used to obtain the structure of a sample. Often rocking curves are measured in order to obtain information about the epitaxy or texture of a film grown on the appropriate substrate. Small angle ($< 15^\circ$) X-ray scattering is often used for characterizing a thin film or multilayer sample. From the oscillations in the small-angle XRD measurements one obtains the layer

thickness and the quality of the interface (rough or flat (smooth)) of a film or multilayer. To obtain information about the structure of a crystalline material Bragg's law is used. According to Bragg's law [30]:

$$2d_{hkl}\sin\Theta = n\lambda \quad (2.32)$$

where d_{hkl} = interplanar distance of the (hkl) planes (h , k and l , are the Miller indices), Θ = smallest angle between the X-ray propagation direction (\vec{k}) and the hkl plane as shown in Fig. 2.8, n = order of reflection, and λ = wavelength of the X-ray used.

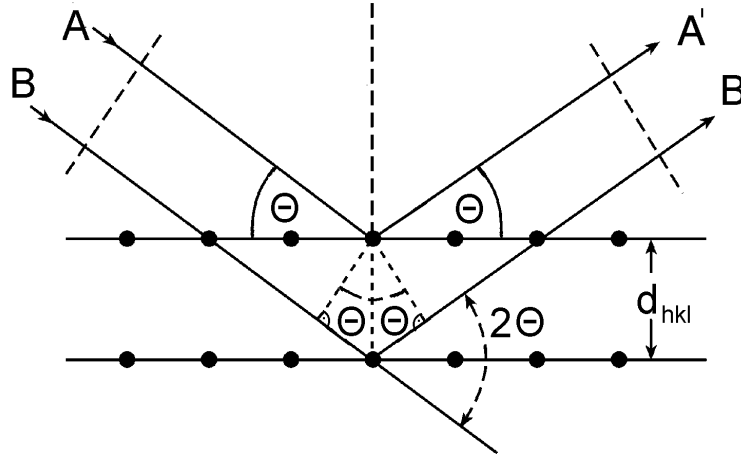


Figure 2.8: Bragg reflection from the planes of a crystal with interplanar spacing d_{hkl} [31].

From eq. (2.32) it is clear that the inter-planar spacing d_{hkl} may be evaluated from an XRD measurement of an angle Θ . The figure (Fig. 2.8) makes it clear that for every angle of rotation Θ of the incident X-ray beam the reflected beam rotates an angle 2Θ . In a goniometer, the sample is rotated with respect to the fixed X-ray beam direction, and the detector is rotated by an angle 2Θ for an angle of rotation Θ of the sample with respect to the X-ray beam. A schematic diagram of the principle of the goniometer is shown in Fig. 2.9.

Along with the large-angle XRD pattern, small-angle XRD may be used to obtain the film thickness from the intensity oscillations which appear due to variation of the electron density of different layers [46–48]. In this case, the X-ray are scattered from the total layer thickness, where the electron density is assumed to be homogenous and it changes by going to the next layer. Hence, coherent scattering is expected, if the layers are periodically arranged (which is equivalent to the periodic arrangement of electron densities), and, as the total layer thickness is much larger than the interatomic spacing, the film diffraction peaks are expected to be at small angles (from eq. (2.32)).

For performing rocking-curve measurement both, the sample and the detector are rotated by the same angle Θ , keeping the detector initially at one of the Bragg peaks of the sample. The angle Θ is scanned around the Bragg peak position. This arrangement works as if the detector is fixed and the sample is rotated in order to get the intensity

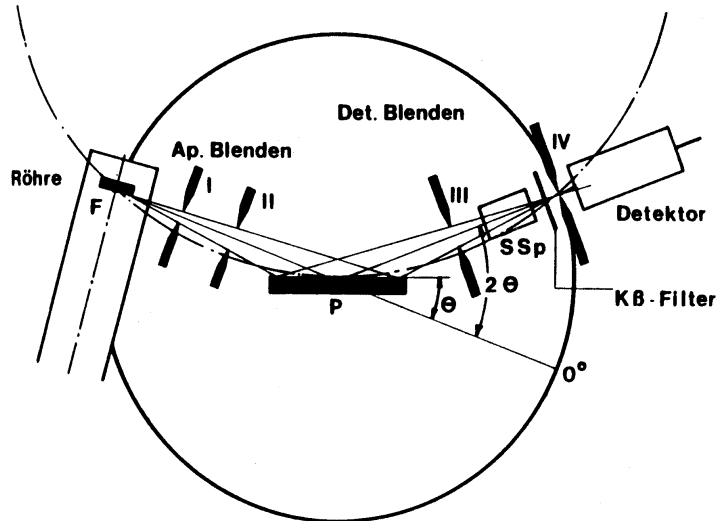


Figure 2.9: Principle of Θ - 2Θ goniometer used for X-ray diffraction [45].

of the Bragg peak for different orientations of the sample. Rocking curves provide information about the quality of epitaxy of the film or about texture.

In this thesis, large- and small-angle X-ray diffraction patterns, along with the rocking curves, were used for structural characterization of various thin films. All the XRD measurements in this work were performed either at the University of California San Diego, USA, or at the University of Duisburg-Essen, Germany. $\text{Cu-K}\alpha$ radiation was used as X-rays, which has a wavelength $\lambda = 1.5418 \text{ \AA}$. The measurements were performed with an angular resolution $\Delta(2\Theta)$ of about 0.01° .

2.6 SQUID Magnetometry

For very small samples such as thin films SQUID (superconducting quantum interference device) magnetometry provides a very accurate measurement of magnetization. The effect of flux quantization in a superconducting ring and the phenomenon of tunnel current through a Josephson contact are the basic phenomena in a SQUID. The magnetic flux quantum is $\Phi_0 = 2.068 \times 10^{-15} \text{ Vs}$. The sample was placed in the homogenous magnetic field of a superconducting solenoid magnet. The induction signal in the receiving coil is proportional to the magnetic moment of the sample. All the SQUID measurements in this work are performed either at the University of California San Diego, USA, by Dr. W. A. A. Macedo or at the University of Ulm, Germany, by Dr. J. Eisenmenger. At the University of Ulm also vector SQUID measurements were performed, which can provide simultaneously the longitudinal (parallel to the field) and the transverse (perpendicular to the field) magnetization of a sample.

The diamagnetic signal of the substrate and the sample holder, which varies linearly with magnetic field, was also measured along with the magnetization, and was then subtracted from the raw data in order to get the magnetization of the sample.

Chapter 3

Nuclear resonant scattering of synchrotron radiation

3.1 Synchrotron radiation: production and control

The radiation from an orbiting electron was observed in a synchro-cyclotron in 1947 [36], henceforth the name synchrotron radiation was used for the radiation obtained from an accelerated electron. All the synchrotron radiation sources existing up to now could be classified into three categories. In the first generation synchrotron radiation sources (such as DORIS at HASYLAB, Hamburg), the synchrotron beam was not optimized for production of synchrotron radiation, but the synchrotron radiation was used in a parasitic mode from the high energy physics experiments on electrons and positrons accelerators. While, in the second generation synchrotron sources (such as the National Synchrotron Light Source (NSLS), at Brookhaven National Laboratory), bending magnets, dipole, quadrupole and sextupole magnets were used for the production of synchrotron radiation. In the third generation, wigglers and undulators were used for enhancing the production of photons and various optical instruments for collimating the photons on to the sample. There are a number of synchrotron radiation sources present all over the world. The Advanced Photon Source (APS), Argonne National Laboratory, Argonne, USA, the European Synchrotron Radiation Facility (ESRF), Grenoble, France, the Super Photon ring - 8 GeV (SPring-8), Osaka, Japan are among the most powerful synchrotron third generation radiation sources. A detailed description about synchrotron radiation and its properties can be found in many books, e.g., [32, 33].

Production of synchrotron radiation is based on the principle that "an accelerated charge radiates" [34]. Many bunches of electrons separated by few nanoseconds, a distance characterized by the time required to cover that distance in nanoseconds, circulate with very high velocity (close to the velocity of light) in a circular-type path (known as storage ring) guided by magnets. The actual path of the electron bunches is not strictly circular, rather it consists of some straight sections connected by a bent section. At the bent sections, the magnets known as bending magnets, bend the direction of the electron bunches and as a result the electrons change their acceleration (direction) and a pulsed radiation from the whole bunch of electrons is generated. In this way, all the bunches of electrons generate a pulsed synchrotron beam.

The total number of photons per second that are emitted by an orbiting electron is

proportional to the radiated power P , is given by [34]:

$$P = \frac{e^2 c}{6\pi\epsilon_0} \frac{1}{(m_0 c^2)^4} \frac{E^4}{R^2} = \frac{e^2 c}{6\pi\epsilon_0} \frac{1}{R^2} \gamma^4 \quad (3.1)$$

with $\gamma = E/m_0 c^2$ and m_0 = rest mass of the electron, E = the total energy of the electron and R = radius of curvature of the path of the electron. The quantity P determines the total flux of a synchrotron radiation source that is measured in the unit of photons/s. However, from the sources a number of photons having all energies (white radiation) are obtained. Due to the very high velocity (relativistic motion) of the electrons the radiation is collimated in the forward direction forming a cone of radiations [34]. The opening angle of the cone is equal to $1/\gamma$ [35]. A schematic diagram of the emitted radiation from a bending magnet is shown in Fig. 3.1.

The synchrotron beam will be very useful when the energy of the beam can be tuned for the required purpose. This is, in fact, achieved by putting additional components inside the storage ring (wigglers, undulators etc.) for changing the energy and also using additional optical components to filter a monochromatic component or to change the path of the beam for various applications to study and discover various useful phenomena.

The critical energy E_c (upper energy limit of the useful radiation (Fig. 3.1)) that can be produced at a bending magnet can be expressed as [35]:

$$E_c = \frac{3\hbar c \gamma^3}{2R} = C \frac{E^3}{R} \quad (3.2)$$

with $C = 2.218 \times 10^{-6}$ m/GeV. From this eq. (2.2), it is suggested that storage rings with electron energies below 2.5 GeV are most suitable for experiments with soft X-rays (below 1.5 keV), but for hard X-rays (needed for experiments like Nuclear Resonant Scattering (NRS)) the electron energies should be more than 2.5 GeV. To characterize the spectral distribution of the radiation one defines the spectral flux as below:

$$\text{Spectral flux} \equiv \frac{\text{Photons/s}}{0.1\% \text{ bandwidth}} \quad (3.3)$$

which is the flux normalized to a relative spectral bandwidth of $\Delta E/E = 10^{-3}$.

Among the components used inside the storage ring are the RF (radio frequency) cavities (resonators), the bending magnets, the wigglers and the undulator. The radio frequency cavities are used to nourish the electrons back their energy which they lost due to the emission of the photons. The bending magnets serve two purposes, (1) to produce X-ray beams and (2) to bend the electron bunches to keep the electrons in the storage ring for further production of X-rays.

The wigglers and undulators are an arrangement of alternating poles of magnets as shown in Fig. 3.1, where the electrons are forced to wiggle in a sinusoidal fashion in a plane (generally horizontal to ground) to produce an intense beam of photons peaked at a certain energy. The wigglers and undulators are mounted in the straight sections of the storage ring. By construction, the wigglers and the undulators are similar except that the magnetic field of the magnets used for wigglers is stronger and the size of the magnets are bigger than that of undulators. However, the number of magnets used in an undulator is often more than that of wigglers. Inside of an undulator the electrons wiggle

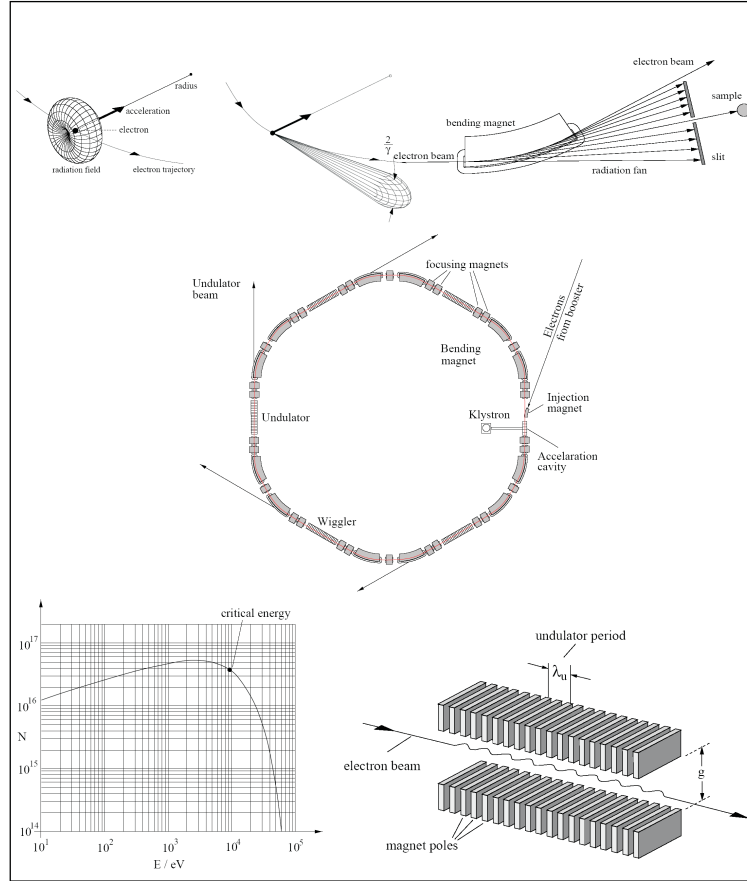


Figure 3.1: Schematic layout and properties of a modern synchrotron radiation source [35]. In the upper left part of the figure, the transformation of the radiated field distribution from the rest frame of the electrons into the laboratory frame is displayed, also shown is a highly directional emission of radiation from relativistic electrons. In the upper right part, the emission of synchrotron radiation from a bending magnet is shown. The lower right part shows the layout of an insertion device (wiggler or undulator) with an alternate arrangement of poles of magnets with period λ_u , that forces the electrons to move in a sinusoidal trajectory as shown. The lower left part shows the spectral flux delivered by a bending magnet with a radius of 12.2 m for an electron energy of 5 GeV. The central part shows the layout of a third-generation synchrotron storage ring.

many more times (many magnets) and less strongly (strength of the magnet is less) than that inside a wiggler. Hence, an undulator produces a well collimated intense X-ray beam with narrow energy bandwidth in comparison to the wigglers. The collimation (opening of cone) of emitted radiation is given by [35]:

$$\sigma_r = \frac{1}{\gamma} \sqrt{\frac{1 + \frac{1}{2}K^2}{2Nn}} \quad (3.4)$$

where N = number of magnet periods, n = number of the harmonics, and K = deflection parameter that is derived from the magnetic period λ_u (in cm) and the peak magnetic field of the magnet (in Tesla) as given below [35]:

$$K = 0.934\lambda_u \frac{B_0}{T} \quad (3.5)$$

Hence, this deflection parameter K basically distinguishes an undulator ($K \leq 1$) from a wiggler ($K \gg 1$, i.e., ~ 10 or more). From this expression, it is clear that one may change the energy of the collimated beam just by changing the gap between the poles of the magnets, i.e., by changing the magnetic field B_0 in the undulator or wiggler. The angular collimation is in general expressed by the brilliance of the beam defined as below:

$$\textit{Brilliance} \equiv \frac{\textit{Photons/s}}{\textit{mrad}^2 \cdot 0.1\% \textit{ bandwidth}} \quad (3.6)$$

Often, the source size has great importance for an efficient use of the optical components such as monochromators and mirrors. The smaller the source size better the focus of the beam on to the sample position, for instance to perform various measurements with a better spatial resolution on the sample. In this respect, the synchrotron source is characterized by Brilliance as following, with a source area of 1 mm^2 :

$$\textit{Brilliance} \equiv \frac{\textit{Photons/s}}{\textit{mrad}^2 \cdot \textit{mm}^2 \cdot 0.1\% \textit{ bandwidth}} \quad (3.7)$$

For the present-day third generation synchrotron sources produces a brilliance up to 10^{17} *photons/s/0.1%bandwidth/mm²/mrad²*.

The electrons circulating inside the storage ring are first produced in a Klystron-based accelerator which is like an accelerator with a small storage ring (booster synchrotron). When there is a loss of the electrons inside the storage ring because of various reasons (like a problem with the vacuum necessary, and scattering of electrons, or due to other reasons etc.), the storage ring should be filled again with electron bunches from the booster synchrotron. Generally, the storage ring is filled twice per day or continuously in some cases (top up mode). The typical current inside a storage ring is about 100 mA or 200 mA. The position, where a bunch of electron may be introduced is called a *bucket*.

In a synchrotron storage ring generally all the buckets are not filled with bunches of electrons, but rather they are separated by a time required by various experiments. For instance, as we will see in the time spectra presented in Chapter 8, there is a time separation of about 160 ns between two pulses of photons and also between two bunches of electrons inside the storage ring.

By nature the synchrotron radiation is completely polarized in the plane of the storage ring. This is strictly true for the radiation emitted exactly in that plane; however, the radiations emitted slightly out-of-plane may exhibit certain degree of ellipticity. One may filter out these unwanted radiations by using polarizing Bragg reflectors. But for some experiments, where polarization of the radiation is a necessity, helical undulators were generally used in this case. The work presented in this thesis was performed by using a plane polarized (linearly polarized) beam at the ESRF, France.

3.2 Introduction to scattering techniques

Light scattering is a quantum mechanical phenomenon where a photon is absorbed by the scattering particle such as an atom and followed by a re-emission of photons. After the re-emission of the photons, the atoms may return back to its original ground state or returns to an excited state such as a state with an energy change in its electronic shells or lattice excitations. Depending on the final state of the scatterer atom the light scattering process could be divided into four different types:

1. Coherent elastic scattering
2. Coherent inelastic scattering
3. Incoherent elastic scattering
4. Incoherent inelastic scattering

When the atom goes back to its original ground state after reemission of the photon, there is no energy change (elastic) of the system and the scatterer is now indistinguishable from the other atoms and in this case, the scattering may happen coherently from all atoms. This process is known as coherent elastic scattering. The example of such scattering is coherent elastic nuclear resonant scattering, where the 14.4125 keV scattered radiation from the ^{57}Fe nuclei of many atoms interfere coherently to give rise to the time spectrum, on which a detailed description will be given in this chapter and the experimental results will be given in Chapter 8.

A typical case of coherent inelastic scattering occurs when an excited electronic state of an atom interacts with the lattice vibrations in the sample that transfers energy to the re-emitted photon (like in Raman scattering). In this case the energy of the system changes (inelastic), but the photons coming from the material scatter coherently.

Conversion electron Mössbauer spectroscopy (CEMS) is the typical case of the incoherent elastic scattering, where the ^{57}Fe atom returns back to its ground state by emitting the photon from the nucleus; but because of internal conversion the energy is absorbed by the *s*-electrons and the coherence of the emitted photons or even the original photon itself is lost (because of the emission of conversion electron).

Nuclear resonant inelastic X-ray scattering (NRIXS) is the example of incoherent inelastic X-ray scattering, where (for example) the ^{57}Fe or ^{119}Sn nucleus goes to the excited nuclear state and one detects the K-fluorescence coming from the atoms. Here we have no coherence of the photons and also the final energy of the system is not same as initial.

3.3 NRS experimental setup

In a typical NRS experiment a monochromatized beam with the required energy for the excitation of the Mössbauer nuclei is used. The work presented in this thesis uses the monochromatized 14.4125 keV synchrotron radiation for excitation of the ^{57}Fe nuclei.

The de-excitation time of all the nuclei is not same and are delayed in time with respect to each other and with respect to the electronic signal (X-rays). The interference pattern of the delayed coherent photons only in the forward direction (propagation direction of the synchrotron beam) is what one measures as a function of time, and the resulting spectrum is known as time spectrum. The details about the time spectrum and the information that can be extracted from it will be provided in the next section (section 3.4).

Fig. 3.2 shows a schematic layout of an NRS experimental setup. Initially the undulator gap is selected in order to optimize the required photon energy. The next step is to monochromatize the beam and align the beam onto the sample and alignment of the detector. The monochromators are highly polished Si crystals with well defined (Miller indices) reflecting planes. The principle of monochromatization uses the simple Bragg equation, as given in eq. (2.32) of Chapter 2.

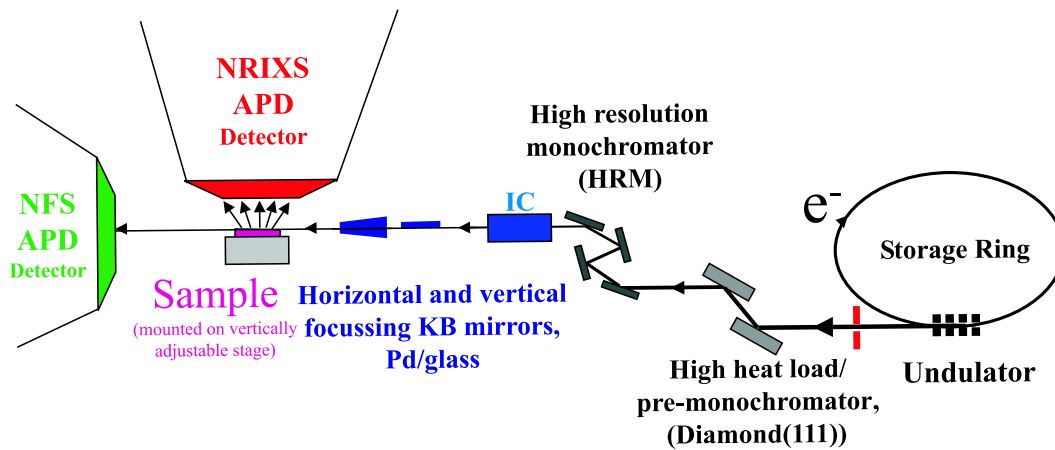


Figure 3.2: Schematic diagram of an nuclear resonant scattering setup (NRS and NRXIS) at a beam line. The beamline optical components (high heat-load monochromator, high resolution monochromator, Kirkpatrick-Baez (KB) mirrors) are also shown. For the nuclear resonant (elastic, forward) scattering the avalanche-photo-diode (APD) detector is used for the measurement of the time spectrum.

For the production of the monochromatized beam with an energy equal to or close to the nuclear transition energy from the almost "white" synchrotron beam a number of optical elements may be used. The energy bandwidth (full width at half maximum) of the white beam that comes out from an insertion device (for example an undulator) inside the storage ring is large and is about 600 eV. For the ^{57}Fe nuclear resonance (14.4125 keV) this beam is then monochromatized to about a bandwidth of 1 eV by using a pre-monochromator, which is also known as high-heat-load monochromator. The high-heat-load monochromator generally consists of liquid nitrogen or water cooled diamond(111) or Si(111) single crystals. A high-resolution monochromator generally consists of three or four highly polished Si single crystals with higher-order reflection planes (close to back-reflection). Behind the high-resolution monochromator, the energy bandwidth of the beam is about 1 meV at the 14.4125 keV photon energy.

As mentioned earlier, the delayed photons that arrive from the sample after the co-

herent superposition are counted by APD detectors. The APD detector provides a very good time resolution (about 1 ns), which is necessary for measurements on our time scale. To avoid the direct beam, the detector is generally protected by delay electronics for a few nanoseconds, when the the incoming direct synchrotron pulse (prompt pulse) hits the sample.

3.4 Nuclear resonant scattering: beat pattern

In the traditional Mössbauer experiments, where one works in the energy domain, the phase relation between the frequency components of the radiation is lost, and, therefore, only the frequency components are revealed. However, in addition to the frequency components, Mössbauer timing experiments, such as NRS, preserves the phase correlation between these frequency components. Therefore, the appearing quantum-beat-like interference patterns (time spectra) (that will be described later) are very sensitive to the relative strength of the frequency components of resonance and to a slight variation of the hyperfine parameters, including the orientation of the hyperfine fields. In addition to the above advantages, the synchrotron radiation technique provides a very good spatial and angular resolution and a high degree of polarization.

In a material which contains an ensemble of Mössbauer nuclei or atoms, when only a single resonant photon is incident on the sample, there is a small probability amplitude that each nucleus in the ensemble is excited. However, quantum mechanically, the sum of all these small amplitudes results in the total probability amplitude that the photon interacts resonantly with the nuclei. For a pulse of photons, if a resonant pulse of photons is short in compared to the nuclear lifetime, these probability amplitudes exhibit the same temporal phase. As a result, a collective excited state is created, where a single excitation is coherently distributed over the resonant nuclei of the sample [37]. The wave function of this collectively excited state is the coherent superposition of states.

The synchrotron pulse has a short time duration (about few ns), hence, it is possible to collectively excite the Mössbauer nucleus (for example ^{57}Fe which has a half life of 97 ns for the 14.4125 keV excited state). In a typical synchrotron radiation experiment, the spectral bandwidth of the synchrotron beam that comes from the high-resolution monochromator (~ 1 meV) is much larger than that of the resonance width of a Mössbauer transition (in the neV range for ^{57}Fe nuclear levels). In this case, the propagating waves (after excitation) have different group velocity, and their interference leads to a beat pattern in the temporal evolution of the transmitted intensity in the forward direction [38]. This results in propagation quantum beats or dynamical beats. In other words, the modulation of the scattered intensity in space and in time is called "propagation" or "dynamical beat". Hence, these dynamical beats result from the *intraresonance* interference of different spectral components within the resonance line. However, if the nucleus is subject to hyperfine interactions (such as electric quadrupole or magnetic dipole interaction), the degeneracy of the nuclear levels is lifted, leading to a splitting of the nuclear transitions into several lines. In this case, the synchrotron pulse excites the various sublevels instantaneously and coherently, which then radiate at their various frequencies. The frequency difference leads to temporal evolution of the decay. As this

results from the superposition of amplitudes of different resonances, this is referred as *interresonance* interferences. This *interresonance* interference pattern between the resolved energy components yields a beat pattern termed as quantum beats. A quantum beat period corresponds to the energetic separation of the resonances. A small energy difference will be translated into a large quantum beat period, which, in principle, will provide a more precise measurement of hyperfine interactions than Mössbauer measurements. This beat pattern, when plotted with respect to the decay time, is known as time spectrum.

Another aspect of nuclear resonant scattering is "speed up". If the decay of the Mössbauer nuclei occurs via many radiative channels, the decay time of the coherently forward scattered wave becomes small, which is known as "speed up" process. For example, when the number of Mössbauer atoms in a material is increased, e.g., by increasing the thickness of a sample, the decay rate is enhanced. This has been demonstrated by using a ^{57}Fe foil [39]. (It will be seen in Chapter 8 that a deviation of the spin direction from the beam direction leads to a faster decay of the time spectrum, as the magnetization rotation of some domains acts as an additional decay channel.)

Again, the sharper the resonance, the slower the de-phasing of the elementary oscillations, and the response time of the nucleus is correspondingly larger. Hence, it is preferable to treat simple cases, when the Mössbauer nuclei in a sample have sharp resonances.

Up to now, no polarization effects are considered. However, polarized synchrotron radiation can be obtained from the storage ring by introducing insertion devices, wigglers, undulators or helical undulators. In general, the direct beam coming from the insertion devices (e.g., undulators) is highly linearly polarized. Further, polarized synchrotron radiation could be used to selectively excite different groups of nuclear transitions. Fig. 3.3 shows the transition rules for exciting the energy levels of Mössbauer nucleus and the corresponding quantum-beat pattern or Mössbauer spectra. The practical rules for the synchrotron radiation scattering geometry and the hyperfine field direction are: the magnetic polarization vector of the incident wave should have a component along the magnetic hyperfine field in order to excite $\Delta m = 0$ transitions, and it should have a component perpendicular to the magnetic hyperfine field direction to excite $\Delta m = \pm 1$ transitions, as shown in Fig. 3.3. This suggests that the polarized synchrotron beam can be used for the determination of the Fe spin structure of various materials, surfaces and interfaces, as the Fe spin direction (or magnetic moment direction) is opposite to the magnetic hyperfine field direction. A detailed description of the extraction of the information about spin direction from the measured time spectra will be given in the next section (section 3.5).

3.5 Simulation of the NRS time spectrum

For the least-squares fitting of all the time spectra, as will be seen in Chapter 8, we have used the computer program CONUSS (COherent NUClear resonant Scattering by Single crystals). The program was initially written by Dr. Wolfgang Sturhahn [41] and later modified and developed by Dr. Ralf Röhlsberger [35, 42, 49] for grazing incidence

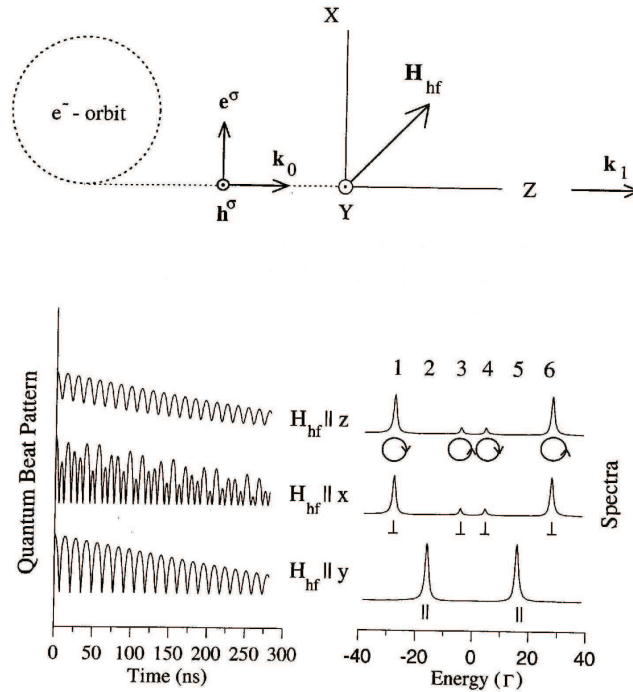


Figure 3.3: Top: the (linear) polarization components of synchrotron radiation propagating along \mathbf{k}_0 [40]. \mathbf{e}^σ is the electric vector component and \mathbf{h}^σ is the magnetic vector component of the σ polarized electromagnetic wave. \mathbf{H}_{hf} is the magnetic hyperfine field direction in the XYZ coordinate system. Bottom: ^{57}Fe Mössbauer spectral composition (right) and time dependence of the nuclear forward scattering of synchrotron radiation (left) by a $0.2 \mu\text{m}$ thick ^{57}Fe foil. The polarization dependency of the nuclear excitations is also shown on the right hand side. The circles represent the circular polarization of light with particular helicity. The \parallel and \perp signs represent the necessity of parallel or perpendicular polarization of the beam in order to excite those particular transitions. [Note: the symbols used in this figure are different from the symbols used for the same physical quantities in this thesis].

geometry in thin films. A brief description of the spectral evaluation formalism of NRS time spectra will be given here.

A very general approach can be formulated, if the polarization states are treated as scattering channels, between which energy of the radiation field can be exchanged. In this way one can describe the strong polarization mixing effects that occur in nuclear resonant scattering. The dynamical theory of X-ray scattering has to include the full polarization dependence of the scattering process. This allows to include these polarization channels with other open channels, like Bragg reflections, into one algebraic structure. The problem is then to find the self-consistent solution for the radiation field in the sample that contains all orders of multiple scattering.

The propagation of electromagnetic waves through a homogeneous medium with thickness d can be described by [35]:

$$\mathbf{A}(d) = e^{i\mathbf{F}d} \mathbf{A}(0) \quad (3.8)$$

where, \mathbf{A} denotes a multidimensional vector representing the set of field amplitudes in the open scattering channels. \mathbf{F} is a supermatrix that describes the coupling between all open scattering channels. The matrix exponential relates the field amplitudes $\mathbf{A}(d)$ at depth d to the incident amplitudes $\mathbf{A}(0)$. The number of scattering channels is determined by:

1. The structure of the sample: in crystalline samples, several Bragg and Laue reflections are possible. In disordered samples at normal incidence there is only forward scattering possible.
2. The scattering geometry: it determines how many scattering channels are actually open, e.g., how many Bragg reflections are simultaneously excited. Regardless of its structure, specular reflection at grazing angles takes place for any sample.

If we assume a transition to have dipole character, the elastic scattering amplitude in the vicinity of a resonance, with the transition energy E , is given by [50]:

$$[f(\omega)]_{\mu\nu} = -(eq)^2 \sum_{\alpha,\beta} \left(\frac{(e_\nu \cdot Q_{\alpha\beta}^*)(e_\mu \cdot Q_{\alpha\beta})}{\hbar\omega - \Delta_{\alpha\beta} + i\Gamma_0/2} \right) \quad (3.9)$$

where the sum runs over all initial and intermediate states. $Q_{\alpha\beta} = \langle \beta | R | \alpha \rangle$ is the dipole matrix element between the ground state $|\beta\rangle$ and the intermediate excited state $|\alpha\rangle$, $\Delta_{\alpha\beta}$ is the energy difference between these states, and Γ_0 is the level width of the transition. The energies $\Delta_{\alpha\beta}$ are determined by the hyperfine interaction in the system. e_μ and e_ν are polarization unit vectors of the incident and the scattered photon, respectively. From this expression (eq. (2.9)), the resonant magnetic scattering amplitude (or scattering length) for a single atom can be written as the sum of three terms [50]:

$$[\mathbf{f}(\omega)]_{ab} = \frac{3}{16\pi} \{ (e_a \cdot e_b) [F_{+1} + F_{-1}] + i(e_a \times e_b) \cdot \hat{m} [F_{+1} - F_{-1}] + (e_a \cdot \hat{m})(e_b \cdot \hat{m}) [2F_0 - F_{+1} - F_{-1}] \} \quad (3.10)$$

where the $F_\nu = F_\nu(\omega)$ are the energy-dependent resonant strengths for dipole transitions with a change in the magnetic quantum number of $\Delta m = \nu$. $\hat{m}(r)$ describes a unit vector with orientation of the magnetic hyperfine field and its spatial dependence. This eq. (3.10) is valid for electric dipole (E1) transitions, and in case of magnetic dipole (M1) transitions, the role of electric and magnetic fields of the wave are interchanged. Then the unit vectors e_a and e_b have to be replaced via $e \rightarrow e \times k_0$, where k_0 is the unit wave vector of the incident photon.

The three terms in eq. (3.10) represent different polarization dependencies. The first term is not sensitive to the sample magnetization. Its polarization dependence given by $e_a \cdot e_b$ is that of non-resonant charge scattering. The second term depends on the difference between the resonant scattering lengths F_{+1} and F_{-1} . It is the same term that is responsible for circular dichroism in ferromagnets. Since its polarization dependence is $e_a \times e_b$, it describes orthogonal scattering, e.g. $\sigma \rightarrow \pi$ and $\pi \rightarrow \sigma$. The third term that is proportional to $2F_0 - F_{+1} - F_{-1}$ describes magnetic linear dichroism. Its polarization and spin dependence allows for all scattering processes within the given polarization basis. The occurrence of optical activity crucially depends on the symmetry of $\hat{m}(r)$. In many cases the medium possesses global symmetries, e.g., a uniformly magnetized material that exhibits axial symmetry. In the following we assume a sample with a unidirectional

magnetization, i.e., $\hat{m}(r) = \hat{m}$. We further assume a linear polarization basis, where the σ polarization lies in the plane of the storage ring.

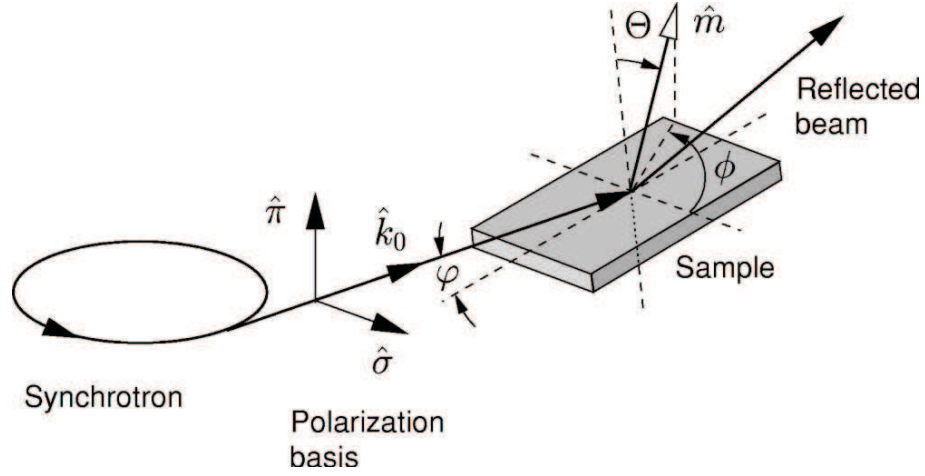


Figure 3.4: Relative orientation (Θ, ϕ) of the incident wave vector \hat{k}_0 to a unidirectional magnetization \hat{m} of the sample [42]. $(\hat{\sigma}, \hat{\pi})$ are the linear polarization basis vectors. The angle of incidence φ is exaggerated here, which has a typical value of about few milli radians.

The scattering geometry, i.e., the orientation of the unit vector of the magnetic moment \hat{m} with respect to the incident wave vector and the linear polarization basis, is introduced in Fig 3.4. For this case the scattering amplitude matrix is given by [42]:

$$\mathbf{f}_{\sigma\sigma} = (3/16\pi)[F_{+1} + F_{-1} + (\pi \cdot \hat{\mathbf{m}})^2(2F_0 - F_{+1} - F_{-1})] \quad (3.11)$$

$$\mathbf{f}_{\sigma\pi} = (3/16\pi)[-i(\mathbf{k}_0 \cdot \hat{\mathbf{m}})(F_{+1} - F_{-1}) - (\sigma \cdot \hat{\mathbf{m}})(\pi \cdot \hat{\mathbf{m}})(2F_0 - F_{+1} - F_{-1})] \quad (3.12)$$

$$\mathbf{f}_{\pi\sigma} = (3/16\pi)[i(\mathbf{k}_0 \cdot \hat{\mathbf{m}})(F_{+1} - F_{-1}) - (\sigma \cdot \hat{\mathbf{m}})(\pi \cdot \hat{\mathbf{m}})(2F_0 - F_{+1} - F_{-1})] \quad (3.13)$$

$$\mathbf{f}_{\pi\pi} = (3/16\pi)[F_{+1} + F_{-1} + (\sigma \cdot \hat{\mathbf{m}})^2(2F_0 - F_{+1} - F_{-1})] \quad (3.14)$$

These matrix elements express the strong polarization-mixing effects that are observed in resonant scattering from magnetized samples. The off-diagonal elements describe the orthogonal scattering that turns incident σ -polarization into π -polarization and vice versa. The representation of the scattering matrix as given above allows to determine the scattering matrix for a given geometry in a convenient way. The analysis of a given scattering geometry becomes particularly simple in the frame of eigen-polarizations of the system which are obtained by diagonalization of \mathbf{f} . In general, \mathbf{f} is not hermitian, so that the eigenpolarizations are not orthogonal and depend explicitly on energy through the functions F_{+1} , F_{-1} and F_0 . However, there are a number of important cases where \mathbf{f} is hermitian and a system of orthogonal eigen-polarizations can be found so that [35]:

$$\mathbf{f}(\omega) = \mathbf{g} \mathbf{f}_D(\omega) \mathbf{g}^{-1} \quad (3.15)$$

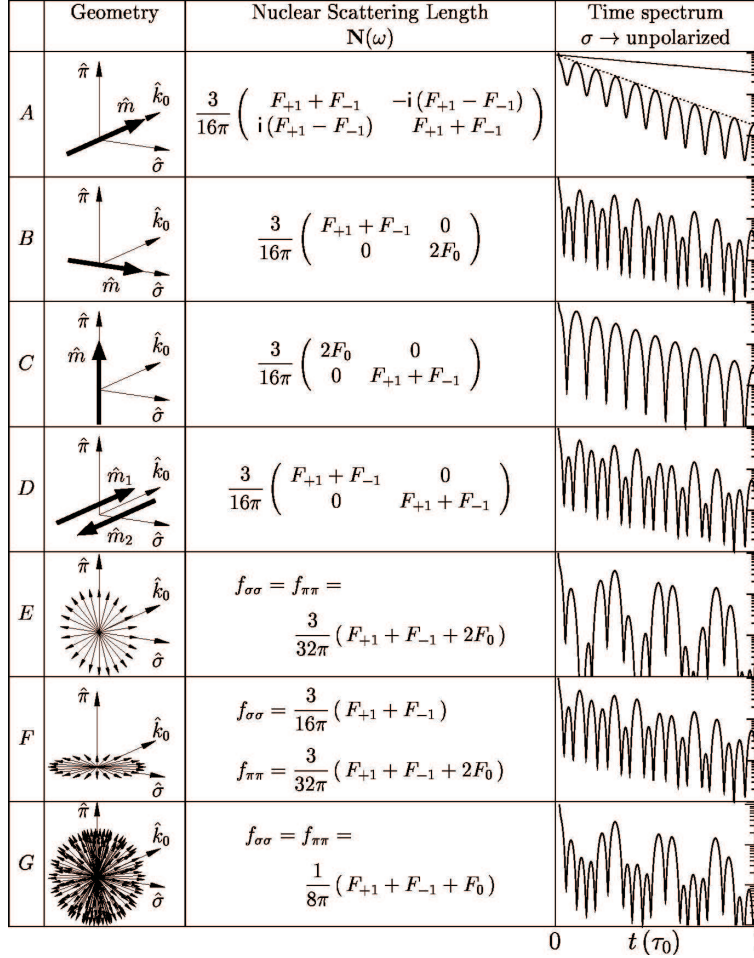


Figure 3.5: Time spectra of nuclear resonant scattering for selected orientation of the magnetic hyperfine field \mathbf{B} , that defines the direction of the quantization axis \hat{m} , relative to the incident wave vector \hat{k}_0 [42]. The matrix of the nuclear scattering length is given in a linear polarization basis $(\hat{\sigma}, \hat{\pi})$. The time spectra were calculated for a 2-nm-thick ^{57}Fe film on a tungsten substrate, assuming purely σ polarized incident radiation. A-C display the results for a unidirectional magnetization of the sample. D results from the superposition of two magnetic sublattices in antiparallel alignment. E and F display results for a two-dimensional random distribution of spin directions. G shows the result for a three-dimensional random orientational distribution. Since the scattering matrix in the case E-G is diagonal, only the diagonal elements are shown. The identical shape of the time spectra in rows B, D, and F demonstrates that the spin structure of the sample cannot be determined from just a single time spectrum. Instead, to lift this degeneracy, a number of spectra at different orientations have to be taken. The envelop of the time spectra (dashed line in the upper right part of Fig. 3.5) indicates that the time response of the film is considerably speeded up compared to the natural decay (solid straight line in the upper right part of Fig. 3.5).

with the diagonal matrix \mathbf{f}_D and a diagonalizing matrix \mathbf{g} that depends only on the geometry. Those are the cases where \mathbf{k}_0 and \mathbf{B} are perpendicular or parallel to each other.

This is illustrated in Fig. 3.5, where the scattering matrices and typical time spectra are displayed. In Fig. 3.5, the time spectra of nuclear resonant scattering for selected orientation of the magnetic hyperfine field \mathbf{B} ($= B_{hf}$), that defines the direction of the quantization axis \hat{m} , relative to the incident wave vector \hat{k}_0 are given. The matrix of the nuclear scattering length is given in a linear polarization basis $(\hat{\sigma}, \hat{\pi})$. The time spectra were calculated for a 2-nm-thick ^{57}Fe film on a tungsten substrate, assuming purely σ polarized incident radiation. A-C in Fig. 3.5 display the results for a unidirectional magnetization of the sample. D results from the superposition of two magnetic sublattices in antiparallel alignment. E and F display results for two-dimensional random distribution of spin directions. G shows the result for a three dimensional random orientational distribution. Since the scattering matrix in the case E-G is diagonal, only the diagonal elements are shown in Fig. 3.5. The identical shape of the time spectra in rows B, D, and F demonstrates that the spin structure of the sample cannot be determined from just a single time spectrum. Instead, to lift this degeneracy, a number of spectra at different orientations have to be taken. The envelop of the time spectra (dashed line in the upper right part of Fig. 3.5) indicates that the time response of the film is considerably speeded up compared to the natural decay (solid straight line in the upper right part of Fig. 3.5).

Further, in Fig. 3.5, as the π -polarization vector is always perpendicular to the film magnetization \hat{m} ,

(1) for the case (B): \mathbf{k}_0 and \mathbf{B} (or \hat{m}) are perpendicular, i.e., $\mathbf{k}_0 \cdot \hat{m} = 0$:

$$\mathbf{f}_D = \frac{3}{16\pi} \begin{pmatrix} F_{+1} + F_{-1} & 0 \\ 0 & F_{+1} + F_{-1} \end{pmatrix} \quad (3.16)$$

and

$$\mathbf{g} = \begin{pmatrix} \cos\varphi & \sin\varphi \\ -\sin\varphi & \cos\varphi \end{pmatrix} \quad (3.17)$$

(where φ = angle of incidence of the synchrotron beam). In this case the linear polarizations are eigenpolarizations of the system.

(2) For the case (A): \mathbf{k}_0 and \mathbf{B} (or \hat{m}) are parallel, i.e., $\mathbf{k}_0 \cdot \hat{m} = 1$:

$$\mathbf{f}_D = \frac{3}{16\pi} \begin{pmatrix} F_{+1} & 0 \\ 0 & F_{-1} \end{pmatrix} \quad (3.18)$$

and

$$\mathbf{g} = \begin{pmatrix} 1 & -i \\ i & 1 \end{pmatrix} \quad (3.19)$$

Here the circular polarizations are the eigen-polarizations of the system.

For all other cases, in Fig. 3.5, the scattering amplitude may be calculated analytically considering the anisotropy directions (angles) of the sample, for example, the in-plane anisotropy of a thin Fe film. However, in all cases the scattering matrix \mathbf{f} is diagonal in a linear polarization basis [35, 51]. The CONUSS program was developed for grazing incident (synchrotron radiation) on thin films by considering the eigen-polarizations of the system.

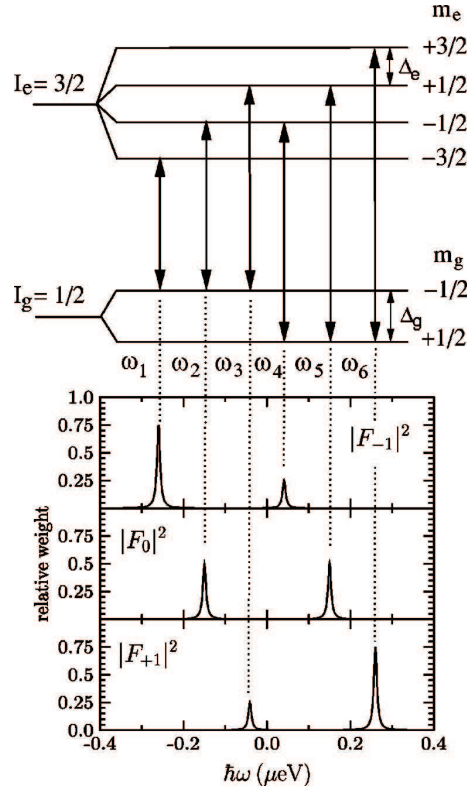


Figure 3.6: Energy dependence of the function F_ν in the case of nuclear resonant scattering [42]. These functions $F_{-1}, 0, F_{+1}$ describe the scattering of left-circular, linear and right circular polarization, respectively, similar to Fig. 3.3.

In the CONUSS program the scattered delayed intensity $I(t)$ is given by [42]:

$$I(t) = e^{-\chi t/\tau_0} [G(0, 0, \Omega_1) \{1 + S^2(\phi)\} + G(\Omega_1 + \Omega_2, \Omega_1 - \Omega_2, \Omega_2) \{1 - S^2(\phi)\}] \quad (3.20)$$

where τ_0 = lifetime of the nuclear excited state, and t = delay time. The exponential factor χ considers the speedup of the decay compared to the natural decay; hence, it is related to the thickness of the sample. The angle ϕ is the azimuthal angle with the σ -polarization direction and the in-plane component of \hat{m} (Fig. 3.4) the function $S(\phi)$ is defined as:

$$S(\phi) = \hat{k}_0 \cdot [\mathbf{D}(\phi)\mathbf{M}] \quad (3.21)$$

where

$$D(\phi) = \begin{pmatrix} \cos\phi & \sin\phi \\ -\sin\phi & \cos\phi \end{pmatrix}$$

and \mathbf{M} = the magnetic structure function of the sample that considers the magnetization directions. For our case of grazing incidence, $\mathbf{M} = (m_x, m_y)$ and $S(\phi)$ is [42]:

$$S(\phi) = m_x \cos\phi + m_y \sin\phi \quad (3.22)$$

For the simplest case, that the magnetization is aligned along the beam direction, $\mathbf{M} = (1, 0)$, $S(\phi) = \cos\phi$. The function G in eq. (3.20) is defined as:

$$G(c_1, c_2, c_3) = \cos c_1 t + a^2 \cos c_2 t + 2a \cos c_3 t \quad (3.23)$$

with $a = a_1/a_4 = a_6/a_3 = 1/3$ being the amplitude ratio of the two resonance lines that comprises $F_\nu(\omega)$. Ω_1 and Ω_2 are frequency differences between the resonance lines, that can be expressed by the level splitting Δ_g and Δ_e of the ground and the excited state, respectively (see Fig. 3.6):

$$\Omega_1 = \omega_4 - \omega_1 = (\Delta_e + \Delta_g)/\hbar \quad (3.24)$$

$$\Omega_2 = \omega_3 - \omega_1 = 2\Delta_e/\hbar \quad (3.25)$$

In this formalism the case of nuclear resonant scattering from the 14.4-keV resonance of ^{57}Fe is considered. As described in the previous Chapter 2, the resonance is a magnetic dipole (M1) transition between the ground state with spin $I_g = 1/2$ and the first excited state with $I_e = 3/2$, with a lifetime of $\tau_0 = 141$ ns. In magnetic materials the spin-polarized $3d$ electrons create a spin-polarization of the s -electrons via exchange interaction. This leads to a strong magnetic hyperfine field at the nuclear position, which, for example, amounts to $\mathbf{B} = 33.3 \text{ T} = B_{hf}$ in the case of ferromagnetic α -Fe at RT. In this magnetic field the energetic degeneracy of ground- and excited states is lifted, resulting in a Zeeman-splitting of the nuclear levels. The dipole selection rule $\Delta m = 0, \pm 1$, leads to six allowed transitions, corresponding to six energetically well separated resonances. The resulting energy dependence of the functions F_ν for $\nu = \Delta m = -1, 0, +1$ is shown in Fig. 3.6. The energetic positions of the resonance lines are determined by the magnetic hyperfine interaction as described in Chapter 2. After simultaneous excitation of these resonances by a synchrotron radiation pulse, the time spectrum of the decay exhibits a characteristic quantum beat pattern. This beat pattern enables to extract precise information about the magnitude and the direction of hyperfine field in the sample. This, in principle, allows to determine magnetic properties with atomic resolution by selectively doping the sample with the Mössbauer nuclei at buried interfaces. This will be described in Chapter 8. For the simulation of the measured time spectra via the CONUSS programm, eqs. (3.20) to (3.25) for the case of an in-plane unidirectional Fe spin direction will be employed.

Chapter 4

Introduction to exchange bias

4.1 Introduction

A ferromagnet is characterized by its Curie temperature (T_C) below which the ferromagnet (FM) transforms from a paramagnetic to the ferromagnetic state. Similarly, below the Néel temperature (T_N) an antiferromagnet (AFM) transforms from the paramagnetic to the magnetically ordered antiferromagnetic state. When a material that contains neighboring antiferromagnetic (AFM) and ferromagnetic (FM) phases is field-cooled below the Néel temperature of the antiferromagnet, a unidirectional anisotropy may be induced in the ferromagnet, which is known as the exchange anisotropy. This phenomenon which is called exchange bias has been discovered by W. H. Meiklejohn and C. P. Bean [1, 172] in 1956, when studying the hysteresis of ferromagnetic Co particles coated by an antiferromagnetic CoO shell.

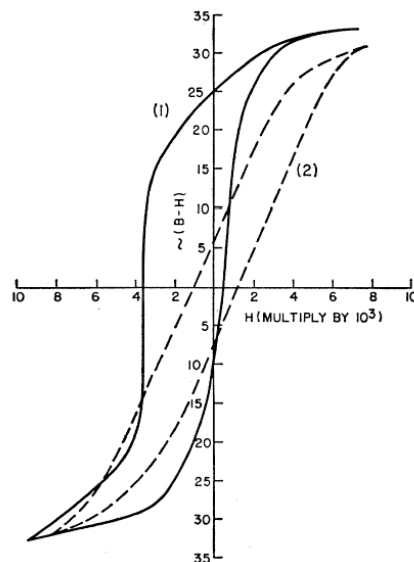


Figure 4.1: Hysteresis loops at 77 K of ferromagnetic Co particles coated by an antiferromagnetic CoO shell [1]. The solid line curve results from cooling the particles in 10 kOe magnetic field. The dashed line curve shows the loop when cooled in zero external field.

An important condition for inducing exchange anisotropy is that T_C of the ferromagnet must be higher than T_N of the antiferromagnet, $T_N < T_C$. The unidirectional exchange anisotropy can be macroscopically observed by cooling the AFM/FM system from a temperature T_S ($T_N < T_S < T_C$) to a temperature T_M ($T_M \leq T_N < T_C$) in the presence of a static magnetic field, and measuring the hysteresis loop at T_M . Generally, a free ferromagnet, no matter soft or hard, has a symmetrical hysteresis loop. However, for the exchange biased AFM/FM case, where a unidirectional anisotropy exists, the absolute values of the coercivity for increasing and decreasing applied fields are different. In other words, the hysteresis loop of the FM magnetization shifts along the applied field axis, generally in the opposite direction of the applied cooling field. This shift of the hysteresis loop is known as the exchange bias field H_E . The hysteresis loop shift from the origin is illustrated in Fig. 4.1.

This shift of the hysteresis loop is also accompanied by an enhanced coercivity. Both effects, the shift of the hysteresis loop and the increase of coercivity generally vanish above T_B , the so-called blocking temperature with $T_B < T_N$. In some systems like Fe/FeF₂ or Fe/MnF₂, exchange bias vanishes below T_N and there is no blocking temperature.

Another macroscopic way for observing exchange bias is torque magnetometry (e.g. [242]). After field cooling, the torque magnetization at a temperature below T_N (or T_B) shows an additional $\sin\phi$ component, where ϕ is the angle between the applied field and the cooling-field direction.

Small particle exchange bias systems are as important as thin film systems from a technological point of view. Because of the enhanced coercivity, exchange-biased particle systems attract attention for applications as permanent magnetic materials and high density recording media. In thin film form, exchange-bias systems have a wide range of applications, like magnetic sensors, stabilizers in reading heads, and spin valve devices. Experimental and theoretical studies on exchange anisotropy are reviewed in reports by J. Nogues and I. K. Schuller [2], A. E. Berkowitz and K. Takano [70], M. Kiwi [136] and R. L. Stamps [229].

4.1.1 Experimental observations of exchange bias

Exchange bias and related effects have been investigated by many experimental techniques [2]. Superconducting quantum interference device (SQUID) magnetometry [64, 71–74, 81, 82, 93, 97, 101, 106, 107, 111, 118, 124, 125, 138, 139, 142, 152, 160–162, 165, 176, 181–183, 187–189, 197, 200, 207, 211, 227, 228, 230, 238–240, 247, 254, 256, 257] and torque magnetometry [1, 172, 210, 211, 224, 242], vibrating sample magnetometry (VSM) [79, 94, 101, 118, 120, 138, 159, 160, 238, 239, 244, 247, 254, 255], the loop-tracer method [60, 119], magneto-optic Kerr effect (MOKE) [67, 102, 131, 171, 210], ferromagnetic resonance (FMR) [174, 199, 235], magnetoresistance [8, 82, 145], AC susceptibility [236], Brillouin light scattering [95, 177], X-ray magnetic dichroism [6, 190, 194, 195], polarized neutron diffraction [7, 9, 64–66, 99, 100, 156, 201, 202], and Mössbauer spectroscopy [135, 147, 167, 241] are among the important techniques used in this respect.

SQUID magnetometry, VSM, and MOKE measure the magnetization versus the ap-

plied field. These techniques provide information about the exchange bias field (hysteresis loop shift), H_E , and the coercivity, H_C . Some information about the magnetic anisotropy can also be measured. Torque magnetometry gives information about the magnetic anisotropy present in the sample by rotating the sample in a field. The additional $\sin\phi$ component observed in the torque magnetization confirms the presence of unidirectional anisotropy in an exchange-biased system.

In ferromagnetic resonance (FMR) the sample is mounted in a microwave cavity and is subjected to a high frequency (GHz) electromagnetic field. A DC magnetic field is swept through resonance. From the resonance position and line shape information about the exchange bias and anisotropies can be obtained. It has been observed by FMR that in an exchange biased system (FM/AFM) the magnetization of the FM is not homogeneous throughout the thickness of the FM layer. In this case the spins at the top are aligned with the field but the interfacial spins have different orientation [see e.g. [235]].

In Brillouin scattering the sample is irradiated with laser light in the visible range. The spectrum of the scattered light, together with the sample geometry and applied magnetic field, give the information about the spin wave frequency and the magnetic anisotropy. From the shift of the spin wave frequency the exchange bias field (H_E) can be obtained [177]. However, the observed exchange bias in Fe/FeF₂ is higher than that observed by SQUID.

By neutron diffraction information about the magnetic and crystallographic structure of an exchange bias system can be obtained. Polarized neutron reflectometry provides the exchange bias hysteresis loop (hence H_E and H_C) and the spin configuration of the different FM layers. From the peak width of the diffraction peaks (magnetic or nuclear) information on the domain size (magnetic or crystallographic) can be extracted. The other information obtained from the high angle neutron diffraction is the possible presence of domains in the AFM, perpendicular (non-collinear) coupling between the AFM and ferrimagnet spins at the interface [see e.g. [125]].

Magnetoresistance measurement on spin valve devices of the type AFM/FM/NM/FM (with NM = non-magnetic layer) can give information about the exchange bias. Measurements of the field dependence of the resistivity up to the saturation field yield the hysteresis loop and also the H_E and H_C values. The important information obtained from these studies is the indication that the FM in contact with the AFM is behaving like a transition layer from purely AFM to purely FM behavior.

Exchange bias is always zero above the Néel temperature of the antiferromagnet. However, in most systems, below T_N or below the blocking temperature T_B the magnitude of the exchange bias field increases rapidly and saturates gradually as $T \rightarrow 0$ K. The thickness of the FM and/or the AFM layer plays an important role in determining the exchange bias. According to many experimental observations exchange bias is roughly inversely proportional to the FM layer thickness ($H_E \propto t_{FM}^{-1}$). This is true as long as the thickness of the FM is larger than the domain wall width which varies from material to material. However, for thicknesses less than the domain wall width (usually a few nanometers) the growth and microstructure of the film will be different, and exchange bias varies in a different manner as compared to the thicker films. Exchange bias is

in general independent of the thickness of a particular AFM for higher thicknesses (although different for different AFM materials), however, the general trend is that below a critical AFM thickness the exchange bias field decreases rapidly and finally vanishes at very low thicknesses [60, 166]. However, along with the FM and AFM thickness, exchange bias also depends on the FM/AFM interfacial roughness. According to most investigations, magnitude of the exchange bias field increases with increasing roughness. The crystallinity, grain size and interface impurity content also play an important role in determining H_E . Medium dilution of the antiferromagnet was found to favor an increase in exchange bias [see e.g. [134, 148, 175]].

According to the proposed theories and supporting experiments the exchange-bias field should be larger for higher antiferromagnetic magnetic anisotropy. Owing to the variation of anisotropy of an antiferromagnet with microstructure, which is difficult to control, the explanation for the variation of H_E with the anisotropy of the AFM is not quantitative. However, qualitatively, $H_E \propto \sqrt{K_{AFM}}$, where K_{AFM} is the anisotropy constant of the antiferromagnet.

Exchange-bias effect have been observed in many different kinds of materials (FM/AFM, FM/Ferrimagnet, spin glasses) with many different forms (particles and thin films). The fine particle system is the first system in which the exchange bias was discovered (Co-CoO) [1]. In particle systems generally the ferromagnetic core is covered by its antiferromagnetic or ferrimagnetic native oxide, nitride or sulphide. The particles are produced by various methods such as electrodeposition, vapor deposition, gas condensation, mechanical alloying and many others. Examples of the numerous reported systems include: Co/CoO [1, 106, 107, 160, 172], Ni/NiO [165, 254], Fe/FeO [173], Fe/Fe₃O₄ [165, 197], Fe/Fe₂N [120], Co/CoN [160], Fe/FeS [115]. NiFe₂O₄/a-NiFe₂O₄ (Ferrimagnet/spin glass) [142] and Fe/NiMn (FM/spin glass) [58] are also examples where exchange bias has been observed. Bulk ferrimagnets, such as amorphous rare-earth based alloy ferrimagnets (a-FeTb [221], a-GdCo [75]) and oxide ferrimagnets (CoTiO₄ [209], CoCr₂O₄ [238]), are also observed to show exchange bias. Among the spin glass systems are mostly alloys of Fe or Mn such as Au_{1-x}Fe_x [78], amorphous(a)-Fe_{1-x}Zr_x [184], Cu_{1-x}Mn_x [126, 143], Ag_{1-x}Mn_x [143], Ni_{1-x}Mn_x [144, 207] etc. It is difficult to measure or control the roughness and thickness of the AFM layer in particle systems. However, the spin glass systems show exchange bias without any defined FM/AFM interface; hence, it is difficult to extract useful basic information about exchange bias.

Many antiferromagnets, such as oxides (CoO [9, 79, 95, 161, 174, 201, 202, 227, 228, 242], NiO [129], FeO [83, 84, 162], Fe₂O₃ [77, 151], Cr₂O₃ [212]), metallic alloys (Ni_xMn_{1-x} [251], Fe₅₀Mn₅₀ [163], Cr_xMn_yM_{1-x-y} (where M = Pt, Rh, Cu, Pd, Ir, Ni, Co, Ti) (e.g.[94, 225, 226]), Pd_xPt_yMn_{1-x-y} [97], pure Cr [67] and pure Mn [230, 247]) and others like sulfide (FeS [112]), fluoride (FeF₂, MnF₂ (e.g.[2, 156, 166, 176, 187, 189])) and nitride (CrN [248]) antiferromagnets have been investigated in thin-film exchange bias systems. The most widely studied exchange-biased oxide systems include Co-CoO, Ni-NiO and Fe-FeO. The metallic exchange biased systems are interesting for their application in GMR based spin valve devices. The fluoride exchange bias systems are widely studied for the understanding of the mechanism and spin structure in the exchange biased state, because of their relatively simple spin structure and viability in controlling the growth properties. Nitride systems are studied because of their high blocking temperature and

corrosion resistance. Good reviews on the materials used for exchange bias and their exchange bias property has been given by Nogues and Schuller [2] and Berkowitz and-Takano [70].

4.1.2 Theoretical Models explaining the observed Exchange Bias Effects

Coherent Rotation Model by Meiklejohn and Bean

Based on the Stoner-Wohlfarth model of coherent spin rotation, the first attempt for modelling the exchange bias was undertaken by Meiklejohn and Bean[1, 172, 173]. Their simple assumption was that when a field is applied in the temperature range $T_N < T < T_C$, the ferromagnetic spins align along the field, while the antiferromagnetic spins remain random because of paramagnetism. By cooling the system below T_N in the presence of the field, the AFM spins in contact to the FM align ferromagnetically because of interfacial exchange coupling. The second AFM layer, next to the interfacial layer, aligns antiparallel to the interfacial layer spins. The third layer aligns antiparallel to the second layer spins, etc. In a similar way the other layers follow the AFM order to produce a zero net magnetization. By reversing the field the ferromagnetic spins start to rotate with the field, but the sufficiently large anisotropy of the AFM does not allow the AFM spins to rotate with the field. With this model of coherent rotation of the magnetization, the energy per unit area is defined by:

$$\mathbf{E} = -\mu_0 H M_{FM} t_{FM} \cos(\theta - \beta) + K_{FM} t_{FM} \sin^2(\beta) + K_{AFM} t_{AFM} \sin^2(\alpha) - J_{INT} \cos(\beta - \alpha) \quad (4.1)$$

where H is the applied field, M_{FM} is the saturation magnetization of the ferromagnet, t_{FM}, t_{AFM} are the thicknesses of the ferromagnetic and antiferromagnetic layer, respectively, K_{FM}, K_{AFM} are the anisotropy of the ferromagnetic and antiferromagnetic layer, respectively, J_{INT} is the interface coupling constant and is an unknown parameter, α is the angle between the antiferromagnetic sublattice magnetization (M_{AFM}) and the antiferromagnetic anisotropy axis, β is the angle between the ferromagnetic magnetization and the ferromagnetic anisotropy axis, and θ is the angles between the applied field and the ferromagnetic anisotropy axis. They are schematically shown in Fig. 4.2.

The first term in eq. (3.1) describes the effect of the applied field on the ferromagnet (Zeeman term). The second and third term account for the ferromagnetic and antiferromagnetic magnetic anisotropy and the last term describes the exchange interaction at the FM/AFM interface. Minimization of the energy for this system results in an exchange bias field (H_E) of

$$H_E = \frac{J_{INT}}{\mu_0 M_{FM} t_{FM}} \quad (4.2)$$

The important information obtained during the energy minimization is that $K_{AFM} t_{AFM} \geq J_{INT}$ should be satisfied for the loop shift. For the opposite condition $K_{AFM} t_{AFM} \leq J_{INT}$, i.e., for a small antiferromagnetic anisotropy, the antiferromagnetic and ferromagnetic spins rotate together, and no loop shift is observed.

The drawbacks of this model are that the magnitude of H_E obtained by this model is several orders of magnitude higher than the experimental values because of an overesti-

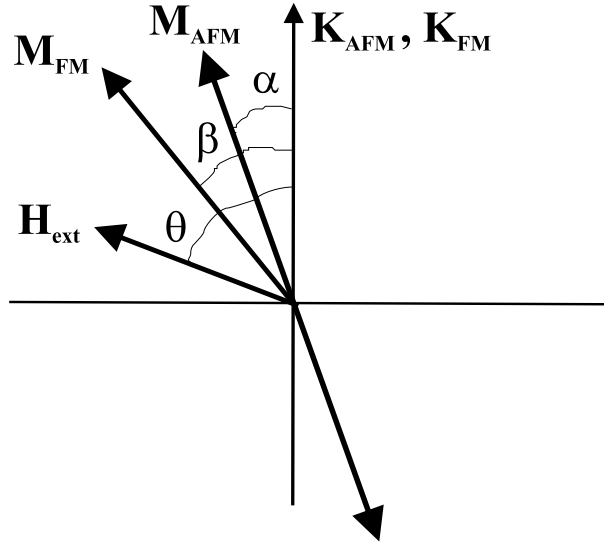


Figure 4.2: Schematic diagram of the angles involved in the coherent rotation model by Meiklejohn and Bean. Note that the AFM and FM anisotropy axes are assumed collinear and that the AFM sublattice magnetization M_{AFM} has two opposite directions.

mation of the interfacial exchange interaction J_{INT} , and the following conclusions of the model are not strictly fulfilled: (a) exchange bias should be always negative ($H_E < 0$), (b) the uncompensated AFM interface should show the highest exchange bias field, $|H_E|$, and (c) roughness of a compensated AFM interface should induce an increase in $|H_E|$.

Antiferromagnetic Domain Wall Model by Mauri

In the model by Mauri et al. [171] a perfectly flat interface has been assumed for a FM slab of thickness t_{FM} much smaller than the FM domain wall width, where the FM magnetization aligns along the easy axis of the AFM in the absence of the external magnetic field, and a domain wall develops inside the AFM. This domain wall plays the main role in determining the exchange coupling energy.

This model does not take into account the following facts: it has been experimentally confirmed that AFM coupling between the FM and AFM interfacial spins has to be considered, especially to explain the positive exchange-bias field observed under certain conditions [see e. g. [285]]. However, in some cases the FM moments are not parallel but rather orthogonal to the AFM easy axis [125, 183]. Also, this model does not provide any clue to understand, how the compensated AFM interface can yield values of H_E as large as or even larger than the uncompensated ones.

Orthogonal FM-AFM Magnetization Model by Koon

In his micromagnetic model [141], Koon considered compensated FM/AFM interfaces. On the basis of the Heisenberg model, Koon's model results in perpendicular orientation of the FM moments relative to the AFM easy axes direction in the ground state magnetic configuration. The model also exhibits a small canting ($\theta < 10^\circ$) of the

AFM magnetic moments of the AFM interface layer or, in other words, an AFM component opposite to the cooling field direction, which yields the minimum energy.

Although this model is relevant in establishing the interface magnetic structure, it fails to yield exchange bias (H_E). In other words, the canted interface magnetic structure by itself is not sufficient to produce the required unidirectional anisotropy.

Random Interfacial Field Models:

(a) Random Interface Model by Malozemoff

Because of the rough FM/AFM interface, the exchange interaction can be random due to the compensated and uncompensated spin configuration at different interfacial positions. This random exchange interaction acts like a random field on the antiferromagnet and creates domains similar to those described by Imry and Ma [127] in the random field problem. This random magnetic field at the interface yields the unidirectional anisotropy. By this model [136, 168, 169] the obtained loop shift is:

$$H_E = \frac{2}{M_{FM}t_{FM}} \sqrt{\frac{J_{AFM}K_{AFM}}{a}} \quad (4.3)$$

where J_{AFM} is the exchange stiffness of the antiferromagnet and a is the lattice parameter. The main reduction factor concerned in this model is $2a/\sqrt{J/aK}$, where $\sqrt{J/aK}$ corresponds to the domain wall width, d_w , of the ferromagnet, $\sqrt{J_{FM}/aK_{FM}}$, and the antiferromagnet, $\sqrt{J_{AFM}/aK_{AFM}}$.

This model reduces the calculated H_E value by two orders of magnitude from that derived by Meiklejohn's coherent rotation model. However, this model has drawbacks, because the H_E value depends on the defect concentration at the interface, which is inconsistent with experimental observation.

(b) Random Orthogonal Magnetic Interface Model by Schulthess and Butler

Schulthess and Butler [217] combined Malozemoff's random interface model [168, 169] with Koon's orthogonal magnetic coupling model [141] for the micromagnetic calculations of exchange bias. In their calculations they combined the atomistic Heisenberg model with the classical Landau-Lifshitz equation for the spin motion. The model considers the usual Zeeman (E_Z), exchange (E_J), anisotropy (E_A) and magnetostatic (E_D) energy terms, as given below.

$$\mathbf{E} = E_Z + E_J + E_A + E_D \quad (4.4)$$

where

$$E_Z = \sum_i \vec{\mu}_i \vec{H}_{ext},$$

$\vec{\mu}_i$ is the 3-dimensional spin vector located on atomic site i .

$$E_J = \sum_{i \neq j} J_{ij} \vec{s}_i \vec{s}_j,$$

\vec{s}_i is $\frac{\vec{\mu}}{|\vec{\mu}|}$.

$$E_A = \sum_i K_i \sin \theta_i,$$

and

$$E_D = \sum_{i \neq j} \frac{\vec{\mu}_i \cdot \vec{\mu}_j - 3(\vec{\mu}_i \cdot \hat{n}_{ij})(\vec{\mu}_j \cdot \hat{n}_{ij})}{|\vec{R}_i - \vec{R}_j|^3},$$

\hat{n}_{ij} is the unit vector parallel to $\vec{R}_i - \vec{R}_j$.

As a special case this model pointed out the inability to explain the unidirectional anisotropy by Koon's model. However, the drawback of this model is that $|H_E|$ also depends on the defect concentration at the FM/AFM interface.

(c) The Normal (Parallel) and Biquadratic (Orthogonal) Exchange Interaction Model by Dimitrov et al.

Assuming the interfacial exchange interaction between the FM and the AFM of the following form, Dimitrov et al. [93] have obtained exchange bias fields of about the same order of magnitude as in experiments:

$$\mathbf{E} = J_1(\vec{m}_{FM} \cdot \vec{m}_{AFM}) + J_2(\vec{m}_{FM} \cdot \vec{m}_{AFM})^2 \quad (4.5)$$

where \vec{m}_{FM} and \vec{m}_{AFM} are FM and AFM moments, and J_1 and J_2 are normal and biquadratic exchange constants. The normal exchange constant (J_1) favors the parallel or antiparallel alignment between the FM and AFM moments, whereas the biquadratic exchange constant (J_2) favors orthogonal (spin-flop-like) coupling. Summing over all interactions Dimitrov et al. have obtained the total energy:

$$E = C_1 + C_2 J_1 \cos \theta + C_3 J_2 \sin^2 \theta \quad (4.6)$$

where θ is the angle between the easy axes of the FM and the AFM. The constants C_1 , C_2 and C_3 can not be calculated without exact knowledge of the interface properties. However, proper guess of the parameters can yield a correct conclusion.

(d) Microscopic Model by Almeida and Rezende

In this model Almeida and Rezende [262] assumed interface roughness as the cause of exchange bias. They have substituted a fraction of the AFM spins randomly in order to represent the interface roughness. They have set up the equations for the local magnetisation in a mean field approximation with Ising interactions and solved numerically for arbitrary temperature. In this way they could explain qualitatively the experimental exchange interaction and also the dependence of H_E and H_C on the cooling field, as observed in the experiments. However, like the above random field models this also depends on the interface roughness and hence, has limitations in correlating theoretical and experimental results.

(e) Spin-glass Model by Radu et al.

Considering the imperfectness of the FM/AFM interface due to chemical intermixing, stoichiometry deviations and structural inhomogeneities etc., the spin glass model by Radu et al. [204] has the following assumptions: (a) the FM/AFM interface is a frustrated spin system (spin-glass), (b) frozen-in uncompensated AFM spins are responsible for EB shift, and (c) low anisotropy AFM spins contribute to the coercivity. Distinguishing the AFM anisotropy as weak (which is affected by the applied magnetic field) and strong, depending on the local inhomogeneity at the interface, they have added an additional anisotropy term to the energy equation of the model by Meiklejohn and Bean. This anisotropy which is called induced anisotropy for the FM layer, behaves like a spin glass at the interface. The magnetic energy of the system in this model is as below [204]:

$$\mathbf{E} = -\mu_0 H M_{FM} t_{FM} \cos(\theta - \beta) + K_{FM} t_{FM} \sin^2(\beta) + K_{AFM} t_{AFM} \sin^2(\alpha) + K_{SG}^{eff} \sin^2(\beta - \gamma) - J_{INT}^{eff} \cos(\beta - \alpha) \quad (4.7)$$

where, γ is the average direction of the non-collinear anisotropies at the interface with spin glass behavior, K_{SG}^{eff} is the effective anisotropy related to the AFM spins with reduced anisotropy at the interface and J_{INT}^{eff} is the reduced interfacial exchange interaction.

Using this model they have explained the exchange bias properties obtained in Co/CoO bilayers by polarised neutron scattering [9, 202–204] and Fe/CoO bilayers by soft X-ray magnetic scattering [204].

Frozen AFM interface model by Kiwi et al.

This model [3–5] assumes that during the cooling process the first AFM (compensated) interface layer freezes into a canted spin configuration that develops at T_N . This assumption is a consequence of different domain wall widths [231] in the FM and AFM due to different anisotropy. The FM domain wall width is about 100 nm thick, while it is just a few monolayers in the AFM because of strong anisotropy of the AFM [80].

The Hamiltonian in this model is given by:

$$\mathcal{H} = \mathcal{H}_{AFM} + \mathcal{H}_{INT} + \mathcal{H}_{FM} \quad (4.8)$$

where,

$$\begin{aligned} \mathcal{H}_{AFM} = & -J_{AFM} \left[S \hat{e}_{AFM} \cdot (\vec{S}^{(\alpha)} - \vec{S}^{(\beta)}) + 2\vec{S}^{(\alpha)} \cdot \vec{S}^{(\alpha)} \right] \\ & - \frac{1}{2} K_{AFM} \left[(\vec{S}^{(\alpha)} \cdot \hat{e}_{AFM})^2 + (\vec{S}^{(\beta)} \cdot \hat{e}_{AFM})^2 \right] \\ & - \frac{1}{2} \mu_B g (\vec{S}^{(\alpha)} + \vec{S}^{(\beta)}) \cdot \vec{H} \end{aligned}$$

$$\mathcal{H}_{INT} = -J_{INT} (\vec{S}^{(\alpha)} + \vec{S}^{(\beta)}) \cdot \vec{S}_1$$

$$\mathcal{H}_{FM} = -2J_{FM} \sum_{k=1}^{N-1} \vec{S}_k \cdot \vec{S}_{k+1} - \sum_{k=1}^N \left[\frac{K_{FM}}{H^2} (\vec{S}_k \cdot \vec{H})^2 + \mu_B \vec{S}_k \cdot \vec{H} \right]$$

In the above expressions \mathcal{H}_{AFM} describes the energy of the AFM substrate, \mathcal{H}_{INT} is the interface coupling, and \mathcal{H}_{FM} describes the energy of the FM slab. $S = |\vec{S}|$, and μ_B and g denote the Bohr magneton and Fe g-factor respectively. \vec{H} is the applied magnetic field. J_μ denotes the Heisenberg exchange parameter and K_ν the uniaxial anisotropy. \hat{e}_{AFM} denote the unit vector in the AFM anisotropy direction. $\vec{S}^{(\alpha)}$ and $\vec{S}^{(\beta)}$ are the canted spin vectors in the AFM interfacial layer. \vec{S}_k is the spin vector of the k th FM layer with the interfacial layer as $k = 1$.

From this model it has been concluded that because of the frozen canted AFM spins at the interface the energy is reversibly stored in a spin spiral, like in a spring magnet or incomplete domain wall (IDW), in the FM layer. By this model the experimental observations like positive and negative exchange bias, exchange bias for compensated and uncompensated interfaces, or orthogonal coupling between FM magnetization and AFM easy direction etc. are qualitatively and quantitatively explained.

Local Pinning Field Variation Model by Stiles and McMichael

According to the assumption of this theory [231–233], the AFM interface consists of polycrystalline grains with stable magnetic order. In the absence of the FM layer, the AFM grains order themselves in many quasi-degenerate arrangements, but in the presence of the FM layer they choose a particular configuration. This magnetic configuration is stable because of the weakness of the Zeeman term. When the AFM orders it retains a memory of the initial FM direction. This memory is also retained when the FM magnetization is later reversed; this is the cause of the unidirectional anisotropy. The idea of possible (partial) domain wall formation in the AFM to lock the interfacial spin configuration is also incorporated in this theory.

Using this model, they could explain the shifted hysteresis loop and the hysteretic effects observed in rotational torque magnetization and FMR experiments. The satisfactory explanation of experimental results are independent of the spin-flop coupling, i.e. the spin-flop coupling does not play a role in the observed unidirectional anisotropy. They also suggested that because of the polycrystalline nature of the AFM, even for the uncompensated interfaces there is a substantial compensation of the magnetic moments due to fluctuating easy axis directions of the individual grains. However, this theory has also limitations, because of its validity only for polycrystalline interfaces. Even for polycrystalline interfaces there should be other assumptions to be taken into account in order to get a satisfactory explanation of experimental results.

Domain State Model by Nowak et al.

Using Monte Carlo simulations with a heat bath algorithm the model by Nowak et al. [191–193] and Mishra et al. [178, 179] explains many of the unidirectional and associate properties of the exchange biased system. It is well known that when a diluted antiferromagnet is cooled below its T_N in an external magnetic field a domain state develops. The driving force for this domain formation is the statistical imbalance of the number of impurities of the two sublattices in a finite region. This is similar to the idea by Imry and Ma [127] to form domains in a diluted antiferromagnet. These magnetic domains in the AFM carry a net remanent magnetization. During the cooling process a part of

this remanent magnetization (known as irreversible domain state magnetization, IDS) is frozen and does not switch during the field reversal process. This frozen magnetization is responsible for the unidirectional anisotropy of the FM. The domain walls pass through the non-magnetic atoms or vacancies which acts like pinning centers for the AFM domains.

The Hamiltonian in this model has the following form:

$$\mathcal{H} = \left[-J_{FM} \sum_{\langle i,j \rangle} \mathbf{S}_i \cdot \mathbf{S}_j - \sum_i (d_z S_{iz}^2 + d_x S_{ix}^2 + \mathbf{S}_i \cdot \mathbf{B}) \right] \\ + \left[-J_{AFM} \sum_{\langle i,j \rangle} \epsilon_i \epsilon_j \sigma_i \cdot \sigma_j - \sum_i \epsilon_i (k_z \sigma_{iz}^2 + \sigma_i \cdot \mathbf{B}) \right] \\ + \left[-J_{INT} \sum_{\langle i,j \rangle} \epsilon_i \mathbf{S}_i \cdot \sigma_j \right]$$

The first part of the Hamiltonian describes the energy of the FM (exchange constant J_{FM}) where S_i denote the normalized spins at the i th site of the FM, and the z -axis is the easy axis with anisotropy constant d_z , while the x -axis is the hard axis with anisotropy constant d_x . The anisotropy keeps the FM spins in the $y - z$ plane. \mathbf{B} is the applied field. The second part describes the behavior of the AFM (exchange constant J_{AFM}) with σ_i denoting the normalized spin at the i th site of the AFM. The AFM is diluted by making $\epsilon_i = 0$ if the site i carries no magnetic moment and $\epsilon_i = 1$ if the site i carries a magnetic moment. The AFM has also the z -axis as easy axis. The third part describes the interaction between the FM and the AFM at the interface (exchange constant J_{INT}).

This model is in agreement with experimental results on Co/CoO bilayer systems with a diluted antiferromagnetic CoO layer [134, 175]. As a result of the theoretical simulations, a part of the remanent magnetization of the AFM domain, which rotate with the applied field, gives rise to a finite area of the hysteresis loop, and the magnetization which does not rotate gives an upward shift of the AFM hysteresis loop. This upward shift determines the exchange bias field. The other phenomena associated with exchange bias are explained in this model as below.

The domains are not sufficiently stable for very thin AFM layers. They become more and more stable with increasing AFM thickness, increasing the IDS magnetization, and formation of a volume domain structure increases the exchange bias. However, for very thick AFM layers the grain boundaries act to decrease the AFM coupling strengths; then the grains act magnetically independent, making the exchange bias constant for higher and higher thicknesses of the AFM.

The domain state, which is frozen at very low temperatures far below T_N , can show metastability because of thermal activation, and can exhibit domain wall motion at elevated temperatures. This domain wall motion reduces the magnetisation of IDS and also the exchange bias.

A small decrease of the exchange bias field or change of sign of H_E is explained by means of the type of coupling between the FM and AFM. For systems like Co/CoO, where the exchange bias does not change its sign, the interface coupling between Co and CoO is positive, but for systems like Fe/FeF₂ and Fe/MnF₂, where the exchange bias field changes its sign (positive exchange bias), have a negative coupling between FM and AFM spins at the interface.

The training effect is explained as the loss of IDS magnetization because of rearrangements of the AFM domain structure. According to the hysteresis loop of the AFM obtained by this simulation, the initial saturation magnetization of the AFM is higher than the next saturation magnetization for increasing fields, i.e. the hysteresis loop does not close. This explains the loss of IDS magnetization, which is strong at the beginning and becomes weaker and weaker as the number of loops increases. This loss of magnetization also leads to a reduction of the exchange bias field.

The dilution or the increase of defects in the AFM enhances the exchange bias field up to a certain optimum dilution. For higher dilution the domain wall energy is not high enough for the upward shift of the AFM hysteresis loop, and, hence, a reduction of the exchange bias field.

There exists also some other theories, e.g. the spin-wave theory of exchange anisotropy [237], which are not thoroughly looked at (although experimentally consistent [177]), because of their complexity and/or inability to explain all of the observed effects in an exchange coupled system.

4.2 Exchange bias and spin structure

As the antiferromagnetic domain structure plays an important role in determining the ferromagnetic spin alignment. For a clear understanding of the exchange bias effects, knowledge of the spin structure at the FM/AFM interface and of the AFM domain structure is important. By employing photoelectron emission microscopy (PEEM) with high spatial resolution, using the phenomenon of X-ray magnetic linear dichroism, the AFM domain structure has been observed in twinned LaFeO₃ films on SrTiO₃ [213]. Nolting et al. [190] have shown that there is a direct correlation between the arrangement of spins in the ferromagnet (Co) and the antiferromagnet (LaFeO₃). Using polarisation dependent X-ray magnetic dichroism spectro-microscopy they have also observed that the alignment of the ferromagnetic spins is determined by the spin direction in the underlying antiferromagnet.

By polarization dependent X-ray photoelectron emission microscopy Ohldag et al. [6, 194, 195] have observed that during the time of ferromagnetic Co layer deposition the antiferromagnetic NiO surface spins rotate in the film plane to reorient parallel to the spins of the Co layer. Development of an interfacial CoNiO_x layer [6] upon deposition of the Co layer on the antiferromagnetic NiO layer was observed (using X-ray absorption spectromicroscopy), carrying some uncompensated moment. These spins align parallel to the AFM layer and align the FM spins in the Co layer. The uncompensated and pinned interfacial spins are tightly locked to the AFM spins and do not rotate in an

external magnetic field. These interfacial spins are claimed to be responsible for the increase in coercivity and for the exchange bias [195] in FM/AFM systems.

Miltényi et al. [175] have used diluted antiferromagnetic CoO layers and have observed that the exchange bias field can be controlled by the extent of dilution. Based on these results the domain state model by Nowak et al. [191] could explain the origin of exchange bias, which suggests that the AFM dilution leads to formation of volume domains in the antiferromagnet, which can cause and control exchange bias.

Assuming that the bulk spin structure for the antiferromagnet is preserved at the FM/AFM interface, in a naive picture the pinning at an uncompensated surface and also the exchange bias field may be assumed to be stronger. On the other hand, for a compensated surface the spins pinning the FM layer may cancel, resulting in zero H_E . However, the exchange bias was observed in many systems with compensated surfaces. In some cases the exchange bias field was found to be even higher for the compensated surface than for the uncompensated surface. In most theoretical cases the AFM surface spin direction is assumed to be parallel to the interface (e.g. $\text{FeF}_2(110)$). However, it has been observed that when the AFM interface spins are parallel to the interface a large exchange bias has been observed, but for AFM spins pointing out of plane (assuming the bulk spin structure) (e.g. $\text{FeF}_2(001)$) the observed $H_E = 0$ Oe. An intuitive explanation for this effect is the interfacial FM/AFM spin-spin interaction strength, which may be written as $\vec{S}_{FM} \cdot \vec{S}_{AFM} = S_{FM} S_{AFM} \cos\alpha$, where α is the angle between the two spins. If the FM spins lie in the plane, then α is the angle between the AFM spins and the interface plane. For in-plane AFM spins $\cos\alpha = 1$ (maximum), hence H_E will be maximum, but for perpendicular AFM spins $\cos\alpha = 0$ and $H_E = 0$ (minimum). Another possible but equivalent explanation for H_E is that $H_E = \sqrt{K_{AFM} A_{AFM} \cos\alpha}$, where K_{AFM} = anisotropy and A_{AFM} = stiffness of the AFM [189].

Although some theoretical models assume collinear FM-AFM spin coupling at the interface, it has been found experimentally that this is not necessarily true. Several systems ($\text{Fe}_{20}\text{Ni}_{20}/\text{FeMn}$ [130], $\text{Fe}_3\text{O}_4/\text{CoO}$ [125], Fe/FeF_2 (single crystal) [183, 188]), $\text{Fe}_{20}\text{Ni}_{80}/\text{CoO}$ [182] etc. exhibit perpendicular exchange coupling at the interface between the FM and AFM spins. Moreover, the temperature dependence of the Fe/FeF_2 system shows that the FM easy axis rotates by 90° between room temperature (RT) and 10 K, with the rotation starting around T_N of the FeF_2 [183]. Intuitively, the lowest energy configuration for the compensated surface is with the FM spins oriented perpendicular to the AFM sublattice spins. However, this can be valid also for uncompensated surfaces, if (e.g due to fluctuations in roughness, domain formation etc.) the AFM spins align antiparallel to each other at the interface making the interface an compensated-type surface. Hence, the exchange bias depends strongly on the spin structure at the interface. Extrinsic effects (roughness, crystallinity etc.) and intrinsic effects (anisotropy, spin orientation etc.) are contributing to H_E .

Although there has been observed the perpendicular coupling between the FM and AFM spins in some exchange-biased systems, there is an intense debate on the type of coupling between FM and AFM at the interface of FM/ FeF_2 systems [see e. g. [285–289]]. In exchange biased FM/ FeF_2 (untwinned) systems showing positive exchange bias field with a layer of Co or Ni as FM, Li et al. [285] have observed a rotation of the FM

spins opposite to the cooling field direction. They have obtained a thermal hysteresis loop of the FM magnetization during field cooling (field applied along the c -axis of FeF_2) suggesting a parallel or antiparallel coupling between the Fe spins of the FM and the AFM (FeF_2). They have explained that the uncompensated AFM spins freeze along the applied field direction and during cooling through T_N the FM spins rotate to couple antiparallel with the uncompensated AFM moments, which are oriented along the c -axis of the AFM. However, this rotation is only seen in systems showing positive exchange bias. For systems showing negative exchange bias the FM spin rotation during thermal cycling has not been observed, suggesting that in these systems the AFM uncompensated spins align opposite to the cooling field direction by overcoming the smaller cooling fields, and the FM moments align along their easy direction along the cooling field.

Despite of intense research, the interfacial spin structure in exchange-biased systems is poorly understood due to the lack of techniques capable of providing detailed information about the spin arrangement at the interface. However, Mössbauer spectroscopy and Nuclear Resonant Scattering (NRS) of synchrotron radiation are viable techniques not only for the observation of the spin structure, but also for the determination of the depth dependence of the spin structure. By placing a Mössbauer active ^{57}Fe probe layer at the required depth, the depth dependent spin structure can be derived from the line intensity ratio of the Zeeman-split Mössbauer sextet. Along with the spin structure other magnetic informations, like the blocking temperature and other magnetic phase transitions, the magnetic hyperfine field and its T -dependence and even structural information can be obtained from the Mössbauer spectrum. NRS of synchrotron radiation provides information on the depth dependent spin structure along with high spatial resolution. An experimental investigation of the Fe and FeF_2 spin structure in exchange-biased Fe/MnF_2 and Fe/FeF_2 systems by using the method of conversion electron Mössbauer spectroscopy (CEMS) and NRS of synchrotron radiation will be described in Chapters 6, 7 and 8.

Chapter 5

Magnetic Anisotropy and Hyperfine Interactions in MnF_2 and FeF_2

5.1 Introduction

For the understanding of the spin structure and exchange bias in $\text{Fe}/\text{MnF}_2/\text{MgO}(001)$ and $\text{Fe}/\text{FeF}_2/\text{MgO}(001)$ films knowledge of the nature of growth of the epitaxial MnF_2 and FeF_2 layer is important. Along with that knowledge of the magnetic anisotropies present in both materials is necessary to understand the unidirectional anisotropy and the influence of the antiferromagnet on the ferromagnetic spin structure. In this chapter the nature of growth, difference in the anisotropies of MnF_2 and FeF_2 and the ^{57}Fe hyperfine parameters in FeF_2 will be discussed.

5.1.1 Crystallographic and magnetic structure of MnF_2 and FeF_2

MnF_2 and FeF_2 have the rutile type of crystal structure [268–270]. Fe (or Mn) ions are on the body centered tetragonal lattice ($a = b \neq c$, $\alpha = \beta = \gamma = 90^\circ$) with D_{2h} symmetry and $P4/mnm$ space group. The point symmetry around the iron (or manganese) atoms is characterized by three mutually perpendicular reflection planes, and the highest rotational symmetry is twofold. For MnF_2 , the lattice constants are $a = b = 4.87 \text{ \AA}$, $c = 3.31 \text{ \AA}$, and for FeF_2 they are $a = b = 4.697 \text{ \AA}$, $c = 3.309 \text{ \AA}$ [263].

The spin structure of bulk MnF_2 and FeF_2 has been obtained from magnetic neutron scattering [263]. The Fe^{2+} or Mn^{2+} ions form a chain running parallel to the c -axis. Each chain has four parallel neighboring chains having antiparallel spins with respect to the spins of the center chain. The magnetic and crystal structure is schematically displayed in Fig. 5.1 [263].

The Néel temperature of MnF_2 and FeF_2 is 67.33 K [261] and 78.2 K [272], respectively. The Néel temperature decreases by an amount of the order of milliKelvin by the application of a magnetic field or pressure [261]. Also many interesting phenomena like the coexistence of internal strain-induced para- and ferro-magnetically behaving ions exactly at T_N , have been observed [261]. However, from the point of view of the exchange anisotropy these phenomena are not important here.

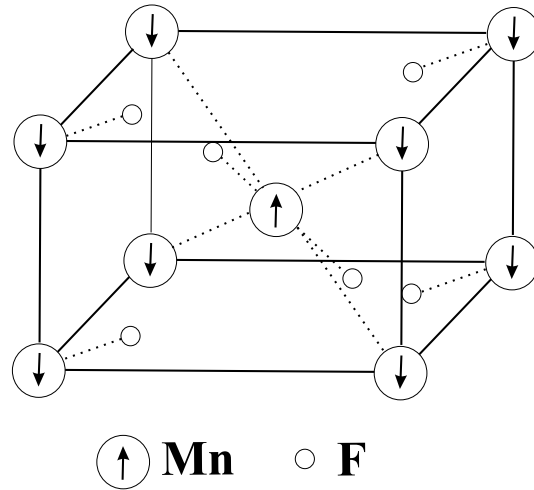


Figure 5.1: Crystal and magnetic structure of MnF_2 and, equivalently, FeF_2 . The large circles show the position of Mn^{2+} (or Fe^{2+}) ions with their magnetic moment directions shown as arrows. The small circles represent the fluorine atoms.

From antiferromagnetic resonance measurements on FeF_2 the observed total magnetic moment corresponds to a g -factor of 2.25. From polarized neutron diffraction results $g = 2.23$ (equivalent to $\mu = 4.46\mu_B$) [262] or 2.31 [263]. However, high energy (115 keV) magnetic X-ray diffraction yields a pure spin magnetic moment of $4.01 \mu_B$, which corresponds to $g = 2$ [265] for the Fe^{2+} ion, as in the free Fe^{2+} ion. This strongly suggests that about 12 % of the Fe^{2+} magnetic moment originates from the orbital contribution in FeF_2 . On the other hand, the contribution from the orbital magnetic moment of Mn^{2+} is zero in MnF_2 ($g = 1.99$) [263, 264].

5.1.2 Anisotropies in MnF_2 and FeF_2

Crystal anisotropy plays an important role in determining the spontaneous magnetization, susceptibility and shape of the hysteresis loop. The magnetic anisotropies are basically of two main types : intrinsic and induced anisotropy.

The intrinsic anisotropy is the anisotropy intrinsic to the material, e.g., magnetocrystalline anisotropy. Although the details of magnetocrystalline anisotropy are not clearly understood, there is no doubt that magnetocrystalline anisotropy, in general, is due to spin-orbit coupling. This is because spin-lattice coupling is too weak and can be neglected, and lattice-orbit interaction is strong, and even a very high magnetic field cannot influence it. The atom inside a solid does not behave like a free atom, and the orientation of the orbits are fixed strongly to the lattice, which results in the quenching of orbital magnetic moments and strong lattice-orbit interaction.

Shape anisotropy, stress anisotropy, exchange anisotropy and other anisotropies, induced by processes like thermomagnetic treatment, stress annealing, plastic deformation and magnetic irradiation, are basically induced anisotropies. The induced anisotropy originates from many different reasons. The shape anisotropy appears because of the different physical shape of the ferromagnetic materials, resulting in magnetic stray fields.

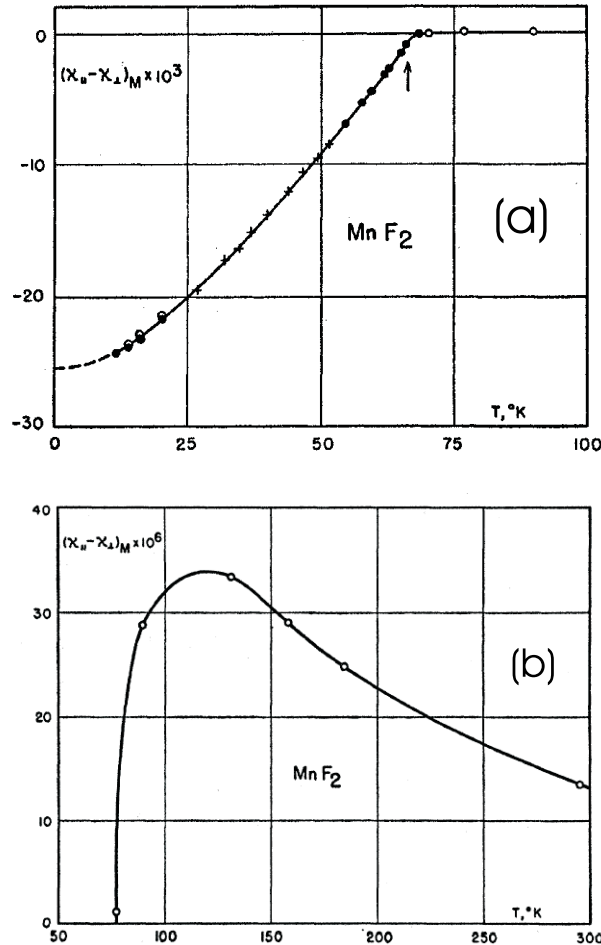


Figure 5.2: Molal magnetic anisotropy $(\chi_{\parallel} - \chi_{\perp})$ versus T of MnF_2 . χ_{\parallel} and χ_{\perp} are molal susceptibilities parallel and perpendicular to the c -axis [268].

The exchange anisotropy appears because of the presence of an AFM near a FM. Different phenomena involved in exchange anisotropy are basically described in chapter 3 and will also be the subject of the next chapters (chapter 5, 6, 7 and 8).

In this section the magnetic anisotropies of antiferromagnetic FeF_2 and MnF_2 will be discussed. The tetragonal symmetry of MnF_2 and FeF_2 makes the principal axes of the magnetic susceptibility tensor (χ) to lie along the c -axis of the crystal, which is the easy axis. The susceptibility in all directions normal to the c -axis is the same. The magnetic anisotropy is the difference between the susceptibility parallel (χ_{\parallel}) to the c -axis and the susceptibility normal (χ_{\perp}) to the c -axis: $(\chi_{\parallel} - \chi_{\perp})$.

The temperature dependence of the anisotropy of MnF_2 and FeF_2 has been thoroughly investigated [266, 267]. The T -dependence of observed anisotropy for MnF_2 and the parallel and perpendicular components of the susceptibility are given in Fig. 5.2 (a), Fig. 5.2 (b) and Fig. 5.3 (a), respectively. From Fig. 5.2 ((a), (b)) it is clear that at high temperature ($T > T_N$) the anisotropy $(\chi_{\parallel} - \chi_{\perp})$ of MnF_2 is quite small. At low temperatures, below about 70 K, this changes remarkably. Notice the vertical scales of Fig. 5.2 (a) and Fig. 5.2 (b). χ_{\parallel} and χ_{\perp} in Fig. 5.2 (b) follow the theory by van Vleck

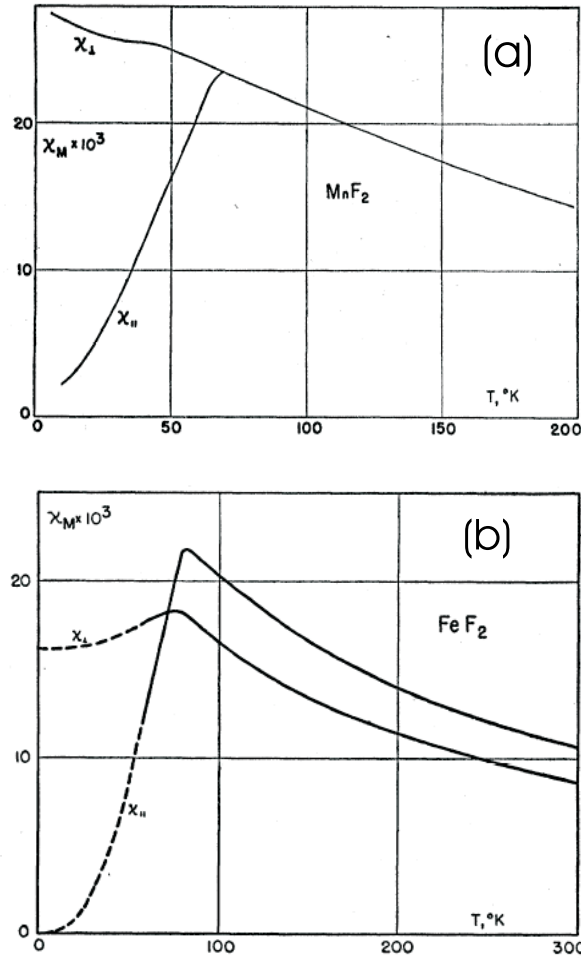


Figure 5.3: Molal magnetic susceptibility of MnF_2 (a) and FeF_2 (b). χ_{\parallel} and χ_{\perp} are molar susceptibilities parallel and perpendicular to the c -axis, respectively [268].

[271].

Comparatively higher susceptibility values parallel to the c -axis (χ_{\parallel}) than perpendicular to the c -axis (χ_{\perp}) of MnF_2 suggests that the paramagnetic moments align preferentially parallel to the c -axis at higher temperatures, $T > T_N$, under an applied field. At these higher temperatures the exchange forces in MnF_2 which cause the antiferromagnetic ordering are mostly isotropic in nature, since the energy is invariant under rotation about the crystal axes [271]. However, the small high-temperature anisotropy of MnF_2 is due to the slight splitting of the 6S level of the Mn^{++} ions by the crystalline electrostatic field. At the vicinity of 100 K, the short-range order caused by the energetically much larger (but isotropic) exchange forces begins to appear in the crystal. As the temperature is still lowered the extent of ordering continues to grow. Below T_N , where Mn spins are co-operatively coupled antiparallel, the large anisotropy is due to the strong exchange coupling between Mn^{++} ions accompanied by strongly anisotropic dipolar interactions. These exchange forces, which can produce a very small anisotropy, but act on a large group of coupled spins, become more significant as compared to $k_B T$ at low temperature. These forces are responsible for aligning the coupled Mn spins parallel to the c -axis. The

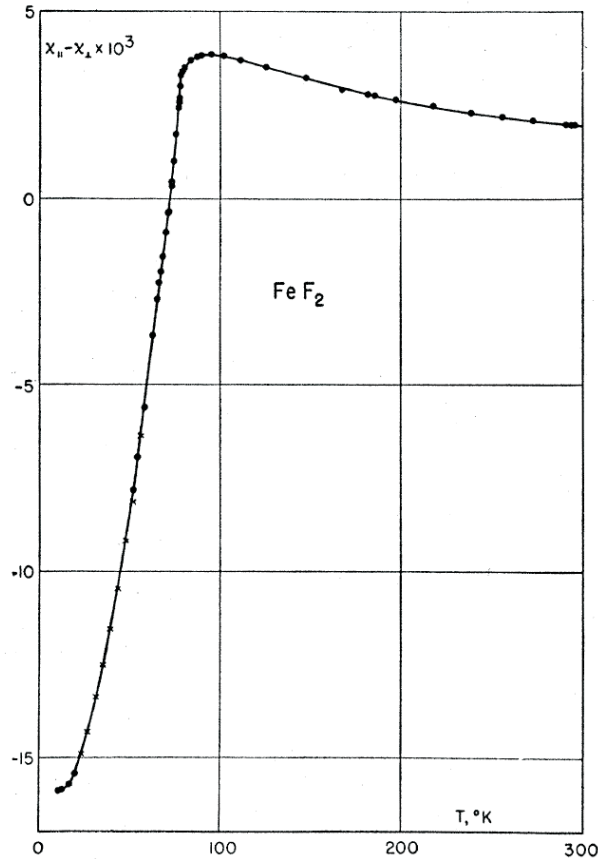


Figure 5.4: Molal magnetic anisotropy of FeF_2 . χ_{\parallel} and χ_{\perp} are molal susceptibilities parallel and perpendicular to the c -axis. Note that the scale (ordinate) is 1000 times smaller than that of Fig.5.2 [268].

magnetic dipole-dipole interaction, which becomes stronger with the development of the strong isotropic exchange field, produces the observed anisotropy. These dipolar forces favor to align the spins parallel to the c -axis [267]. The spin alignment is clearly understood from neutron diffraction measurements [263].

The measured anisotropy ($\chi_{\parallel} - \chi_{\perp}$) for FeF_2 is shown in Fig. 5.4 [266]. Like MnF_2 , the susceptibility at higher temperatures ($T > T_N$) is larger in the direction of the c -axis, but the magnitude of the anisotropy is much greater than that of MnF_2 . The anisotropy rises with decreasing temperature, but it decreases rapidly after reaching maximum at about 95 K. The behavior of χ_{\parallel} and χ_{\perp} is given in Fig. 5.3(b) [266], which are qualitatively in agreement with the theory [271]. However, as discussed in the previous section, in FeF_2 the orbital contribution to the total magnetic moment is nonzero. The orbitals contribute about 12 % to the total magnetic moment. So the interaction between orbital motion of the electrons and the crystalline electrostatic fields (lattice-orbit interaction) produces a larger magnetic anisotropy in FeF_2 than in MnF_2 at higher temperatures. The energy level scheme of FeF_2 under the action of the crystalline fields is given in Fig. 5.5. On the other hand, contrary to MnF_2 , due to the increase of the number of d -shell electrons beyond that of the half-filled shell in the ferrous ion, the magnitude of exchange anisotropy is expected to be less, which may be the cause of the decrease of

the perpendicular susceptibility in FeF_2 below T_N .

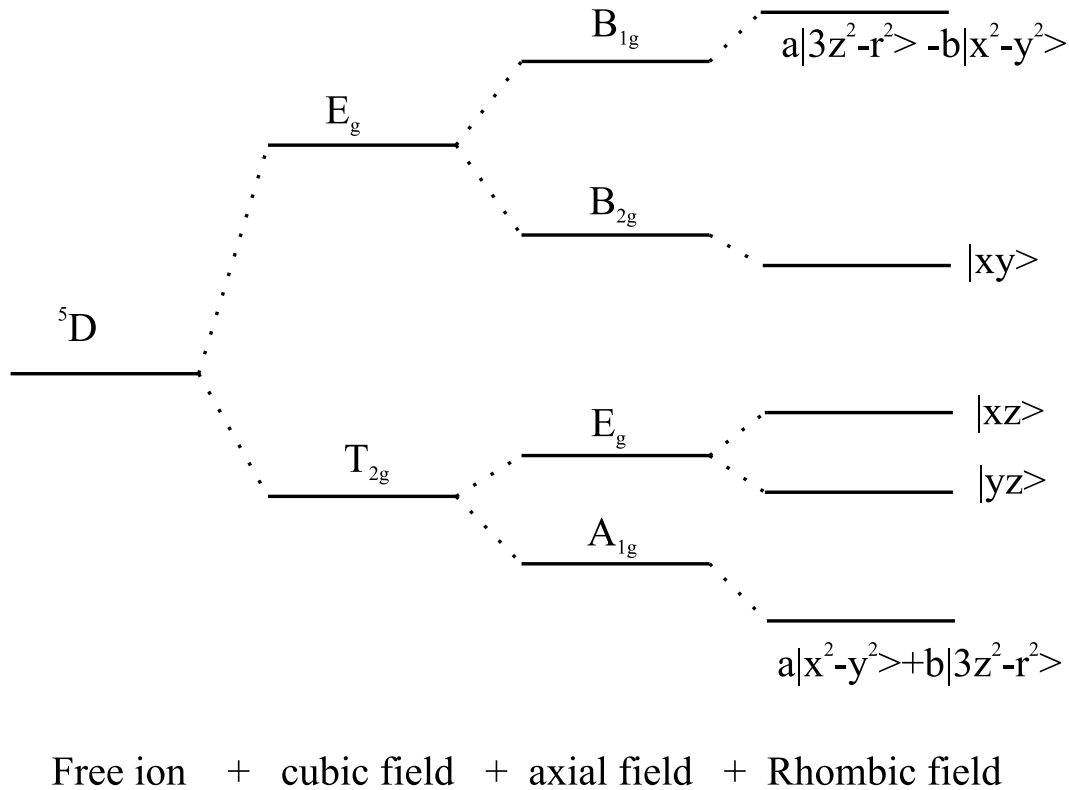


Figure 5.5: The electronic energy level scheme for FeF_2 under the action of the crystalline electric field [277].

In order to understand the nature of growth and the anisotropic properties and hyperfine interactions thin films of FeF_2 grown epitaxially onto $\text{MgO}(100)$ substrates have been studied. The details will be given in the following sections.

5.2 Sample preparation and characterization

A tremendous amount of literature is available on the preparation and growth of antiferromagnetic MnF_2 and FeF_2 on $\text{MgO}(001)$ substrates. Single-layer FeF_2 or MnF_2 samples were prepared by electron beam evaporation onto $\text{MgO}(100)$ substrates. [The sample was prepared and characterized by X-ray diffraction by Dr. W. A. A. Macedo at the University of California, San Diego, USA]. The MnF_2 or FeF_2 ingots were used for the preparation. Prior to deposition the substrates were heated to 450°C for 15 minutes and then cooled to the MnF_2 or FeF_2 growth temperature. The typical growth temperature was 325°C for MnF_2 and 200°C for FeF_2 . The film thickness during growth was monitored by quartz crystal oscillators. The growth rate was about $2 \text{ \AA}/\text{s}$. MgO has cubic structure with a lattice parameter of 4.216 \AA . FeF_2 and MnF_2 have body centered tetragonal structure. In order to releav the strain between the MnF_2 layer and $\text{MgO}(001)$ substrate, a 160 \AA thick ZnF_2 buffer layer was deposited first. ZnF_2 has also the body centered tetragonal structure with $a = b = 4.7034 \text{ \AA}$ and $c = 3.1335 \text{ \AA}$ [276]. A cap layer

of 30 Å Al was also evaporated to protect the sample from oxidation. After growth the samples were characterized by high and small angle X-ray diffraction. A 1500 Å FeF_2 film was characterized by Mössbauer spectroscopy.

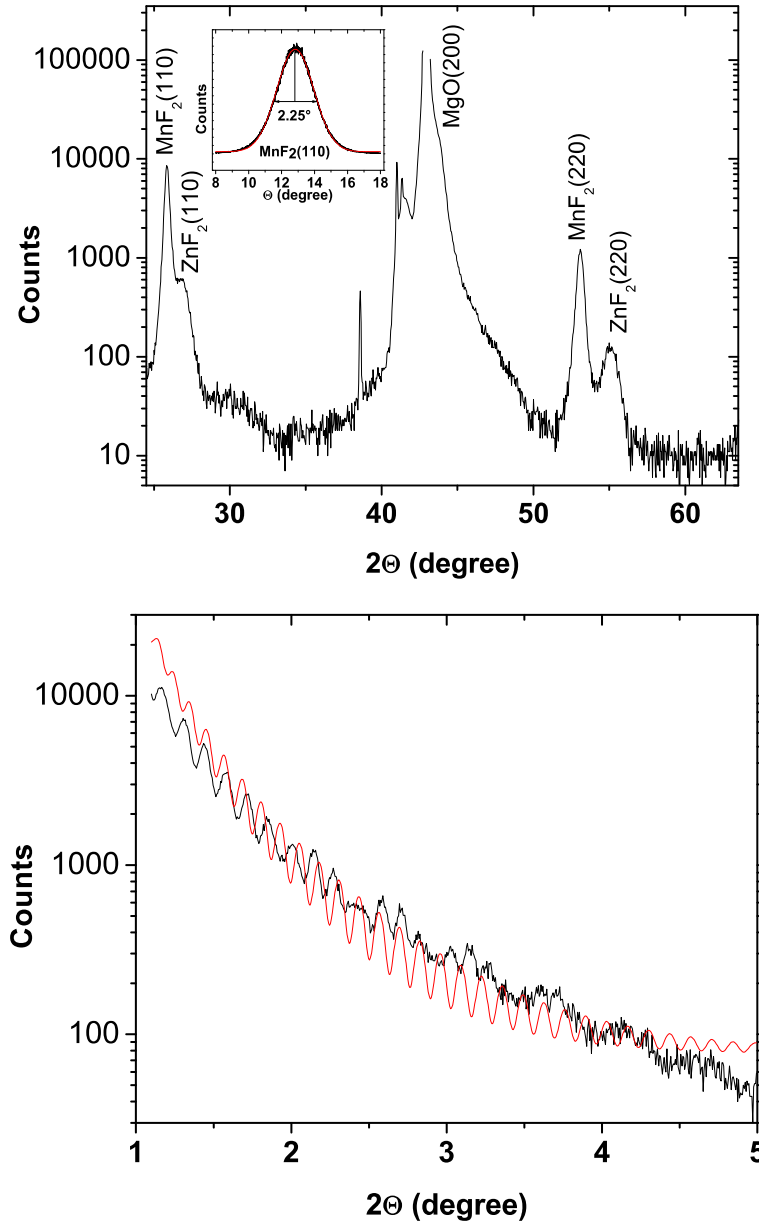


Figure 5.6: (a) X-ray diffraction pattern of (520 Å) MnF_2 / (160 Å) ZnF_2 / $\text{MgO}(100)$. The epitaxial nature of the MnF_2 film is revealed by the (110) and (220) reflections. (The c-axis is in the plane of the film). The FWHM of the rocking curve of the $\text{MnF}_2(110)$ peak (insert) is about 2.25° . The red curve in the insert is the fitting to the measured rocking curve data. (b) Small angle XRD pattern of the same film. The red curve is a fitting to the data for the MnF_2 layer. (Cu-K_α radiation)

Fig. 5.6 and Fig. 5.7 shows the typical X-ray diffraction pattern for a 30 Å Al / 520 Å MnF_2 / 160 Å ZnF_2 film and 30 Å Al / 450 Å MnF_2 / 160 Å ZnF_2 film, respectively, on $\text{MgO}(001)$ substrates. The epitaxial nature of the film with (110) orientation is clearly

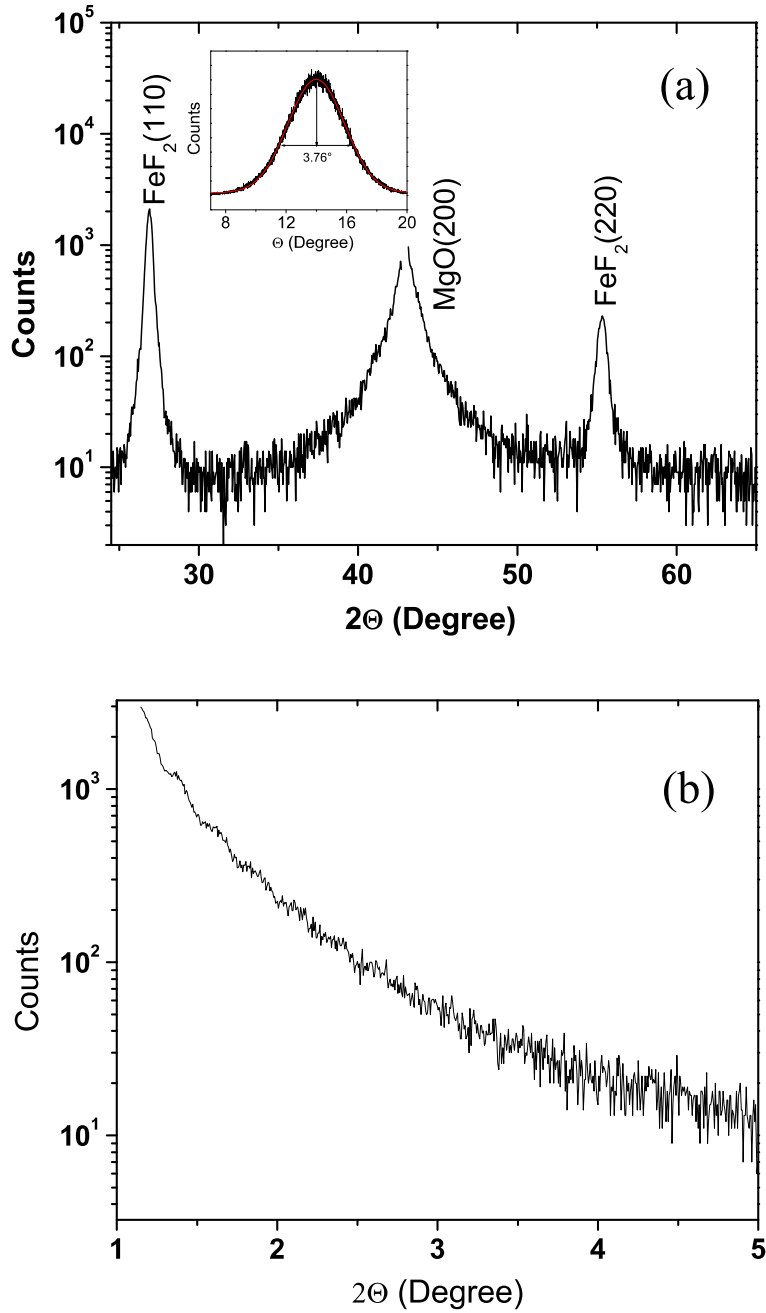


Figure 5.7: (a) X-ray diffraction pattern of a typical film of 450 Å $\text{FeF}_2/\text{MgO}(100)$. The epitaxial nature of the FeF_2 film is revealed by the (110) and (220) reflections. (The c -axis is in the plane of the film). The FWHM of the rocking curve of the $\text{MnF}_2(110)$ peak (insert) is about 3.76° . The red curve in the insert is the fitting to the measured rocking curve data. (b) Small angle XRD pattern of the same film. (Cu K_α radiation)

evident. As the substrate ($\text{MgO}(001)$) has cubic structure, the films have two equivalent in-plane directions for the orientation of the c -axes. This causes pseudo-twinning of the FeF_2 or MnF_2 films, i.e., the c -axes of the $\text{FeF}_2(110)$ or $\text{MnF}_2(110)$ are oriented towards either of the two diagonals of the $\text{MgO}(100)$ substrate surface, namely towards $\text{MgO}[110]$ and $\text{MgO}[\bar{1}\bar{1}0]$ (as shown in the Fig. 5.8). This feature has been observed by grazing incidence X-ray diffraction as shown in Fig. 5.9 for a typical $\text{Al}/\text{Fe}/\text{FeF}_2(110)/\text{MgO}(001)$

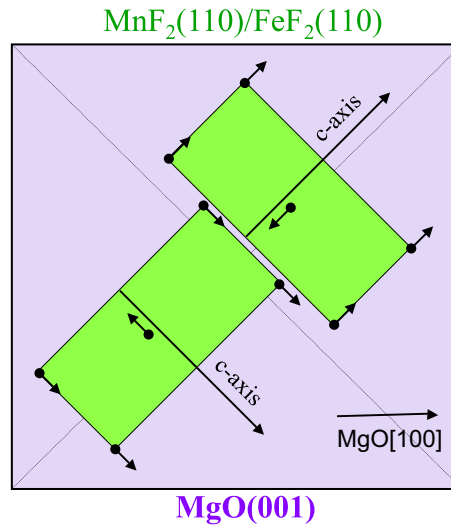


Figure 5.8: Schematic diagram of the antiferromagnetic pseudo-twin domains (green areas). The c -axes of the MnF_2 or FeF_2 domains are oriented along the diagonals of the square-shaped $\text{MgO}(001)$ substrate.

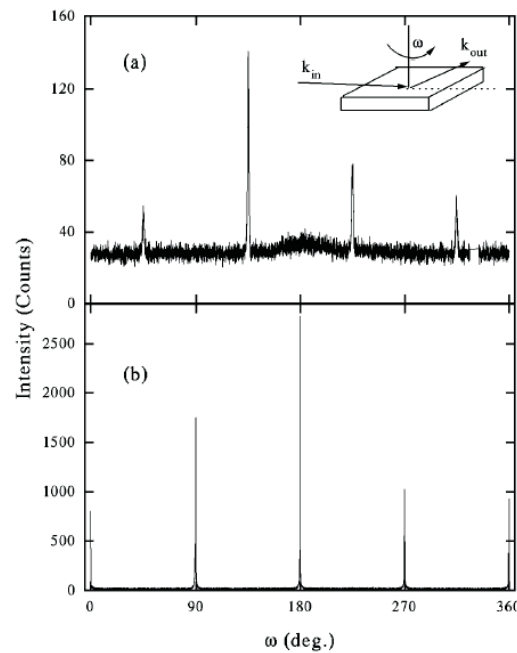


Figure 5.9: (a) In-plane x-ray diffraction of the FeF_2 (002) in-plane peak for an FeF_2 -Fe bilayer film. The insert shows the scattering geometry (ω -scan). (b) In-plane x-ray diffraction of the $\text{MgO}(200)$ substrate in-plane peak [188].

film [188]. In grazing incidence X-ray diffraction the detector angle 2θ is set to one of the MnF_2 and FeF_2 reflections (e.g. FeF_2 (002), $2\theta = 55.54^\circ$), with the X-ray coming almost parallel to the plane of the film. The sample is then rotated about its normal. The inset of Fig. 5.9 (a) shows the scattering geometry. The result for the film is shown in Fig. 5.9(a). The four-fold symmetry appears because of the pseudo-twinning of the rectangular $\text{FeF}_2(110)$ surface unit cell. The four-fold symmetry of the in-plane reflections of

the substrate $\text{MgO}(200)$ peak ($2\theta = 42.91^\circ$) is shown in Fig. 5.9 (b). This four-fold symmetry appears because of the fact that $\text{MgO}(100)$ surface unit cell is a square. With respect to the substrate, the in-plane domains are determined by $\text{FeF}_2[001] \parallel \text{MgO}[110]$ and $\text{FeF}_2[1\bar{1}0] \parallel \text{MgO}[\bar{1}10]$. Now it is clear that the $\text{FeF}_2(110)$ and $\text{MnF}_2(110)$ films grow epitaxially on $\text{MgO}(001)$ with their c-axes in the plane of the substrate, but with domains tilted by $\pm 45^\circ$ relative to the $\text{MgO}(100)$ surface direction.

For comparison commercial FeF_2 (N_2 flushed) powder from ACROS with 99 % purity was also studied in order to confirm the line positions of the FeF_2 Mössbauer spectrum.

5.3 Hyperfine interaction in FeF_2

The CEMS study has been done on a Al-coated 1500 Å FeF_2 thin film grown by electron beam evaporation on the $\text{MgO}(100)$ substrate. The FeF_2 powder was measured in Mössbauer transmission geometry. The Mössbauer spectra of the film and the powder were measured at 80 K and 18 K in a variable temperature bath cryostat. For CEMS, a channel electron multiplier was used as detector, whereas for transmission Mössbauer spectroscopy a proportional counter was used. All the spectra are fitted by using the computer program 'NORMOS' by R. A. Brand [28, 29]. Above T_N , there is no magnetic ordering of the antiferromagnet and it behaves like a paramagnet. This gives rise to a electric quadrupole doublet at 80 K. This spectrum has been fitted by a symmetrical doublet. The CEM spectrum at 18 K, i.e., below T_N , has an eight-line pattern and has been least-squares fitted by considering the full Hamiltonian for the magnetic-plus-electric hyperfine interaction of FeF_2 . The Hamiltonian is given by:

$$H = \frac{eQ}{4I(2I-1)} \{V_{zz}[3I_z^2 - I(I+1)] + (V_{xx} - V_{yy})(I_x^2 + I_y^2)\} + H_{\text{nucl-Zeeman}} \quad (5.1)$$

This eight-line spectrum has been clearly observed for the FeF_2 powder, and it has been least-squares fitted in a similar manner. However, the presence of some other phase containing Fe^{3+} ions in the powder makes the spectrum complicated. Different Mössbauer spectral parameters for the thin film and the powder will be discussed below. The Mössbauer spectroscopical parameters have been listed in Table 5.1.

FeF_2 powder

The transmission Mössbauer spectra for the powder at 80 K and 18 K are given in Fig. 5.10 (a) and (b), respectively. The spectrum measured at 80 K has been fitted by five different subspectra. The dominant doublet (subspectrum #1) (isomer shift (IS)= 1.47 mm/s, quadrupole splitting (ΔE_Q) = 2.91 mm/s) has been assigned to the FeF_2 phase (Table 4.1). The other spectra are due to oxides and other (Fe-F) phases present in the sample. The other weaker doublet (subspectrum #5) is due to some Fe^{3+} impurities. Out of the three fitted sextets, the sextet with a hyperfine field of 45 T at 80 K (subspectrum #4) and 49 T at 18 K (subspectrum #5) has been assigned to the Fe_3O_4 phase of iron oxide. The other sextets having very high hyperfine field values, could be the FeF_3 phase and some oxide-fluoride (Fe-F-O) state of Fe, but their origin is not clearly understood; however, they are not important for our purpose. At 18 K, the spectrum has been fitted by six subspectra. The dominant subspectrum (subspectrum #1)

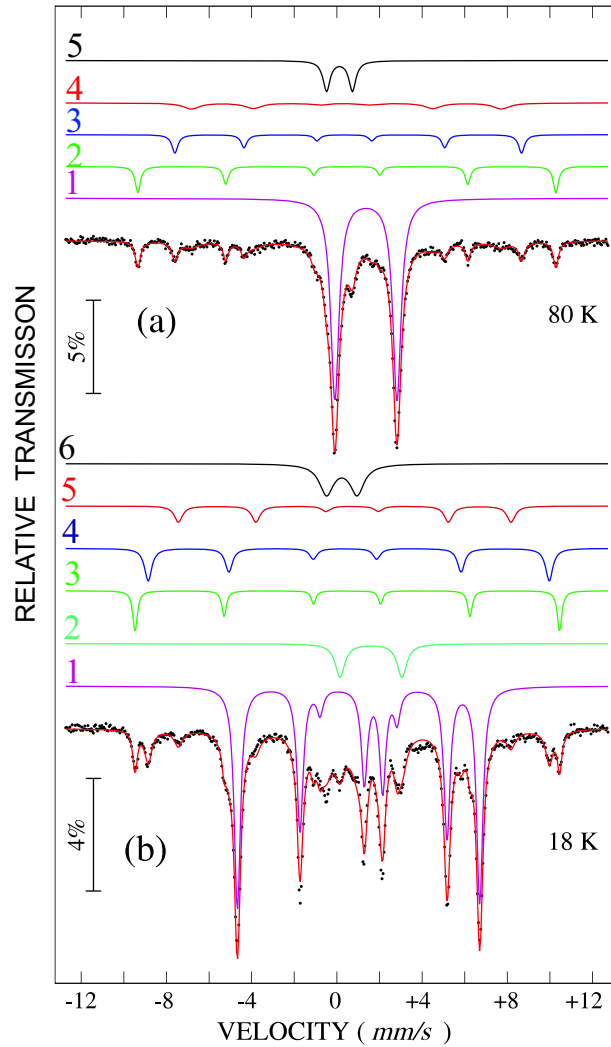


Figure 5.10: Transmission Mössbauer spectra of FeF_2 powder, taken at 80 K ($> T_N$) (a) and 18 K ($< T_N$) (b). Spectrum (a) has been least-squares fitted with three Zeeman sextets and two quadrupole doublets. The dominant doublet with large quadrupole splitting (pink) originates from FeF_2 . Spectrum (b) has been least-square fitted with three Zeeman sextets, two quadrupole doublets and an eight line subspectrum. The latter (pink), which is attributed to FeF_2 , was fitted by using the full hyperfine Hamiltonian method because of similar magnitude of quadrupole and Zeeman interactions in FeF_2 . All other subspectra were fitted by considering the strong Zeeman interaction and a small perturbation of quadrupole interaction.

which is fitted by eight-lines, by using the full Hamiltonian method, has been assigned to FeF_2 by considering the literature values of the isomer shift, quadrupole splitting and magnetic hyperfine field [272]. From the two doublets used for fitting, the doublet with a small quadrupole splitting has been assigned to Fe^{3+} impurities. The doublet with a large quadrupole splitting and high isomer shift is assigned to very small FeF_2 particles, whose blocking or Néel temperature is less than 18 K. Again, out of the three sextets, only one (with $B_{hf} = 49$ T) is assigned to Fe_3O_4 . The other two sextets have very high B_{hf} values of 61 T (subspectrum #3) and 58 T (subspectrum #4), and could originate from the FeF_3 phase [274, 275] and from some oxide-fluoride state of Fe, respectively;

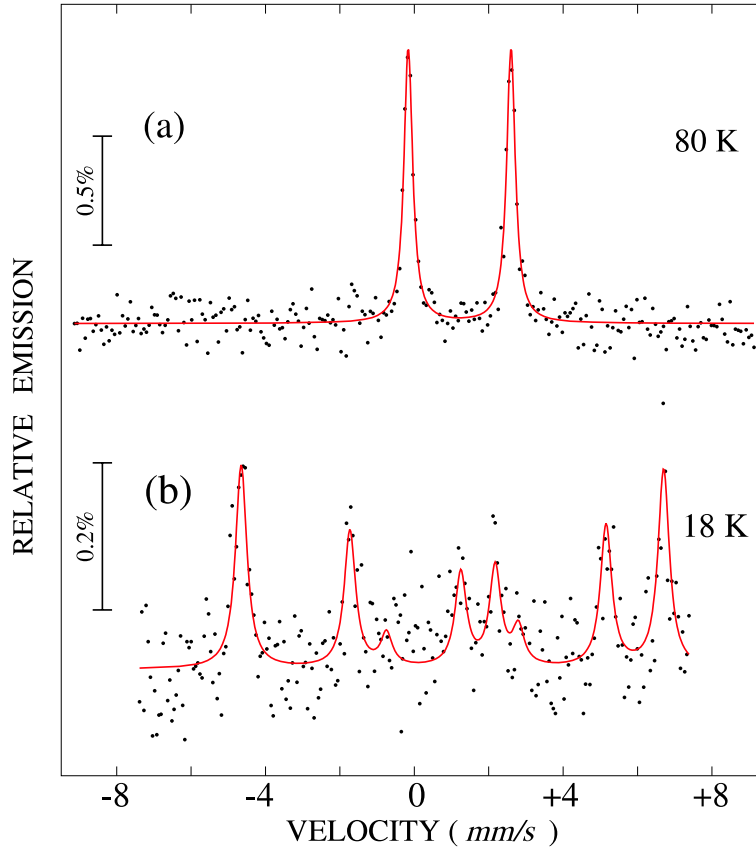


Figure 5.11: CEM spectra of a 1500-Å thick FeF_2 (twinned) thin film grown on $\text{MgO}(100)$, taken at 80 K ($> T_N$) (a) and 18 K ($< T_N$) (b). Spectrum (a) has been least-squares fitted with a quadrupole doublet. Spectrum (b) has been least-squares fitted with an eight-line spectrum, by using the full hyperfine Hamiltonian method.

however, their origin is not clearly understood. The important information obtained from the fittings of the FeF_2 subspectrum is that the angle between the main component of the EFG (V_{zz}) and the magnetic hyperfine field (B_{hf}) is 90° . All the observed hyperfine parameters for the FeF_2 powder at 80 K and at 18 K (Table 4.1) are in good agreement with the corresponding literature values [272].

FeF_2 Thin Film

The CEMS spectra for the 1500-Å thick FeF_2 film are shown in Fig. 5.11. From the fitting of the spectrum, the obtained isomer shift value at 80 K (Fig. 5.11(a)) is about 1.33 mm/s (relative to $\alpha\text{-Fe}$ at RT), which is in good agreement with the value reported in the literature [273]). This large isomer shift is typical for ferrous compounds. Hence, this confirms the ferrous state in our FeF_2 film.

According to the literature [23, 273], the quadrupole splitting (ΔE_Q) observed in FeF_2 is quite large. The observed value of $\Delta E_Q = 2.76$ mm/s at 80 K for our FeF_2 film is in good agreement with the literature value [273]. This large quadrupole splitting appears because of the presence of a large anisotropic crystal field acting on the six d -electrons of the Fe^{2+} ions. No asymmetry in the line intensities of the two lines in the FeF_2 doublet

has been found at 80 K, as would be expected for an epitaxial film.

At low temperature (18 K), below T_N (78 K), the spectrum of the FeF₂ thin film (Fig. 5.11 (b)) has been fitted again by using the full hyperfine Hamiltonian method. The statistics of the spectrum is rather modest due to the fact that the film was not enriched in ⁵⁷Fe. The best fitting for the spectrum was obtained for an asymmetry parameter (η) of 0.4. This confirms the presence of crystal field components with lower than axial symmetry, because for cubic and axial fields $V_{xx} = V_{yy}$ and, hence, the asymmetry parameter should be zero by definition ($\eta = (V_{xx} - V_{yy})/V_{zz}$). The η value is in good agreement with the literature value [273]. It has been confirmed by Mössbauer spectroscopy [273] and neutron diffraction [263] that below T_N , the sublattice magnetization is along the c-axis of the FeF₂ crystal. The angle between V_{zz} and B_{hf} obtained from the fitting is 90°. Point charge calculations show that V_{zz} should be oriented along the FeF₂[110] direction. However, the charge distribution of the Fe atoms can change this direction and this argument may not be conclusive. Again, the modest statistics of the spectrum at 18 K does not allow the accurate determination of the direction of the EFG components in FeF₂. As the point symmetry around the iron atoms is characterized by three mutually perpendicular reflection planes, and the highest rotational symmetry is two-fold, one would expect that the principal axes of the EFG tensor are along the two-fold axes. This will be discussed in detail in Chapter 7.

Table 5.1 The Mössbauer spectroscopical parameters obtained after least-squares fitting the Mössbauer spectra of the FeF₂ powder and thin film. (IS = isomer shift relative to α -Fe at RT, QS = quadrupole splitting = $\frac{1}{2}eQV_{zz}$ at 80 K and $\frac{1}{2}eQV_{zz}(1+\frac{1}{3}\eta^2)^{1/2}$ at 18 K for the FeF₂ subspectra (η is the asymmetry parameter = 0.4), (QS = 2ϵ for all the sextets, and QS = ΔE_Q = line separation for the quadrupole doublets), B_{hf} = magnetic hyperfine field, Area = relative spectral area). The number of the subspectra (SS #) and their origin (phases given in the bracket) are given in the third column.

Sample	Temperature	SS # (Phases)	IS (mm/s)	QS (mm/s)	B_{hf} (T)	Area (%)
Powder	80 K	1(FeF ₂)	1.47(5)	2.91(5)	-	65
		2(FeF ₃)	0.58	0.005	60.8	10
		3(Fe-F-O)	0.55	0.18	50.4	9
		4(Fe ₃ O ₄)	0.47	0.15	45.1	8
		5(Fe-O)	0.23	1.21	-	8
	18 K	1(FeF ₂)	1.48	2.86	32.6	62
		2(FeF ₂)	1.71	2.90	-	6
		3(FeF ₃)	0.59	0.013	61.8	7
		4(Fe-F-O)	0.58	0.18	58.4	10
		5(Fe ₃ O ₄)	0.65	-0.35	48.4	6
		6(Fe-O)	0.34	1.43	-	9
Thin film	80 K	(FeF ₂)	1.33(5)	2.76(5)	-	100
	18 K	(FeF ₂)	1.48(10)	2.71(10)	32.9	100

Chapter 6

Fe Spin Structure in Exchange Biased Fe/MnF₂ Bilayers

6.1 Introduction

Exchange biased Fe/MnF₂ bilayers have been thoroughly investigated in particular for the understanding of the mechanism of exchange bias. In Fe/MnF₂, the exchange bias was found to depend on several parameters, like the thickness of the Fe and MnF₂ layer, interfacial roughness, cooling field, temperature etc.

The dependence of the exchange bias on the antiferromagnetic MnF₂ thickness (t_{AFM}) has been investigated by Lund et al. [166]. They have observed in Fe/MnF₂ that below a certain critical thickness (about 150 Å) of the MnF₂ layer the exchange bias field (H_E) vanishes, and that above a certain thickness (about 350 Å) H_E attains a constant value. The lower critical thickness is always associated with an increase in coercivity (H_C). The reason for this increase in H_C is associated with the energy loss in the MnF₂ layer during the sweep of the magnetic field in a hysteresis loop.

The ferromagnetic thickness dependence of the exchange bias field and coercivity has been studied by Leighton et al. [153]. They have explored the power law dependencies of H_E (i.e., $H_E \propto 1/(t_{FM})^m$) and the coercivity ($H_C \propto 1/(t_{FM})^n$). In Fe/MnF₂, the exponents are found to be: $m = 1.02 \pm 0.12$ and $n = 1.05 \pm 0.08$. The value of m is in agreement with that predicted by Stiles et al. [231–233]. However, the value of n disagrees with the values $n = 2$ and 1.5 suggested by Stiles et al. [231–233] and by Li et al. [158], respectively.

Like in other systems, the magnitude of the exchange bias field in Fe/MnF₂ is decreasing with increasing temperature [153, 154] and vanishes at and above $T_N = 67$ K of MnF₂. This variation is not linear, but is rather comparable to a $S = 5/2$ Brillouin function [100]. However, roughness plays a decisive role in determining the temperature dependence of exchange bias. For very rough interfaces (e.g., for a root-mean-square roughness of $\sigma_{rms} = 18$ Å) H_E is almost constant at low temperatures and decreases fast to zero as T_N is approached [100].

The cooling-field dependence of H_E and H_C has been investigated by Leighton et al. [154, 157, 199] and correlated with roughness. For Fe/MnF₂ samples with a rough

interface ($\sigma_{rms} = 30 \text{ \AA}$) H_E is found to increase very slightly (it is almost constant) with cooling fields up to 70 kOe, and H_C shows very similar behavior. The coercivity of this sample is higher than that of a sample with a smoother interface ($\sigma_{rms} = 6 \text{ \AA}$), indicating that the coercivity is an extrinsic quantity which is often determined by parameters like the defect density. However, for the sample with the smoother interface ($\sigma_{rms} = 6 \text{ \AA}$), a crossover from negative to positive exchange bias at cooling fields of about 13 kOe has been observed. This crossover is associated with an enhancement of H_C at about the crossover field. These observed effects are related to the modification of the MnF₂ surface spin structure for higher cooling fields. However, the strong coercivity enhancement at the crossover cooling field occurs because of maximum frustration of the AFM surface spins. The interesting point to notice here is that just by changing the cooling field one can control the coercivity of an exchange bias system, which is a desired property in many devices. In other words, the surface spin structure can be varied just depending on the cooling fields. The same authors [154, 157] have also shown by modeling that in the Fe/MnF₂ system the increased coercivity (which is proportional to the exchange coupling between layers) is due to enhanced pinning of the propagating domain walls in the ferromagnetic layer resulting from interfacial magnetic frustration.

The temperature dependence of H_C for various thicknesses of the Fe and/or MnF₂ layer in the exchange biased Fe/MnF₂ system has been investigated in ref. [154]. Keeping the MnF₂ thickness constant (650 \AA), the coercivity is monotonically dependent on temperature for very low Fe thicknesses and shows a sharp increase upon cooling through T_N , followed by a gradual saturation as $T \rightarrow 0 \text{ K}$. For higher Fe thickness the temperature dependence of H_C is dominated by a broad maximum near T_N , in addition to a weak increase as $T \rightarrow 0 \text{ K}$. These two regimes are characterized by a crossover thickness (about 90 \AA), where the two contributions compete, resulting in a coercivity which is nearly temperature independent up to 100 K.

The above behavior of H_C has also been observed for constant Fe layer thickness (120 \AA), but varying MnF₂ layer thickness [153]. For a larger MnF₂ layer thickness (2200 \AA) the coercivity behaves in a similar manner as in the first case (sharp increase below T_N and a gradual saturation as $T \rightarrow 0 \text{ K}$). The second behavior of the coercivity (peaked at about T_N) has been observed for a smaller MnF₂ thickness (210 \AA). It was suggested by Stiles et al. [231, 232] that the two different regimes in the temperature dependence of the coercivity occur because of the relative dominance of the anisotropy of the Fe or MnF₂ layer. This implies that when the FM (Fe) layer anisotropy is strong enough it induces a significant spin reorientation of the AFM (MnF₂) layer during the reversal process. On the other hand, when the Fe layer anisotropy is weak the Fe layer reverses without perturbing the MnF₂ layer *in the vicinity of T_N* . Hence, the behavior of the coercivity depends on the FM and AFM thickness ratio, t_{Fe}/t_{MnF_2} .

The training effect which is present in many other systems (e.g. Co/CoO [9] and Fe/FeSn₂ [148]), is absent in the Fe/MnF₂ system. The absence of the training effect [154] provides a good measure of exchange bias and coercivity.

The different magnetization states of the Fe layer in exchange biased Fe/MnF₂ at the two different (left and right) coercive fields have been studied by Krivorotov et al. [8, 145] by using anisotropic magneto-resistance (AMR) as a probe. The variation of

the electrical resistance with the angle between the magnetization and current is due to AMR. (The resistance is maximum when the current is parallel or antiparallel to the magnetization direction). It has been established that the magnetization states at the two coercive fields of the hysteresis loop are different. At the left coercive field (when the applied field is opposite to the unidirectional easy axis of exchange bias) the magnetization is oriented perpendicularly to the applied field direction. By contrast, the state of magnetization at the right coercive field (the easy direction of exchange bias) consists of domains that are parallel and anti-parallel to the applied field. Krivorotov et al. [8, 145] have also suggested the possibility of a partial domain wall in the AFM (MnF₂) layer. They also presented an indication of perpendicular coupling between spins of MnF₂ and Fe, which has been reported also for some other systems like Fe/FeF₂ [183] and Fe/FeRh [147].

Although the behavior of exchange bias in the Fe/MnF₂ system has been thoroughly investigated, the direct observation of the interfacial spin structure is still a challenging task, which is expected to provide a key for the understanding of details of the mechanism of exchange bias. Most theoretical model neglect the possibility of a depth dependent variation of the spin structure in the Fe layer except the model by Kiwi et al. [3–5]. These authors suggest the possibility of an incomplete domain wall in the ferromagnet, starting at the FM/AFM interface in the Fe/FeF₂ and Fe/MnF₂ systems. In the following chapter, a detailed CEMS investigation of the Fe-layer spin structure and its dependence on depth, temperature and cooling field in Fe/MnF₂ will be presented.

6.2 Sample preparation and characterization

Two kinds of exchange biased Al/Fe/MnF₂/ZnF₂/MgO(001) samples were prepared by sequential electron beam evaporation [52]. In both kinds of samples a 160 Å ZnF₂ buffer layer was deposited first in order to relax the large (8 %) lattice mismatch between the MgO substrate and MnF₂. The typical thicknesses of the Al, Fe and MnF₂ layers are 30 Å, 80 Å and 520 Å, respectively. The samples differ only in their ferromagnetic Fe layer. Out of the 80 Å Fe layer, a 10 Å ⁵⁷Fe probe layer was deposited just at the Fe/MnF₂ interface, and this kind of sample will be called "interface sample" (labelled MFEMF01). Hence, the FM layer of the interface sample contains 70 Å ^{nat}Fe/10 Å ⁵⁷Fe. The typical structure of the interface sample is given in Fig. 6.1 (left). The other kind of sample is called "center sample" (labelled MFEMF03). In this sample the ⁵⁷Fe probe layer was deposited at the center of the Fe layer (35 Å ^{nat}Fe/ 10 Å ⁵⁷Fe/35 Å ^{nat}Fe), i.e., 35 Å away from the Fe/MnF₂ interface. The typical structure of the center sample is depicted in Fig. 6.1 (right). Prior to deposition, the MgO(001) substrate was heated to 450 °C for 15 minutes and then cooled to 200 °C for ZnF₂ deposition. The base pressure of the system was 3×10^{-8} mbar and the pressure during MnF₂ deposition was around 6×10^{-7} mbar. The deposition temperature for the Al, Fe, MnF₂ and ZnF₂ layers were 150 °C, 150 °C, 325 °C and 200 °C, respectively. The corresponding deposition rates were 0.5 Å/s, 1 Å/s, 2 Å/s and 2 Å/s, respectively. The thickness of the fluoride layers were monitored by calibrated quartz crystal oscillations. However the position of the shutter was not allowing the correct determination of the Fe layer thickness during deposition, and, therefore, the Fe thickness was monitored by optical sensors.

<u>Interface sample</u> (MFEMF01)			<u>Center sample</u> (MFEMF03)	
Al	30 Å	Cap layer	Al	30 Å
^{nat} Fe	70 Å	FM layer with ⁵⁷ Fe probe layer	^{nat} Fe	35 Å
⁵⁷ Fe	10 Å		⁵⁷ Fe	10 Å
MnF ₂ (110)	520 Å	AFM layer MnF ₂	MnF ₂ (110)	520 Å
ZnF ₂ (110)	160 Å	Buffer layer	ZnF ₂ (110)	160 Å
MgO(100) substrate			MgO(100) substrate	

Figure 6.1: Schematic structure of the Fe/MnF₂ samples prepared on MgO(100) substrates. In the interface sample (left) the ⁵⁷Fe probe layer is at the AFM(MnF₂)/FM(Fe) interface, while for the center sample (right) the ⁵⁷Fe probe layer is at the center of the FM (Fe) layer, i.e., 35 Å away from the interface. (^{nat}Fe: iron of natural isotopical composition with ca. 2% ⁵⁷Fe; ⁵⁷Fe: 95% isotopically enriched ⁵⁷Fe).

After deposition the structural characterization of the samples was performed by high and small angle X-ray diffraction (XRD) (Cu-K_α radiation, $\lambda = 1.5418 \text{ \AA}$) [53]. The high angle X-ray diffraction pattern for the interface sample (MFEMF01) is shown in Fig. 6.2 and the small angle XRD pattern in Fig. 6.3. The high angle XRD pattern confirms the epitaxial nature of the film with the MnF₂(110) plane lying in the sample plane. The relatively sharp rocking curve (fitted with a Gaussian, insert in Fig. 6.2) of the MnF₂(110) reflection has a full width at half maximum (FWHM) of about 2.53°. This suggests the good epitaxial growth of the sample. The small angle XRD suggests homogeneity and flatness of the MnF₂ and Fe layers. The high frequency oscillations are due to the fluoride layer and the low frequency oscillations are due to the total Fe layer thickness. The red curve results from least-squares fitting of the theoretical intensity to the measured black curve. The fitting gives a value of about 8.5 Å for the interface roughness. The epitaxial nature of the center sample (MFEMF03) has been verified by the high angle XRD pattern shown in Fig. 6.4. The least-squares fitting (Gaussian) rocking curve results in a FWHM of about 2.36°, suggesting good epitaxial quality. However, it is worthwhile mentioning that, as discussed in the previous chapter, all the MnF₂ layers (in interface and center sample) are pseudo-twinning epitaxial layers. The small angle X-ray diffraction pattern (taken at Duisburg) is displayed in Fig. 6.5. In comparison to the interface sample, the small angle scattering indicates a higher roughness for the center sample.

The samples were also characterized by conversion electron Mössbauer spectroscopy (CEMS). The Mössbauer spectrum of the interface sample (MFEMF01) taken at room temperature (RT) is shown in Fig. 6.6. The spectrum clearly shows a dominant six-line

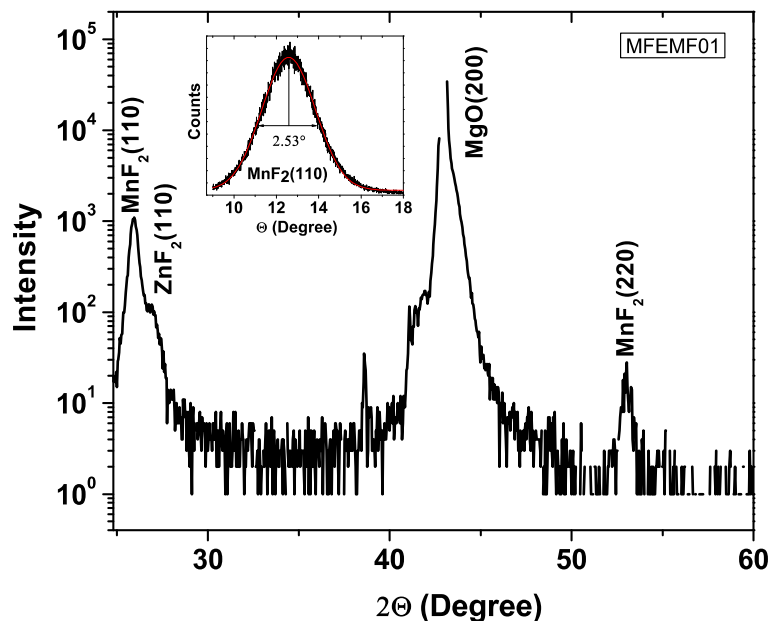


Figure 6.2: X-ray diffraction pattern of the Fe/MnF₂ interface sample (MFEMF01). The film grows epitaxially with the c-axis ([001] direction) in the plane of the film. The FWHM of the MnF₂(110) peak (rocking curve, insert) is about 2.53°. The red curve in the insert is the fitting of a Gaussian to the measured rocking curve data of the MnF₂(110) peak.

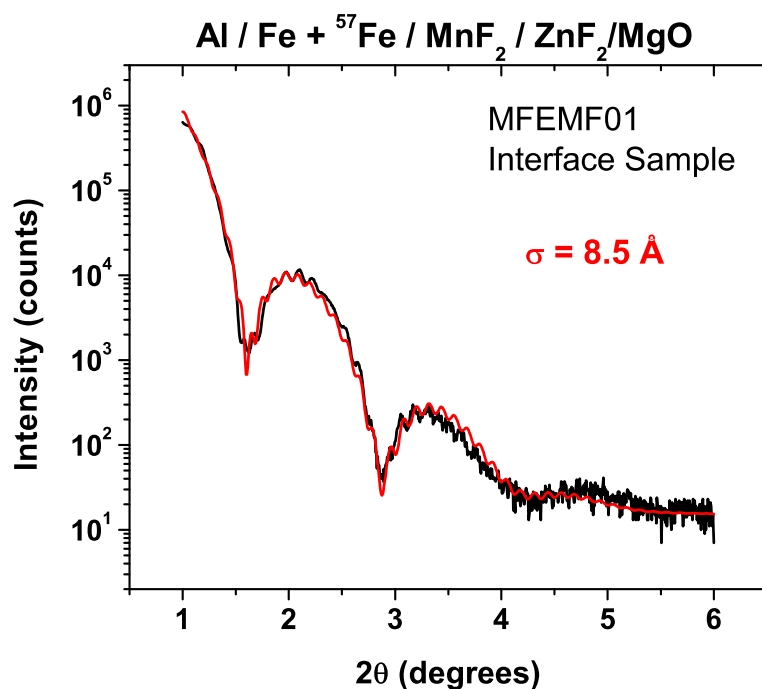


Figure 6.3: Small angle XRD pattern of the Fe/MnF₂ interface sample (MFEMF01). The interfacial roughness of 8.5 \AA was obtained from the fitting (red curve) to the measured data.

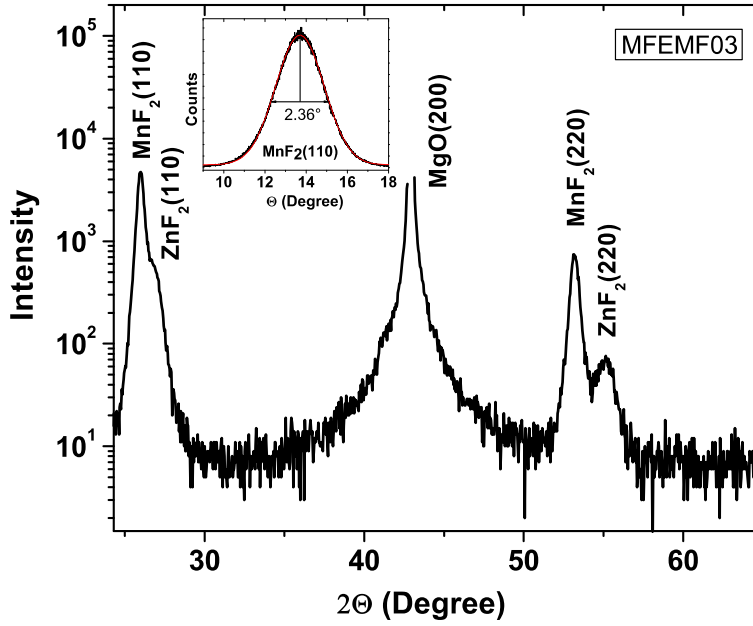


Figure 6.4: X-ray diffraction pattern of the Fe/MnF₂ center sample (MFEMF03). The film grows epitaxially with the *c*-axis ([001] direction) in the plane of the film. The FWHM of the MnF₂(110) peak (rocking curve, insert) is about 2.36°. The red curve in the insert is the fitting of a Gaussian to the measured rocking curve data of the MnF₂(110) peak.

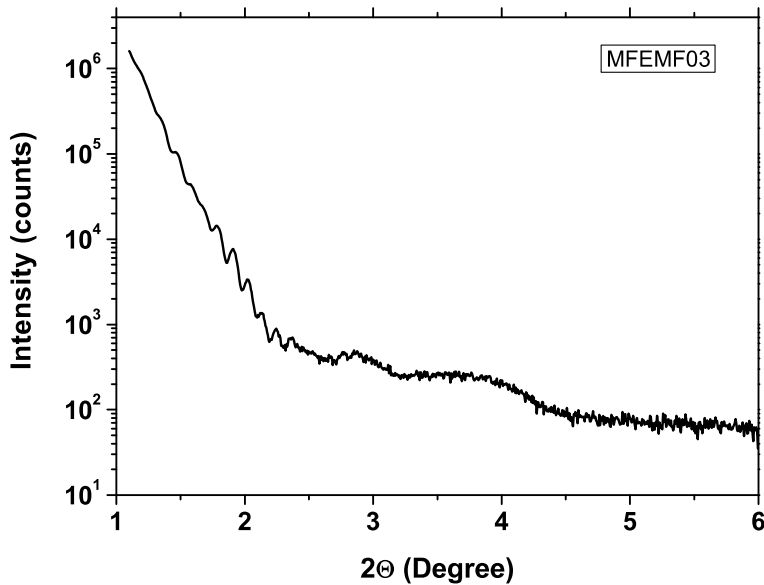


Figure 6.5: Small angle XRD pattern of the Fe/MnF₂ center sample (MFEMF03).

Zeeman pattern superimposed to a weak component with a distribution of hyperfine hyperfine fields, $P(B_{hf})$. The spectrum has been least-squares fitted by a dominant Zeeman sextet with sharp Lorentzian lines (hyperfine field $B_{hf} = 32.8$ T) and a distribution of hyperfine fields, $P(B_{hf})$, which is shown on the right-hand side of the spectrum. Because of the value of B_{hf} the dominant sextet is unambiguously assigned to the bcc-Fe layer,

while the distribution of hyperfine fields, which has a peak at about 26 T, is attributed to a thin interfacial layer produced by chemical intermixing at the Fe/MnF₂ interface. The spectral area under the hyperfine field distribution is about 15 % of the total spectral area. Considering the ⁵⁷Fe layer thickness (10 Å), 15 % intermixing results in about 1.5 Å of the ⁵⁷Fe layer, i.e., effectively about one ⁵⁷Fe monolayer (ML) is chemically intermixed at the interface of the interface sample. It should be noticed that the roughness of 8.5 Å obtained from the simulation of the small angle XRD results (Fig. 6.3) is physically different from the 1.5 Å intermixing at the interface. The measured intensity ratio between the 2nd and 3rd (or 5th and 4th) line (R₂₃) of the dominant Mössbauer sextet is 4.0. This demonstrates that the Fe layer spins lie in the plane of the sample.

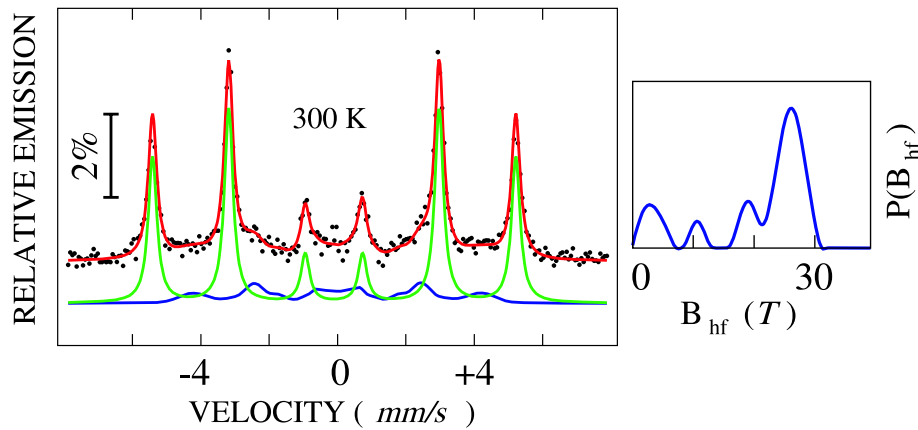


Figure 6.6: Room temperature (300 K) CEM spectrum of the Fe/MnF₂ interface sample (MFEMF01). The spectrum has been fitted by a dominant Zeeman sextet assigned to bcc-Fe and a component with a distribution of hyperfine fields, $P(B_{hf})$, (right hand side) to account for the chemical intermixing at the interface.

6.3 SQUID magnetometry: results

Magnetic hysteresis loops above and below T_N of MnF₂ for the interface and the center sample were measured using superconducting quantum interference device (SQUID) magnetometry [57]. The results are shown in Fig. 6.7 and Fig. 6.8. The samples were first field-cooled (FC) to 80 K in an applied magnetic field of 2 kOe, applied at 150 K along the MgO[100] direction of the MgO(001) substrate (x -direction, as will be discussed in section 5.5). Both hysteresis loops at 80 K (Fig. 6.7 (a)) show no exchange field (H_E), i.e., no shift of the hysteresis loop from the origin. However, a small difference in the coercive field (H_C) of both samples has been observed. By field-cooling the samples from 150 K to 10 K in an applied field of 2 kOe (Fig. 6.7 (b)) H_C is observed to increase. For the interface sample (MFEMF01), H_C increases from 32 Oe at 80 K to 132 Oe at 10 K. For the center sample (MFEMF03), however, H_C changes from 52 Oe at 80 K to 450 Oe at 10 K, the latter value being rather large. The difference in the change of H_C might be due to a different microstructure of the two samples, because H_C generally depends on the microstructure, e.g. grain size. Both samples (at 10 K) clearly show a negative shift of the hysteresis loop and exchange-bias field H_E of about -60 ± 2 Oe and -70 ± 5

M_0 for the interface and center sample, respectively, which is in agreement with previous reports [153].

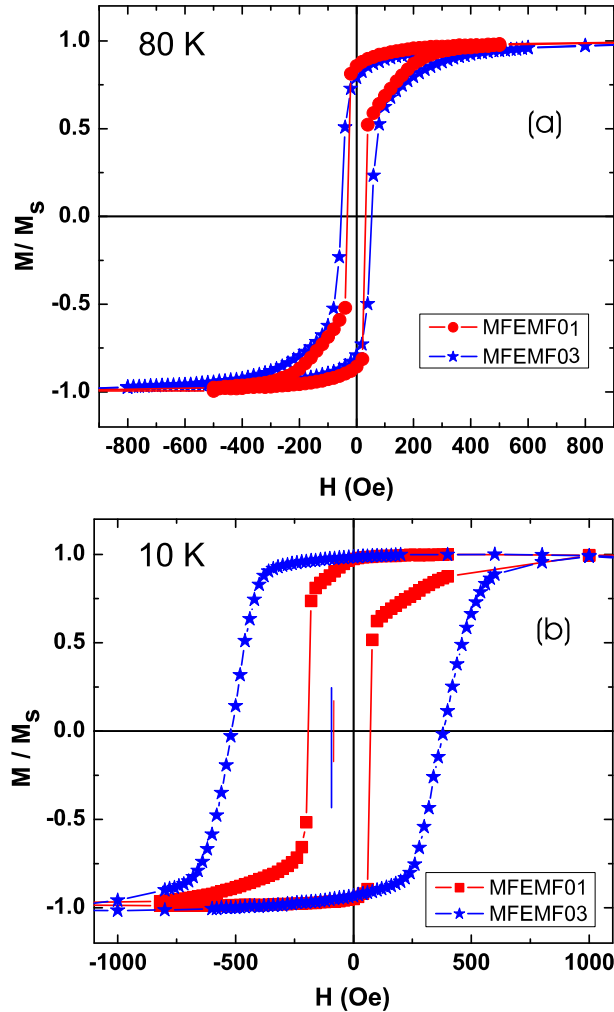


Figure 6.7: Normalized hysteresis loops for the interface (red) and center (blue) Fe/MnF₂ sample measured at 80 K (a) (above T_N) and at 10 K (b) (below T_N). The samples were cooled to 10 K in an applied field of 0.2 T oriented along MgO[001], starting from 150 K. A shift of the hysteresis loop of both samples at 10 K can be noticed. (M_S = saturation magnetization).

Hysteresis loops for both samples after zero-field cooling from 150 K to 10 K in remanence, are shown in Fig. 6.8. The remanence was established by an external field of 4 kOe applied in the plane at 150 K along the [100] direction of the MgO(001) substrate. After that the applied field was switched off, and the sample was zero-field cooled in remanence to 10 K, when the hysteresis loop was then measured. Upon cooling to 10 K, the increase in coercivity H_C of the center sample is higher than that of the interface sample. The reason for this increase may be related to the microstructural difference between the two samples. Interestingly, by cooling in remanence, the samples show H_E values comparable to the field cooling cases. At 10 K, H_E is -50 ± 5 Oe and -60 ± 5 Oe for the interface and center sample, respectively, according to Fig. 6.8. This establishes

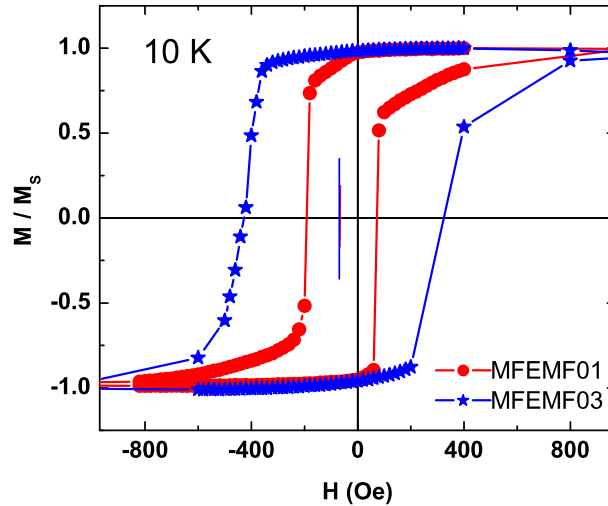


Figure 6.8: Normalized hysteresis loops for the interface (red) and center (blue) Fe/MnF₂ sample measured at 10 K (below T_N) of MnF₂. The samples were zero-field cooled from 150 K to 10 K in remanence. The remanent magnetization was induced at 150 K by an applied field of 0.4 T along MgO[001]. (M_S = saturation magnetization).

the fact that for moderate cooling fields H_E does not depend on the strength of the cooling field, but rather depends on the magnetization state of the ferromagnetic layer [176].

6.4 Conversion electron Mössbauer spectroscopy of Fe/MnF₂ bilayers

6.4.1 CEMS measurement geometry

To determine the spin structure of the Fe layer in an exchange biased Fe/MnF₂ bilayer, we have adopted a certain type of geometrical arrangement in our CEMS experiments, as shown in Fig. 6.9. x , y and z are the laboratory co-ordinate axes. The sample plane is in the xy -plane. The magnetic hyperfine field B_{hf} (which has opposite direction to the Fe atomic magnetic moment) is assumed to be in the sample plane. CEMS with unpolarized γ -radiation cannot distinguish between the two opposite directions of B_{hf} (or opposite directions of the Fe magnetic moment). Let the angle between the x -axis and the B_{hf} direction, the γ -ray and the B_{hf} direction, and the γ -ray and the x -axis be φ , Ψ and Φ , respectively.

All the CEMS experiments for this work were performed at zero external magnetic field. However, most of the CEM spectra, which will be shown later, were taken after introducing remanence in the sample. The remanence was induced by an external field B_{ext} of 0.4 T (4 kOe) applied at RT along the x -direction (equal to the [100] direction of the MgO(001) substrate). Then, the sample was zero-field cooled to the required temperature in remanence, referred to as 'virgin remanence'. However, for field cooling, the sample was cooled in the presence of the external field, applied again along the

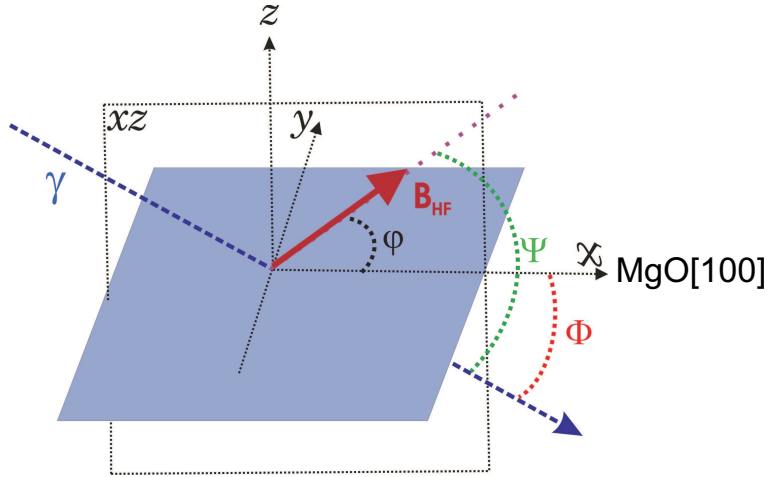


Figure 6.9: Schematic figure of the geometry in a CEMS measurement. The xy -plane is the sample plane. γ indicates the direction of the incident γ -ray, which lies in the xz -plane. ϕ is the angle between the γ -ray direction and the x -axis, φ is the angle between the hyperfine field (B_{hf}) direction (antiparallel to the Fe magnetic moment direction) and the x -axis, and Ψ is the angle between the γ -ray direction and the direction of B_{hf} . B_{hf} is assumed to lie in the sample plane (xy -plane). The external magnetic field B_{ext} that was applied and subsequently switched off in order to produce remanence in the Fe film was oriented along the x -axis, which is the [100] direction of the MgO(001) substrate.

x -direction (or MgO[100] direction). The magnetic field was then switched off before the CEMS measurement. In this case, the remanence of the sample is referred to as 'conventional remanence'. In both, virgin and conventional remanence the remanent magnetization is expected to be oriented along the x -axis (the B_{ext} direction). If the Fe spins are completely aligned along the x -axis, the two angles Ψ and Φ (Fig. 6.9) are equal ($\Psi = \Phi$).

In order to properly determine the angle Ψ between the γ -ray and the magnetic hyperfine field B_{hf} (or Fe spin direction) in thin films, one needs to measure the Mössbauer spectrum with different angles between the γ -ray and a defined axis of the film. The intensity ratio of the 2nd and 3rd line (or the 5th and 4th line) is related to the angle Ψ and is given by [see, e.g., [17]]:

$$R_{23} = \frac{4\sin^2\Psi}{1 + \cos^2\Psi} \quad (6.1)$$

Variation of the angle Ψ from 0° to 180° results in different R_{23} ratios. For example, for $\Psi = 0^\circ, 45^\circ, 90^\circ, 135^\circ$ and 180° the intensity ratios (R_{23}) are 0, 1.33, 4, 1.33 and 0, respectively. It is interesting to note that it is enough to consider the first quadrant for Ψ ($\Psi = 0^\circ \sim 90^\circ$) because of the quadratic dependence of R_{23} on sine and cosine of Ψ . From the CEM spectrum one obtains the R_{23} ratio. Then, the angle Ψ can be determined by solving the above equation. The formula is given by:

$$\Psi = \arccos\sqrt{\frac{4 - R_{23}}{4 + R_{23}}} \quad (6.2)$$

However, this consideration is valid only for the case of a unidirectional (δ -function type

of) angular Fe spin distribution. In the case of an arbitrary angular distribution of Fe spins R_{23} is given by:

$$R_{23} = \frac{4 \langle \sin^2 \Psi \rangle}{1 + \langle \cos^2 \Psi \rangle} \quad (6.3)$$

where the brackets indicate averaging over all Fe-spin directions in the sample.

6.4.2 In-plane spin distribution models

The line intensity ratio of the six Mössbauer lines can be represented by $3:R_{23}:1::1:R_{23}:3$, where R_{23} can be expressed as in eq. (5.1), where Ψ is the angle between γ -ray and the in-plane Fe spin direction (see Fig. 6.9).

If we consider an angular probability distribution of Fe spins $P(\Psi)$ in the angle Ψ , instead of a unique Fe spin direction, the above formula can be written like:

$$R_{23} = 4 \frac{\int_{\Psi} \sin^2 \Psi P(\Psi) d\Psi}{1 + \int_{\Psi} \cos^2 \Psi P(\Psi) d\Psi} \quad (6.4)$$

with

$$\int_{\Psi} P(\Psi) d\Psi = 1$$

In the present case of Fe/MnF₂ (or Fe/FeF₂), the bcc-Fe spin distribution $P(\Psi)$ is observed to be within the sample plane. Hence, it is convenient to introduce the angle φ (see Fig. 6.9) and its probability $P(\varphi)$ instead of Ψ and $P(\Psi)$. (φ = angle between the x -axis (or external field or MgO[100] direction) and the hyperfine field (B_{hf}) or Fe spin direction). Then, eq. (6.4) can be rewritten by using the new variable φ [146, 149]:

$$R_{23} = 4 \frac{1 - \cos^2 \Phi \langle \cos^2 \varphi \rangle}{1 + \cos^2 \Phi \langle \cos^2 \varphi \rangle} \quad (6.5)$$

with

$$\langle \cos^2 \varphi \rangle = \int_0^{2\pi} (\cos^2 \varphi) P(\varphi) d\varphi$$

and

$$\int_0^{2\pi} P(\varphi) d\varphi = 1,$$

where Φ = incident angle between the γ -ray direction and the sample plane (or x -axis). Eq. (6.5) is the most general formula and can be applied to obtain a modeled in-plane spin distribution $P(\varphi)$ from the measured value of R_{23} . As in all cases studied here the Fe spins are distributed in the plane of the sample, we will consider a few relevant model distributions.

Unidirectional distribution model

Assuming that all Fe spins are pointing to only one direction ($\varphi = \varphi_0$ with a Dirac-type probability distribution ($P(\varphi) = \delta(\varphi - \varphi_0)$), eq. (5.5) can be expressed as [146, 149]:

$$R_{23} = 4 \frac{1 - \cos^2 \Phi \cos^2 \varphi_0}{1 + \cos^2 \Phi \cos^2 \varphi_0} \quad (6.6)$$

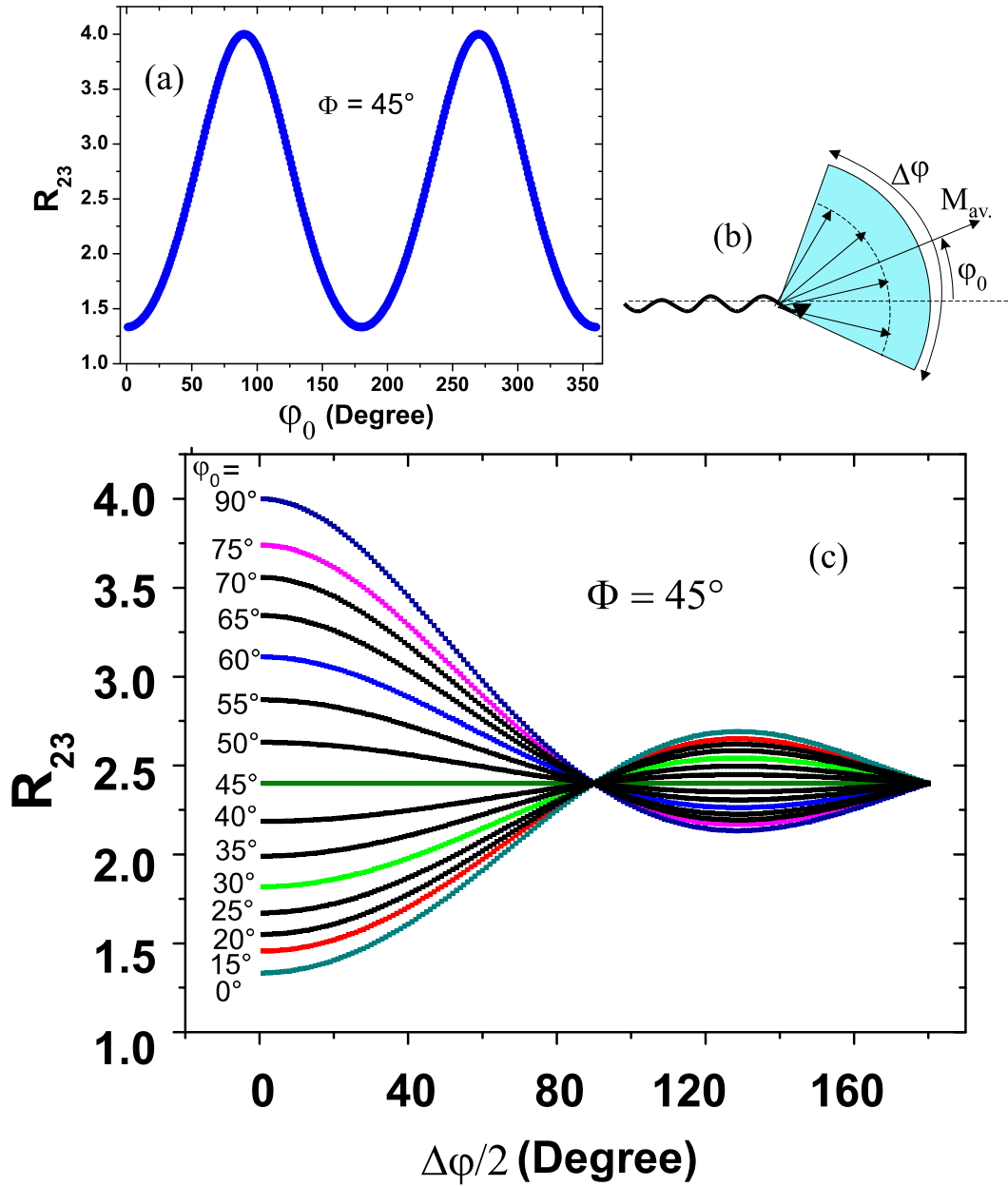


Figure 6.10: (a) Calculated R_{23} ratio versus the spin rotation angle φ_0 for in-plane spin rotation (unidirectional model). (b) Schematic picture of step-shaped spin fanning. (c) Calculated R_{23} ratio versus the spin fanning angle $\Delta\varphi/2$ for in-plane spins at an angle of incidence of $\Phi = 45^\circ$ and at various angles φ_0 ranging from $\varphi_0 = 0^\circ$ to $\varphi_0 = 90^\circ$ (step-shaped model).

In this model the spin orientation described by φ_0 can be deduced from the R_{23} ratio obtained from just a single Mössbauer spectrum taken at an incident angle Φ . In Fig. 6.10(a), the calculated R_{23} ratio is plotted versus the angle φ_0 , according to eq. (6.6), for an incident angle $\Phi = 45^\circ$, as used in the present experiments.

Step-shaped distribution model

Sometimes, a more realistic distribution model is the step-shaped distribution model

[146, 149] or spin fanning model. It is useful for the case of a non-collinear in-plane angular spin distribution, e.g., a spin distribution with "ripple". It describes the situation, where the in-plane Fe spins or hyperfine fields are pointing with equal probability only into the angular aperture $\Delta\varphi = 2\varphi'$ (Fig. 6.10(b)) centered at an angle φ_0 with respect to the x -axis (Fig. 6.9). The probability density for the internal $\varphi_0 - \varphi' < \varphi < \varphi_0 + \varphi'$ is $P(\varphi) = P_0$, and $P(\varphi) = 0$ for the rest of the 2π interval. Using these conditions eq. (6.5) becomes:

$$R_{23} = 4 \frac{1 - \cos^2\Phi \langle \cos^2\varphi \rangle}{1 + \cos^2\Phi \langle \cos^2\varphi \rangle}$$

with

$$\langle \cos^2\varphi \rangle = \int_0^{2\pi} (\cos^2\varphi) P(\varphi) d\varphi = \frac{1}{2} + \frac{1}{2} \frac{\sin(2\varphi')}{(2\varphi')} \cos(2\varphi_0) \quad (6.7)$$

This model contains the two parameters φ_0 and $\Delta\varphi = 2\varphi'$. In principle, this spin distribution can be obtained from two independent measurements of R_{23} at different incident angles Φ . Fig. 6.10 (c) displays the calculated R_{23} ratio versus the semiaperture angle $\Delta\varphi/2 = \varphi'$ at an angle of incidence of $\Phi = 45^\circ$ and at various angles φ_0 ranging from $\varphi_0 = 0^\circ$ to $\varphi_0 = 90^\circ$.

6.4.3 Experimental details and CEMS results

All CEMS measurements were performed in zero external field. Fig. 6.11 shows the CEM spectra of the Fe/MnF₂ interface sample (MFEMF01) measured at an angle of incidence of $\Phi = 90^\circ$ (a), (b) and $\Phi = 45^\circ$ (c), (d), measured at 80 K ($T > T_N$) (a), (c) and at 18 K ($T < T_N$) (b), (d) ($T_N = 68$ K). The samples were zero-field cooled at remanence to either 80 K or 18 K. The remanence was introduced into the sample at RT by an external magnetic field of 0.4 T applied along the x -direction (Fig. 6.9). The measurements were performed by using a variable temperature bath cryostat. For the 80 K measurement (above T_N) a He-CH₄ gas-filled proportional counter was used, whereas for the 18 K measurement a channeltron detector was used. ⁵⁷Co in a Rh-matrix was used as a source. For $\Phi = 90^\circ$, the incident 14.4 keV γ -ray was parallel to the sample normal with the x -axis parallel to the laboratory floor. For measurements at $\Phi = 45^\circ$, the sample was rotated by 45° about the y -axis (Fig. 6.9) with the incident γ -ray direction fixed.

All the CEM spectra for this interface sample were least-squares fitted by assuming a dominant Zeeman sextet with sharp Lorentzian lines attributed to the bcc-Fe layer, and a weak contribution with a hyperfine field distribution, $P(B_{hf})$, taking into account of some chemical intermixing at the Fe/MnF₂ interface (interfacial component). The Mössbauer spectroscopical parameters obtained from the fittings are listed in Table 6.1.

The center sample (MFEMF03) was also measured at remanence by CEMS at $\Phi = 90^\circ$ (Fig. 6.12 ((a), (b)) and $\Phi = 45^\circ$ (Fig. 6.12 (c), (d)) at a measurement temperature of 80 K ((a), (c)) and 18 K ((b), (d)). A similar remanence and zero-field cooling procedure was used as for the interface sample.

In case of the center sample one may not expect any contribution from the interfacial intermixing, because the ⁵⁷Fe probe layer is about 35 Å away from the interface. In fact, the interfacial component is not observed in the CEM spectra of the center sample, as

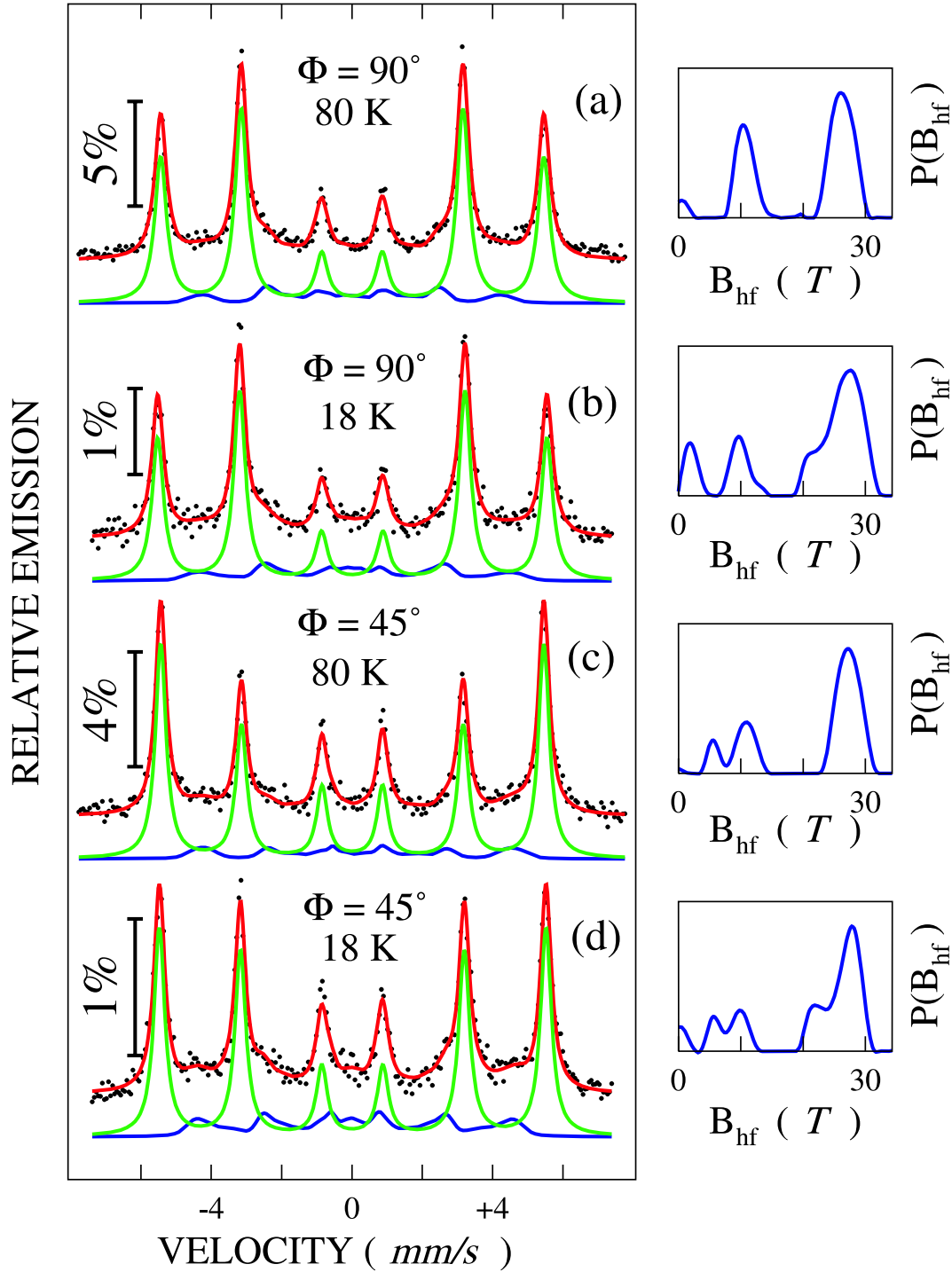


Figure 6.11: CEM spectra of the Fe/MnF₂ interface sample (MFEMF01), measured at an angle of incidence of $\Phi = 90^\circ$ at 80 K (a) and 18 K (b), and at $\Phi = 45^\circ$ at 80 K (c) and 18 K (d). Before each measurement the sample was zero-field cooled from 300 K in remanence. Each spectrum was least-squares fitted by a dominant Zeeman sextet with sharp Lorentzian lines superimposed by a spectral component (interfacial component) with a distribution of the magnetic hyperfine fields, $P(B_{hf})$, (right-hand side).

expected (Fig. 6.12). Hence, all spectra of the center sample were fitted by a single Zee-

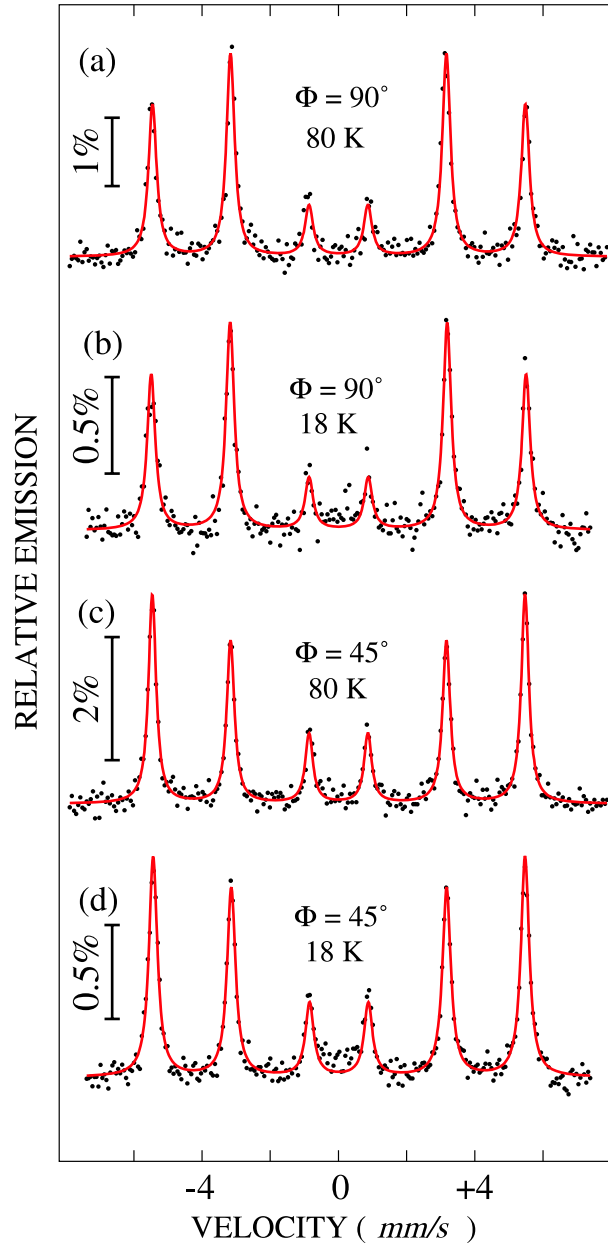


Figure 6.12: CEM spectra of the Fe/MnF₂ center sample (MFEMF03), measured at an angle of incidence of $\Phi = 90^\circ$ at 80 K (a) and 18 K (b), and at $\Phi = 45^\circ$ at 80 K (c) and 18 K (d). Before each measurement the sample was zero-field cooled from 300 K in remanence. Each spectrum was least-squares fitted by a Zeeman sextet with sharp Lorentzian lines.

man sextet with Lorentzian lines. The Mössbauer spectroscopical parameters obtained from the least-squares fitting are listed in Table 6.1.

Fig. 6.13 shows the CEM spectra of the interface sample measured at 18 K after field cooling from RT in an external field B_{ext} of 0.2 T [(a), (c)] and 0.35 T [(b), (d)]. The CEMS measurements were performed at $\Phi = 90^\circ$ [(a), (b)] and $\Phi = 45^\circ$ [(a), (c)] in zero external magnetic field. The spectra are fitted in a similar manner as those for the interface sample in remanence (i.e., with one Zeeman sextet and an interfacial compo-

ment with a distribution of hyperfine fields). The Mössbauer spectroscopical parameters obtained are listed in Table 6.1.

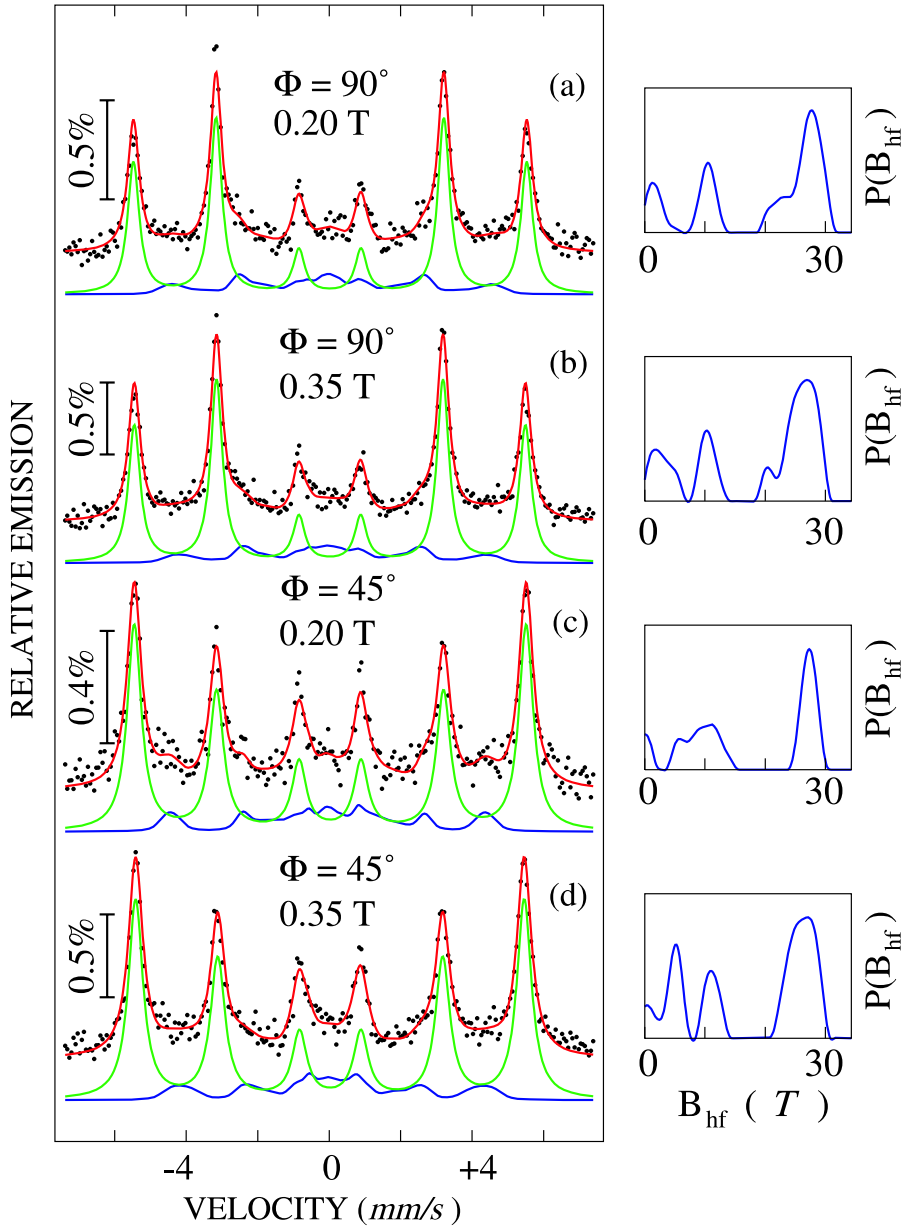


Figure 6.13: CEM spectra of the Fe/MnF₂ interface sample (MFEMF01) for different cooling fields. The spectra are measured at $\Phi = 90^\circ$ (a), (b), and at $\Phi = 45^\circ$ (c), (d). The sample was cooled from 300 K to 18 K in an in-plane cooling field of 0.2 T (a), (c) and 0.35 T (b), (d), and measured at 18 K in zero field (remanence). Each spectrum was least-squares fitted by a dominant Zeeman sextet for bcc-Fe and a component (interface component) with a distribution of magnetic hyperfine fields, $P(B_{hf})$, (right-hand side).

CEMS has also been performed at $\Phi = 45^\circ$ on the interface sample at remanence at various measurement temperatures starting from 300 K down to 18 K. The spectra are shown in Fig. 6.14. Again, the spectra were fitted with two components (a sextet for bcc-like iron and an interfacial component with a distribution of hyperfine fields).

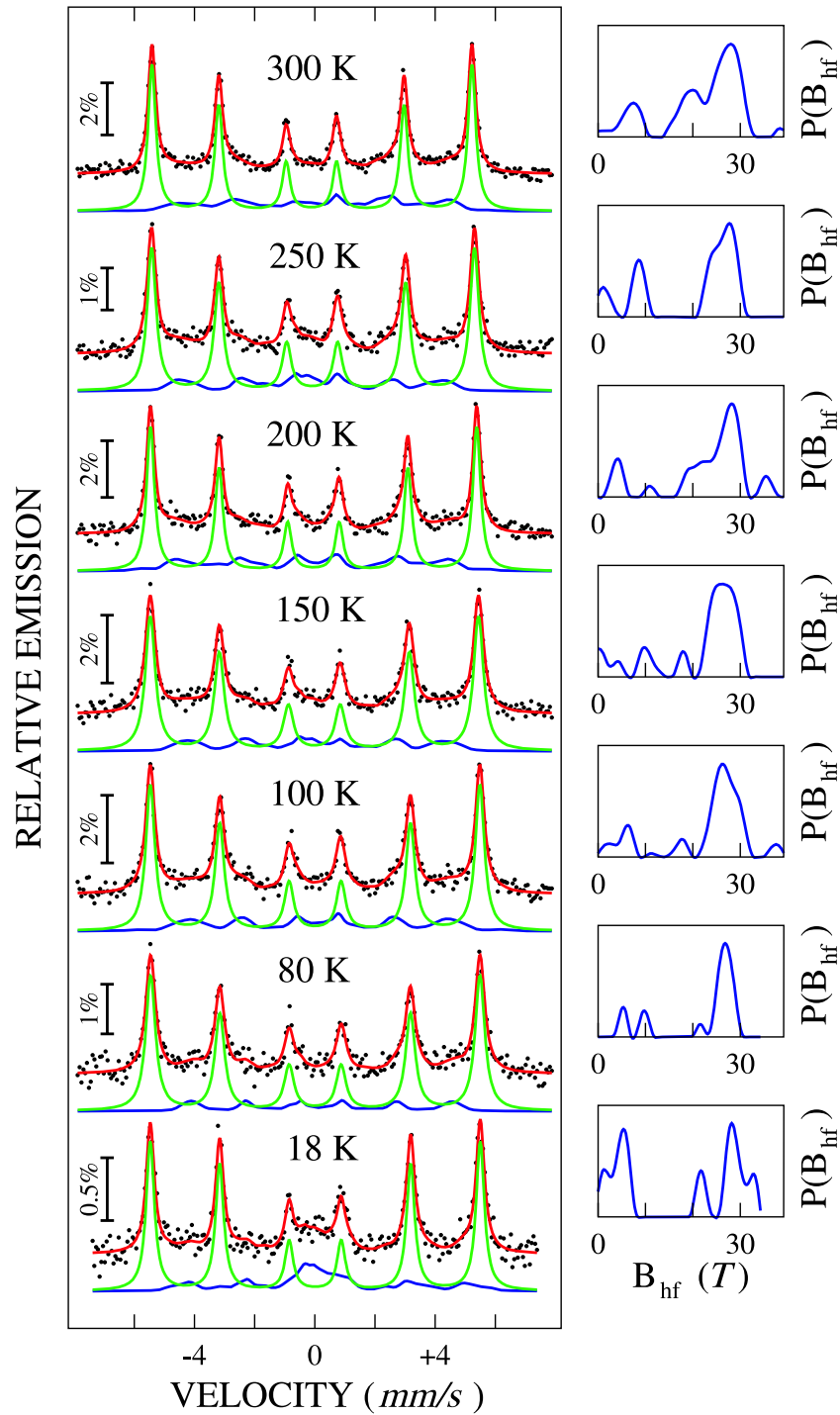


Figure 6.14: CEM spectra of the Fe/MnF₂ interface sample (MFEMF01) taken at an angle of incidence of $\Phi = 45^\circ$. The spectra were measured at different temperatures (300, 250, 200, 150, 100, 80 and 18 K, from top to bottom, respectively) during zero-field cooling to that particular temperature in remanence. Each spectrum was least-squares fitted by a dominant Zeeman sextet for bcc-Fe and a component (interface component) with a distribution of magnetic hyperfine fields, $P(B_{hf})$, (right-hand side).

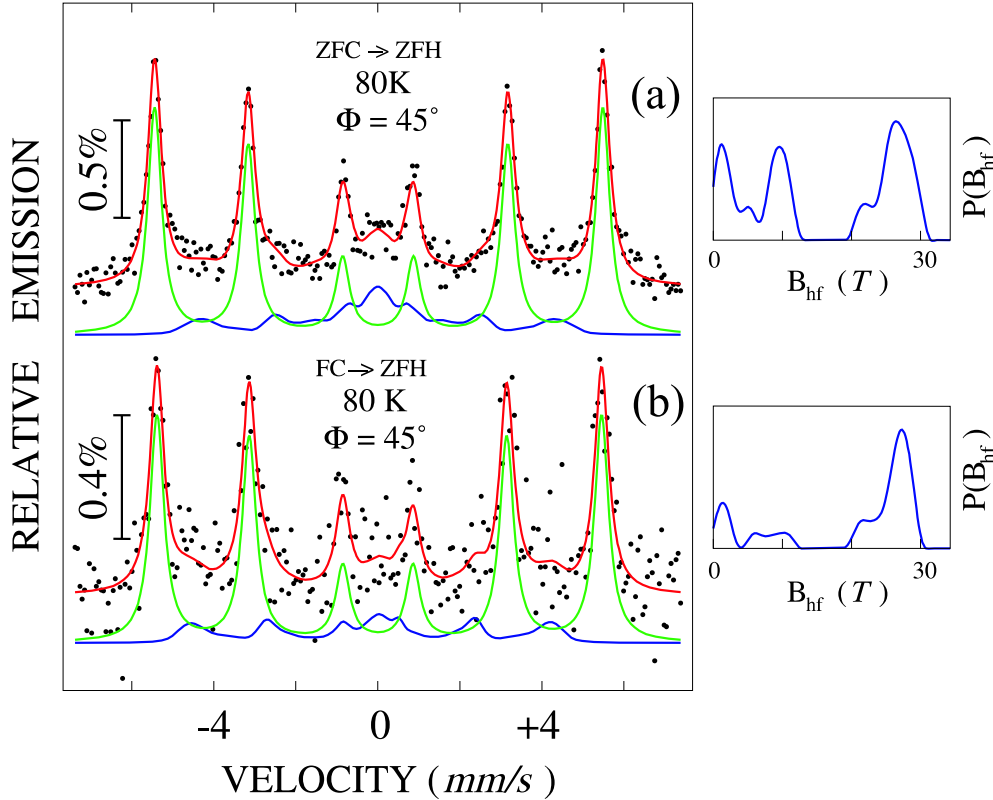


Figure 6.15: CEM spectra of the Fe/MnF₂ interface sample (MFEMF01) taken at $\Phi = 45^\circ$ after different thermal history: (a) after zero-field cooling in remanence from 300 K to 18 K followed by zero-field heating to 80 K, (b) after field cooling from 300 K to 18 K in an external field of 0.35 T, followed by zero-field heating to 80 K. Each spectrum was least-squares fitted by a dominant Zeeman sextet and a component with a distribution of magnetic hyperfine fields, $P(B_{hf})$, (right-hand side). The measurement temperature was 80 K in (a) and (b).

In order to study possible memory effects, CEMS measurements were performed on the interface sample (MFEMF01) at 80 K after two different histories of the sample: (1) The sample was zero-field cooled to 18 K after inducing remanence at 300 K ($B_{ext} = 0.4$ T along the x -direction, i.e., exactly between the MnF₂ twin directions). After that the sample was zero-field heated back to 300 K and then zero-field cooled to 80 K. Then CEMS was performed at that temperature (80 K) in zero external field with an angle of incidence of $\Phi = 45^\circ$ (Fig. 6.15 (a)). (2) The sample was field cooled from 300 K to 18 K in an external field $B_{ext} = 0.35$ T along the x -axis (when CEMS was performed in zero-field as shown in Fig. 6.13 (d)) followed by zero-field heating to 80 K and a zero-field CEMS measurement also at 80 K (Fig. 6.15 (b)). The first case means effectively ZFC in remanence to 18 K and then zero-field heating (ZFH) to 80 K (as will be discussed in section 6.5.4), and the second case means FC to 18 K in a magnetic field of 0.35 T and then ZFH to 80 K. The two corresponding Mössbauer spectra are shown in Fig. 6.15. As usual, the spectra were least-squares fitted by a dominant Zeeman sextet for bcc-Fe and a distribution of hyperfine fields $P(B_{hf})$ for the interfacial component. The Mössbauer spectroscopical parameters for the dominant Zeeman sextet are listed in the last two rows of Table 6.1.

Table 6.1 *The Mössbauer spectroscopical parameters obtained after least-squares fitting the Mössbauer spectra of the Fe/MnF₂ interface sample (MFEMF01) (Int.) and Fe/MnF₂ center sample (MFEMF03) (Cent.). (ZFC = zero-field cooling (in remanence), ZFH = zero-field heating, FC = field cooling, T = measurement temperature, Φ = angle of incidence of the γ -ray relative to the film plane, IS = isomer shift relative to α -Fe at RT, QS = nuclear-quadrupole line shift ($= 2\epsilon$), B_{hf} = hyperfine magnetic field, R_{23} ($= R_{54}$) = intensity ratio of the 2nd (or 5th) and 3rd (or 4th) Mössbauer line for the bcc-Fe layer, Dist. area = relative spectral area of the component with hyperfine field distribution $P(B_{hf})$ (interface component), $B_{hf}(\text{peak})$ = peak value of the distribution $P(B_{hf})$). The center sample does not exhibit the interfacial contribution $P(B_{hf})$, but shows only the pure Zeeman sextet of bcc-like Fe. The error bars for R_{23} , IS, QS, B_{hf} and Dist. area are 0.1, 0.005 mm/s, 0.001 mm/s, 0.05 T and 5%, respectively. However, the error bar for R_{23} in the last row is 0.3.*

Sample	Type of field cooling	T (K)	Φ (degree)	R_{23}	IS (mm/s)	QS (mm/s)	B_{hf} (T)	Dist. area (%)	B_{hf} peak(T)
Int.	ZFC	80 K	90	4.00	0.113	0.01	33.8	13	26
	ZFC	80 K	45	1.86	0.117	0.00	33.8	12	27
	ZFC	18 K	90	4.00	0.117	0.00	34.3	17	27
	ZFC	18 K	45	2.67	0.123	0.01	34.1	20	28
Cent.	ZFC	80 K	90	4.00	0.114	0.01	33.9	-	-
	ZFC	80 K	45	2.34	0.111	0.01	33.9	-	-
	ZFC	18 K	90	4.00	0.113	0.00	34.1	-	-
	ZFC	18 K	45	2.58	0.124	0.00	33.8	-	-
Int.	FC(0.2 T)	18 K	90	4.00	0.130	0.00	34.1	20	28
	FC(0.2 T)	18 K	45	2.02	0.133	0.00	34.0	17	28
Int.	FC(0.35 T)	18 K	90	4.00	0.125	0.00	33.9	17	28
	FC(0.35 T)	18 K	45	2.11	0.131	0.00	33.70	17	28
Int.	ZFC \rightarrow ZFH	80 K	45	2.5(1)	0.121	0.02	33.9	21	27
Int.	FC(0.35 T) \rightarrow ZFH	80 K	45	2.7(3)	0.126	0.03	33.7	18	27

6.5 CEMS results: discussion

6.5.1 Depth-dependent Fe spin structure at remanence

Above T_N the antiferromagnet behaves like a paramagnet. For MnF₂, the magnetic anisotropy ($\chi_{\parallel} - \chi_{\perp}$) as well as the susceptibility above $T_N = 68$ K are very small, as discussed in chapter 5. Hence, the influence of MnF₂ on the Fe spin structure at 80 K $> T_N$ is negligibly small and may not be considered for the discussion.

The shape anisotropy of the polycrystalline thin bcc-Fe film (80 Å in thickness for both, interface and center sample) is very strong and forces the Fe spins to lie in the plane of the film at any temperature. For $T > T_N$, applying a strong magnetic field parallel to the film plane the Fe layer spins align along the field direction (magnetic saturation). After switching off the magnetic field the relatively weak magnetic anisotropy within grains of the polycrystalline Fe film will act on the Fe film to form in-plane magnetic Néel-type of domains separated by Néel walls. However, a remanent magnetization (oriented along the original field direction) remains in the film, as is evidenced in the hysteresis loops (Fig. 6.7 (a)).

Below $T_N = 68$ K the antiferromagnetic ordering of MnF₂ is present, and the influence of the AFM (MnF₂) on the FM (Fe) cannot be neglected. As the anisotropy of the antiferromagnet increases faster with decreasing temperature below T_N and becomes stronger than that of the Fe layer, the Fe spins are forced by interfacial exchange interaction to respond to the ordering of the Mn spins.

In most experiments performed in this work the remanence was induced by B_{ext} at a temperature $T \gg T_N$ and subsequently switching off the field, followed by zero-field cooling (ZFC) to a certain measurement temperature $T > T_N$ or $T < T_N$. This means that at that measurement temperature the sample did not experience an external field. We call this the "virgin remanence" of the sample, contrary to the "conventional remanence" obtained from a hysteresis loop at the measurement temperature. The measured M_{rem}/M_{sat} ratio (M_{rem} = conventional remanent magnetization measured in a hysteresis loop using a sweeping field at a certain temperature, e.g., 80 K (Fig. 6.7 (a)) is rather high ($M_{rem}/M_{sat} = 0.80$ and 0.86 at 80 K for the center and interface sample, respectively, Fig. 6.7 (a)), which means that nearly a single domain state remains at that temperature after switching off the field.

Interface sample

The results for the interface sample will be presented and discussed first. From the zero-field CEMS measurements (Fig. 6.11 (a), (b)) of the interface sample at remanence with $\Phi = 90^\circ$ (perpendicular incidence of the γ -ray relative to the film plane) an intensity ratio R_{23} of 4.0 has been obtained, both above and below T_N . This confirms the fact that as expected the Fe layer spins lie in the plane of the film above and below T_N of the antiferromagnet. However, measurements at inclined incidence with $\Phi = 45^\circ$ (Fig. 6.11 (c), (d)) reveal that a remarkable change of the line intensity ratio R_{23} from 1.86 at 80 K to 2.67 at 18 K is observed (Table 6.1). If all the Fe spins were aligned along one direction (the x -direction or B_{ext} direction for inducing remanence), the intensity ratio R_{23} should be 1.33 for $\Phi = 45^\circ$ according to eq. (6.6). However, the higher intensity ratio of 1.86 observed at $T = 80$ K ($T > T_N$) suggests that the Fe spins are not all aligned along the x -direction (or original applied field direction). By using the model of coherent spin rotation (where all Fe spins (or hyperfine fields B_{hf}) are unidirectionally aligned and rotate coherently in the film plane by an angle φ (see Fig. 6.9), the Fe spins are found at an angle $\varphi_0 = \pm 31^\circ$ away from the remanent magnetization direction (positive x -direction) according to eq. (6.6). The possible explanation for this effect can be given in the framework of domain formation at remanence, as a result of the magnetic anisotropy within different grains of the polycrystalline Fe film. Some magnetic domains have a magnetization that is not perfectly aligned along the x -direction, but the magnetization of the individual domain shows an in-plane angular distribution centered at the x -direction. This "anisotropy dispersion" in the polycrystalline Fe layer causes "fanning" of the in-plane domain magnetization and leads to a higher intensity ratio R_{23} in the CEM spectrum above T_N . It is important to note again that the possibility of any domain with out-of-plane magnetization is discarded, because for $\Phi = 90^\circ$ the (zero-field) CEMS measurements give $R_{23} = 4.0$, as is expected from the strong shape anisotropy which forces the Fe spins to lie within the film plane.

At the measurement temperature of 18 K ($T < T_N$) the intensity ratio R_{23} is found to increase drastically to 2.67 for $\Phi = 45^\circ$, as compared to 1.86 at 80 K (Table 6.1 and Fig. 6.17). In combination with the $\Phi = 90^\circ$ results ($R_{23} = 4.0$), which demonstrates that all Fe spins lie in-plane, one may infer a larger in-plane angular deviation of the Fe spins from the remanent magnetization direction (positive x -direction). By using the model of coherent spin rotation (unidirectional model), at 18 K, the Fe spins are found at an angle $\varphi_0 = \pm 51^\circ$ away from the original applied field direction (x -direction). The difference in the in-plane spin configuration for 80 K and 18 K is related to the fact that MnF₂ orders antiferromagnetically below 68 K. As was discussed in Chapter 5, the epitaxial MnF₂(110) on MgO(001) has a twinned structure with the c -axes parallel to the plane, but at an angle of $\pm 45^\circ$ with respect to the MgO[010] and MgO[100] directions. This means that the MnF₂ antiferromagnetic easy axes (c -axes) in the film are in the film plane and at angles of $\pm 45^\circ$ with respect to the x -axis of Fig. 6.9. The Fe spin direction in the interface sample, calculated from the unidirectional model, are $\varphi_0 = \pm 31^\circ$ at 80 K and $\pm 51^\circ$ at 18 K; the 80 K value clearly deviate from the $\pm 45^\circ$ -directions of the MnF₂ easy axes, while the 18 K value overshoots the $\pm 45^\circ$ direction only by 6° .

It is understood that below T_N there is AFM exchange coupling between the antiferromagnetic and ferromagnetic spins [285, 286, 289]. Considering this fact and the MnF₂ twinning, one would expect that the Fe spins in zero external field, exchange coupled to the Mn spins, will lie along the c -axes of either of the MnF₂ twin directions, i.e. at $\pm 45^\circ$ relative to the x -axis. A perfect alignment of all Fe spins along the two MnF₂ twin directions (irrespective of the parallel or perpendicular exchange coupling, suggested in ref. [183, 285, 286, 289]) will lead to an intensity ratio R_{23} of 2.40, according to eq. (6.6). However, the observed intensity ratio of $R_{23} = 2.67$ at 18 K is definitely higher than 2.40, and the corresponding angle of $\pm 51^\circ$ overshoots the $\pm 45^\circ$ -twin directions. This difference could be due to a roughness-driven fluctuation of the magnetization direction [100]. Thus, the roughness of the Fe/MnF₂ interface, although small, might lead to a change of the very interfacial spontaneous Fe spin structure. It is worthwhile mentioning in this context that an interfacial layer with spin-glass properties has been suggested in order to explain the exchange bias effect [9]. It is conceivable that magnetic coupling with such a spin-glass interlayer causes deviation of the Fe-spin direction from the $\pm 45^\circ$ -easy axis directions of bulk MnF₂.

Center sample

Now, we will discuss the CEMS results of the Fe/MnF₂ center sample. The spins of the center sample also lie in the plane, both above and below T_N , because of the obtained value of $R_{23} = 4.0$ (Fig. 6.12 (a),(b) and Table 6.1) for $\Phi = 90^\circ$ (perpendicular incidence). The spectrum at 80 K (Fig. 6.12 (c)) with $\Phi = 45^\circ$ after zero-field cooling in remanence gives an intensity ratio R_{23} of 2.34 (Table 6.1), which is much higher than that of a unidirectional Fe spin alignment along the x -axis ($R_{23} = 1.33$ according to eq. (5.1)). The reason can be the stronger roughness-driven magnetization fluctuation (consistent with the fact of coercivity enhancement) and/or larger anisotropy dispersion in the Fe-layer of this sample. This means that the Fe spins are oriented away from the x -axis and/or have an angular distribution around the x -axis. The value of $R_{23} = 2.34$ (equivalent to $\varphi_0 = \pm 43^\circ$, according to the unidirectional model, eq. (6.6)) for the center sample at 80 K is clearly larger than the value of $R_{23} = 1.86$ (equivalent to $\varphi_0 = \pm$

31° according to eq. (6.6)) for the interface sample at 80 K (Table 6.1). This means that the deviation from the unidirectional Fe spin orientation along the x -axis is larger for the center sample at 80 K than for the interface sample at 80 K. This is also consistent with the observation that the "conventional" remanent magnetization, M_{rem} , of the interface sample (measured by SQUID at 80 K) is higher than that of the center sample (Fig. 6.7 (a)). This difference reflects the different microstructures (e.g., different grain sizes, different roughnesses) of the two samples, as revealed also by their large difference in coercivities. ($H_c = 32$ Oe and 52 Oe for the interface and center sample, respectively, at 80 K.) It is remarkable that the Fe-spin directions obtained from the unidirectional model for the center sample at 80 K ($> T_N$) coincides within error bars with the two MnF₂ twin directions at $\pm 45^\circ$ relative to the x -axis. This might be accidental; it could also mean, however, that there is a growth induced magnetic anisotropy in the polycrystalline bcc-Fe layer on top of the pseudo-twinned MnF₂ film.

The CEMS measurements on the center sample at 18 K result in values of $R_{23} = 4.0$ and 2.58 for $\Phi = 90^\circ$ and 45° , respectively (see Table 6.1). The first value demonstrates again that the Fe spin lie in the film plane. The value of $R_{23} = 2.58$ at 18 K (equivalent to $\varphi_0 = \pm 49^\circ$ according to eq. (6.6)) should be compared with $R_{23} = 2.34$ at 80 K (equivalent to $\varphi_0 = \pm 43^\circ$ according to eq. (6.6)) for the center sample (Table 6.1). By cooling the sample to 18 K in remanence antiferromagnetic ordering of the MnF₂ layer is established. One would expect that the effect of exchange coupling between the AFM and FM spins drives the Fe spins to align towards either of the MnF₂ c -axes directions, i.e., $\pm 45^\circ$ away from the original external field (or x -axis) direction. However, the higher value of $R_{23} = 2.58$ (equivalent to $\varphi_0 = \pm 49^\circ$) observed at 18 K suggests that the effect of roughness-driven magnetization fluctuation or spin-glass-like interfacial layer might be responsible for the increase of the intensity ratio to a value larger than 2.40 (which is the ideal R_{23} value for a unidirectional Fe spin alignment along the c -axes of MnF₂ pseudo-twins according to eq. (6.6)). The higher R_{23} value of 2.58 (or $\varphi_0 = \pm 49^\circ$) at 18 K as compared to $R_{23} = 2.34$ (or $\varphi_0 = \pm 43^\circ$) at 80 K is quantitatively consistent with an Fe spin reorientation upon zero-field cooling below T_N , i.e., in the average the Fe spins are orientated farther away from the x -axis at 18 K than at 80 K due to exchange coupling. Further, a comparison of the R_{23} ratios for the interface sample at 18 K ($R_{23} = 2.67(10)$) and the center sample at 18 K ($R_{23} = 2.58(10)$) shows that those values are equal within error bars. Apparently, the spontaneous Fe spin structure in both samples at 18 K is similar.

Hence, the Fe spin structure in the remanent state of the exchange-biased Fe/MnF₂ system at 18 K ($T \ll T_N$) is found to be not different within the depth range from the Fe/MnF₂ interface up to 45 Å, although the interface and center samples are characterized by different roughnesses (see section 6.2). It is reported [176] that the roughness at the interface plays also a role in determining the remanent state Fe spin structure and magnetization, which is also responsible for the exchange bias. In our case we expect that the difference in the degree of roughness of both samples might not be large to induce large differences in H_E . Both samples show almost the same H_E ($H_E = 50 \pm 5$ Oe for the interface sample and $H_E = 60 \pm 5$ Oe for the center sample). In addition, the Fe spin structure of both samples at 18 K is very similar.

6.5.2 Influence of the cooling field on the Fe spin structure

By field cooling (FC) the interface sample (MEFMF01) in an external field of 0.2 T or 0.35 T from 300 K to 18 K, the "conventional" remanence has been induced. The zero-field CEMS measurements at $\Phi = 90^\circ$ give an intensity ratio $R_{23} = 4.0$ (Fig. 6.13 (a), (b) and Table 6.1), confirming again the fact that the Fe spins lie in the plane of the sample. The measurements with $\Phi = 45^\circ$ (Fig. 6.13 (c), (d)) result in $R_{23} = 2.02$ and 2.11 for 0.2 T and 0.35 T, respectively (Table 6.1). These R_{23} ratios are equal within the error bar (± 0.10) and are significantly smaller than those observed for the zero-field cooled (ZFC) state of the same sample at 18 K ($R_{23} = 2.67$, Table 6.1), demonstrating that in the FC case the Fe spins are more aligned towards the cooling field direction (x -direction) than in the ZFC case. According to the unidirectional model (eq. (6.6)), these R_{23} values correspond to angles $\varphi_0 = \pm 36^\circ$ at 0.2 T and $\varphi_0 = \pm 38^\circ$ at 0.35 T, as compared to $\varphi_0 = \pm (49^\circ \sim 51^\circ)$ for the ZFC state at 18 K. The results can be qualitatively explained as follows.

Cooling the interface sample from room temperature in an applied field (0.2 T or 0.35 T), all the spins are expected to be aligned along the field at all temperatures above T_N , where the influence of the MnF₂ layer is not important. By cooling further below T_N , the antiferromagnetic ordering starts and the anisotropy of the antiferromagnetically ordered MnF₂ increases. The exchange-bias effect also sets in. The strong anisotropy of the AFM, combined with the exchange interaction below T_N , tends to align the very interfacial Fe spins along the easy axis of the AFM, i.e., along the two MnF₂ twin directions (at $\pm 45^\circ$ with respect to the x -axis). Due to the presence of the external field the Fe spins that are farther away from the interface are aligned closer along the external field direction than the interfacial Fe spins. This may result in a spiral-like or incomplete domain-wall-type of spin arrangement in the Fe film, as suggested in the model by Kiwi et al. [3–5]. In this case the competition between the interfacial exchange energy due to coupling along the easy-axes directions of the AFM twins, exchange energy within the FM and the Zeeman energy due to the external field is responsible for a possible spiral-like spin arrangement.

After field cooling and removing the applied field at 18 K, the Zeeman energy is missing. However, as discussed in the literature, e.g., ref. [285], the uncompensated spins of the AFM existing at the FM/AFM interface, align and freeze along the applied field direction (x -direction) during FC below T_N (uncompensated Mn spins in the present case of Fe/MnF₂). This aligns the interfacial Fe spins in opposite direction to the uncompensated AFM spins [285], i.e., along the external cooling field direction. Hence, there is an additional driving force for the Fe spins to align along the cooling field direction, even after the external field is switched off, and an additional exchange-coupling energy term between interfacial Fe-spins and uncompensated interfacial AFM moments should be involved. Hence, expectedly, in comparison to the ZFC measurements, a lower Mössbauer line intensity ratio of $R_{23} = 2.02$ and 2.11 is measured after field cooling in 0.2 T and 0.35 T fields, respectively, and switching off the external field (Fig. 6.13, Table 6.1). These smaller values of R_{23} provide indirect evidence of the existence of such uncompensated AFM spins, which appear due to interface roughness and/or intermixing, and may behave like a spin-glass, with its spins frozen along the external field direction. The exchange interaction between these frozen AFM spins and the interfacial

Fe spins does not allow the Fe spins to rotate far away from the field cooling direction (x -direction), unlike in the case of ZFC, where the interfacial uncompensated AFM spins probably freeze in more random anisotropy directions, which are, however, influenced by the ($\pm 45^\circ$) anisotropy directions of the bulk AFM twin domains beneath, and also by the exchange coupling with the interfacial Fe spins at remanence and (indirectly) with the exchange energy within the FM.

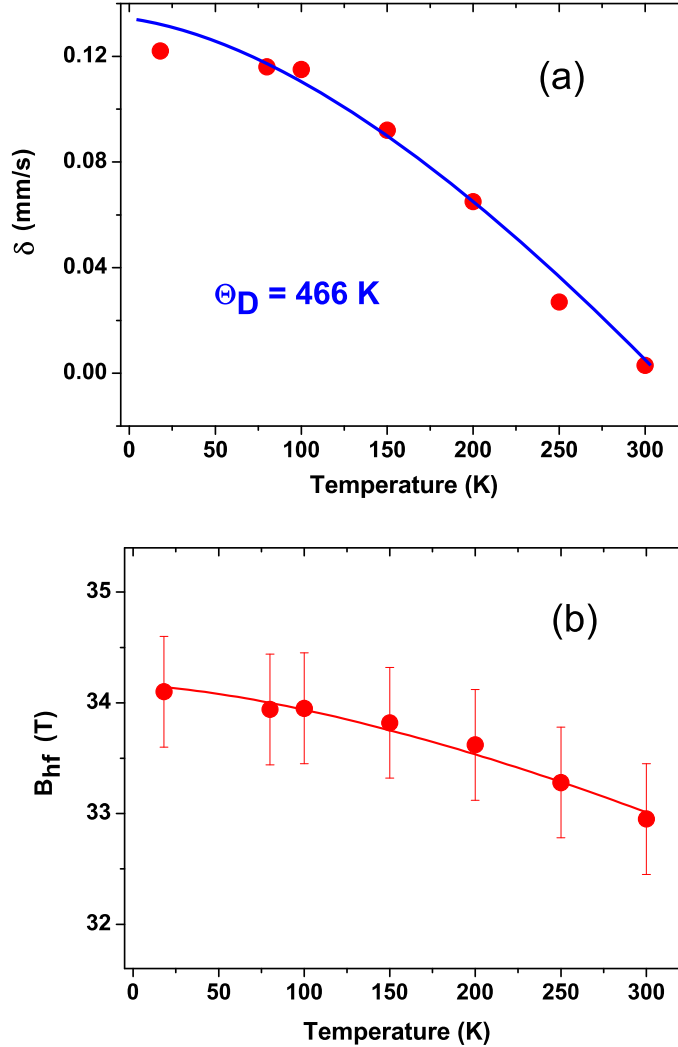


Figure 6.16: The T-dependence of the center line shift (δ) (relative to α -Fe at RT) (a) and of the magnetic hyperfine field B_{hf} (b) of the dominant Zeeman sextet (bcc-Fe) obtained from Fig. 6.14 for the interface sample. The fitted curve in (a) follows the Debye model. The fitted curve in (b) follows Bloch's $T^{3/2}$ spin-wave law.

6.5.3 Temperature dependence of the Fe spin structure

From all CEMS measurements at $\Phi = 90^\circ$ it is clear that the Fe-layer spins lie in the film plane at all temperatures and for different depths (0 - 10 Å and 35 - 45 Å) away from the Fe/MnF₂ interface of the Fe film. The CEM spectra measured at $\Phi = 45^\circ$ on the

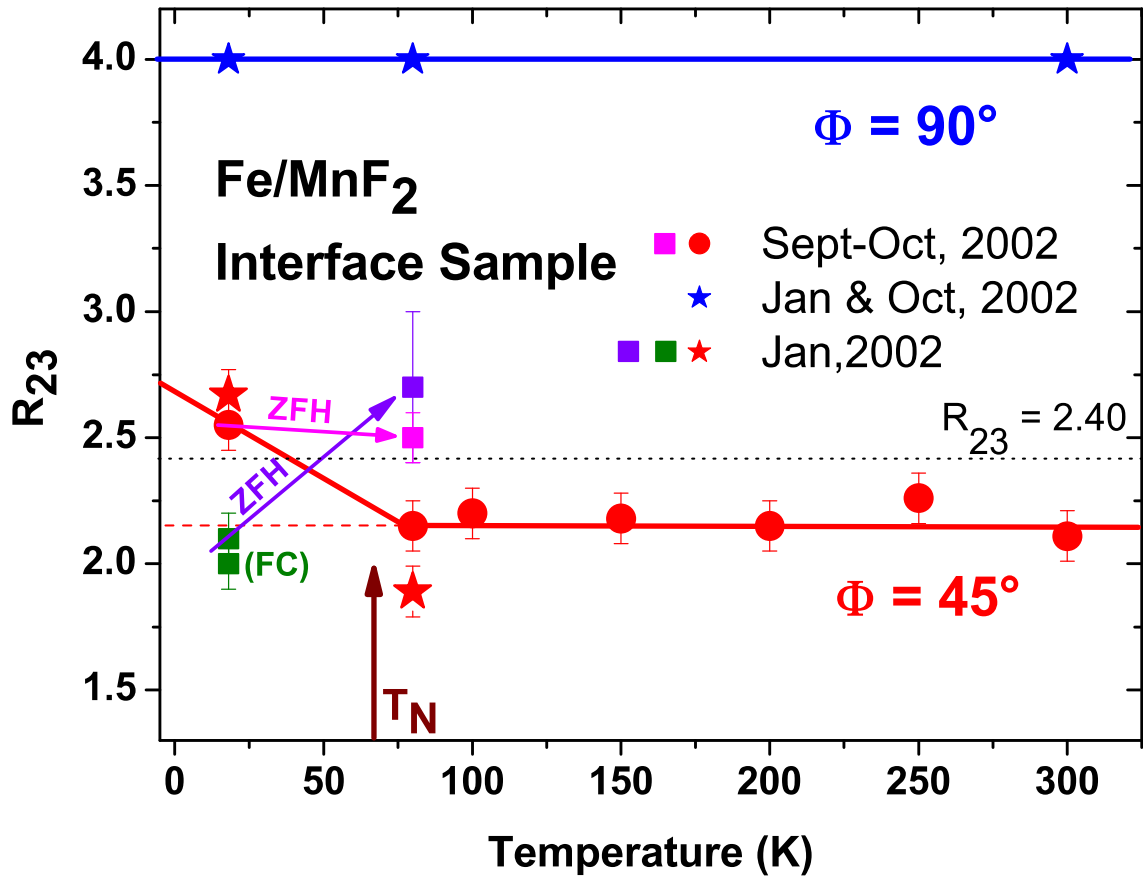


Figure 6.17: The R_{23} ratio obtained for the interface Fe/MnF₂ sample (MFEMF01) at $\Phi = 90^\circ$ (blues stars) and 45° (red circles and stars) measured at different temperatures in remanence (according to Fig. 6.14). The red stars are for another set of measurements (see Fig. 6.11) performed about eight months before the other measurements. The lines are a guide for the eye. T_N indicates the Néel temperature of bulk MnF₂. R_{23} ratios obtained from the FC measurements and the ZFH measurements are also shown for comparison (arrows). The dotted line signifies the ideal R_{23} ratio for Fe spins aligned along the $\pm 45^\circ$ antiferromagnetic anisotropy directions of the pseudo-twinned MnF₂ domains.

Fe/MnF₂ interface sample in remanence at decreasing temperatures between 300 K and 10 K, are shown in Fig. 6.14. Again, all spectra were least-squares fitted by a Zeeman sextet and a contribution from the very interface with a distribution of hyperfine fields $P(B_{hf})$ (Fig. 6.14). The spectral component with a distribution of hyperfine fields, which shows a strong peak at about 26 T for all temperatures, is attributed to weak chemical intermixing (about 15 % of the 10 Å thick ⁵⁷Fe probe layer thickness, according to the relative spectral area of the interfacial component) at the interface. From the fittings, the average hyperfine field $\langle B_{hf} \rangle$ of the distribution of hyperfine fields (interfacial component) is observed to remain almost constant at about 25 T in the measured temperature range between 18 K to 300 K [208]. This means the magnetic ordering temperature of the interfacial phase is far above room temperature. The dominant Zeeman sextet is attributed to the bcc-Fe layer. The temperature dependence of the Mössbauer spectroscopical parameters namely isomer shift (or the center shift) δ , and hyperfine

field B_{hf} of the bcc-Fe phase, is shown in Fig. 6.16. (The temperature dependence of the isomer shift is fitted by assuming a Debye-like behavior for the second-order Doppler shift, which results in a Debye temperature (θ_D) of 466 K, which is typical for bcc-Fe). The temperature dependence of B_{hf} of the bcc-Fe phase is found to follow Bloch's $T^{3/2}$ - behavior for spin-wave excitation, $B_{hf}(T) = B_{hf}(0)(1-b \cdot T^{3/2})$, which yields $B_{hf}(0) = 34.16$ T and $b = 6.46 \times 10^{-6} \text{ K}^{-3/2}$. Both values are typical for bcc-Fe.

The most important result is the temperature dependence of R_{23} for bcc-Fe layer as shown in Fig. 6.17. No change of the R_{23} ratio is observed from 300 K down to 80 K; however, further cooling to 18 K results in a significant increase of R_{23} . This demonstrates that after producing the remanence by switching off the external field at RT, the Fe spin structure does not change upon zero-field cooling to about the Néel temperature $T_N = 68$ K of MnF₂. Since there is almost no change of the magnetic anisotropy of MnF₂ above T_N , which is very small anyway (see Chapter 5), the spin structure and supposedly also the magnetic domain structure at remanence remain the same down to the Néel temperature of MnF₂.

By contrast, below T_N , when the twinned antiferromagnet orders, the interfacial exchange coupling of Fe layer with the antiferromagnetic domains beneath lets the Fe spins align towards the easy axes directions of the AFM (twin-directions). This lets the Fe spins rotate more and more towards the twin directions, because the anisotropy of the AFM and the exchange anisotropy becomes stronger with decreasing T . Consideration of the rotation of the whole Fe layer spins due to the exchange interaction averages ideally to an angle of $\pm 45^\circ$ (along the c -axes of AFM) on both sides of the remanent magnetization direction. The measured higher intensity ratio of $R_{23} = 2.55$ (at 18 K) than that for a $\pm 45^\circ$ rotation (ideally $R_{23} = 2.40$) can be qualitatively explained by the roughness-driven magnetization fluctuation at the interface as mentioned in section 6.5.1.

6.5.4 Memory effect of the Fe spin structure

It was observed earlier in Ni₈₁Fe₁₉/CoO bilayers [108] that exchange bias is an accumulative memory effect, dependent on the thermal and field history of the FM/AFM bilayer. Further, from previous sections (sections 6.5.1 and 6.5.2) we have observed that FC (in $B_{ext} = 0.35$ T) or ZFC in remanence produces different spin structure of the Fe layer at low temperature (at 18 K, below T_N). In both cases, the Fe spins tend to orient (to different degrees) towards the c -axis (easy axis) of MnF₂ pseudo-twins. In the first experiment, the sample was ZFC in remanence from 300 K to 18 K, then ZFH to 300 K, and subsequently ZFC to 80 K for the CEMS measurement. As observed in section 6.5.3, the spin structure is preserved during cooling from 300 K down to 80 K (Fig. 6.17). Hence, it is justified to assumed that the procedure (300 K (ZFC) \rightarrow 18 K (ZFH) \rightarrow 300 K (ZFC) \rightarrow 80 K) is equivalent to the procedure (300 K (ZFC) \rightarrow 18 K (ZFH) \rightarrow 80 K). Both, during ZFC to 18 K and ZFH to 80 K the spins tend to align more and more towards the anisotropy directions (easy axes) of MnF₂. Hence, a perfect alignment of Fe spins along $\pm 45^\circ$ with respect to the x -axis should be ideally observed, corresponding to $R_{23} = 2.40$. The observed intensity ratio $R_{23} = 2.50(10)$ (Table 6.1) also confirms that. Our observed value of 2.50 is very close to 2.40, thus proving the preferred alignment of Fe spins along the easy axes of MnF₂. The small difference from the ideal value could be due to formation of magnetization ripples, e.g., because of anisotropy dispersion or

roughness-driven magnetization fluctuations throughout the film.

By field cooling in 0.35 T to below T_N the interfacial uncompensated AFM (which might behave like a spin glass) freeze (more or less) oppositely to the applied field direction. After switching off the magnetic field at low temperature (18 K), the Fe layer spins are influenced by the anisotropy directions of the pseudo-twinned AFM (MnF₂) layer (i.e., at an angle of $\pm 45^\circ$ with respect to the applied field direction), and by the anisotropy direction of the frozen uncompensated interfacial spins (whose freezing direction is determined by the applied field). Hence, as described in the previous section (section 6.5.3) an Fe spin structure will be formed, whose direction is in-between the applied field direction (0°) and the AFM easy axes ($\pm 45^\circ$). Further, during ZFH to 80 K, the originally frozen interfacial uncompensated moments will defreeze more and more, and the spins of the Fe layer, due to increased thermal energy and missing exchange coupling to the uncompensated interfacial moments, tend to align along the AFM easy axes, because the exchange interaction with the bulk AFM spins is the force acting during ZFH to T_N of MnF₂. Finally, at 80 K, the Fe spins align in the average along the MnF₂ easy axes direction. The least-squares fitting of our spectrum measured after ZFH at 80 K (Fig. 6.15 (b)) (although with modest statistic) results in a Mössbauer line intensity ratio of $R_{23} = 2.71(30)$, which is within error bars very close to the ideal value of $R_{23} = 2.40$ for a unidirectional spin alignment along the ($\pm 45^\circ$) MnF₂ easy directions.

Hence, for both of the above cases, (300 K (ZFC) \rightarrow 18 K (ZFH) \rightarrow 80 K, or 300 K(FC) \rightarrow 18 K (ZFH) \rightarrow 80 K) equal values (within error bars) of R_{23} , and thus, the same Fe spin structure, have been observed at 80 K (Fig. 6.17). The striking effect is that the R_{23} values at 80 K, obtained by ZFH from 18 K, i.e., $R_{23} = 2.50(10)$ and $2.71(30)$ at 80 K, are significantly larger than the value of $R_{23} = 2.15$ measured at 80 K after ZFC from 300 K (Fig. 6.17). This observation demonstrates that the Fe spin structure has a "memory" at $T = 80$ K ($> T_N$): it "remembers" the $\pm 45^\circ$ AFM easy axes after having been in the exchange biased state (at 18 K), while the $\pm 45^\circ$ directions are not sensed by the Fe spins at 80 K after ZFC from RT.

6.6 Modeled angular Fe spin distributions in Fe/MnF₂

6.6.1 Angular Fe spin distribution in remanence

First we describe the Fe spin distribution after ZFC the sample in remanence from 300 K. Using the unidirectional distribution model (section 6.4.2, eq. (6.6)) the remanent-state Fe spin structure for the interface and the center samples of Fe/MnF₂ have been analyzed on the basis of measured R_{23} values (Table 6.1). The results are displayed in Fig. 6.18. According to this model, at 80 K (above T_N), the Fe spin direction deviates by an angle of $\varphi_0 = \pm 31^\circ$ and $\varphi_0 = \pm 43^\circ$ from the x -axis (external field or remanent magnetization direction) for the interface and center sample, respectively. It is not physically reasonable to say that the polycrystalline Fe layer is in a single domain state with its magnetization pointing along $\varphi_0 = \pm 31^\circ$ and $\varphi_0 = \pm 43^\circ$ away from the external field direction, but φ_0 rather indicates the average angle at which the Fe spins are present (averaged over all the magnetic domains formed in the sample). However, below T_N , when the antiferromagnet orders, at the very interface the Fe spins rotate by the interfacial exchange coupling to the spin axis of the AFM which is at $\pm 45^\circ$ with

respect to the applied field during remanence; due to the strong exchange energy within the Fe film the other Fe spins farther away from the interface also rotate towards the easy axes of MnF₂. By using the unidirectional model for remanent spin structure at 18 K, spin rotation angles of about 51° and 49° have been obtained for the interface and the center sample, respectively (Fig. 6.18 (a), (b)). Although the unidirectional model provides physically reasonable values for the average angle of the Fe spin structure, we have used also the step shaped distribution model, because the implied Fe spin fanning might represent the angular distribution of the domain magnetization and/or ripples in the domain. This is discussed below.

A single domain polycrystalline ferromagnetic Fe film breaks into a multidomain state when the external magnetic field is switched off. The demagnetizing field is zero within the film plane, but the anisotropy dispersion plays the main role in creating a multidomain state from the single domain state after switching off the external field [87]. This anisotropy dispersion may arise due to growth-induced variation of the easy axes of the Fe film grown on the crystallographically twinned MnF₂ in our case, and/or inhomogeneity in the structure of the film due to roughness and intermixing, as observed by XRD and the Mössbauer interfacial spectral component. As a result, the local spin direction of the Fe film may vary slightly from point to point within a domain. This non-parallelism adds exchange energy to the system, and, in addition, free magnetic poles are created within a domain, because of the divergence of magnetization, causing stray fields and magnetostatic energy. In order to minimize these effects, the local magnetization can vary in a ripple-like manner (called magnetization ripple) within a domain. However, the energy in the film due to anisotropy dispersion may not overcome the Zeeman energy or exchange energy of the system to form domains pointing randomly along all directions. One can expect that a sizable amount of magnetization at remanence still remains in form of domains with magnetization components pointing along the original external field direction.

As explained above, the step-shaped distribution model is a physically reasonable alternative for explaining the spin structure of the Fe layer in our Fe/MnF₂ system. Presumably, this model might be suited in explaining the spin structure of the Fe layer at high temperatures (above T_N of the MnF₂), because of magnetic domain formation influenced by the anisotropy dispersion of the Fe layer, after switching off B_{ext} . At 80 K (above T_N), spin fanning angles (eq. 6.6) of about 114° and 170° have been obtained for the interface and the center sample, respectively (Fig. 6.19). This difference in the spin fanning angles might occur due to different remanent states of the samples caused by different anisotropy dispersion, or different microstructure of the samples. Further, higher fanning angles (i.e. low remanence) of the center sample can be due to higher roughness of the center sample as compared to the interface sample, (as exhibited by the small-angle XRD plot, Fig. 6.5), which causes higher anisotropy dispersion via different microstructure. The higher coercivity of the center sample at 80 K (measured by SQUID, section 6.3) also supports this idea. (The higher roughness could lead to a different microstructure in the two samples, leading to higher H_C in the center sample).

Below T_N , the step-shaped distribution model also may provide a physically meaningful alternative for the spin configuration, using the argument that the very interfacial layer Fe spins couple with the MnF₂ pseudo-twin domains underneath. The AFM do-

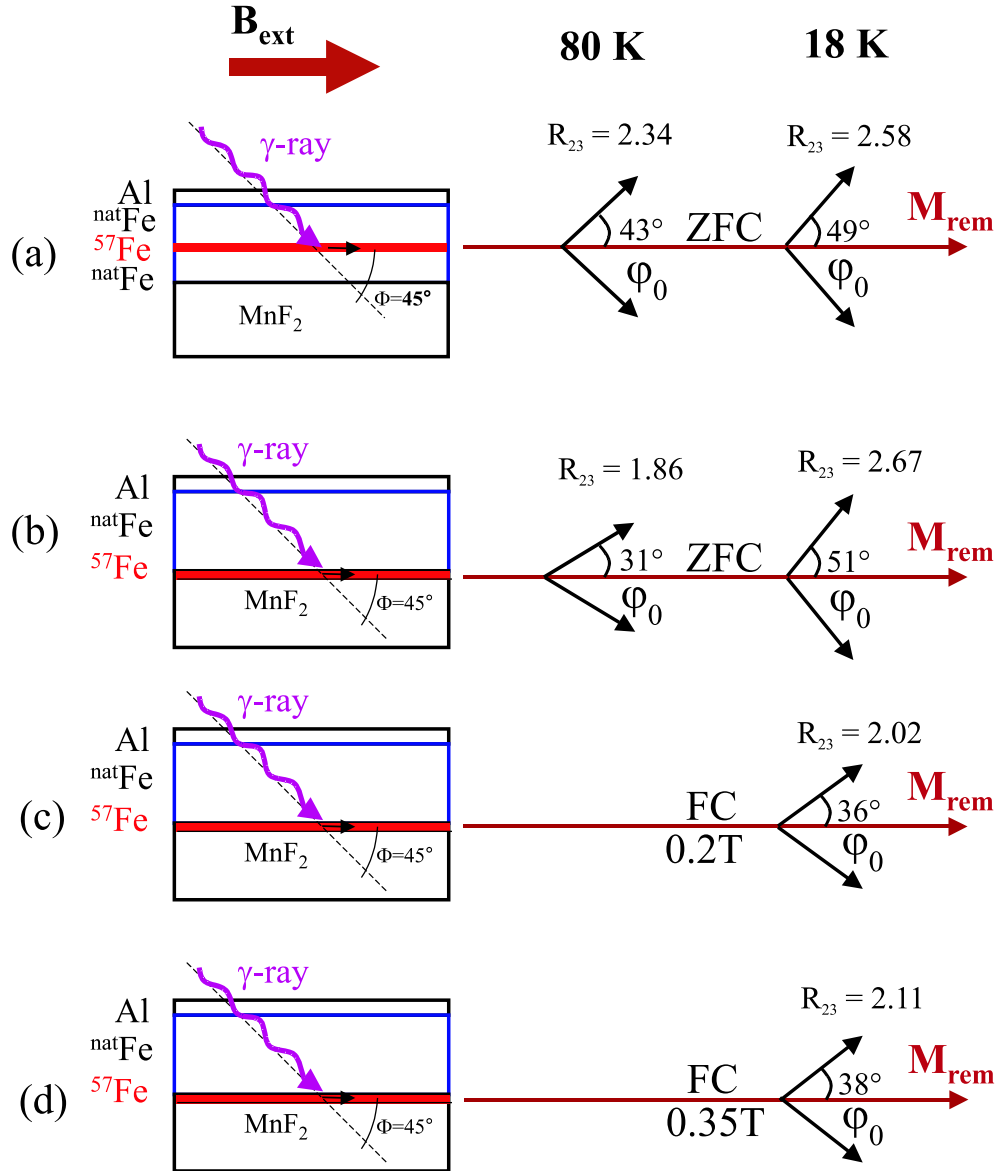


Figure 6.18: Remanent-state Fe spin rotation angles φ_0 according to the unidirectional distribution model after zero-field cooling (ZFC) or field cooling (FC) from room temperature (RT) to measurement temperatures of 80 K or 18 K for the Fe/MnF₂-center sample (a) and the Fe/MnF₂-interface sample (b),(c), (d). Right-hand side: view onto the sample plane (xy -plane) showing the average Fe spin directions (black arrows) and the remanent magnetization (M_{rem}) direction (x -direction). (a) After ZFC the center sample in remanence from RT, (b) after ZFC the interface sample in remanence from RT, (c) after FC the interface sample from RT in an external field of 0.2 T and measuring in remanence, and (d) after FC the interface sample from RT in an external field of 0.35 T and measuring in remanence. The corresponding R_{23} ratios measured by CEMS are also given. Left-hand side: schematic cross-sectional view of the corresponding Fe/MnF₂ layered structure. The direction of the external field B_{ext} and the incident γ -ray are also indicated.

main size of these pseudo-twins presumably is much smaller (~ 100 Å [285, 289]) than

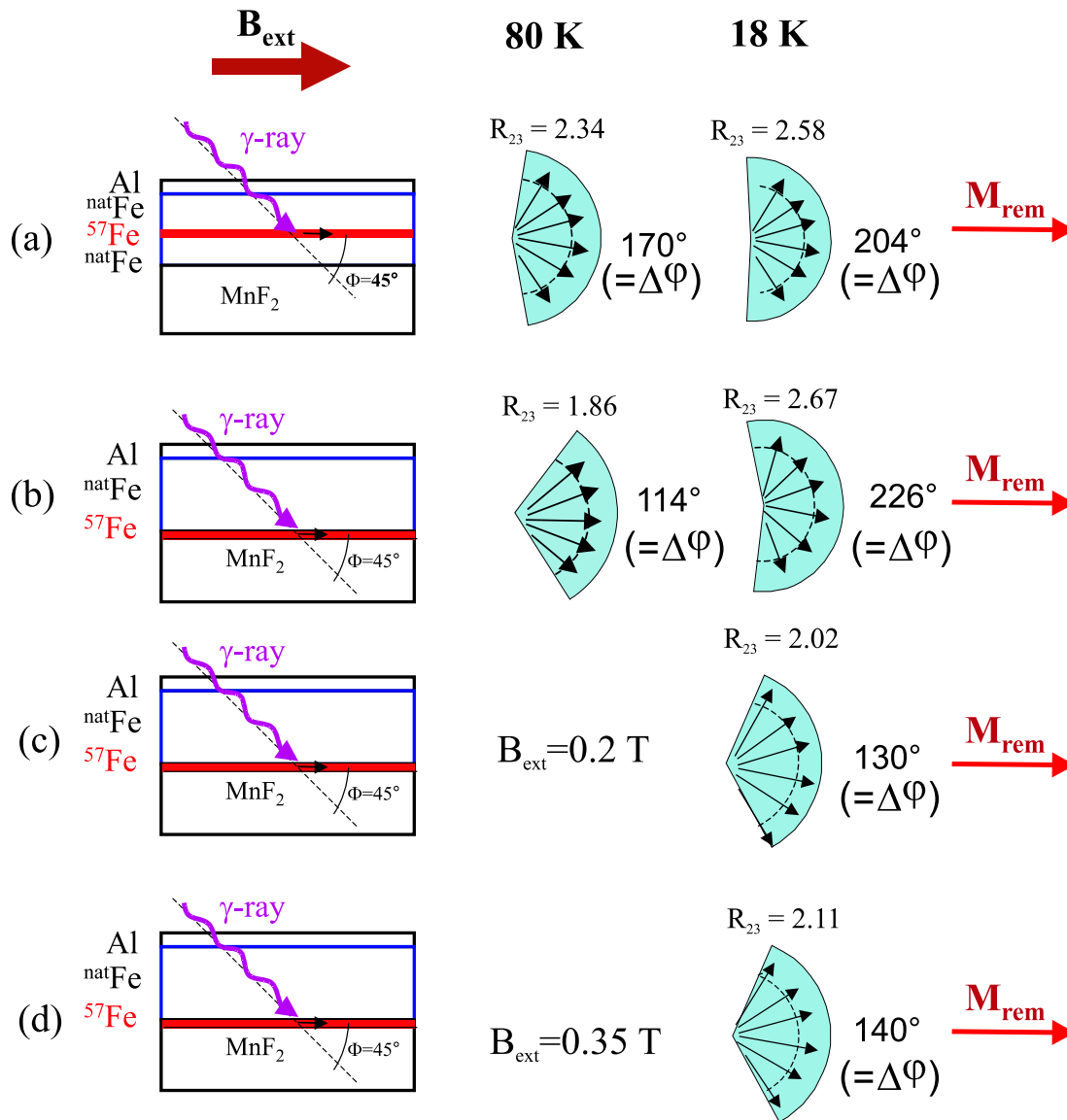


Figure 6.19: Remanent-state Fe spin fanning angles $\Delta\varphi$ according to the step-shaped distribution model ($\varphi_0 = 0^\circ$) of the Fe/MnF₂ samples after ZFC or FC from room temperature (RT) to measurement temperatures of 80 K or 18 K for the center sample (a) and the interface sample (b),(c), (d). Right-hand side: view onto the sample plane (xy -plane) showing the Fe spin directions (black arrows) and the remanent magnetization (M_{rem}) direction (x -direction). (a) after ZFC the center sample in remanence from RT, (b) after ZFC the interface sample in remanence from RT, (c) after FC the interface sample from RT in an external field of 0.2 T and measuring in remanence, and (d) after FC the interface sample from RT in an external field of 0.35 T and measuring in remanence. The corresponding R_{23} ratio measured by CEMS are also given. Left-hand side: schematic cross-sectional view of the corresponding Fe/MnF₂ layered structure. The direction of B_{ext} and the incident γ -ray are also displayed.

the domain size of the ferromagnet, and also the AFM anisotropy directions are at an angle of $\pm 45^\circ$ away from the initial external field direction (x -axis). Further, there is a distribution of AFM domain sizes throughout the film. Hence, it is possible that mag-

netization ripples are formed in the Fe domains of the whole film after ZFC from 300 K to 18 K at remanence due to frustration of the Fe interfacial spins within a FM domain. Because of these arguments the Fe spin structure may be described as spin fanning, and the step-shaped distribution model might be applicable. By using the step-shaped distribution model and assuming that the average magnetization direction (along the x -axis) is preserved during cooling (i.e., $\varphi_0 = 0^\circ$), the obtained Fe spin fanning structure is shown in Fig. 6.19 (a), (b). Below the Néel temperature (at 18 K), Fe spin fanning angles $\Delta\varphi$ of 226° and 204° have been obtained for the interface and center sample, respectively. However, within the error bar of the measured R_{23} (value ± 0.1), these resulting $\Delta\varphi$ values are equal. The large increase in the spin fanning angle from 114° (170°) for the interface (center) sample at 80 K to 226° (204°) at 18 K may be qualitatively understood by considering the FM/AFM coupling at the interface and the strong anisotropy (along the $\pm 45^\circ$ directions) of the AFM in the Fe/MnF₂ system.

As the anisotropy dispersion is considered, it is worthwhile to point out here that the higher coercivity measured by SQUID at 80 K and at 18 K for the center sample in comparison to the interface sample is very likely caused by the different microstructure of the two samples. The slow saturation of the magnetization (at higher applied field values, e.g., close to 100 Oe in Fig. 6.7 (a) and close to 250 Oe in Fig. 6.7 (b)) may be due to the presence of ripple-type of structure in the domains of the Fe layer.

6.6.2 Angular Fe spin distribution after field cooling

In the pseudo-twinned Fe/MnF₂ system, at room temperature (i.e. far above T_N), the spins of the whole Fe layer are aligned along the applied field direction. ($B_{ext} = 0.2$ T was applied along the MgO[100] (x -axis), which is at 45° to either of the twin directions). At such a high T ($\gg T_N$) the anisotropy of the MnF₂ layer is ineffective. During field cooling to low temperatures ($T < T_N$) the antiferromagnet orders, with the Mn spin axis at $\pm 45^\circ$ to the cooling field direction, and a strong magnetic anisotropy develops in the MnF₂ layer. One expects that the interfacial Fe spins, which couple antiferromagnetically with the Mn spins, are influenced by the anisotropy of MnF₂ and, if this anisotropy is strong enough, will rotate away from the applied field direction towards the two AFM easy axes directions at $\pm 45^\circ$. This rotation will be more effective if the FM/AFM exchange coupling at the interface is high. During field cooling in the strong field of 0.2 T the Fe spins are expected to align along the external field in the presence of B_{ext} , because of the high Zeeman energy of the FM. However, switching off the field at low temperature ($T < T_N$) the interfacial FM/AFM energy will cause the interfacial spins to rotate (or fan out) towards the AFM spin axis. Strong Fe-Fe exchange interaction will drive the Fe spins that are farther away from the interface to align also towards the AFM easy axes.

As discussed previously in section 6.5.2, by field cooling the interface sample to 18 K (and measuring at remanence), Mössbauer line intensity ratios of $R_{23} = 2.02$ and 2.11 are obtained for cooling fields of 0.2 T and 0.35 T, respectively, (at $\Phi = 45^\circ$). Using the unidirectional model, spin rotation angles of 36° and 38° (away from the x -axis, towards the AFM easy axes) are obtained for the cooling fields of 0.2 T and 0.35 T, respectively (Fig. 6.18 (c), (d) and Table 6.1). This confirms that after switching off the external field the Fe spins rotate towards the AFM easy directions, but significantly less than in the case of ZFC (section 6.6.1). This behavior may be explained by the presence of

uncompensated interfacial AFM spins, which may behave like a spin-glass, and which will be frozen along the external field direction during field cooling below T_N . This will create a different type of interfacial anisotropy for the Fe spins, which will be aligned more along the applied field direction (at a local minimum of energy). This anisotropy will try to prevent the complete rotation of the Fe layer spins to align along the MnF₂ pseudo-twin easy directions.

However, a ripple-type of spin structure could also be expected in this FC case after removing B_{ext} (because of the variation of the AFM domain size and anisotropy dispersion), and the step-shaped spin distribution model may be applied. Using the step-shaped distribution model, in-plane angular spin fanning angles $\Delta\varphi$ of 130° and 140° are obtained at 18 K for the cooling fields of 0.2 T and 0.35 T, respectively. The results are schematically shown in Fig. 6.19 (c) and (d).

6.6.3 Memory of the angular Fe spin distribution

As described in section 6.5.4, the least-squares fitting of the spectra measured at 80 K, after ZFC to 18 K and then ZFH to 80 K (Fig. 6.15 (a)), or FC to 18 K and then ZFH to 80 K (Fig. 6.15 (b)) yields the same R_{23} values (2.5(1) and 2.7(3), respectively) within the error bars. Applying the unidirectional model (section 6.4.2 and Fig. 6.10(a)), spin rotation angles of $47^\circ \pm 2^\circ$ and $52^\circ \pm 8^\circ$ are obtained. Applying the step-shaped distribution model (section 5.4.2 and Fig. 6.10(c)) with $\varphi_0 = 0^\circ$ spin fanning angles $\Delta\varphi$ of (a) 200° and (b) 228° are obtained, as shown in Fig. 6.20 (right column) for the sample history: (a) ZFC to 18 K and then ZFH to 80 K, and (b) FC to 18 K and then ZFH to 80 K. These angles are significantly different from the angle $\Delta\varphi = 110^\circ$ that obtained after ZFC (in remanence) the same sample from 300 K to 80 K (Fig. 6.19 (a), (b)). However, these angles are equal (within the error bar) to the angles obtained for the interface sample at 18 K after ZFC in remanence to 18 K (Fig. 6.19 (a), (b)). Hence, this observation demonstrates that the Fe spin structure has a "memory" at $T = 80$ K ($> T_N$): it "remembers" its spin structure at $T < T_N$ (the $\pm 45^\circ$ AFM easy axes) after having been in the exchange biased state (at 18 K), while the $\pm 45^\circ$ directions are not sensed by the Fe spins at 80 K after ZFC from RT.

It is worthwhile mentioning here that, although CEMS cannot decide the two opposite directions (along or opposite to the applied field), the spin rotation or fanning are assumed to be relative to the initial applied field direction (x -direction), because of the fact that a large M_{rem}/M_{sat} ratio is measured by SQUID on these samples. One may predict at this stage of the work that just by performing few thermal cycles (to temperatures far above and far below T_N) on an exchange bias AFM/FM bilayer sample which has not been exposed to any magnetic field, and which is not strongly intermixed at the interface creating its own strong anisotropy, the Fe spins will spontaneously align along the easy directions of the AFM (in the present case, all the four directions ($\pm 45^\circ$ and $\pm 135^\circ$) of the pseudo-twined MnF₂ domains).

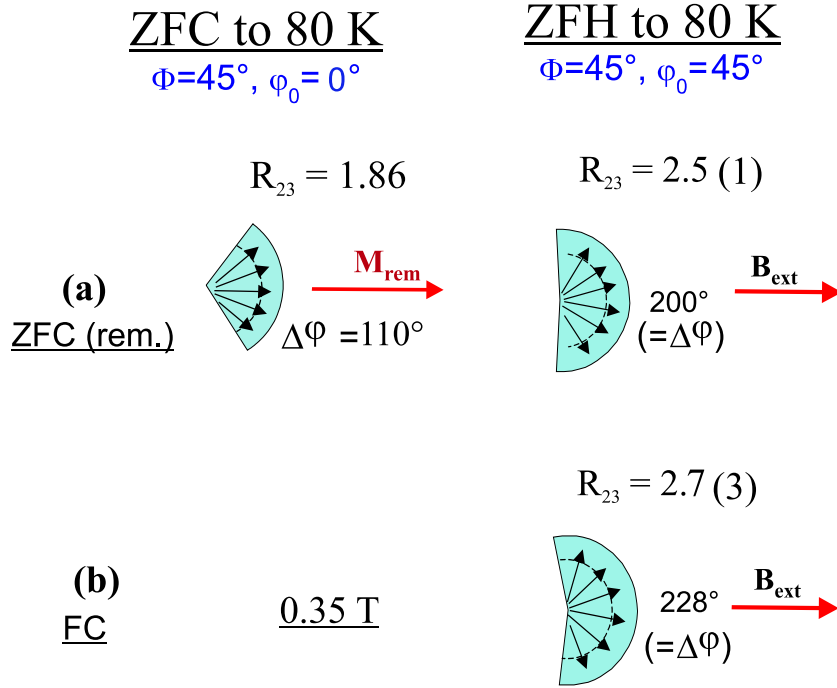


Figure 6.20: Fe spin fanning angles ($\Delta\varphi$) of the interface Fe/MnF₂ (MFEMF01) sample according to the step-shaped distribution model with $\varphi_0 = 0^\circ$. Right-hand side: view onto the sample plane (xy -plane) showing the Fe spin directions (black arrows) (a) spin fanning after ZFC in remanence from 300 K to 18 K and then ZFH to 80 K, (b) spin fanning after FC to 18 K in an external field of 0.35 T and then ZFH to 80 K. The corresponding R_{23} ratio measured by CEMS is also given (according to Fig. 6.15). Left-hand side: (a) the spin fanning after ZFC in remanence from 300 K to 80 K is also shown for comparison. The direction of B_{ext} and of the remanent magnetization for the ZFC case is also given. The CEMS measurements were performed in zero external field. Notice the remarkable difference in the Fe spin structure obtained by ZFC to 80 K and ZFH to 80 K.

6.7 Supplementary vector SQUID magnetometry: results and discussion

Magnetic hysteresis loops measured by vector SQUID magnetometry at decreasing temperatures for the center sample in the "virgin" remanent state (i.e., measured at different temperatures during zero-field cooling in remanence) are shown in Fig. 6.21 (a) [57]. For comparison with the CEMS results, the T -dependence of the remanent magnetic moment components m_L (parallel to the external field H and MgO[100]) and m_T (transverse to the external field H and MgO[100], in the film plane) of the center sample were measured at $H = 0$ Oe during cooling in remanence (virgin remanent state). The results for m_L and the total magnetic moment $m_{tot} = (m_L^2 + m_T^2)^{1/2}$ are shown in Fig. 6.21 (b). The m_T values were found to be one order-of-magnitude smaller than the m_L values, making m_L and m_{tot} comparable within the whole temperature range.

The CEMS results (section 6.5) for the Fe spin structure are supported by the T -dependence of m_L and m_{tot} for the center sample (Fig.6.21 (b)). First, the saturation

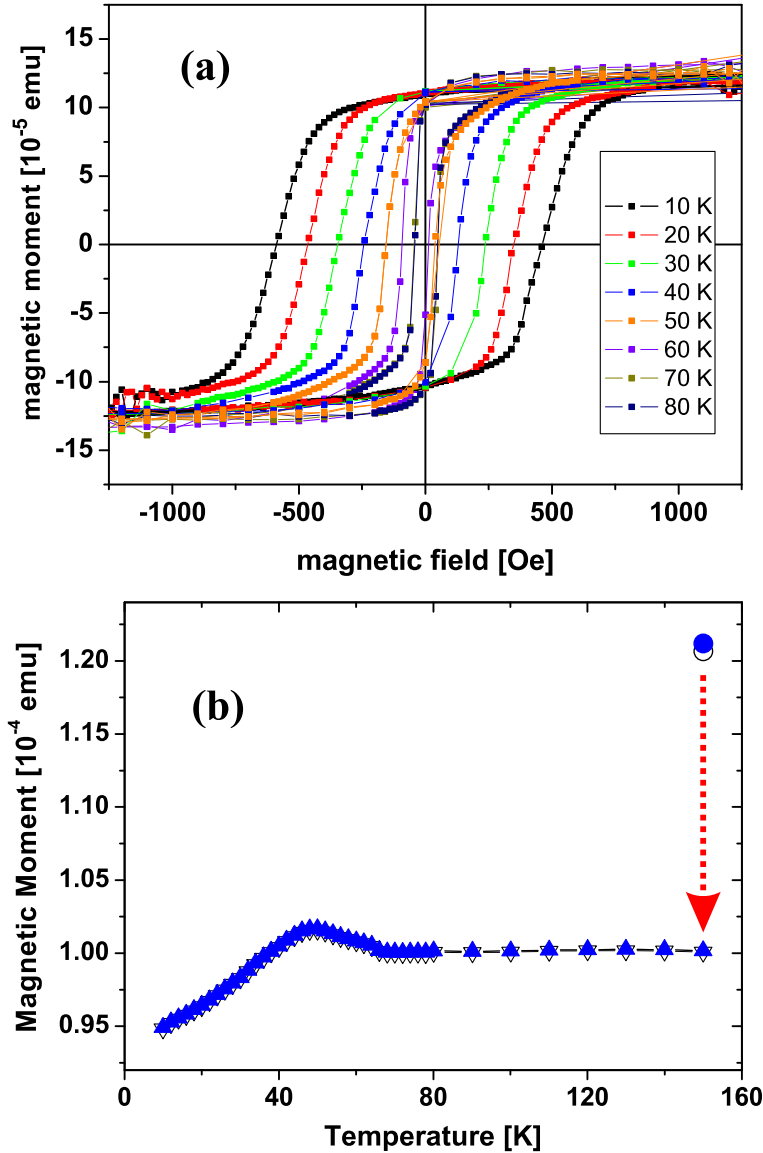


Figure 6.21: (a) Magnetic hysteresis loops for the center sample measured by vector SQUID at different temperatures during cooling in remanence. (b) Temperature dependence of the remanent longitudinal moment m_L (open triangles) and total moment m_{tot} (solid triangles) ($m_{tot} = \sqrt{m_L^2 + m_T^2}$) of the center sample measured for $H = 0$ Oe during ZFC from 150 K to 10 K. The prior saturation magnetization m_L (open circle) and m_{tot} (full circle) of the sample at $H = 2$ kOe at 150 K is also shown. ($m_T =$ transverse moment).

magnetization m_L (open circle) and m_{tot} (full circle) were measured at 150 K in a field of 2 kOe (Fig. 6.21). Then, upon zero-field cooling in remanence from 150 K, m_L and m_{tot} first remain constant down to $T_N = 67$ K, then rise and show a maximum at ~ 49 K (whose origin is not yet understood), followed by a significant decrease upon ZFC to 10 K. The decrease of m_L and m_{tot} is the indication of rotation (or fanning) away from the initial external field (MgO[100] direction) due to exchange bias, in accordance with CEMS. Moreover, the observed very small m_T values suggest that (averaged over the entire sample) this rotation or fanning is bidirectional, i.e., essentially symmetrical

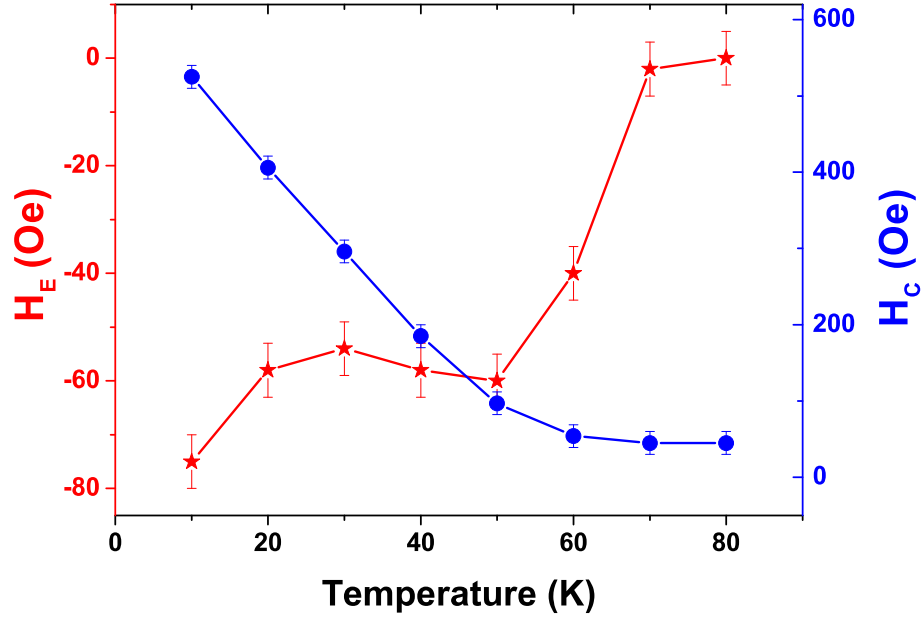


Figure 6.22: Temperature dependence of the exchange-bias field H_E (red stars, left scale) and coercive field H_C (blue circles, right scale) for the Fe/MnF₂ center sample (MFEMF03) obtained from the vector-SQUID measurements during warming up from 10 K, after ZFC to 10 K.

with respect to the initial external field (MgO[100] axis). After ZFC to 10 K, a virgin remanent moment of $m_L = 0.9482(2) \times 10^{-4}$ emu at $H = 0$ Oe was measured. Following this 10 K measurement, an external field H of 2 kOe was applied, and a saturation moment of $m_{sat} = 1.234(104) \times 10^{-4}$ emu was measured at 10 K, which is about equal to m_{sat} at 150 K. Finally, after switching off the 2 kOe field, the (conventional) remanent moment was measured to be $m_L = 1.106(4) \times 10^{-4}$ emu at $H = 0$ Oe. Note that there is a difference between m_L at virgin and conventional remanence at 10 K: the conventional remanence is ~ 16 % larger than the virgin remanence. This confirms qualitatively the decrease of the Fe spin rotation angle φ_0 (or fanning angle $\Delta\varphi$) obtained by CEMS at remanence after FC the sample to 18 K (Fig. 6.13 and Table 6.1) in comparison to the case of ZFC the sample in remanence to 18 K.

The Fe spin rotation or fanning angles can be obtained independently by the vector SQUID measurements, providing an independent check of the corresponding angles determined by CEMS. The rotation (or fanning) angles are obtained as follows.

Assuming $P(\varphi)$ as the in-plane angular Fe spin distribution, which is supposed to be homogenous within an angular interval from $-\varphi'$ to $+\varphi'$, and zero otherwise (step-shaped distribution model, section 6.4.2), the average longitudinal moment is given by

$$\langle m_L \rangle = \frac{\int_{-\varphi'}^{+\varphi'} m_{sat} \cos\varphi P(\varphi) d\varphi}{\int_{-\varphi'}^{+\varphi'} P(\varphi) d\varphi} = \frac{1}{2\varphi'} \int_{-\varphi'}^{+\varphi'} m_{sat} \cos\varphi d\varphi = \frac{m_{sat}}{\varphi'} \sin\varphi',$$

with the normalization $\int_{-\varphi'}^{+\varphi'} P(\varphi)d\varphi = 1/2\varphi'$.

$$\Rightarrow \frac{\langle m_L \rangle}{m_{sat}} = \frac{\sin\varphi'}{\varphi'} \quad (6.8)$$

Hence, from the measured quantity, $\left[\frac{\langle m_L \rangle}{m_{sat}}\right]$, the fanning angle ($\varphi' = \Delta\varphi/2$) can be obtained (φ' = semiaperture). Using measured values $m_{sat} = 1.234 \times 10^{-4}$ emu and $m_L = 0.9482 \times 10^{-4}$ emu and 1.106×10^{-4} emu for virgin and conventional remanence, respectively, the following values were calculated from eq. (6.8), at 10 K: the fanning angles $\Delta\varphi$ for the center sample at 10 K are $\Delta\varphi = 140^\circ$ at virgin remanence (after ZFC in remanence), and $\Delta\varphi = \pm 84^\circ$ at conventional remanence (after FC in 0.2 T). These angles are in rough agreement with the CEMS results on the center sample at 18 K (Fig. 6.19): $\Delta\varphi = 204^\circ$ at virgin remanence, and $\Delta\varphi = 130^\circ$ at conventional remanence. Using the unidirectional model, we obtained $\langle m_L \rangle/m_{sat} = \cos\varphi_0$. In this model the following angles are calculated from the vector SQUID results at 10 K: $\varphi_0 = \pm 40^\circ$ at virgin remanence and $\varphi_0 = \pm 26^\circ$ at conventional remanence. These values are in fair agreement with the corresponding CEMS results: $\varphi_0 = \pm 49^\circ$ at virgin remanence and $\varphi_0 = \pm 36^\circ$ at conventional remanence (Fig. 6.18). The temperature dependence of the exchange bias field H_E and the coercive field H_C , obtained from the ZFC measurements, are shown in Fig. 6.22. The observed behavior is in fair agreement with previous reports [157].

6.8 Conclusions for the Fe spin structure in Fe/MnF₂

Two exchange-biased Fe/MnF₂ samples with 10-Å thick ⁵⁷Fe probe layer at or 35 Å away from the Fe/MnF₂ interface were deposited on MgO(001) substrates by electron beam evaporation and characterized by XRD, SQUID magnetometry and CEMS. The MnF₂(110) films have a twinned crystallographic structure with the c-axes at $\pm 45^\circ$ relative to MgO[100] direction. For field cooling at 0.2 T and for zero-field cooling in remanence, equal values of exchange bias fields H_E were obtained by SQUID for both, the interface and center sample. The remanent-state Fe spin structure has been obtained for both samples by CEMS, after zero-field cooling the samples at remanence from room temperature to either 80 K (above T_N of MnF₂) or 18 K (below T_N). According to the CEMS results the Fe spins always lie in the sample plane. We have observed a different remanent state of the two samples at 80 K, because of the magnetic anisotropy dispersion in the Fe films, related to the microstructural difference of the two samples as observed by XRD. Below T_N , when the exchange bias sets in, an in-plane rotation of the Fe spins away from the remanent magnetization direction towards the AFM easy axes of the (pseudo-twinned) MnF₂ occurs. The average Fe spin rotation angle φ_0 or fanning angle $\Delta\varphi$ were obtained from the Mössbauer line intensity ratio R_{23} by using the unidirectional or step-shaped distribution model for the in-plane angular Fe spin distribution. Both, interface and center samples show equal Fe spin rotation or fanning angles (within error bars) in the remanent state at 18 K (below T_N of MnF₂) due to exchange coupling of Fe spins with the AFM spins and the strong antiferromagnetic anisotropy of MnF₂. Upon zero-field cooling from 300 K to 80 K, no change of the Fe spin rotation angle or Fe spin fanning angle has been observed, suggesting that the domain structure does not change by ZFC to a temperature $T > T_N$ (where the anisotropy of the AFM does not play a role). By contrast, the observation of increasing Fe spin rotation (or spin

fanning) upon ZFC to a temperature below T_N suggests that the Fe spins couple to the AFM spins at the interface and the interfacial exchange interaction change the spin structure of the Fe layer in the exchange-biased state. This behavior was confirmed by supplementary vector SQUID magnetometry measurements. Besides the coupling of the Fe spins to the Mn spins preferentially along the AFM easy directions of the MnF₂ film, the observed intermixing at the interface, which presumably leads to spin glass behavior and to the uncompensated interfacial AFM spins, plays a major role in aligning the Fe spins towards the applied field direction during field cooling. This conclusion can be done, because smaller Fe spin rotation angles (or smaller fanning angles) in comparison to the case of zero-field cooling were observed. The observed different remanent-state Fe spin structures created by ZFC or FC to a temperature $T < T_N$ provides indirect evidence for the presence of uncompensated AFM interfacial spins that align antiparallel to the external field. The remanent state Fe spin structure after FC to $T < T_N$ may evolve from a competition between interfacial antiparallel exchange coupling of Fe spins with frozen uncompensated AFM spins (aligned antiparallel to the external field direction) and exchange coupling with Mn spins oriented along the AFM easy axes of pseudo-twinned MnF₂. Upon zero-field heating the prior remanent state (created by ZFC or FC to $T < T_N$) to a temperature $T > T_N$, the same Fe spin structure as that at $T < T_N$ after ZFC is retained to temperatures $T > T_N$. This means that the Fe spin structure above T_N shows a memory effect.

Chapter 7

Fe and FeF₂ Spin Structure in Exchange Biased Fe/FeF₂ Bilayers

7.1 Introduction

FeF₂ has the same crystal structure and spin structure, and similar magnetic properties as MnF₂, but has a higher Néel temperature ($T_N = 78$ K) and a larger magnetic anisotropy. The anisotropy field is about 7 kOe in MnF₂ ($S=5/2$) while it is 149 kOe for FeF₂ ($S=2$) [166]. This is believed to be the key in explaining the difference in exchange bias and coercivity observed in FeF₂. More specifically, the reason for the higher exchange bias field and the difference in coercivity in the Fe/FeF₂ system as compared to Fe/MnF₂ is the larger FM-AFM interfacial exchange constant $J_{FM/AFM}$ of Fe/FeF₂ [2], which is in turn related to the high anisotropy of FeF₂ as given below. For Fe, the value of the ferromagnetic exchange constant is $J_{FM} = 16$ meV, and the stiffness constant is $K_{FM} = 0$ meV/spin. Similarly, the antiferromagnet exchange constant $J_{AFM} = -1.2$ meV and the stiffness constant $K_{AFM} = 2.5$ meV/spin for FeF₂, and $J_{AFM} = -1.3$ meV and $K_{AFM} = 0.12$ meV/spin for MnF₂ [[4], and references therein]. Depending on the values of the measured exchange bias field, Kiwi et al. [4, 5] have calculated obtained the interfacial exchange constants of $J_{FM/AFM} = -1.2$ meV and -0.35 meV for Fe/FeF₂ and Fe/MnF₂, respectively. Obviously, the magnitude of $J_{FM/AFM}$ and K_{AFM} is much larger for Fe/FeF₂ than for Fe/MnF₂.

At very low thickness (in the range of 10 Å to 45 Å) of the AFM layer the roughness of the films are high, because the films grow as islands. When the islands start to coalesce the roughness decreases and the film becomes smoother (after 45 Å). However, by growing a thicker (900 Å) FeF₂ film on MgO(001) the film roughness (i.e. film thickness fluctuation) increases with increasing growth temperatures (from 200 °C to 300 °C) [187, 189], which is in contrast with the growth of the (600 Å) MnF₂ film on MgO(001)[157] between temperatures 200 °C and 375 °C, where the roughness decreases with increasing growth temperature. FeF₂ films grown at 200 °C had a root-mean-square roughness σ_{rms} of about 15 Å, while σ_{rms} was 39 Å for the growth at 300 °C [187, 189].

Unlike in the Fe/MnF₂ system, a crossover from negative ($H_E < 0$) to positive ($H_E > 0$) exchange bias in Fe/FeF₂ has been observed for a rough film ($\sigma_{rms} = 39$ Å) (for cooling fields of about 13 kOe), but for the smoother films the magnitude of exchange bias was decreasing and was always negative up to a cooling field of about 70 kOe [188].

Also at moderate fields (e.g., at 2 kOe, which is more than the bulk Fe low-temperature saturation magnetization of 1.74 kOe [187]), where the exchange bias field was negative, the highest magnitude of the exchange bias was obtained for the smoothest film.

Like in the Fe/MnF₂ system, the magnitude of the exchange bias field increases with increasing antiferromagnetic thickness, and it gradually saturates at about 250 Å of FeF₂ [166]. For very small FeF₂ thickness (below 10 Å) the exchange bias disappears. This critical thickness is much smaller than that of MnF₂ (about 150 Å), which suggests that the critical thickness is primarily determined by the magnetic anisotropy of the antiferromagnet, which is larger for FeF₂.

In the Fe/FeF₂ system, the exchange bias field depends on the Fe layer thickness t_{Fe} in a similar way as in case of Fe/MnF₂ system. The exchange bias decreases by increasing the Fe layer thickness [187] ($H_E \propto t_{Fe}^{-n}$, with n close to 1), which is very close to the power law followed by the Fe/MnF₂ system [153].

The training effect, where the magnitude of exchange bias field decreases by repeating the hysteresis loop cycles, is absent in both, the Fe/MnF₂ and Fe/FeF₂ systems [187]. Along with the absence of the training effect, which provides a good measure of the exchange bias field and coercivity, the larger value of the exchange bias field and coercivity make the Fe/FeF₂ system more suitable for the study of the microscopic properties associated with exchange bias.

The importance of the cooling field is that it decides on the freezing direction of the uncompensated interfacial AFM moment S_{AF} during the first cooling procedure below T_N . This has been verified by many different experiments [188] on a Fe/FeF₂ sample. When the sample [188] was field-cooled in a 2-kOe field and the system hysteresis loop was measured by sweeping the field between the +2 kOe and -2 kOe, the observed loop shift is the same (within 5 % of the cooling field) as that observed by sweeping the field between +70 kOe and -70 kOe, leading to a negative exchange bias field ($H_E < 0$). However, cooling the sample in a strong field of 70 kOe (i.e., when the cooling field ≥ 13 kOe) and sweeping the field between +2 kOe and -2 kOe, results in a loop shift in the positive direction, i.e., a positive exchange bias field ($H_E > 0$) was obtained.

Thus, field cooling the Fe/FeF₂ system at 2 kOe and 70 kOe results in a negative and positive exchange bias, respectively. At different measurement temperatures the value of the exchange bias field changes. More accurately, the absolute value of the exchange bias field, $|H_E|$, decreases with increasing temperature in both cases [188]. Further, the sign of H_E remains the same until the exchange bias vanishes at $T_N = 78$ K of FeF₂. This indicates that the antiferromagnetic ordering is responsible for determining the negative and positive exchange bias. In case of positive exchange bias, any possibility of a spin flop in FeF₂ has been ruled out, because the spin flop field in FeF₂ is 419 kOe, which is well above the highest cooling field [128]. Furthermore, for the above two cooling fields of 2 kOe and 70 kOe, the observed coercivities are the same for the same measurement temperature. This suggests that the ferromagnetic domain structure is not responsible for determining the sign of the exchange bias.

For polycrystalline Fe films grown on FeF₂(110) or FeF₂(100) single crystals, when

the cooling field H_{FC} was applied in the plane and perpendicular to the FeF₂ spin axis (easy direction, c-axis) (i.e. $H_{FC} \parallel \text{FeF}_2[010]$ and $H_{FC} \parallel \text{FeF}_2[1\bar{1}0]$), the obtained exchange bias field is almost zero [183], but is maximum and positive when the cooling field was applied along the antiferromagnetic easy axis. This indicates that the cooling field is ineffective when there is a large crystal anisotropy in the AFM, which tends to align the FM spins along the AFM easy axis, which is perpendicular to the cooling field. If the cooling field makes an angle θ with the AFM easy axis, then the positive exchange bias field will be reduced by a factor of $\cos\theta$ [188]. Accordingly, for pseudo-twinned AFM, FeF₂, the maximum positive exchange bias field has been obtained for $\theta = 45^\circ$, where H_{FC} is oriented along the bisector between the twin (c-axes) directions. For moderate cooling fields, when a negative exchange bias field is obtained, a similar (although not strictly) directional dependence has been observed.

In Fe/FeF₂, the value of the exchange bias field decreases with increasing temperatures in a way which is close to that of Fe/MnF₂. The temperature behavior for both, positive and negative exchange bias fields, is similar [188].

The temperature behavior of the coercivity H_C has been investigated by Moran et al. [183] on exchange biased Fe/FeF₂ systems, with FeF₂(011) being a single crystal. If the sweeping field for the hysteresis loop is applied along the FeF₂ easy axis (FeF₂[001]) direction and in the plane of the sample, H_C shows a clear maximum at about T_N . However, for sweeping fields along the $[1\bar{1}0]$ direction, which is perpendicular to the easy axis of FeF₂[110], the coercivity starts to increase just below T_N and has the maximum at $T \simeq 0$ K. Combining these two observations Moran et al. [183] claimed that the easy axis of the Fe layer rotates by 90° below T_N . For pseudo-twinned Fe/FeF₂(110) systems the coercivity is almost constant at all cooling fields, when the cooling field is applied parallel to either of the twin easy axes. However, for cooling fields applied between the twin axes, i.e., at $\theta = 45^\circ$ to either of the twin easy axes, the coercivity increases and saturates at a cooling field of about 15 kOe. This saturation value of H_C is almost the same as the constant value observed, when the field was applied along the twin easy axis.

In this chapter a detailed study of the Fe spin structure in the Fe layer (remanent state) and in the FeF₂ layer will be presented. The spin structure is believed to be the key in understanding details of the exchange bias phenomenon in exchange-biased Fe/FeF₂ bilayers. The spin structure will be discussed on the basis of conversion electron Mössbauer spectroscopy (CEMS) and SQUID magnetometry results. The direction of the electric field gradient (EFG) in FeF₂, which is a major contribution in determining the quadrupole splitting and the line positions of the Mössbauer spectrum, will be determined on the basis of the obtained results.

7.2 Sample Preparation and Characterization

Two different kinds of Fe/FeF₂ samples, similar to those discussed in chapter 5, have been prepared by e-beam evaporation. The typical geometrical structure of the interface sample (Fig.7.1(a)) and center sample (Fig.7.1(b)) were (30 Å)Al/ (70Å)^{nat}Fe/(10 Å)⁵⁷Fe/(450 Å)FeF₂/MgO(001), and (30 Å)Al/(35Å)^{nat}Fe/(10 Å)⁵⁷Fe/(35Å)^{nat}Fe/(450 Å)FeF₂/MgO(001), respectively. The growth temperatures for the Al, Fe and FeF₂ lay-

ers were 150°C, 150°C and 200°C, respectively, and the deposition rates were 0.5 Å/s, 1 Å/s and 2 Å/s, respectively. The FeF₂ layer thickness was monitored by calibrated quartz crystal oscillations, and the Al and Fe layer-thicknesses were monitored by optical sensor. No buffer layer was used for the growth of the FeF₂, i.e., the FeF₂ layer was directly deposited on the MgO(001) substrate. In comparison to the Fe/MnF₂ system, where the lattice strain is relaxed by the ZnF₂ buffer layer, the strain in the Fe/FeF₂ film thus will be higher. The interface sample was labelled JF05 [55] and the center sample was labelled MEFFF05 [52].

<u>Interface sample</u> (JF05)			<u>Center sample</u> (MEFFF05)	
Al	30 Å	Cap layer	Al	30 Å
^{nat} Fe	70 Å	FM layer with ⁵⁷ Fe probe layer	^{nat} Fe	35 Å
⁵⁷ Fe	10 Å		⁵⁷ Fe	10 Å
^{nat} FeF ₂ (110)	450 Å	AFM layer	^{nat} FeF ₂ (110)	450 Å
MgO(100) substrate			MgO(100) substrate	

Figure 7.1: Schematic structure of the Fe/FeF₂ samples prepared on MgO(100) substrates. In the interface sample (left) the 10 Å thick ⁵⁷Fe probe layer is at the AFM(FeF₂)/FM(Fe) interface, while for the center sample (right) the ⁵⁷Fe probe layer is at the center of the FM (Fe) layer, i.e., 35 Å away from the interface. (^{nat}Fe: iron of natural isotopical abundance with ca. 2% ⁵⁷Fe; ⁵⁷Fe: 95% isotopically enriched ⁵⁷Fe).

After preparation the structural characterization was performed by high and small angle X-ray diffraction (XRD). The XRD results are shown in Fig. 7.2 (a), (b) and Fig. 7.3 (a), (b) for the interface sample (JF05) and the center sample (MEFFF05), respectively. The epitaxial growth of both FeF₂ samples has been observed, with FeF₂(110) in the plane of MgO(100). However, according to previous reports [188, 189] the FeF₂ film is pseudo-twinned, i.e., the c-axis of FeF₂ is at $\pm 45^\circ$ with respect to the MgO[100] direction. The rocking curve of the FeF₂(110) peak for the interface sample (insert in Fig. 7.2 (a)) has a FWHM of 5.30°, which reflects the degree of strain-induced misorientation of the epitaxial grains. The top and the bottom curves in Fig. 7.2 (b) belong to the small angle XRD of the interface sample, taken before and after depositing the Fe layer, respectively. For clarity, the top curve in Fig. 7.2 (b) has been shifted upwards by a factor of 100 counts. A rough estimation (based on the angular position of the peaks of the oscillations) suggests that the Fe and FeF₂ layer thicknesses are ~ 50 Å and 460 Å, respectively, for this interface sample. The FWHM of the rocking curve (insert in Fig. 7.3 (a)) for the center sample (MEFFF05) is about 3.12°. Comparison with the corresponding FWHM of 5.30° for the interface sample shows that better epitaxy is achieved for the center sample than for the interface sample. The red curve (insert in Fig. 7.3 (a)) is a Gaussian fit to the measured rocking curve data. The nature of

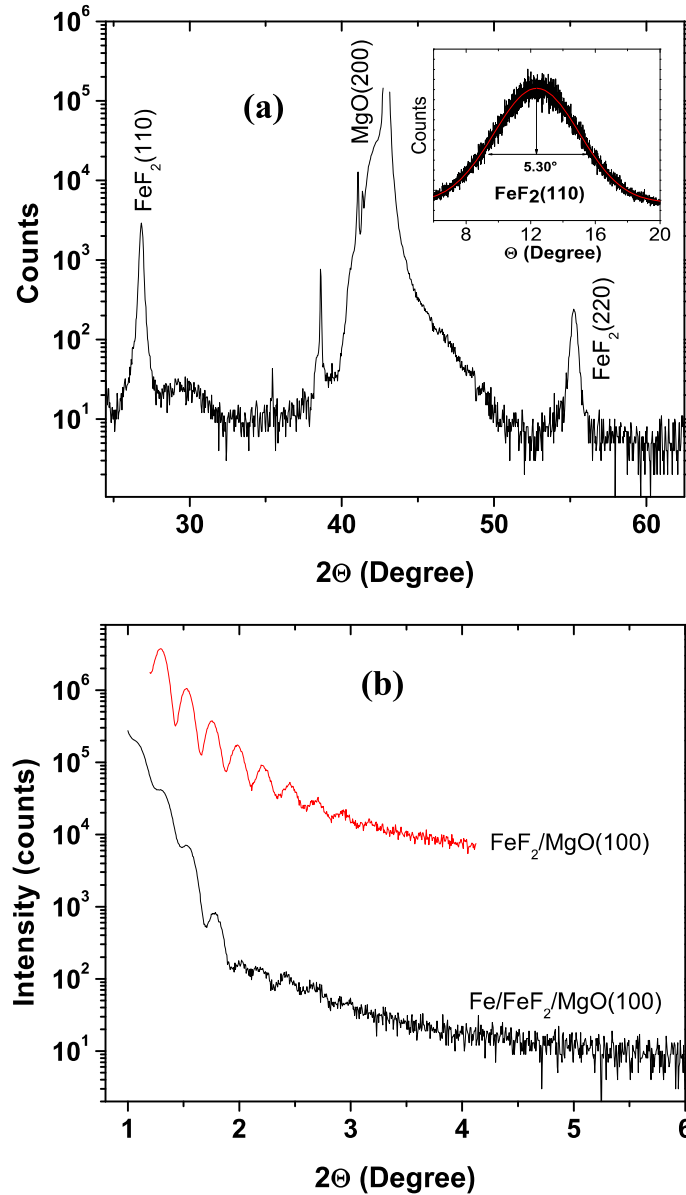


Figure 7.2: (a) High-angle X-ray diffraction pattern of the Fe/FeF₂ interface sample (JF05). The epitaxial nature of the film is observed, with the c-axis in the plane of the film. The FWHM of the rocking curve FeF₂(110) peak (insert) is about 5.30°. The red curve in the insert is a Gaussian fit to the measured rocking curve of the FeF₂(110) peak. (b) Small angle XRD pattern of the Fe/FeF₂ interface sample (JF05) before (top) and after (bottom) deposition of the Fe layer (the top curve has been shifted by a factor of 100 for clarity). (Cu-K_α radiation).

the polycrystalline, but textured, Fe(200) film is also clearly seen. A rough estimation (based on the angular position of the peaks of the oscillations) suggests that the Fe and FeF₂ layer thicknesses are ~ 80 Å and 390 Å, respectively. Comparing the clarity of the oscillations in the small-angle XRD patterns of both, interface and center sample, it is clear that interface of the Fe and the FeF₂ layers in the center sample has a higher roughness than the interface sample.

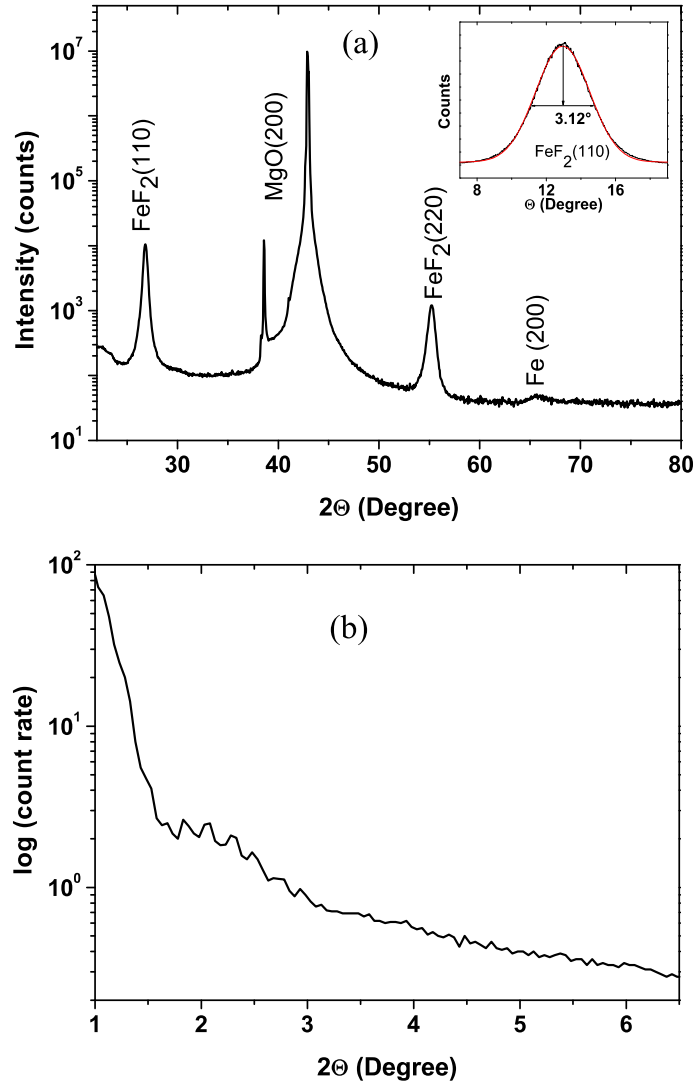


Figure 7.3: (a) High-angle X-ray diffraction pattern of the Fe/FeF₂ center sample (MF-EFF05). The epitaxial nature of the film is observed, with the c-axis in the plane of the film. The FWHM of the rocking curve FeF₂(110) peak (insert) is about 3.12°. The red curve in the insert is a Gaussian fit to the measured rocking curve of the FeF₂(110) peak. (b) Small angle XRD pattern of the Fe/FeF₂ center sample (MFEFF05). (Cu-K_α radiation).

The samples were also characterized by CEMS and vector SQUID magnetometry. The CEMS measurements were performed in a variable temperature bath cryostat by using either a (He - CH₄) gas filled counter or a channel electron detector. The magnetization measurements at different temperatures for both samples were performed in a SQUID magnetometer [57]. CEMS and SQUID magnetometry results will be discussed in sections 7.3 and 7.4, respectively.

7.3 CEMS Results

7.3.1 Experimental details and the hyperfine parameters

Conversion electron Mössbauer spectroscopy at various temperatures has been performed on the interface and center samples, both in remanence. For all cases discussed below, the remanence was induced in the samples at RT with an applied field of 0.4 T in the MgO[100] direction (x-direction). The measurements were performed by using either a (He - CH₄) gas filled proportional counter or a channel electron multiplier.

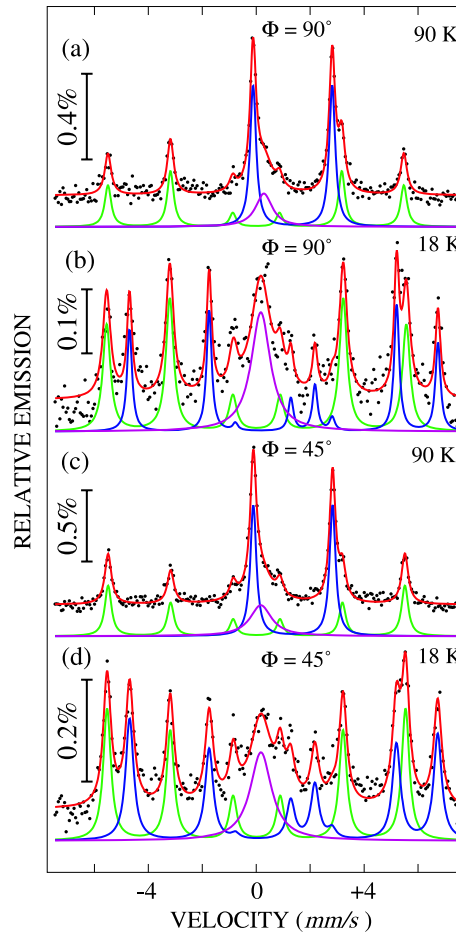


Figure 7.4: Mössbauer spectra of the Fe/FeF₂ interface sample (JF05) for an incident angle of $\Phi = 90^\circ$ ((a), (b)) and $\Phi = 45^\circ$ ((c), (d)). The spectra are measured in remanence at 90 K ((a), (c)) and 18 K ((b), (d)). The remanence was induced at room temperature with an applied field of 0.4 T before zero-field cooling to low temperature. Each of the spectra was least-squares fitted by three subpeaks. At 90 K ((a), (c)), the spectra were fitted by a sextet due to bcc-Fe film, a quadrupole doublet due to the FeF₂ substrate, and a central singlet (artifact from the channeltron holder). At 18 K ((b), (d)), the spectra were fitted by a sextet due to the bcc-Fe film, an octet obtained by considering the full Hamiltonian for FeF₂, and a central singlet (artifact from the channeltron holder).

For the measurements done with the channel electron multiplier, in some cases, due to technical difficulty, a weak central single line component has been obtained in the

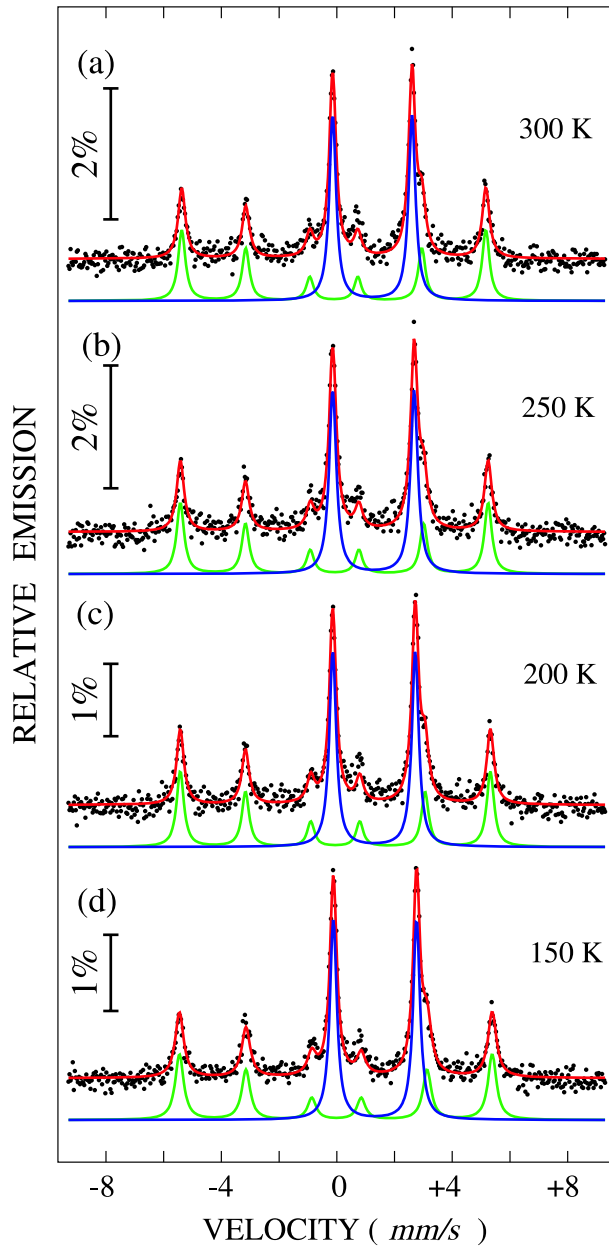


Figure 7.5: Mössbauer spectra of the Fe/FeF₂ interface sample (JF05) for an angle of incidence of $\Phi = 45^\circ$. The spectra were measured at different temperatures (300 K (a), 250 K (b), 200 K (c) and 150 K (d)) during zero-field cooling in remanence. The remanence was induced at room temperature with an applied field of 0.4 T. Each spectrum was least-squares fitted by a Zeeman sextet and a quadrupole doublet assigned to bcc-Fe and FeF₂, respectively.

CEM spectrum, which is an artifact originating from the stainless steel wall of the channeltron holder. This artifact was included in least-squares fitting the spectra, but it is of no significance for the results on the spin structure inferred from the CEMS spectra.

The geometry of the Mössbauer measurements is same as that given in Fig. 6.9 of Chapter 6. Fig. 7.4 shows the CEM spectra for the interface sample at an angle of

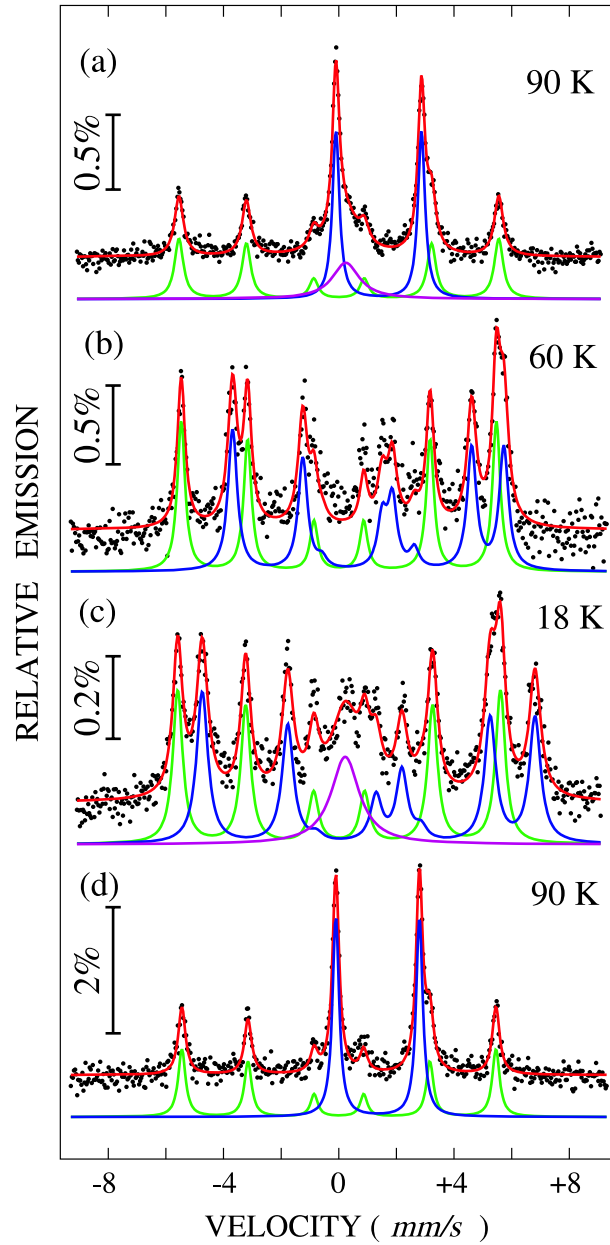


Figure 7.6: Mössbauer spectra of the Fe/FeF₂ interface sample (JF05) at an angle of incidence of $\Phi = 45^\circ$. The spectra were measured at different temperatures (90 K (a), 60 K (b) and 18 K (c)) during zero-field cooling in remanence. After zero-field cooling to 18 K, the sample was zero-field heated to 90 K (above T_N) and measured at that temperature (90 K (d)). The remanence was introduced at room temperature with an applied field of 0.4 T. Each spectrum above T_N (90 K ((a), (c))) was least-square fitted by a Zeeman sextet due to bcc-Fe and a quadrupole doublet due to FeF₂ (an additional broad, weak singlet in (a) is an artifact of the channeltron holder). The two spectra below T_N ((b), (c)) were fitted by a Zeeman sextet for bcc-Fe and an octet for FeF₂, by considering the full hyperfine-interaction Hamiltonian for FeF₂ (an additional broad singlet in (c) is an artifact of the channeltron holder).

incidence of $\Phi = 90^\circ$ ((a), (b)) and $\Phi = 45^\circ$ ((c), (d)) measured in remanence at 90 K

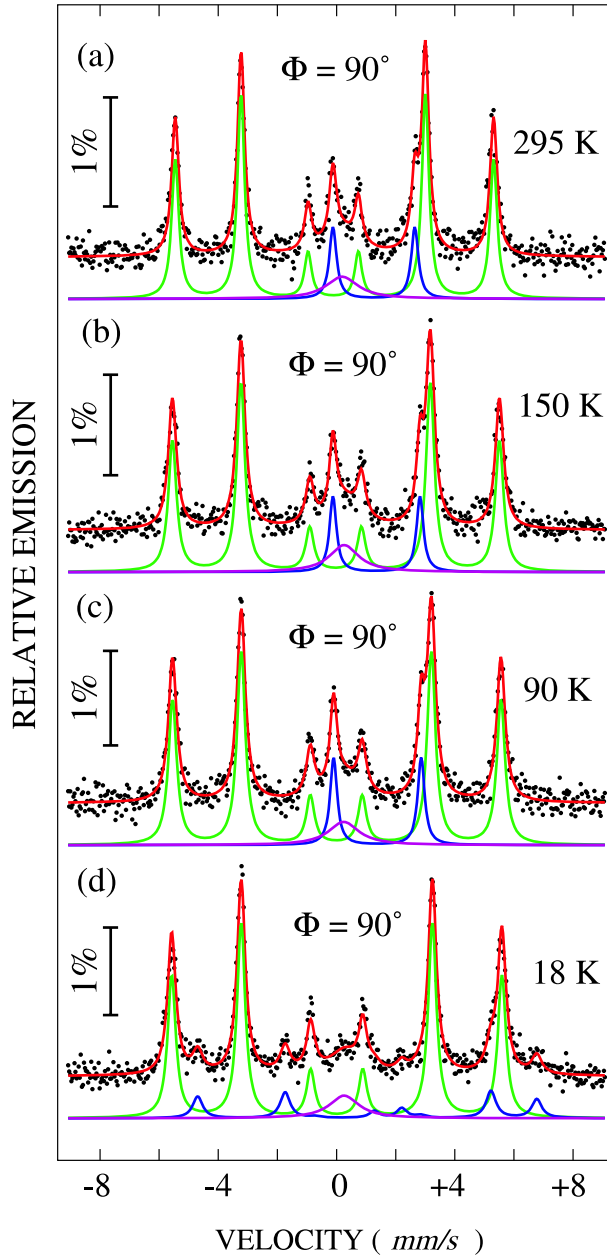


Figure 7.7: Mössbauer spectra of the Fe/FeF₂ center sample (MFEFF05) at a perpendicular incidence, $\Phi = 90^\circ$. The spectra were measured at different temperatures (295 K (a), 150 K (b), 90 K (c) and 18 K(d)) during zero-field cooling in remanence. The remanence was introduced at RT by an applied magnetic field of 0.4 T. Each spectrum at and above 90 K was least-squares fitted by a Zeeman sextet for bcc-Fe, a quadrupole doublet for FeF₂ and a central single line (artifact of the channeltron holder). The spectrum at 18 K was fitted by a Zeeman sextet for bcc-Fe, an octet for FeF₂ (by considering the full hyperfine-interaction Hamiltonian for FeF₂), and a singlet (artifact).

((a), (c)) and 18 K ((b), (d)). The spectra at 90 K ((a), (c)) were least-squares fitted by a sextet and a doublet. The sextet has been assigned to the bcc-Fe layer, and the quadrupole doublet to the contribution from the FeF₂ substrate layer, which is about 450 Å thick. The relative intensity of the FeF₂ doublet is surprisingly strong. As the

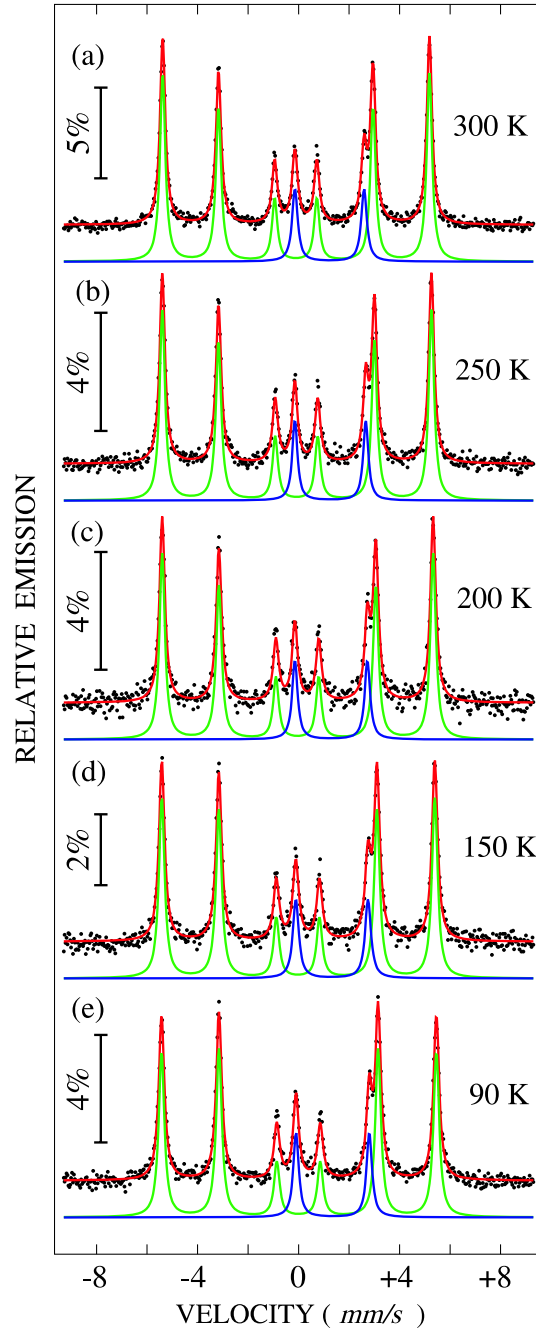


Figure 7.8: Mössbauer spectra of the Fe/FeF₂ center sample (MFEFF05) at $\Phi = 45^\circ$ incidence. The spectra were measured at different temperatures (300 K (a), 250 K (b), 200 K (c), 150 K (d) and 90 K (e)) during zero-field cooling in remanence. The remanence was introduced at RT by an applied magnetic field of 0.4 T. Each spectrum was least-squares fitted by a Zeeman sextet for bcc-Fe and a quadrupole doublet for FeF₂.

natural abundance of ⁵⁷Fe is about 2.14%, 450 Å natural FeF₂ corresponds to an effective ⁵⁷FeF₂ thickness of 9.6 Å or an effective ⁵⁷Fe thickness in FeF₂ of ~ 3 -4 Å. This is about one-third of the 10 Å thick ⁵⁷Fe probe layer in the bcc-Fe film. On the other hand, the measured spectral areas of the Mössbauer subspectra for bcc-Fe (~ 52 %) and

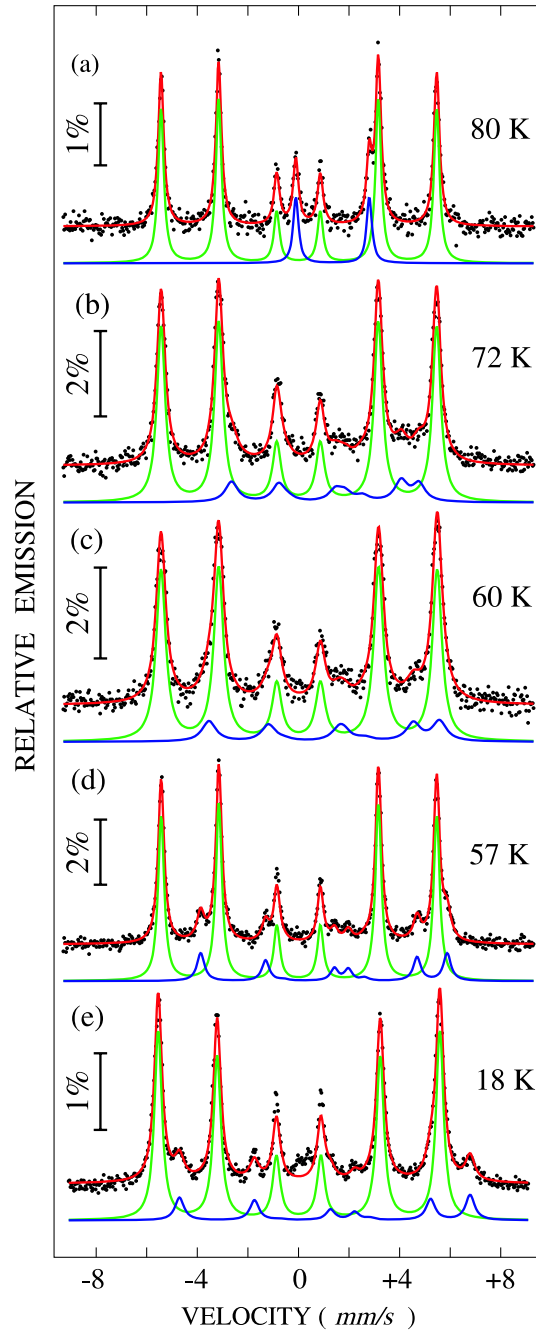


Figure 7.9: Mössbauer spectra of the Fe/FeF₂ center sample (MFEFF05) at $\Phi = 45^\circ$ incidence. The spectra were measured at different temperatures (80 K (a), 72 K (b), 60 K (c), 57 K (d) and 18 K (e)) during zero-field cooling in remanence (a continuation of the measurements of Fig. 7.8). The spectrum at 80 K is least-squares fitted by a Zeeman sextet for bcc-Fe and a quadrupole doublet for FeF₂. Each of the other spectra are least-squares fitted by a Zeeman sextet for bcc-Fe and an octet for FeF₂, by considering the full hyperfine-interaction Hamiltonian for FeF₂. (The central single line (not considered) in (e) is an artifact of the channeltron holder).

FeF₂ ($\sim 48\%$) are nearly equal. Assuming about equal Debye-Waller factors for bcc-Fe and FeF₂, this means that also the effective ⁵⁷Fe thickness of the ⁵⁷Fe probe layer and

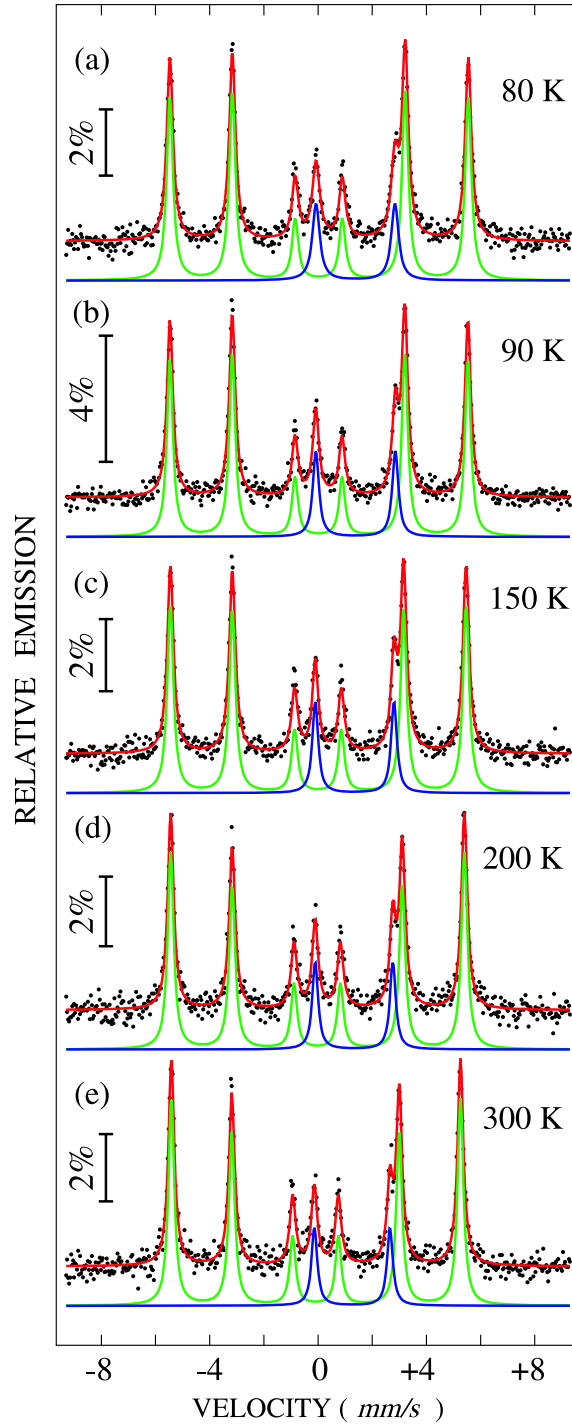


Figure 7.10: Mössbauer spectra of the Fe/FeF₂ center sample (MFEFF05) at $\Phi = 45^\circ$ incidence. The spectra were measured at different temperatures (80 K (a), 90 K (b), 150 K (c), 200 K (d) and 300 K (e)) during heating in remanence. The sample was first cooled to 5 K in remanence (induced by 0.4 T at RT). Each spectrum is least-squares fitted by a Zeeman sextet for bcc-Fe and a quadrupole doublet for FeF₂.

the FeF₂ substrate should be about equal, i.e. $\sim 3\text{-}4 \text{ \AA}$. This demonstrates that the real thickness of the ⁵⁷Fe probe layer is rather $\sim 3\text{-}4 \text{ \AA}$ and smaller than the nominal thickness of 10 \AA . The spectra measured at 18 K (Fig. 7.4 ((b), (d))) were fitted by

three subspectra. The central single line (artifact) originates from the stainless steel channeltron holder and will not be discussed further. The sextet (with isomer shift $\delta = 0.0$ mm/s, relative to Co⁵⁷ source (Rh matrix)) (blue) has been assigned again to the bcc-⁵⁷Fe layer. The other subspectrum showing eight lines is obtained by using the full Hamiltonian fitting procedure and is assigned to the contribution from the FeF₂ layer. The Mössbauer parameters obtained for the FeF₂ substrate, i.e., basically the obtained angles between the γ -ray, B_{hf} of FeF₂ and the electric field gradient (EFG), has been tabulated in Table 7.1. In Table 7.1, Φ = angle between x -axis and γ -ray, η = asymmetry parameter, α = RTH = angle between V_{zz} and B_{hf} , β = BEX = angle between V_{zz} and γ -ray, γ = GAX = angle between V_{xx} and γ -ray.

Table 7.1 *Asymmetry parameter and the angles between different components of EFG, B_{hf} and γ -ray obtained after least-squares fitting the low-temperature Mössbauer spectra of Fe/FeF₂ films. (Φ = angle between x -axis and γ -ray, η = asymmetry parameter, α = RTH = angle between V_{zz} and B_{hf} , β = BEX = angle between V_{zz} and γ -ray, γ = GAX = angle between V_{xx} and γ -ray)*

Sample	Temperature (K)	Φ	η	α	β	γ	FeF ₂ Area(%)
JF05 (Interface)	18	90°	0.4	90°	51° ± 5°	88° ± 10°	45
	18	45°	0.39	90°	50° ± 5°	65° ± 10°	50
	60	45°	0.4	90°	54° ± 5°	58° ± 10°	53
	18	45°	0.41	90°	58° ± 5°	58° ± 10°	53
MFEFF05 (Center)	18	90°	0.4	90°	50° ± 5°	90° ± 10°	17
	18	45°	0.4	90°	44° ± 5°	50° ± 10°	14
	57	45°	0.4	90°	47° ± 5°	44° ± 10°	17
	60	45°	0.4	90°	48° ± 5°	52° ± 10°	15
	72	45°	0.4	90°	58° ± 5°	65° ± 10°	16

CEMS measurements performed at decreasing temperatures between 300 K and 18 K in remanence at an incident angle of $\Phi = 45^\circ$ are shown in Fig. 7.5 and Fig. 7.6. Except for the last spectrum (Fig. 7.6 (d)) which is measured after zero-field heating the sample to 90 K (just after the 18 K measurement in remanence, Fig. 7.6 (c)), for all spectra above T_N (78 K) a quadrupole doublet was obtained for FeF₂, while below T_N , when the antiferromagnet orders, the quadrupole doublet is observed to split into an eight line spectrum as reported earlier [272]. The latter is fitted by considering the full hyperfine-interaction Hamiltonian for FeF₂. For the Fe layer, a sextet pattern has been fitted at all temperatures.

The spectra measured in remanence at $\Phi = 90^\circ$ at decreasing temperatures between 300 K and 18 K for the center sample (MFEFF05) are shown in Fig. 7.7. Fig. 7.8 and Fig. 7.9 displays the Mössbauer spectra for the same sample (MFEFF05) measured in the same way at decreasing temperatures between 300 K and 18 K at an angle of incidence of $\Phi = 45^\circ$. In order to check, whether the spin structure in the exchange-biased state is reversible with temperature or not, the Mössbauer spectra for the center sample were measured in remanence at $\Phi = 45^\circ$ during the process of zero-field heating from 18 K to 300 K (Fig. 7.10). This measurement was continued after the prior zero-field cooling experiments, hence the exchange bias effect has already been induced before. All the spectra were least-squares fitted by using the computer program 'NORMOS' [28, 29]. All the spectra above T_N were fitted by two subspectra, a sextet for the bcc-⁵⁷Fe layer

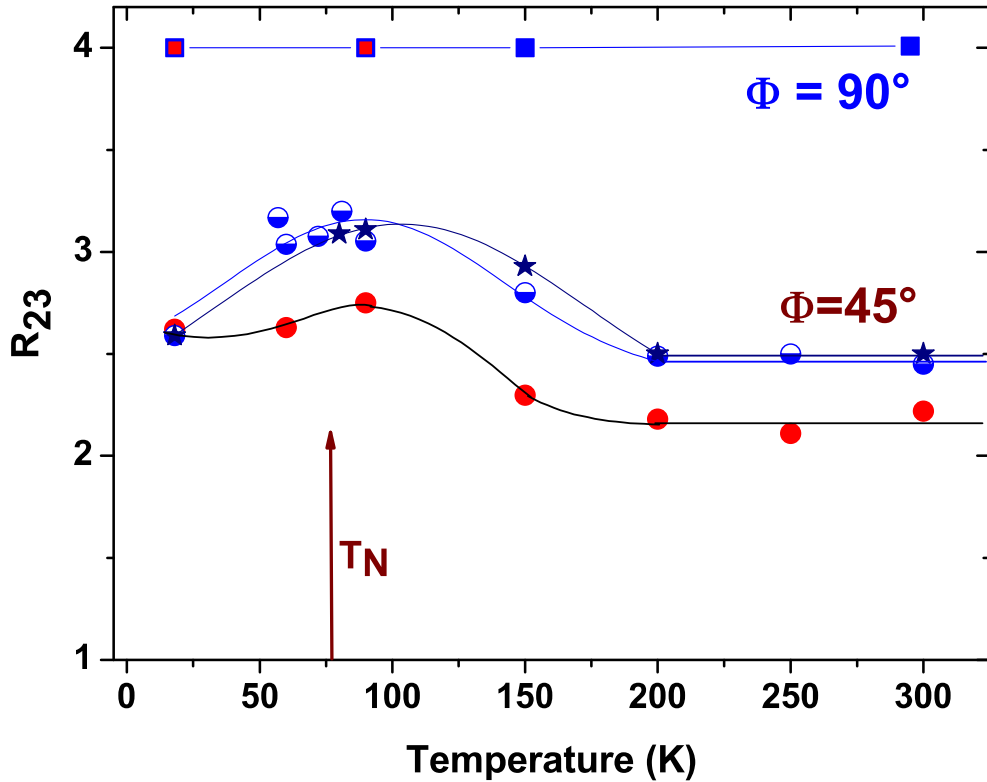


Figure 7.11: The measured T-dependence of the R_{23} ratio for the interface sample (JF05) (filled red circles and red squares) and the center sample (MFEFF05) (blue asterisks, blue squares and blue half-filled circles). The blue half-filled circles and red full circles were taken during the process of cooling in remanence and the asterisks are for heating in remanence. The circles and asterisks represent data for $\Phi = 45^\circ$, and the squares represent data for $\Phi = 90^\circ$. All lines are a guide for the eye. T_N indicates the Néel temperature of bulk FeF₂.

contribution and a quadrupole doublet for the FeF₂ contribution. For the spectra below T_N , in addition to the bcc-Fe sextet, the full hyperfine-interaction Hamiltonian of FeF₂ has been considered. The spectral parameters obtained from the fitting, i. e., angles between the γ -ray, B_{hf} and the components of the electric field gradient (EFG) for FeF₂, have been listed in Table 7.1.

All the R_{23} ratios of the bcc-Fe layer obtained from the fitting of all of these Mössbauer spectra are plotted in Fig. 7.11 versus the measurement temperature and also listed in Table 7.2. The squares (blue and red) corresponds to the measurements at $\Phi = 90^\circ$, with the blue squares representing the center sample and the red squares the interface sample (all measured in remanence at decreasing temperatures). Red-filled circles represent the $\Phi = 45^\circ$ measurements for the interface sample (measured in remanence at decreasing temperatures). Blue half-filled circles and blue asterisks represent the $\Phi = 45^\circ$ measurements for the center sample, measured in remanence at decreasing and increasing temperatures, respectively. The FeF₂ Néel temperature is also indicated in Fig. 7.11. The obtained isomer shifts and hyperfine fields for the Fe layer are shown in Fig. 7.12. The quadrupole splitting of the Fe subspectrum is always very close to 0.00 mm/s and

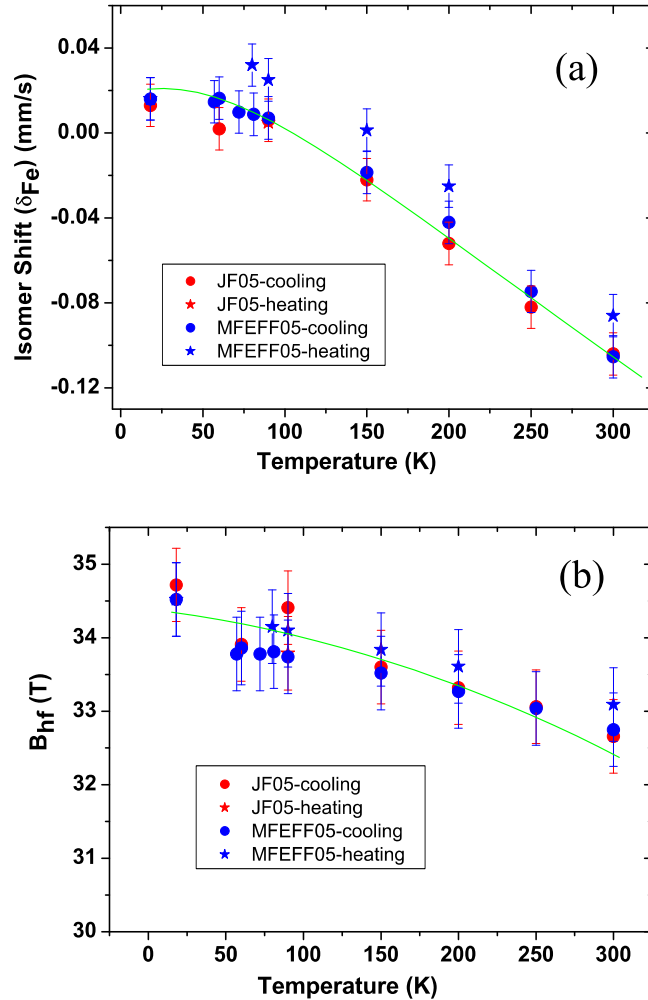


Figure 7.12: Temperature dependence of the isomer shift of bcc-Fe (δ_{Fe}) (a), and the magnetic hyperfine field of bcc-Fe (B_{hf}) (b), for the interface sample (JF05) and the center sample (MFEFF05). The filled red circles and red asterisks correspond to the spectra of JF05 during cooling and heating in remanence, respectively. The blue filled circles and asterisks correspond to the spectra of the center sample MFEFF05 during cooling and heating in remanence, respectively. All lines are a guide for the eye.

is not shown in the figure. These parameters suggest that the ^{57}Fe layer is clearly in the normal bcc-Fe phase.

The hyperfine interaction parameters (isomer shift, quadrupole splitting and magnetic hyperfine field) belonging to the FeF₂ substrate layer of the interface and center samples are shown in Fig. 7.13. The isomer shift (Fig. 7.13(a)), which is large for both samples, is following a normal Debye-like behavior versus T. The FeF₂ quadrupole splitting for both samples (Fig. 7.13(b)) is typical for Fe²⁺ (see Chapter 2 and Chapter 3) and quite high, and is slightly increasing with decreasing T down to 90 K. However, as discussed in Chapter 5, there is a decrease in the low temperature quadrupole splitting due to the spin-orbit coupling. The T-dependence of the FeF₂ hyperfine field (Fig. 7.13 (c)) shows a Brillouin-function-type behavior ($J = 1/2$).

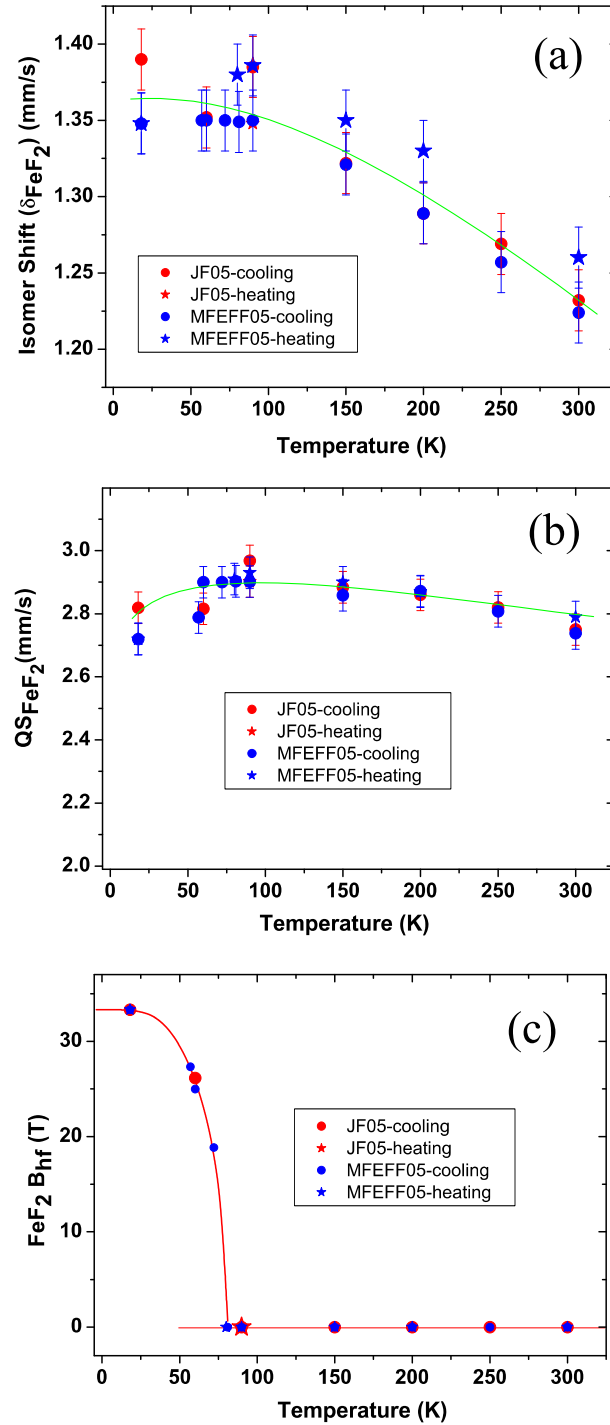


Figure 7.13: Temperature dependence of the FeF₂ isomer shift (δ_{FeF_2}) (a), quadrupole splitting (QS_{FeF_2}) (b), and magnetic hyperfine field ($FeF_2 B_{hf}$) (c) for the interface sample (JF05) and the center sample (MFEFF05). The filled red circles and red asterisks correspond to the spectra of JF05 during cooling and heating in remanence, respectively. The blue filled circles and asterisks correspond to the spectra of the center sample MFEFF05 during cooling and heating in remanence, respectively. The lines in (a) and (b) are guide for the eye. The solid line in (c) is a Brillouin ($J = 1/2$) function least-squares fit to the data points.

Table 7.2 *The Mössbauer spectroscopical parameters obtained after least-squares fitting the Mössbauer spectra of the Fe/FeF₂ interface sample (MFEMF01) (Int.) and Fe/FeF₂ center sample (MFEMF03) (Cent.). (T = measurement temperature, For all data given here, angle of incidence of the γ -ray relative to the film plane $\Phi = 45^\circ$, R_{23} (= R_{54}) = intensity ratio of the 2nd (or 5th) and 3rd (or 4th) Mössbauer line for the bcc-Fe layer. The temperatures were given in the same sequence as the CEMS measurement at zero-field.*

Sample	T (K)	R ₂₃
Int.	300 K	2.15
	250 K	2.11
	200 K	2.18
	150 K	2.297
	90 K	2.75
	60 K	2.63
	18 K	2.62
	90 K	2.46
Cent.	300 K	2.45
	250 K	2.50
	200 K	2.49
	150 K	2.80
	90 K	3.05
	81 K	3.20
	72 K	3.08
	60 K	3.04
	57 K	3.17
	18 K	2.59
	80 K	3.09
	90 K	3.11
	150 K	2.93
	200 K	2.50
300 K	2.50	

7.3.2 Temperature and depth dependent Fe spin structure

The R_{23} ratios (4.0) obtained from the Mössbauer spectra measured at different temperatures with $\Phi = 90^\circ$ for both samples (Fig.7.11) confirm again that (like in case of Fe/MnF₂ system) the Fe layers spins are oriented in the sample plane at all temperatures. The shape anisotropy is responsible for this in-plane alignment of spins. The in-plane Fe spin arrangement makes the case relatively simple in order to apply the models as discussed in Chapter 6.

As discussed in Chapter 5, FeF₂ has a significantly stronger magnetic anisotropy than MnF₂ both below and above the Néel temperature. Further, the interfacial exchange constant $J_{FM/AFM}$ of Fe/FeF₂ (-1.2 meV) is much larger than $J_{FM/AFM}$ of Fe/MnF₂ (-0.35 meV) [4, 5]. This strong anisotropy and interfacial exchange of FeF₂ influences the Fe layer spin structure in Fe/FeF₂ systems both above and below the Néel temperature. At about 300 K, the in-plane spin structure of the two samples (interface and center sample)

in the remanent state is not very different considering the difference in the R_{23} ratios ($R_{23} = 2.15$ for the interface sample and $R_{23} = 2.50$ for the center sample), as obtained from the Mössbauer spectra measured at $\Phi = 45^\circ$ incidence. By using the unidirectional spin distribution model, the spin rotation angles for these intensity ratios are $\varphi_0 = 40^\circ$ and 47° , respectively. Hence, the average direction of the Fe-layer spins at RT are at an angle of $\varphi_0 = \pm 40^\circ$ and $\pm 47^\circ$ from the remanence direction (the applied field direction or x -direction) for the interface and center sample, respectively. This demonstrates that, in the average, the Fe spins are close to the anisotropy directions ($\pm 45^\circ$) of the twinned FeF₂ layer even at RT. This effect may be related due to the large magnetic anisotropy of the FeF₂ layer and to Fe/FeF₂ interfacial exchange interaction even at 300 K. The small difference in the Fe spin direction for the interface and center sample at RT could be caused by a different domain structure, small anisotropy dispersion due to different microstructures of the two samples; further, the real Fe thickness of the two samples are probably somewhat different, as discussed in the previous section 7.3.1.

As the temperature is decreased from RT, with the samples in remanence, the R_{23} ratio of either samples first remains constant down to ~ 200 K (Fig. 7.11), and then starts to increase until it reaches a maximum for both samples at about 90 K ($R_{23} = 2.75$ (or $\varphi_0 = 52^\circ$) and 3.20 (or $\varphi_0 = 59^\circ$) for the interface and center sample, respectively, at 90 K). As the temperature is further decreased to $T < T_N$, R_{23} decreases, and, interestingly, Mössbauer spectra of both samples provide the same intensity ratio $R_{23} = 2.6$ at 18 K. It is striking that a similar value has been obtained for the Fe/MnF₂ system at 18 K (Table 6.1) also for the interface and center sample. This proves that the same Fe-layer spin structure is achieved at 18 K (in the exchange biased state), when the magnetic anisotropy of both antiferromagnets (MnF₂ and FeF₂) reaches strong values.

These results at different temperature will be discussed below. As the temperature is decreased, the same Fe spin structure as that at 300 K is retained down to 200 K (because the anisotropy of FeF₂ domains below remains almost unchanged) in both samples. As seen in Chapter 5, the anisotropy $\chi_{\parallel}-\chi_{\perp}$ of FeF₂ becomes stronger as the temperature decreases towards T_N , and has a maximum at about 90 K (Fig. 5.4). Upon further cooling the anisotropy ($\chi_{\parallel}-\chi_{\perp}$) changes sign (from positive above T_N to negative below T_N) at about 80 K (close to T_N), and then ($\chi_{\parallel}-\chi_{\perp}$) decreases sharply and reaches a large minimum value close to 0 K. This behavior of ($\chi_{\parallel}-\chi_{\perp}$) is reflected in the T-dependence of the Fe spin structure. Apparently, the interfacial Fe layer spin structure is influenced by the strong anisotropy of the AFM, because, upon cooling, the spins (or Fe domains) gradually rotate from their previous average position ($\varphi_0 = \pm 40^\circ$ or $\pm 47^\circ$ at $T \geq 200$ K) to $\varphi_0 = \pm 52^\circ$ and $\pm 59^\circ$ at ~ 90 K, away from the remanence direction. Upon further cooling to 18 K, the Fe-layer spins rotate back to $\varphi_0 = \pm 48^\circ$ for both, the interface and center sample. Again as seen (Fig. 6.17) for the center sample this temperature dependent rotation of Fe spins is reversible. This behavior of $R_{23}(T)$ or $\varphi_0(T)$ is phenomenologically similar to the temperature dependence of the FeF₂ magnetic anisotropy ($\chi_{\parallel}-\chi_{\perp}$) and, hence, the observed anomalous $R_{23}(T)$ behavior is believed to be related to the anisotropy of FeF₂. It is worthwhile mentioning in this context that also the T-dependence of the coercivity H_c of Fe/FeF₂ shows a maximum at T_N , as reported earlier [113, 183, 189].

The essential question is, how the AFM spins of FeF₂ in the paramagnetic state (T

$> T_N$) can influence the Fe layer spin structure. This aspect has been discussed by Grimsditch et al. [113] for the Co/FeF₂ system, which is supposed to behave similarly to our Fe/FeF₂ system. There is experimental evidence for antiferromagnetic ordering above the bulk Néel temperature T_N , when the AFM is exchange coupled to another magnetically ordered system [256]. Accordingly, Grimsditch et al. explained their experimental results above T_N "as due to short-range order induced in the antiferromagnet by the ferromagnet" [113]. These authors have determined the exchange bias H_E and the uniaxial magnetic anisotropy constants K_1 ($K_1 < 0$) and K_2 ($K_2 > 0$) of the ferromagnetic Co layer on a single crystalline FeF₂ film as a function of temperature between 30 K and 300 K. By postulating that interfacial exchange coupling between the FM (Co) and the AFM (FeF₂) persists above T_N , Grimsditch et al. [113] developed a model that describes $H_E(T)$ and $K_1(T)$, $K_2(T)$ over the whole temperature range, both above and below T_N . In context with the present results it is important to mention that $K_2(T)$ was found to have a maximum near T_N of FeF₂ and to decrease to zero over a wide T-range for temperatures $T < T_N$ and $T > T_N$ (up to ~ 200 K). Similarly, $K_1(T)$ was found to have a minimum near T_N and to increase rapidly to zero for temperatures $T < T_N$, but slowly for $T > T_N$; even at 300 K, nonzero values of K_1 were found [113].

By analogy with the results by Grimsditch et al. [113], I assumed that also for the present twinned Fe/FeF₂ system interfacial short-range local order is induced in antiferromagnetic FeF₂ by the ferromagnetic Fe film above the bulk Néel temperature T_N . I assume further that $K_1(T)$ and $K_2(T)$ have a similar functional dependence for Fe/FeF₂ and Co/FeF₂. However, as Grimsditch et al. [113] have pointed out, in a twinned FeF₂(110) system the first order anisotropies K_1 from the two twins should lead to an average isotropic magnetic energy term (independent of the angle θ between the Fe magnetization direction and one of the AFM easy axes direction), while the second-order anisotropies K_2 from the two twins should lead to a $[\sin^4\theta + \cos^4\theta]$ dependence of the magnetic energy term. The latter term causes the macroscopic FM easy axis to be 45° to the c-axes of twinned FeF₂, for instance, in a hysteresis loop measured by SQUID.

Now, the T-dependence of the R_{23} in Fig. 7.11 may be qualitatively explained in the following way. At high temperatures $T > T_N$, antiferromagnetic local short-range order is induced in the FeF₂ film by the ferromagnetic Fe film. The relative high magnetic anisotropy of FeF₂ causes the AFM spin direction of the short-range correlated regions to be along the c-axes (at $\pm 45^\circ$ with respect to the x -axis) of the two twin domains. In the remanent state of the Fe layer, even at 300 K, the Fe spins are coupled via interfacial exchange interaction to the short-range correlated AFM moments underneath and orient preferentially along the c-axes of the twin domains. Upon cooling, this situation persists down to ≈ 200 K; however, upon further cooling to about 90 K, as a result of the increase of the uniaxial anisotropy K_2 , the Fe spins are forced to orient towards the macroscopic FM easy direction which are at 45° relative to the c-axes, i.e., along the bisectors of the c-axes directions (or y -direction). One would expect that the Fe spins equally populate the latter two directions. However, as our experimental results in Fig. 7.14 and Fig. 7.15 demonstrates, at 90 K the Fe spins at remanence are rotated preferentially towards the y -axis (i.e., preferentially perpendicular to the x -axis or original external field direction). This effect might be the result of the remanent magnetization direction and the corresponding interfacial mean field, which in the average is oriented along the x -axis and thus breaks the four fold symmetry. The observed preferred perpendicular

Fe spin orientation at 90 K $>$ T_N is reminiscent of the model by Schulthess and Butler [217], where a spin-flop type of spin arrangement was predicted, although for $T < T_N$.

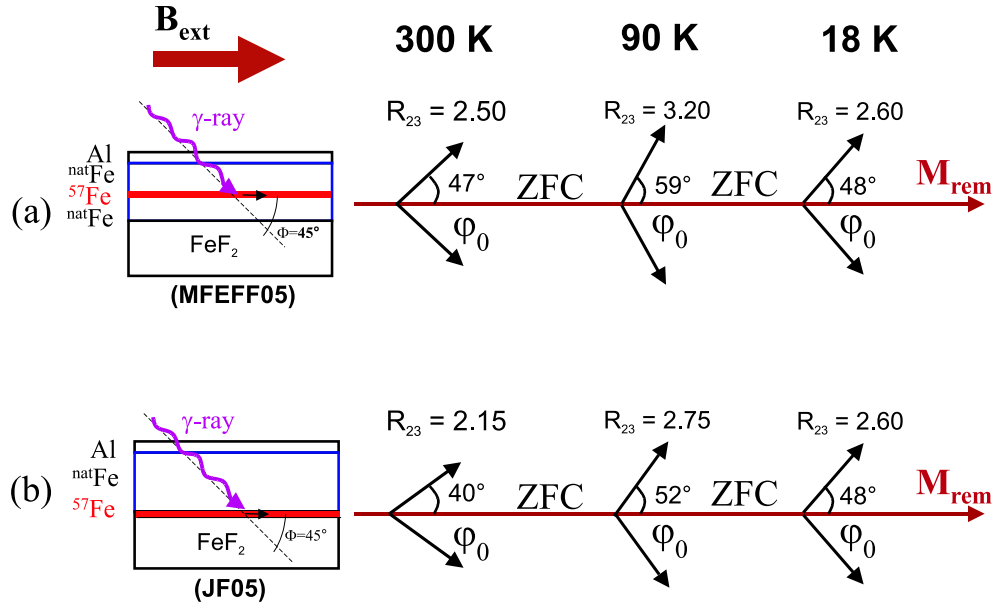


Figure 7.14: Remanent-state Fe spin rotation angles φ_0 according to the unidirectional distribution model, after zero-field cooling (ZFC) from room temperature to measurement temperatures of 300 K, 90 K or 18 K for the Fe/FeF₂-center sample (a) and the Fe/FeF₂-interface sample (b). Right-hand side: view onto the sample plane (xy -plane) showing the average Fe spin directions (black arrows) and the remanent magnetization (M_{rem}) direction (x -direction). Remanence was induced in the sample in an applied field of 0.4 T. The corresponding R_{23} ratios measured by CEMS are also given. Left-hand side: schematical cross-sectional view of the corresponding Fe/FeF₂ layered structure. The direction of the external field B_{ext} and the incident γ -ray are also indicated.

Upon further cooling to 18 K, the Fe-layer spins rotate back to $\varphi_0 = \pm 48^\circ$ for both the interface and center sample, which is close to the antiferromagnetic easy axes of pseudo-twin FeF₂. This decrease of R_{23} and the spin rotation by cooling from 90 K to 18 K can be understood as given below. Upon cooling, the anisotropy constant K_2 decreases to zero [113]. This causes the Fe layer spins to rotate away from the macroscopic easy direction (at 90 K) back to the ($\pm 45^\circ$)- AFM c -axes directions at 18 K. Further, as assumed by Grimsditch et al. [113], for FeF₂ or for other antiferromagnets below (but near) T_N , there exists a distribution of blocking temperatures (T_B) depending on the various properties of the film (such as crystallographic domain size, anisotropy of the antiferromagnet etc.). In our Fe/FeF₂ case, as the temperature is decreased below T_N , the Fe spins couple with the blocked antiferromagnetic spins (blocked along the easy axes, $\pm 45^\circ$) decreasing the average Fe spin direction below T_N . As suggested by Grimsditch et al. [113] the coupling with the blocked uncompensated AFM spins provides the small exchange bias observed in SQUID loops (as is given in section 7.4) at high temperatures close to T_N . The other spins coupled according to the anisotropy of the AFM give rise to the enhanced coercivity close to T_N . When the sample is zero-field cooled to very low temperature (e.g., 18 K in our case) all the domains are blocked and the uncompensated

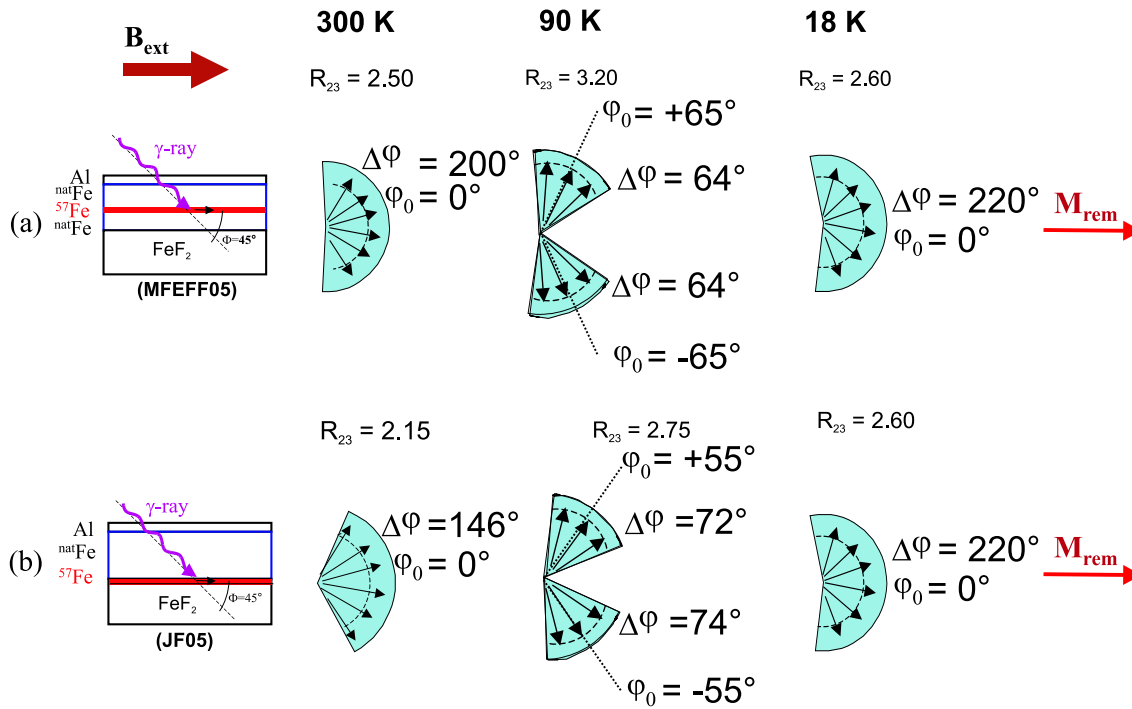


Figure 7.15: Remanent-state Fe spin fanning angles $\Delta\phi$ according to the step-shaped distribution model of the Fe/FeF₂ samples after ZFC from room temperature to measurement temperatures of 300 K, 90 K or 18 K for the center sample (a) and the interface sample (b). Right-hand side: view onto the sample plane (xy -plane) showing the Fe spin directions (black arrows) and the remanent magnetization (M_{rem}) direction (x -direction). The corresponding R_{23} ratio measured by CEMS, the angle ϕ_0 used for the modeling and the obtained fanning angles $\Delta\phi$, are also given. Left-hand side: schematic cross-sectional view of the corresponding Fe/FeF₂ layered structure. The direction of B_{ext} and the incident γ -ray are also displayed.

spins are frozen along the easy axes direction $\pm 45^\circ$. The coupling of the Fe spins to these frozen uncompensated AFM spins, which gives rise to exchange bias, decreases the average spin orientation angle at 18 K in comparison to that at 90 K.

In the temperature dependence of R_{23} for the center sample measured at remanence at increasing temperatures from 18 K, the Fe-layer spins follow the same path or rotation angles as those obtained during the zero-field cooling measurements. This is clear from the obtained R_{23} ratio in Fig.7.11(blue asterisks). This suggests that the Fe spin structure is reversible during cooling and heating of the sample. The reversibility of R_{23} may be inferred from the above discussion that, as the sample is zero-field heated through T_N (or T_B), the uncompensated AFM spins starts to defreeze and the coupling of the Fe is then influenced by the AFM (high temperature) anisotropy. The Fe spins are then forced to follow the same path as they have taken during cooling.

As described in Chapter 6, the unidirectional model and the step-shaped distribution model (described in Chapter 5, section 6.4.2) may be used in the case of Fe/FeF₂ to obtain the spin rotation or fanning angles, respectively, from the obtained Mössbauer line intensity ratio R_{23} . The spin rotation angles ϕ_0 obtained from the unidirectional

model for three different temperatures, 300 K, 90 K and 18 K are shown in Fig. 7.14. For temperatures $T = 300$ K, 90 K and 18 K, $\varphi_0 = 40^\circ$, 52° and 48° were obtained for the interface sample, and $\varphi_0 = 47^\circ$, 59° and 48° were obtained for the center sample, respectively, for the average Fe spin orientation with respect to the external field direction. The corresponding angles obtained for the spin fanning are demonstrated in Fig. 7.15. At 300 K, 90 K and 18 K, Fe spin fanning angles of $\Delta\varphi = 200^\circ$ ($\varphi_0 = 0^\circ$), 64° ($\varphi_0 = 65^\circ$) and 220° ($\varphi_0 = 0^\circ$) were obtained for the center Fe/FeF₂ sample, and $\Delta\varphi = 146^\circ$ ($\varphi_0 = 0^\circ$), 72° ($\varphi_0 = 55^\circ$) and 220° ($\varphi_0 = 0^\circ$) were obtained for the interface Fe/FeF₂ sample, respectively.

7.3.3 FeF₂-layer spin structure and the EFG components

As discussed in Chapter 5, the FeF₂ spin structure is clearly understood from neutron scattering [263] and Mössbauer spectroscopical results [273] on single crystals. The Fe atoms are located at the corners and at the body center of the tetragonal unit cell. Below $T_N = 78$ K, the Fe spins order antiferromagnetically with the Fe spins either parallel or antiparallel to the *c*-axis. From studies of the growth of the FeF₂ film on MgO(100) it is clear that FeF₂ films grow quasi-epitaxially with the *c*-axes in the plane of the film. The compensated FeF₂(110) plane is parallel to the MgO(100) surface. The FeF₂ film is twinned in two directions, with FeF₂[001]|| MgO[110] and FeF₂[001]|| MgO[1 $\bar{1}$ 0]. In other words, the spin axes of the FeF₂ film are perfectly in the plane and are along the MgO[110] and MgO[1 $\bar{1}$ 0] directions.

The large asymmetry parameter ($\eta = 0.4$) for FeF₂ obtained from the fitting of the Mössbauer spectra of the Fe/FeF₂ bilayers confirms the difference in the magnitude of the EFG components (V_{xx} , V_{yy} and V_{zz}). Point-charge calculation show that the strongest component (V_{zz}) should be normal to the FeF₂(110) plane, i.e., V_{zz} should be normal to the film, but the electronic configuration of the Fe atom itself can change this situation substantially [273]. On the other hand, according to the point symmetry of FeF₂, the smallest component of EFG (V_{xx}) should be along the spin axis of the crystal, i.e., V_{xx} should be along the *c*-axis, which is in the plane of the film. The other two components, V_{zz} and V_{yy} , should be along the two other crystal axes, i.e., along the *a* and *b* axes of FeF₂, which are at 45° to the film normal. However, this indicates that the two components V_{yy} and V_{zz} may be equal in magnitude.

The fitting results of the FeF₂ subspectra for the two different samples and at different temperatures with two measurement geometries ($\Phi = 90^\circ$ and $\Phi = 45^\circ$) have been used to confirm the directions of the EFG components. The typical angles obtained between the γ -ray, B_{hf} , and V_{xx} , V_{yy} and V_{zz} are shown in Fig. 7.16 for the typical γ -ray angles of incidence of $\Phi = 90^\circ$ (Fig. 7.16(a)) and $\Phi = 45^\circ$ (Fig. 7.16(b)). The obtained angles for the FeF₂ films (within the error bars shown in Table 7.1) are in fair agreement with those predicted from point symmetry arguments for bulk FeF₂ [272].

7.4 SQUID magnetometry results

The hysteresis loops of the Fe/FeF₂ interface sample (JF05), measured at increasing temperatures between 10 K and 80 K (after field-cooling the sample to the measurement

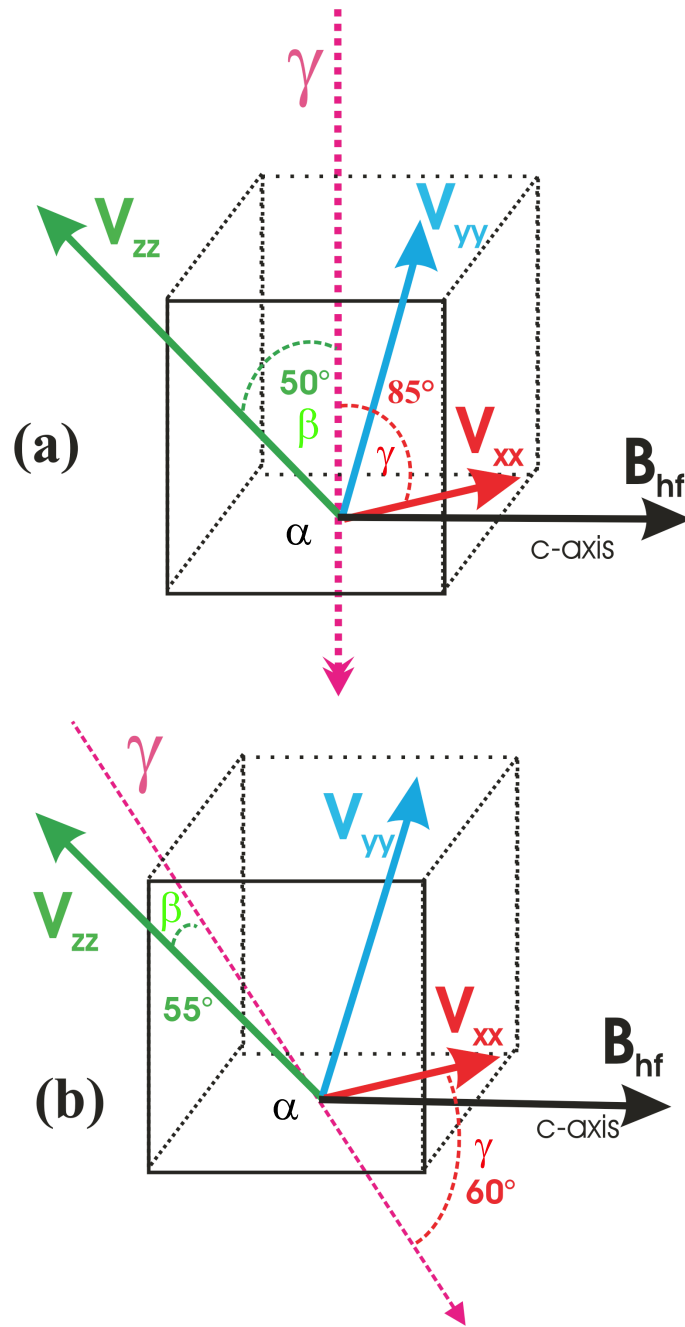


Figure 7.16: Schematic diagram of the directions of the EFG components (V_{xx} , V_{yy} and V_{zz}) in the FeF₂ film. The angles obtained from the fitting of the Mössbauer spectra (Fig. 7.4) for the FeF₂ film in the Fe/FeF₂ interface sample (JF05) for $\Phi = 90^\circ$ (a) and $\Phi = 45^\circ$ (b) are also shown. Φ = angle of incidence relative to the x -axis (making an in plane angle of 45° with the B_{hf} direction), α = angle between V_{zz} and B_{hf} , β = angle between V_{zz} and γ -ray, and γ = angle between V_{xx} and γ -ray. The unit cell for one of the FeF₂ twin directions is also indicated.

temperature in a field of 2 kOe directed along the MgO[100] direction), are shown in Fig. 7.17 (a). The obtained exchange bias field (H_E) and coercive field (H_C) are plotted versus temperature in Fig. 7.17 (b). The magnitude of the exchange bias field (the

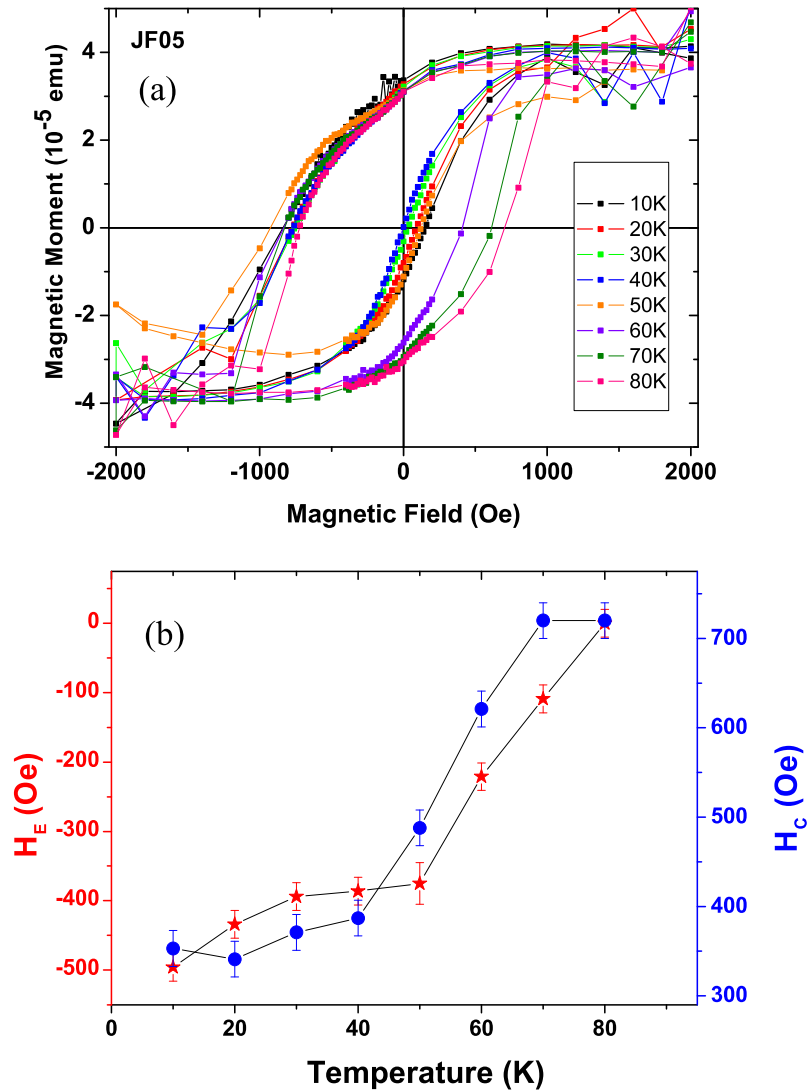


Figure 7.17: (a) The SQUID magnetization loops for the Fe/FeF₂ interface sample (JF05) at various temperatures. (b) Temperature dependence of the exchange bias field (H_E) and coercivity (H_C) of the interface sample obtained (a). Prior to the measurement the sample was field cooled from 150 K to the measurement temperature of 80 K, and then the SQUID loops were taken during cooling further in an applied field of 2 kOe and measuring the hysteresis loops. The cooling field was applied along MgO[100], i.e., between the two FeF₂ pseudo-twin directions of the sample.

loop shift) decreases as the temperature is increased. Simultaneously H_C increases with rising of T . The observed temperature dependence of H_E and H_C (which has a maximum at about $T_N = 78$ K of FeF₂) is in fair agreement with that in previous reports [183, 188].

The hysteresis loops of the Fe/FeF₂ center sample (MFEFF05), measured at increasing temperatures between 10 K and 80 K (after field cooling to the measurement temperature in a field of 2 kOe along MgO[100]), are shown in Fig. 7.18 (a). The temperature dependence of H_E and H_C (obtained from Fig. 7.18 (a)) is shown in Fig. 7.18 (b). The T -dependence of H_E and H_C agrees with that of previous reports [183, 188]. The increase in coercivity at 10 K is accounted for by considering that the sample was field

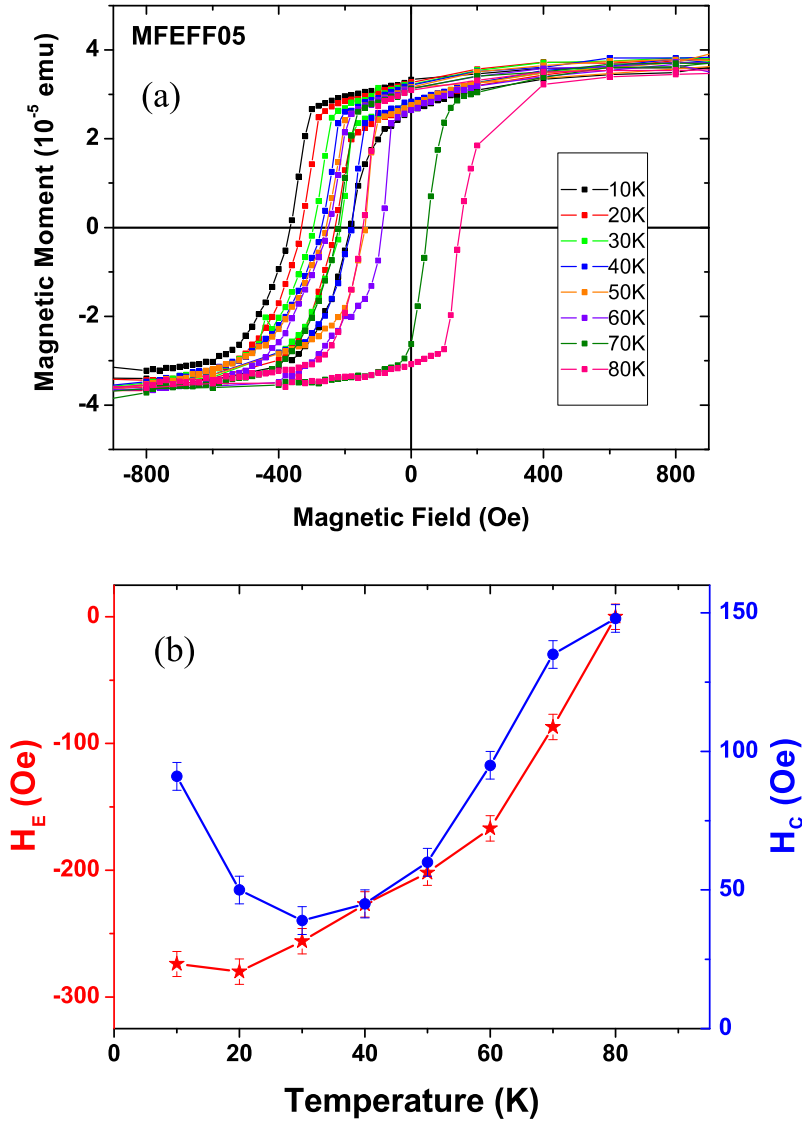


Figure 7.18: (a) The SQUID magnetization loops for the Fe/FeF₂ center sample (MFEFF05) at various temperatures. (b) Temperature dependence of the exchange bias field (H_E) and coercivity (H_C) of the center sample obtained from (a). Prior to the measurement the sample was field cooled from 150 K to the measurement temperature of 80 K and then the SQUID loops were taken during cooling further in an applied field of 2 kOe and measuring the hysteresis loops. The cooling field was applied along MgO[100], i.e., between the two FeF₂ pseudo-twin directions of the sample.

cooled with the field applied along the MgO[100] direction, i.e., between the two twin directions. According to literature [183, 188] the coercivity varies differently for different cooling field direction. Cooling an Fe film grown on single crystalline FeF₂ with the field applied along the spin axis of the AFM (*c*-axis) a clear maximum at about T_N has been observed [183]. If the cooling field was perpendicular to the spin-axis of the AFM, the coercivity had a maximum at very low temperature (10 K). However, in twinned samples, if the field is applied between the twin directions (like in our case) the effective field has a component parallel and perpendicular to the spin-axis of the AFM. This causes a competition between the above two behaviors resulting in an additional increase of H_C

at very low temperatures (10 K). There is a hint for such a behavior also in the interface sample (Fig. 7.18 (b)), although it is small and within the experimental uncertainty.

7.5 Conclusions for the Fe spin structure in Fe/FeF₂

Two exchange-biased Fe/FeF₂ samples with a 10-Å thick ⁵⁷Fe probe layer at or 35 Å away from the Fe/FeF₂ interface were deposited on MgO(001) substrates by electron beam evaporation and characterized by XRD, SQUID magnetometry and CEMS. By SQUID magnetometry, we have confirmed the presence of exchange bias in the two samples. The FeF₂(110) films have a twinned crystallographic structure with the *c*-axes at ± 45° relative to MgO[100] direction. Mössbauer spectroscopy provided the components of the electric field gradient (EFG) tensor and their direction with respect to the magnetic hyperfine field direction in the antiferromagnetic FeF₂ film. The T-dependence and the depth dependence of the Fe spin structure was inferred by CEMS via the line intensity ratio R₂₃. Prior to the CEMS measurements, remanence was induced in the samples by an in-plane external field of 0.4 T applied along the MgO[100] direction. The remanent-state Fe spin structure at different temperatures has been obtained for both samples by CEMS, after zero-field cooling the samples in remanence from room temperature (RT) to a range of temperatures extending down to 18 K (below T_N).

According to the CEMS results the Fe spins always lie in the sample plane. A slightly different remanent-state Fe spin structure of the interface and the center samples was observed at a particular temperature (e.g., at 300 K), very likely due to different magnetic anisotropy dispersion in the two Fe films, which could be related to the microstructural difference of the two samples, as observed by XRD. It is remarkable that even at 300 K (> T_N) the average Fe spin direction in both samples at remanence is close to the ± 45° *c*-axes directions of the twinned FeF₂ film, i.e., ± 45° away from the direction of the applied field used to induce remanence. (During zero-field cooling in remanence, a continuous in-plane rotation of the Fe spins away from the remanent magnetization direction occurs in both, the interface and the center sample.) As the temperature is decreased from RT the R₂₃ ratio (i.e., the Fe spin structure) of both samples remains almost constant down to 200 K, and then starts to increase and reaches a maximum at about 90 K. As the temperature is further decreased to 18 K the R₂₃ ratio again decreases for both samples, but, surprisingly, at 18 K the R₂₃ ratio (i.e., the Fe spin structure) of the two samples are found to be equal.

The average Fe spin rotation angle φ_0 or fanning angle $\Delta\varphi$ were obtained from the Mössbauer line intensity ratio R₂₃ by using the unidirectional or step-shaped distribution (spin fanning) model for the in-plane angular Fe spin distribution. Upon zero-field cooling from ~ 200 K to ~ 90 K, a continuous rotation of the Fe spins away from the direction of the *c*-axes of the FeF₂ twins is observed overshooting the (± 45°)- *c*-axes by an angle of about 15° ($\varphi_0 \approx 60^\circ$). It is suggested that this effect is due to the influence of remarkable the high-temperature magnetic anisotropy of FeF₂, combined with short-range order induced in FeF₂ by the Fe film above T_N. Further decrease of the temperature from 90 K to 18 K results in a decrease of the Fe spin rotation or fanning angles back to the (± 45°) AFM easy axes directions. This effect could be related to the disappearance of the second order anisotropy K₂ of the FeF₂ at low T. This decreasing

Fe spin rotation (or spin fanning) upon ZFC from 90 K to a temperature below T_N suggests that the Fe spins couple to the AFM spins at the interface, and the interfacial exchange interaction change the spin structure of the Fe layer in the exchange-biased state. Both, interface and center samples show equal Fe spin rotation or fanning angles (with Fe spins aligned close to the easy ($\pm 45^\circ$) axes of the FeF₂ pseudo-twins) in the remanent state at 18 K due to exchange coupling of Fe spins with the AFM spins and the strong antiferromagnetic anisotropy of FeF₂. Upon zero-field heating from a temperature below T_N to a temperature above T_N , the memory of the low temperature spin structure is not retained (maybe due to the strong high-temperature anisotropy of FeF₂). It was found that the Fe spin structure is reversible with temperature by zero-field cooling to $T < T_N$) and subsequently zero-field heating to $T > T_N$. No memory effect in the Fe spin structure was observed for Fe/FeF₂, contrary to the case of Fe/MnF₂.

Chapter 8

Nuclear Resonant Scattering: Fe Spin Structure in Fe/MnF₂

8.1 Introduction

In exchange biased systems, the ferromagnetic spin structure is closely associated with the exchange bias effect. As discussed in the previous chapters the magnitude of exchange bias field, H_E , and the coercivity in Fe/MnF₂ is higher for smaller thickness of the Fe layer. Although exchange bias is well known as an interfacial effect, the depth dependent variation of the exchange bias and its associated effects has not been observed macroscopically or microscopically by any of the present experimental methods. In addition to the unexplored depth dependent variations, most theoretical models neglect the possibility of a varying FM spin structure at different depths in the Fe layer. An exception is the model by Kiwi et al. [3–5], as discussed in Chapter 4, which predicts the possibility of an applied-field-induced incomplete domain wall (spiral-type spin structure) in the ferromagnet, starting at the FM/AFM interface, while the first few monolayers of the AFM at the interface freeze in a canted spin structure. Such a non-collinear spin structure is typically observed in spring magnets.

Another important aspect associated with exchange bias is the mechanism of magnetization reversal. According to polarized neutron reflectometry (PNR) investigations by Fitzsimmons et al. [7, 99, 100] and Leighton et al. [156] on twinned Fe/MnF₂ and Fe/FeF₂, when the cooling field was applied along the bisector between the AFM twins, the reversal for the left branch of the hysteresis loop occurs via Fe spin rotation, while the right branch occurs via domain formation and propagation. Further, these results are in agreement with the asymmetry observed in the magnetoresistance measurements by Krivorotov et al. [8]. By contrast, the PNR study on the Co/CoO system by Radu et al. [9, 201, 202] demonstrates that domain nucleation and propagation in that system is associated with the left branch of the hysteresis loop, where an asymmetry exists, and domain rotation for the right branch of the hysteresis loop, where no asymmetry appears.

The study of the unexplored depth dependence of the Fe layer spin structure is challenging because of the difficulties encountered by experimental techniques to investigate buried interfaces. Only a few experimental methods like X-ray magnetic circular dichroism (XMCD)[190], PNR [98], CEMS [167] and nuclear resonant scattering (NRS) [42] of synchrotron radiation can be used in order to explore the interfacial ferromagnetic

spin structure. Moreover, in principle, the depth dependent spin structure in the FM layer can be investigated by CEMS and NRS. The Fe spin structure inferred by CEMS is described in the previous chapters. Both, CEMS and NRS are methods based on hyperfine interactions. However, the important difference between CEMS and NRS is that the investigation of the Fe layer spin structure with near-monolayer resolution by CEMS needs long measurement times and, usually, only weak external fields may be applied because of the emitted electrons. On the other hand, because of the availability of third-generation synchrotron radiation, NRS drastically shortens the measurement times and allows application of external fields. Further, NRS offers spatial resolution by focussing of the X-ray beam.

A brief description of the NRS technique was given in Chapter 3. In this chapter the mechanism of magnetization reversal (MR) in both branches of the hysteresis loop will be discussed according to the observed NRS results. The NRS investigation of the depth dependent Fe layer spin structure during MR will also be described. The temperature dependent spin rotation mechanism will be analyzed. The observed Fe spin structure at remanence after switching off the applied field at different temperatures will also be explained.

8.2 Sample preparation and characterization

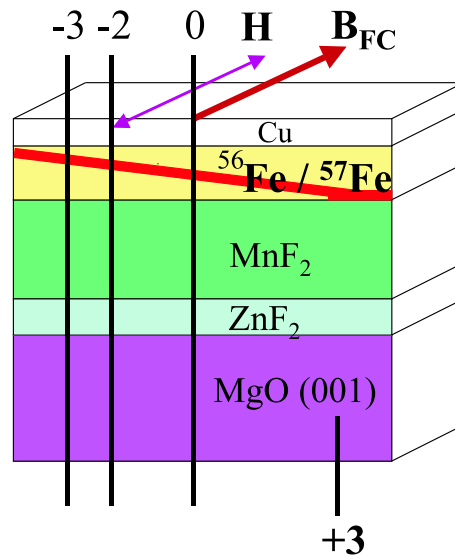


Figure 8.1: Schematic diagram of the Fe/MnF₂ wedge sample prepared on the MgO(100) substrate. The 10 Å ⁵⁷Fe probe layer is deposited on a ⁵⁶Fe wedge and covered by a second reverse ⁵⁶Fe wedge as shown. The length of the sample was 8 mm. The vertical lines represent the lateral measurement beam positions (in mm) from the center (position '0'). The lateral positions -3, -2, and 0 correspond to distances of 60 Å, 48 Å and 24 Å, respectively, from the Fe/MnF₂ interface.

An exchange biased Cu/Fe/MnF₂/ZnF₂/MgO(001) sample was prepared [52, 55] by sequential electron beam evaporation. In this sample a 160 Å ZnF₂ buffer layer was deposited in order to relax the large (8%) lattice mismatch between the MgO substrate

and MnF₂. The typical thicknesses of the Cu, Fe and MnF₂ layers are 30 Å, 80 Å and 520 Å, respectively. Out of the 80 Å Fe layer, a 10 Å ⁵⁷Fe probe layer was deposited on an isotopically enriched ⁵⁶Fe wedge and again covered by another inverse ⁵⁶Fe wedge, making the Fe layer homogenous. Hence, along the wedge, the 10 Å thick ⁵⁷Fe probe layer is located at different distances from the Fe/MnF₂ interface. The schematic structure of the interface sample is given in Fig. 8.1. Prior to deposition, the MgO(001) substrate was heated to 450 °C for 15 min and then cooled to 200 °C for ZnF₂ deposition. The base pressure of the system was 3×10^{-8} mbar and the pressure during MnF₂ deposition was around 6×10^{-7} mbar. The deposition temperatures and deposition rates for Cu, Fe, MnF₂ and ZnF₂ layers were 150 °C, 150 °C, 325 °C and 200 °C, and 0.5 Å/s, 1 Å/s, 2 Å/s and 2 Å/s, respectively. The thickness of the fluoride layers were monitored by calibrated quartz crystal oscillations, and the Fe layer thickness during deposition was monitored by optical sensors.

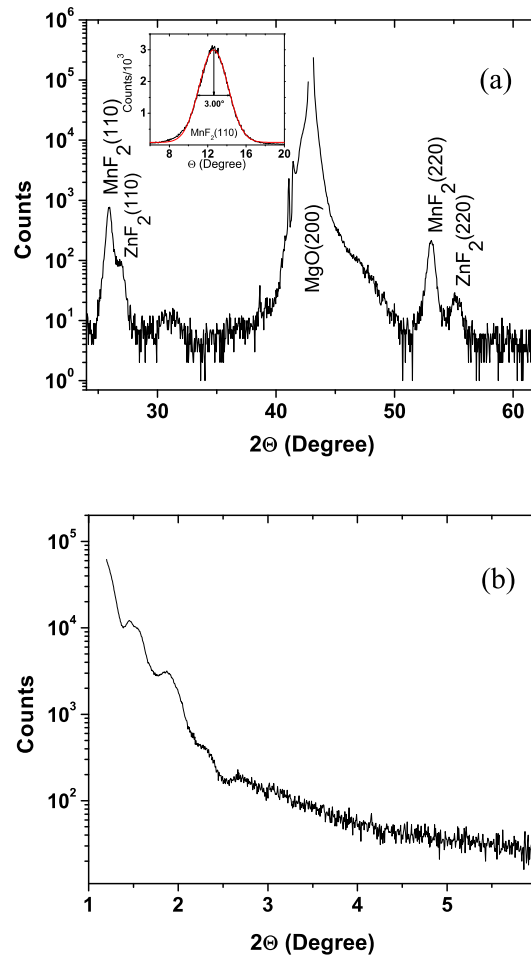


Figure 8.2: X-ray diffraction pattern of the Fe/MnF₂ wedge sample (MXJM01). The epitaxial nature of the MnF₂ film is observed, with the c-axes [001] in the plane of the film. The FWHM of the MnF₂(110) peak (rocking curve, insert) is about 3.00°. The red curve in the insert is the least-squares fitting to the measured rocking curve data of the MnF₂(110) peak. (b) Small angle XRD pattern of the same sample (MXJM01).

After deposition the structural characterization of the samples was performed by

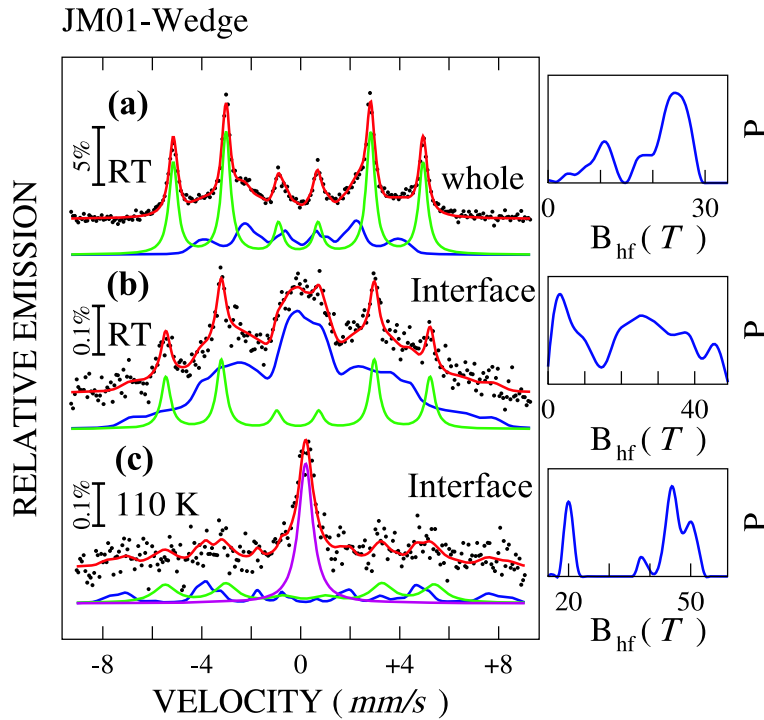


Figure 8.3: CEM spectra of the Fe/MnF₂ wedge sample (MXJM01) taken at RT (a), (b) and at 110 K (c). The spectra for the whole sample surface is shown in (a) and only for one third of the sample surface towards the interface is shown in (b) and (c). All spectra are least-squares fitted by assuming a Zeeman sextet with sharp Lorentzian lines assigned to bcc-Fe and a component with a hyperfine field distribution in order to account for the intermixing at the interface. The central broad single line in (c) is the artifact of the channeltron holder used for the measurement.

high-angle and small angle X-ray diffraction (Cu-K_α radiation, $\lambda = 1.5418 \text{ \AA}$) [53]. The high-angle X-ray diffraction pattern for the wedge sample (MXJM01) is shown in Fig. 8.2 (a) and the small angle X-ray diffraction pattern in Fig. 8.2 (b). The high angle X-ray diffraction pattern confirms the epitaxial nature of the film with MnF₂(110) in the plane of the sample. The relatively sharp rocking curve (inset in Fig. 8.2 (a)) of the MnF₂(110) reflection has a full width at half maximum (FWHM) of about 3.0°. This demonstrates the good epitaxy quality of the sample. The small-angle XRD suggests good homogeneity of the MnF₂ and Fe layer. However, it is worth to note that, as discussed in the previous chapter, all the MnF₂(001) layers are twinned epitaxial layers.

The sample was also characterized by conversion electron Mössbauer spectroscopy (CEMS). Typical Mössbauer spectra of the sample (MXJM01) taken at room temperature (RT) or 110 K are given in Fig. 8.3. The spectra clearly show a six-line pattern superimposed to a second component with a distribution of hyperfine fields, $P(B_{hf})$. The spectra have been least-squares fitted by a sextet ($B_{hf} = 32.8 \text{ T}$) and a distribution of hyperfine fields. $P(B_{hf})$ is shown at the right to the spectra. The dominant sextet is unambiguously assigned to the bcc-Fe layer, and the distribution of hyperfine fields, which has a peak at about 26 T, is attributed to the effect of chemical intermixing at the Fe/MnF₂ interface. The intensity ratio between the 2nd and 3rd line (R_{23}) of the bcc-Fe

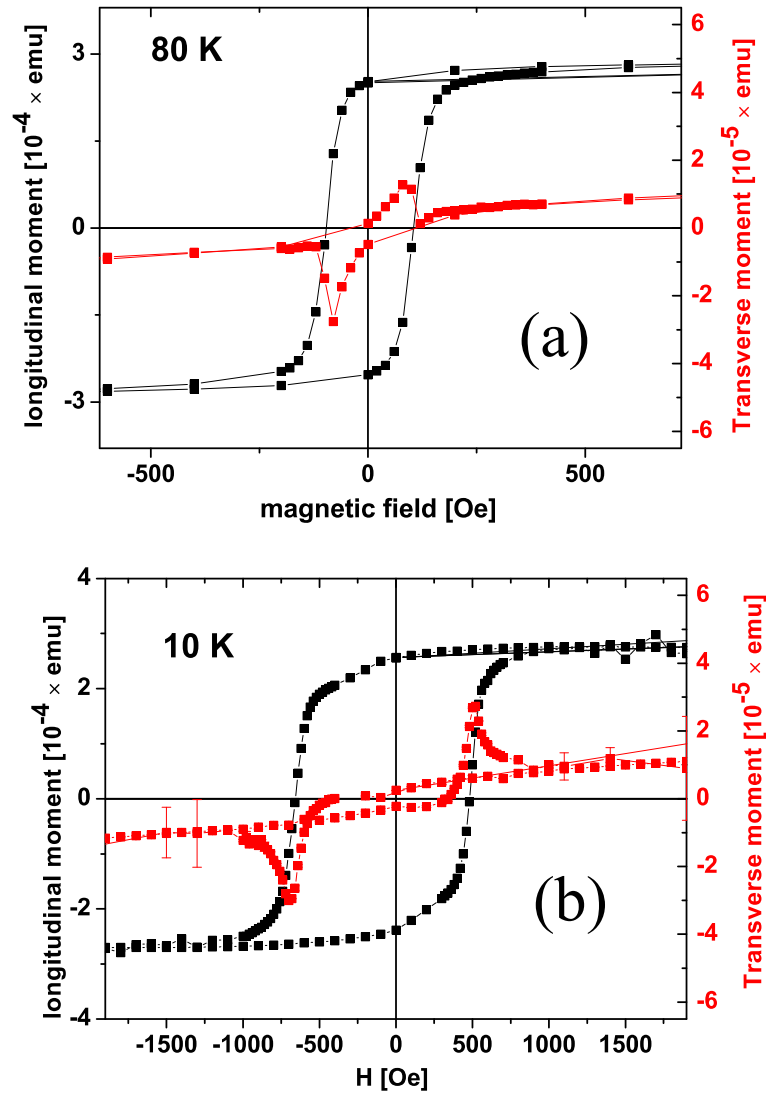


Figure 8.4: Vector SQUID magnetization loops for the Fe/MnF₂ wedge sample (MXJM01) measured at 80 K (a) and 10 K (b). The longitudinal and transverse magnetic moments are shown in black and red color, respectively. The cooling field and the sweeping field were applied along the MgO[001] direction, i.e., at 45° relative to the AFM easy axes direction.

Mössbauer sextet is 4.0. This demonstrates that the Fe layer spins are oriented in the plane of the sample. The spectrum of Fig. 8.3 (a) was taken from the whole sample. In the case of Fig. 8.3 (b) and (c) only one third of the sample surface (close to the Fe/MnF₂ interface) was free, while the rest was covered by an Al foil. Therefore, in case of Fig. 8.3 (b) and (c) the interfacial spectral contribution is enhanced relative to Fig. 8.3 (a). The spectra demonstrate that considerable interfacial intermixing has occurred in this wedge sample.

Magnetic hysteresis loops above and below T_N of MnF₂ for this wedge sample were measured by vector SQUID magnetometry. The results are shown in Fig. 8.4 (a) for 80 K and Fig. 8.4 (b) for 10 K. The samples were first field cooled to 80 K and 10 K in an

applied magnetic field of 2 kOe, applied at 150 K along the MgO[100] direction, i.e., at $\pm 45^\circ$ relative to the AFM easy axes directions. The hysteresis loops at 80 K (Fig. 8.4 (a)) does not show exchange bias ($H_E = 0$ Oe). By field cooling the samples from 150 K to 10 K (Fig. 8.4 (b)) H_C has been observed to increase from 95 Oe at 80 K to 550 Oe at 10 K, and a shift of the hysteresis loop is clearly observed, resulting in an exchange bias field $|H_E|$ of 70 ± 10 Oe at 10 K.

8.3 NRS experimental procedure

The power of NRS to explore the depth dependent spin structure in thin films has been explained in Chapter 3. For the unambiguous data analysis, a clear beat pattern is the important factor which is necessary for a straightforward interpretation of the spectra. To obtain a well-defined beat pattern a clear Mössbauer line separation of the probing nuclei is necessary. As ^{57}Fe in bcc-Fe has a favorable hyperfine field of 33.0 T (at RT) with well separated Mössbauer lines due to large Zeeman splitting, the study of a possible depth-dependent spin structure profile in the ^{57}Fe layer of exchange biased Fe/MnF₂ by NRS with a synchrotron beam of small spot size is experimentally feasible. Fe/MnF₂ served as a model system for this study.

The experiments were performed at beamline ID-18 of the European Synchrotron Radiation Facility (ESRF), Grenoble, France. The sample was about 8 mm long along the ^{57}Fe wedge, and 5 mm wide. The measurements were performed by positioning the synchrotron beam at different locations along the ^{57}Fe wedge, resulting in signals from different distances relative to the center of the Fe film. The center position is labeled as position '0', and the edge of the wedge, at which ^{57}Fe and MnF₂ forms the interface, is at a lateral distance of 4 mm from the center (the total length of the sample was 8 mm). The location at which the ^{57}Fe probe layer is farthest away from the Fe/MnF₂ interface and at the top of the Fe layer is also at a lateral distance of 4 mm from the center position '0', but in opposite direction. The measurements were generally done at positions +3, +2, +1, 0, -1, -2 and -3 (Fig. 8.1). These positions represent the lateral distance from the center position of the ^{57}Fe wedge in millimeters. Converted into distances from the Fe/MnF₂ interface these lateral positions corresponds to about 0 Å, 0 Å, 12 Å, 24 Å, 36 Å, 48 Å and 60 Å away from the interface. For the measurement a variable temperature bath cryostat with a superconducting split-coil arrangement have been used. The sample was placed in the exchange-gas chamber of the cryostat with the wedge perpendicular to the synchrotron beam. The beam used had a size of about $1 \text{ mm} \times 0.1 \text{ mm}$. The cryostat was placed on a rotatable table to align the sample horizontal to the ground. The sample height was adjusted in order to allow the synchrotron beam to fall onto the sample with a glancing angle of about $4800 \mu\text{rad}$ to the sample surface. The schematic diagram of the experimental set up is shown in Fig. 8.5.

The time spectra were collected at different external fields by changing the current in the superconducting coil inside the cryostat and in turn sweeping the magnetic field. The magnetic field was always applied along the incident synchrotron beam direction \vec{k}_0 (see Fig. 8.5). The incident beam was always perpendicular to the wedge direction. Prior to applying the field the sample was first field cooled (FC) in an in-plane

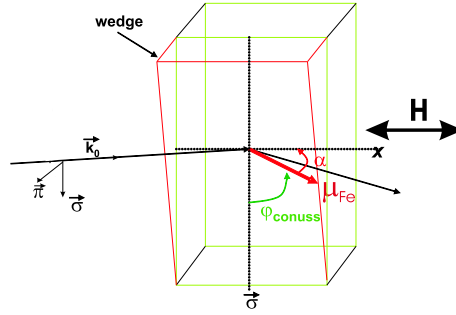


Figure 8.5: Schematic diagram of the experimental setup showing the relevant angles used in the CONUSS program. φ_{conuss} = the angle φ obtained from the CONUSS program, which is the minimum angle between the σ -polarization direction of the synchrotron beam (horizontal to the ground) and the magnetic moment (μ_{Fe}) or hyperfine field direction of Fe. α is the angle between the x -axis (i.e., sweeping field direction or \hat{k}_0 direction) and the Fe magnetic moment (μ_{Fe}) or hyperfine field direction. Hence, $\varphi_{conuss} + \alpha = 90^\circ$.

field of 2 kOe applied either along the wedge direction (perpendicular to the incident beam) or perpendicular to the wedge direction (parallel to the incident beam), as will be mentioned later. Further, the external field was at $\pm 45^\circ$ relative to the AFM easy axes directions. The time spectra were fitted by using the computer program 'CONUSS' written by W. Sturhahn [41] and modified and extended by R. Röhlsberger [42] for thin films and for grazing incidence geometries.

8.4 NRS results and discussion

8.4.1 Field dependent Fe spin rotation during magnetization reversal

First, NRS time spectra were measured site selectively at center position '0' on the ⁵⁷Fe wedge corresponding to the distance of 24 Å from the Fe/MnF₂ interface. The external field was applied parallel to the incident beam direction (x -direction). Typical NRS time spectra measured at 10 K for decreasing fields after field cooling from 150 K in a field of 2 kOe are shown in Fig. 8.6 (Appendix B). All spectra were simulated by using the hyperfine field of bcc-Fe at 10 K, i.e., 34.1 ± 0.2 T, for the whole sweeping field range. For the spin structure, the unidirectional model was used (Chapter 6, section 6.4.2). The obtained spin rotation angle φ ($= \varphi_{conuss}$) corresponding to each applied field is given at each spectrum. Further measured time spectra are shown in Fig. 10.1 and Fig. 10.2, in the Appendix, Chapter 10.

All the angles φ ($= \varphi_{conuss}$) obtained by the CONUSS programm are the angles between the σ polarization of the synchrotron beam and the in-plane Fe spin direction (see Fig. 8.6). This means that when $\varphi = \varphi_{conuss} = 90^\circ$ the spins are completely parallel to the applied field direction, which is the \vec{k}_0 direction of the incident synchrotron beam. The angle $\varphi = \varphi_{conuss}$ can be converted into the angle α between the (in-plane) Fe spin direction and the applied field (or x -) direction by $\alpha = 90^\circ - \varphi_{conuss}$. (One should note

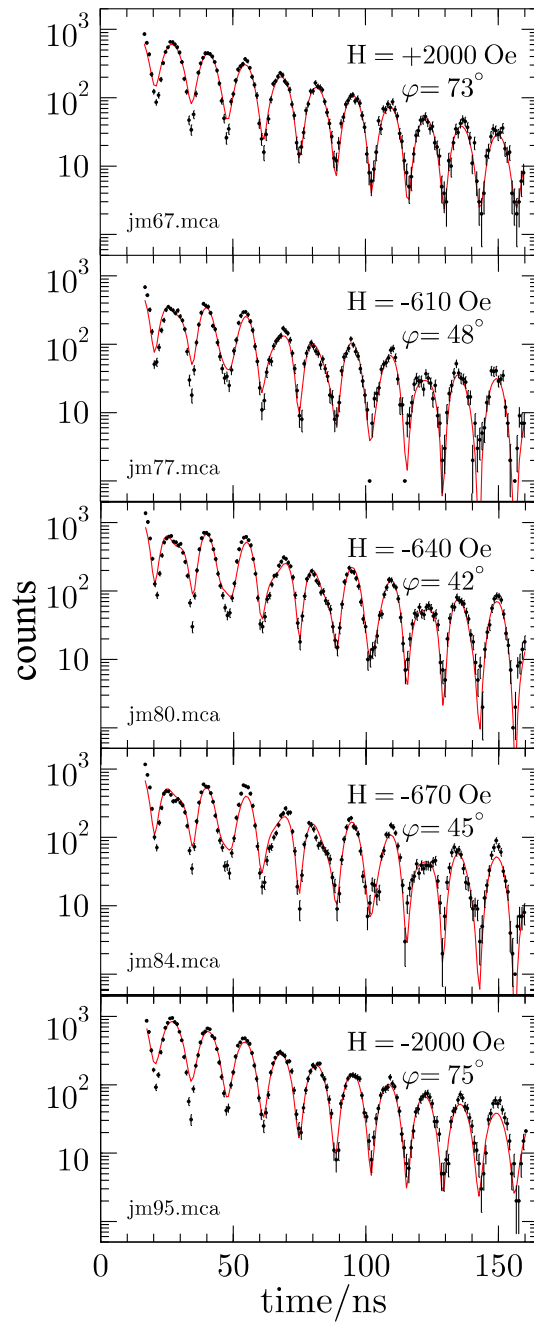


Figure 8.6: Typical NRS time spectra measured at 10 K at decreasing magnetic fields with the beam at position '0' of the ⁵⁷Fe wedge sample. The red solid lines were least-squares fitted to the data points by using the computer program CONUSS. Prior to the measurements the sample was cooled from 150 K to 18 K in a field of +2 kOe applied along the MgO[100] direction (bisector between the easy axes of the MnF₂ twins). The sweeping field H was applied also along the MgO[100] direction. The spectra given here are representative for five different field values that follow the left branch of the hysteresis loop. Here, $\varphi = \varphi_{\text{conuss}}$ is the angle between the σ -polarization of the synchrotron beam and the Fe spin direction (assumed to be unidirectional).

that the angle α used here corresponds to the angle φ between the Fe spin direction and

the x -direction defined earlier in Chapter 6 (section 6.4.1) to describe modeled Fe spin distributions (Fig. 6.9). Fig. 8.7 shows the angles α obtained from the fitting versus the applied field H . One should remember that NRS can not distinguish between angles α within $-90^\circ < \alpha < +90^\circ$ (Fe spin components along positive H) and angles $\alpha + 90^\circ < \alpha < +180^\circ$ and $-180^\circ < \alpha < -90^\circ$ (Fe spin components along negative H). Therefore, after transforming these angles α to the angle β formed by the Fe spins with the negative saturating field (-2 kOe) direction ($-x$ -direction), the resulting angles will form a hysteresis loop, as shown in Fig. 8.8. The exchange bias field and the coercivity obtained from this site-selected "angular hysteresis loop" in the (lateral) center of the iron film are $H_E = -50 \text{ Oe} \pm 10 \text{ Oe}$ and $H_c = 620 \text{ Oe} \pm 10 \text{ Oe}$, which is in fair agreement with the exchange bias field and coercivity obtained from the (global) magnetization (SQUID) measurements ($H_E = -70 \text{ Oe}$, $H_c = 550 \text{ Oe}$) for the same sample at 10 K.

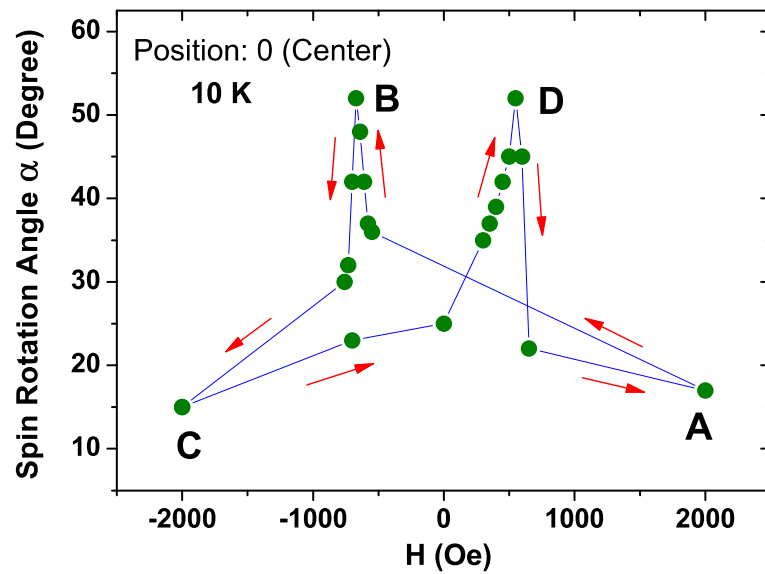


Figure 8.7: Field dependence of the Fe spin-rotation angle α measured at 10 K and at position '0', of the wedge. α is the angle between the Fe spins (assumed to be unidirectional) and the applied field direction. The field was sweeping along both branches of the hysteresis loop. (The lines are a guide for the eye). The ^{57}Fe probe layer is about 24 Å away from the Fe/MnF₂ interface (center position).

The striking feature of the angular hysteresis loop is that for the increasing and decreasing branch of the hysteresis loop the in-plane Fe spins first rotate continuously and weakly from a direction close to the applied field direction (ideally $\beta = 0^\circ$ or $\beta = 180^\circ$) by an angle of about $\pm 45^\circ$, which are the two easy axes of the AFM MnF₂ twin domains. The in-plane Fe spins at $\beta = 45^\circ$ and 135° , are equivalent to angles $\beta = 225^\circ$ and 315° , and these direction theoretically result in the same time spectra. Hence, these directions cannot be distinguished by NRS. According to the magnetization measured by vector SQUID (Fig. 8.4), the transverse magnetization on this sample is about an order of magnitude smaller than the longitudinal magnetization. This proves that during magnetization reversal the Fe spins rotate bidirectionally with respect to the applied field direction. This bidirectionality at 10 K appears to be caused by the presence of the AFM twin axes. At low T ($T < T_N$) the Fe spins tend to couple along the easy directions

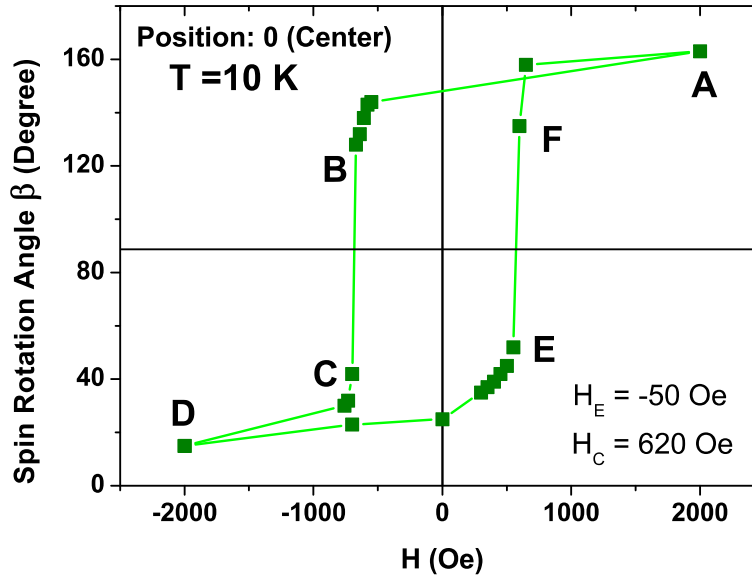


Figure 8.8: Fe spin-rotation angles β at 10 K with respect to the negative applied field direction ($-x$ -direction) obtained after transforming the angle α in Fig. 8.7: $\beta = 180^\circ - \alpha$ from $A \rightarrow B$ and $F \rightarrow A$, and $\beta = \alpha$ from $C \rightarrow D$ and $D \rightarrow E$.

of the MnF₂ spins. Now, it can be concluded that, during magnetization reversal the Fe spins just above those AFM domains with the c -axis in the $+45^\circ$ direction rotate towards the $+45^\circ$ direction ($\beta = 45^\circ$ or 225°) because of antiparallel exchange coupling, while the Fe spins just above the MnF₂ domains with the c -axis in the -45° direction rotate towards the -45° direction ($\beta = 135^\circ$ or 315°). For the $+45^\circ$ case (MnF₂ c -axis at $+45^\circ$), and upon decreasing the field from A to B (Fig. 8.8) the Fe spins may rotate 'clockwise', while 'anticlockwise' rotation occurs for the latter case (MnF₂ c -axis at -45°). The situation is schematically shown in Fig. 8.9. Secondly, by decreasing the field further from B to C (Fig. 8.8) around the negative coercive field of the left branch, the Fe spins surprisingly jump by 180° from the $\beta = 225^\circ$ direction to the $\beta = 45^\circ$ direction (or from $\beta = 135^\circ$ to $\beta = 315^\circ$). After that, the Fe spins rotate again continuously from C to D (from $\beta = 55^\circ$ and $\beta = 315^\circ$) to align nearly completely with the negative field direction. The right branch of the angular hysteresis loop can also be explained by a similar spin rotation mechanism.

However, according to polarized neutron reflectivity (PNR) results by Fitzsimmons et al. [7, 99, 100] and Leighton et al. [156], the left and right branch of the hysteresis loop is associated with spin rotation and domain formation/propagation, respectively. A similar result is also obtained by Krivorotov et al. [8] in the asymmetry observed by magnetoresistance measurements. This is also reflected in the observed asymmetry of the hysteresis loop. By polarized neutron reflectometry these authors [7, 99, 100, 156] have observed that a perpendicular spin component (perpendicular to the external field) exists, which explains the spin rotation for the left branch of the hysteresis loop. For the right branch of the hysteresis loop, however, no perpendicular magnetization component was observed, which was explained as the sign for domain propagation. These observations in ref. [7, 99, 100, 156] are not consistent with the present observations by NRS. Strong evidence for magnetization rotation for both branches of the hysteresis loop is

also provided by our observation of equal and higher transverse magnetization when the sweeping field is equal to H_C for both branches of the hysteresis loop, as measured by vector SQUID (Fig. 8.4).

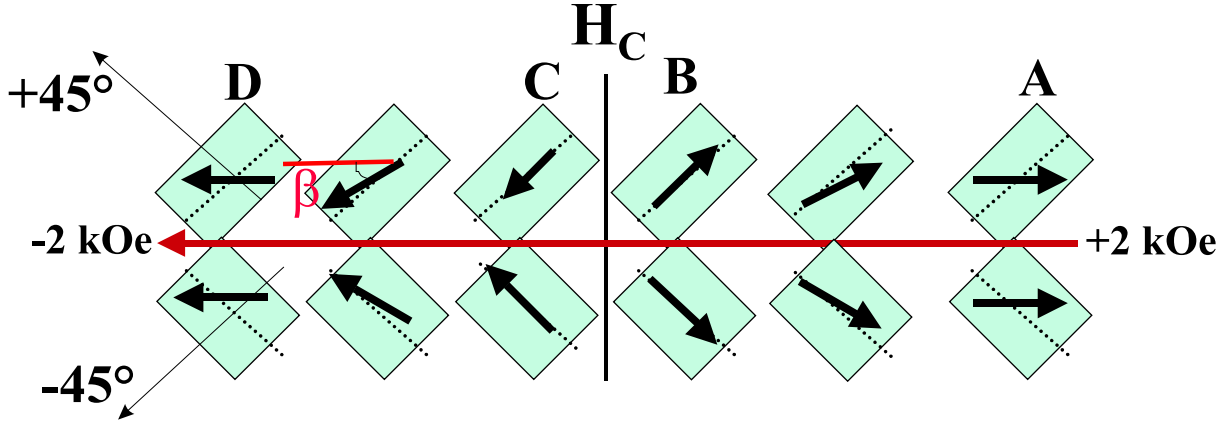


Figure 8.9: Schematic diagram of the Fe spin rotation observed at 10 K when the applied field is swept from +2 kOe to -2 kOe. The dotted line indicates the c -axes of the MnF₂ twin domains, which are symbolized by the rectangles. The bold arrows represent the Fe spin direction within the 10 Å thick ⁵⁷Fe probe layer in the center of the 80 Å Fe film. Notice the jump in the spin directions by 180° above and below H_C . (The A, B, C and D are equivalent to the same positions in the angular hysteresis loop of Fig. 8.8).

In the same work Fitzsimmons et al. [7] have concluded that the magnitude of the anisotropy of the AFM plays little role in the Fe spin reversal mechanism in Fe/MnF₂ or Fe/FeF₂. Our spin rotation mechanism observed by NRS suggests that the AFM anisotropy plays an important role in pinning the FM Fe spins, by their strong anisotropy along the c -axis ($\pm 45^\circ$), as discussed above. The anisotropy in both FeF₂ and MnF₂ is quite large at very low $T \ll T_N$ (Chapter 5), and both AFM materials affect the magnetization reversal mechanism equally strongly. Further, the high temperature ($T > T_N$) anisotropies are very different in these two AFM systems (FeF₂ and MnF₂) (Chapter 5). As we will see later (in section 8.3.3), in Fe/MnF₂ the Fe spins reverse continuously via rotation (as the magnetic anisotropy of MnF₂ above T_N is close to zero). The spin rotation mechanism above and below T_N of Fe/MnF₂ was not studied in detail here, but one may expect a difference in the reversal mechanism of the two systems above T_N , as the anisotropy of FeF₂ just above T_N is of the similar order of magnitude as that at very low temperature ($T \ll T_N$).

The magnetization reversal mechanism has also been studied by Radu et al. [9, 201, 202]. In contrast to Fitzsimmons et al. [7, 99, 100], they have observed that in the Co/CoO system the first magnetization reversal (decreasing field branch) occurs by domain nucleation and propagation and the second reversal (increasing field branch) occurs by spin rotation. Then, the next reversal, which occurs at a smaller field (because of the training effect), does not occur by domain nucleation and propagation, but rather by spin rotation. All other subsequent reversals occur via spin rotation.

From the above discussion it is clear that all asymmetric hysteresis loops are associated with both, the spin reversal by domain formation/propagation and spin rotation. However, in contrast to the results by Fitzsimmons et al. [7, 99, 100], the Fe spin rotation is the favored mechanism during spin reversal in Fe/MnF₂, as there is no asymmetry and training effect observed in the hysteresis loop of this system. However, theoretically, Beckmann et al. [10] have observed an asymmetry in their calculated hysteresis loops of the twinned Fe/FeF₂ when the cooling field direction is slightly (even few degrees) different from the exact x direction (exactly along the bisector between the twins).

8.4.2 Depth dependent Fe layer spin structure during magnetization reversal

The sample was again field cooled from 150 K to 10 K at an in-plane field of 2 kOe applied along the x -direction (bisecting the two easy axes of the twinned MnF₂). The depth dependent measurements for the wedge sample were performed at $T = 10$ K, exactly in the same way as described in the previous section 8.3.1. The measurements at different positions (-3, -2 and 0) were performed by moving the cryostat together with the sample with respect to the synchrotron beam. The measured time spectra are shown in Fig. 10.3, Fig. 10.4 and Fig. 10.5 (in Appendix, Chapter 10) for the beam position -3, -2 and 0, respectively. This corresponds to distances relative to the Fe/MnF₂ interface of 60, 48 and 24 Å, respectively. The field dependence of the angle α and of the obtained angles β between the Fe spin direction and the negative applied field direction is given in Fig. 8.10 (a) and (b), respectively. Again, unidirectional Fe spins were assumed. The rotation angles β are plotted in Fig. 8.10 for positions '-3', '-2' and '0'. From the figure it is clear that the ⁵⁷Fe spins at position '-3', '-2' and '0' align completely along the -2 kOe field direction ($\beta = 0^\circ$). But for the +2 kOe field the Fe spins at position '-3', '-2' and '0' differ in their spin alignment along the applied field. The top layer spins (position '-3'), which are about 60 Å away from interface, are perfectly aligned along the positive field direction ($\beta = 180^\circ$). However, the ⁵⁷Fe spins at position '0' (i.e., only about 24 Å away from interface) do not align completely along the +2 kOe field direction ($\beta = 160^\circ$). This is reminiscent of a non-collinear Fe spin spiral structure as predicted by Kiwi et al. [3–5]. This suggests that the Fe spins closer to the interface are pinned more strongly by a unidirectional anisotropy (which is responsible for the shift of the hysteresis loop) than Fe spins farther away from the interface. However, we have not enough data points to conclude about the position '-2'. Considering the published Fe layer thickness (t_{Fe}) dependence of exchange bias [153], the magnitude of the exchange bias field H_E increases with decreasing t_{Fe} . Our obtained result suggests that the contribution of the interfacial Fe spins to the exchange-bias field may be higher than that of the Fe spins farther away from the interface. This confirms the fact that exchange bias is a purely interfacial effect.

Another important observation from Fig. 8.10 (b) is that the top layer (position: '-3') Fe spins rotate earlier upon decreasing the field than the spins closer to the interface (e.g., at position: '0'). At this interfacial distance range, i.e., from 24 Å to 60 Å, the Fe spins at position '-3' (60 Å) reverses about 40 Oe earlier than the Fe spins at position '0' (24 Å). This demonstrates that the Fe spins closer to the interface are pinned more strongly than the Fe spins further away from the interface. There appears to exist a depth dependence of the coercivity. The depth-resolved coercivity is higher closer to the

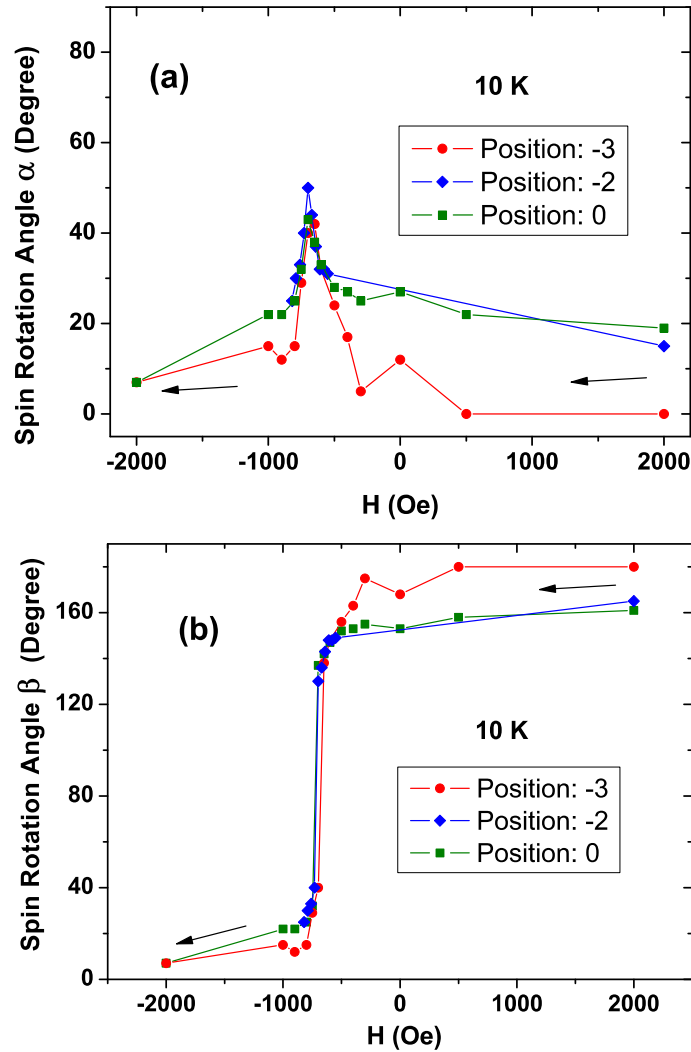


Figure 8.10: Field dependence of the Fe spin rotation angle α (a), and β (b) (with respect to the negative applied field direction), obtained by NRS and assuming a unidirectional spin distribution model, for different depths (positions: -3, -2 and 0) of the wedge samples, measured at 10 K. The positions -3, -2 and 0, at which the measurements were performed, correspond to distances of 60 Å, 48 Å and 24 Å, respectively, to the interface. The field was swept along the MgO[100] direction (i.e., the bisector between the MnF₂ twins) from +2 kOe to -2 kOe (along the left branch of the hysteresis loop), after field cooling the sample from 150 K to 10 K at +2 kOe along the same (MgO[100]) direction. The measurements at different positions were done by moving the cryostat and the sample with respect to the synchrotron beam and keeping the magnetic field constant. Hence, the error bar in the applied field for the three different positions at a particular field is extremely small. Notice the significant difference in the angles β for two different depths (position: 0 and -3) at different magnetic fields (particularly on the positive field side in comparison to the negative field side). Also notice that the reversal of the Fe spins for position -3 (60 Å away from the Fe/MnF₂ interface), occurs at a smaller field (~ 40 Oe smaller) than the reversal of Fe spins closer to the interface at position 0 (i.e., 24 Å away from the Fe/MnF₂ interface).

interface than farther away from the interface in the Fe layer.

8.4.3 Temperature dependence of the Fe spin rotation during magnetization reversal

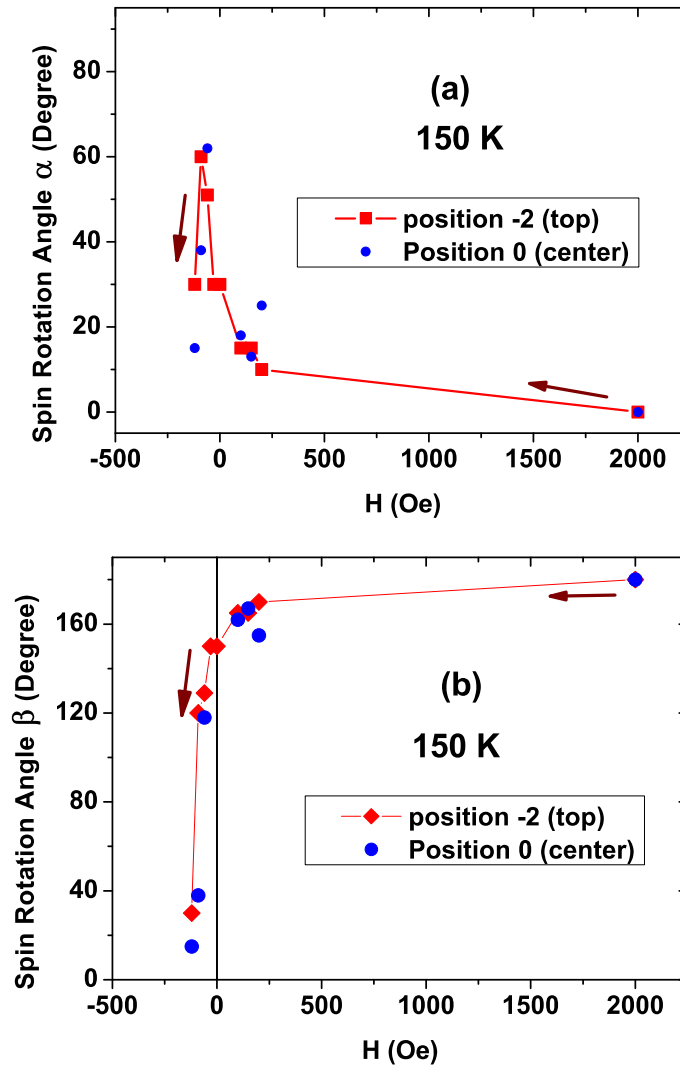


Figure 8.11: Field dependence of the Fe spin-rotation angle α (a), and β (b) (with respect to the negative applied field direction), obtained by NRS and assuming a unidirectional Fe spin distribution. The angles were measured at 150 K for different distances from the interface in the wedge sample. The different distances are shown as wedge positions (-2 and 0) at which the measurements were performed, corresponding to 48 Å and 24 Å, respectively. The field was swept from +2000 Oe to -120 Oe.

The obtained Fe spin rotation mechanism at 10 K ($T < T_N$) has been discussed in the previous sections, where the Fe spins were observed to continuously rotate from $\beta = 180^\circ$ to the $\beta = 135^\circ$ or 225° direction away from the cooling field axis, upon applying a magnetic field, and then jump from the 135° or 225° direction to $\beta = 45^\circ$ or 135° (or $\beta = -45^\circ$). Upon further increasing the negative field they continuously rotate towards the negative field direction with $\beta = 0^\circ$ at negative saturation. However, the Fe spin

reversal mechanism at 150 K ($> T_N$) was found to be different from this behavior. The observed behavior, which will be discussed below, is due to the disappearance of the AFM anisotropic axes of MnF₂ at 150 K ($> T_N$).

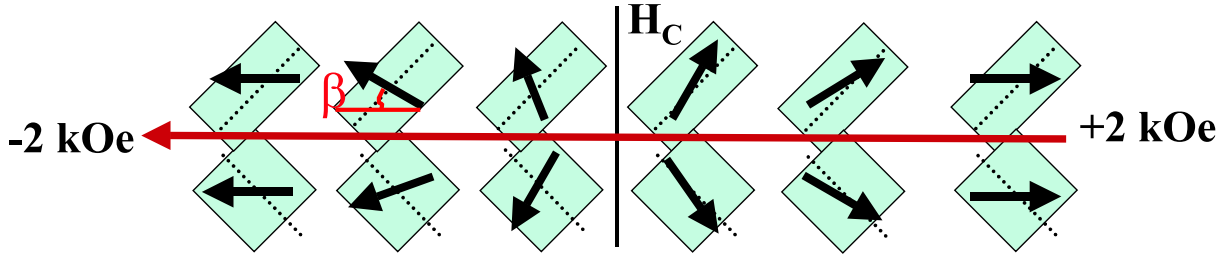


Figure 8.12: Schematic diagram of the Fe spin rotation observed at 150 K when the applied field was swept from +2 kOe to negative fields. The dotted lines indicate the *c*-axes of the MnF₂ twin domains which are symbolized by the rectangles. The bold arrows represent the Fe spin direction within the 10 Å thick ⁵⁷Fe probe layer of the 80 Å Fe film. Notice the continuous rotation, which differs from the jump in Fig. 8.9.

After the measurements at 10 K ($> T_N$), the sample was heated in zero-field to 150 K and the NRS time spectra were measured at 150 K starting from an applied field of +2 kOe followed by decreasing the field. The field was applied between the two *c*-axes of the MnF₂ twins. The measured time spectra for $T = 150$ K are shown in Fig. 10.6 and Fig. 10.7 (in the Appendix, Chapter 10) for position '-2' and '0', respectively. These positions corresponds to the ⁵⁷Fe layer at 48 Å and 24 Å away from the interface. The spectra were fitted by using the ⁵⁷Fe hyperfine parameters in the CONUSS program. The evaluated Fe spin rotation angles α and β are shown in Fig. 8.11 (a) and (b), respectively. Comparing with the results at 10 K (Fig. 8.10) it is clear that a jump in the rotation angle does not occur at 150 K, and the Fe spins above 150 K rotate continuously (Fig. 8.11). The reason for this is the fact that angles β of 70°, 120° and 130° could be observed below a negative applied field of 78 Oe, in contrast to the case of Fig. 8.10, where no values of β could be measured in the interval $50^\circ < \beta \leq 130^\circ$, because of the spin jump (instability). The schematic diagram for the Fe spin rotation at 150 K is given in Fig. 8.12. There is no jump, but continuous rotation. Another important observation is that unlike the spin rotation at 10 K, there is no depth dependence observed at 150 K (Fig. 8.11). This confirms the observation at 10 K that the presence of the high anisotropy of the AFM (MnF₂) twin axes determines the Fe spin rotation mechanism in the exchange biased condition.

8.4.4 Virgin and conventional remanent state spin structure

As remanence provides many interesting information on the anisotropy of a ferromagnetic material, it is important to observe the spin structure in the remanent state. For a thin Fe film the shape anisotropy plays the important role to keep the Fe spins in the film plane. Further, in a non-magnetized ferromagnetic film the domains are so arranged that the net magnetization is zero. The domains in this case may be arranged

isotropically. However, when the thin Fe film is in contact with an anisotropic antiferromagnet (e.g. MnF₂) which has a preferred anisotropy direction, the anisotropy of the AFM induces a new anisotropy in the Fe film via exchange coupling. Hence, the Fe film acquires the anisotropy induced by the AFM. Because of the absence of any external field the AFM anisotropy is the decisive factor.

In case of the exchange biased Fe/MnF₂ system this phenomenon is interesting, because the antiferromagnetic twinned MnF₂ domains play the role to align the Fe spins by exchange coupling to these four-fold anisotropy axes. Hence, these four-fold axes may tend to randomize the Fe spin directions in the remanent state depending on the strength of the FM-AFM exchange coupling and the magnetic anisotropy of the AFM. The time spectra for the Fe/MnF₂ wedge system measured in remanence at 300 K and 10 K are shown in Fig 10.8 (in Appendix, Chapter 10). It is observed that the Fe spins go more and more away from the original remanent magnetization direction, as the angle between the Fe spin direction and the previously applied field direction at 300 K (at virgin remanence) is 47° at position '+3', and is 68° and 74° at 10 K (at conventional remanence) for beam position '0' and '-3', respectively.

8.4.5 Fe spin rotation: H is perpendicular to cooling field H_{FC}

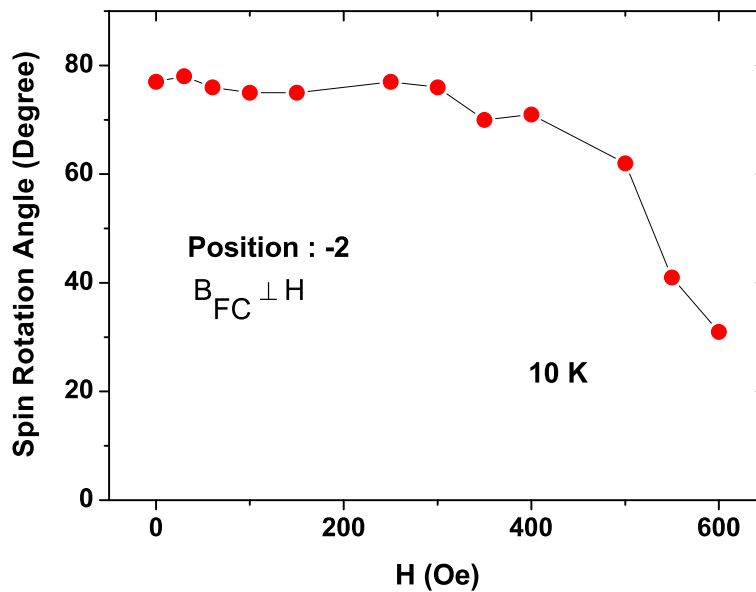


Figure 8.13: Field dependence of the Fe spin rotation angle β (with respect to the positive applied field direction) obtained by NRS and assuming a unidirectional Fe spin distribution. The angle β was measured at 10 K for a distance of 48 Å away from the Fe/MnF₂ interface (position: -2). The in-plane sweeping magnetic field H was applied perpendicular to the cooling field. (The cooling field was oriented along MgO[100] and was switched off at 10 K). The field H was swept from 0 Oe to +600 Oe.

An experiment was performed, where the sample was field cooled (at 2 kOe) to 10 K as before, but the sweeping field H was applied perpendicular to the cooling field (H_{FC}) direction (by rotating the cryostat by 90°). At first, the sample was field cooled from 150 K to 10 K at an applied field of 2 kOe (the field was applied parallel to the the long side

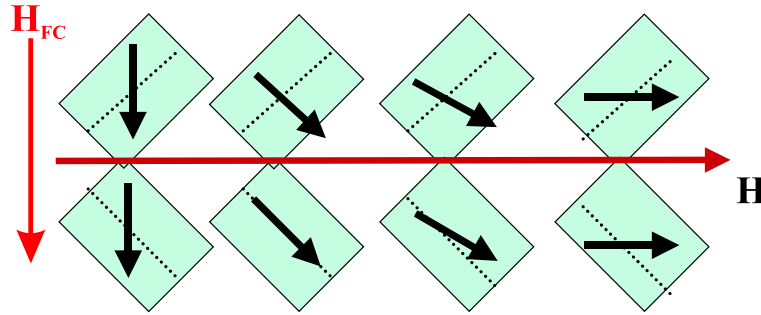


Figure 8.14: Schematic diagram of the Fe spin rotation observed at 10 K when the sweeping magnetic field (H) was perpendicular to the cooling field (H_{FC}). The dotted lines are the c-axes of the MnF₂ twin domains which are symbolized by the rectangles. The bold arrows represent the Fe spin direction within the 10 Å thick ⁵⁷Fe probe layer of the 80 Å Fe film.

of the sample, wedge direction) and then the field was switched off at 10 K. The cryostat was then rotated by 90° and the sweeping field was applied parallel to the synchrotron beam direction, as before (but the cooling field direction is now 90° to the synchrotron beam direction). Then, the measured time spectra at 10 K for position -2 at increasing sweeping fields from 0 Oe to 600 Oe are shown in Fig. 10.9 (in the Appendix, Chapter 10). The sweeping field dependence of angles β obtained after fitting the spectra are shown in Fig. 8.13. The results can be interpreted as follows. The cooling field of 2 kOe aligns all the Fe spins along the field direction, and after removal of the field at 10 K the Fe spins are frozen more or less along the H_{FC} direction. When the sweeping field was applied perpendicular to the cooling field direction, the Fe spins, as expected, start to rotate continuously towards the sweeping field direction as the sweeping field is increased. The schematic diagram for the spin rotation is given in Fig. 8.14.

8.5 Conclusions: NRS results for Fe spin structure in Fe/MnF₂

Using nuclear resonant scattering NRS, we have investigated a Fe/MnF₂ (twinned) sample, where the ⁵⁷Fe-probe layer was embedded in a (wedge-type) inclined manner in the ⁵⁶Fe layer, so that the distance of the ⁵⁷Fe-layer from the Fe/MnF₂ interface varies when one proceeds from one end of the sample to the other end. The sample was characterized by XRD, vector SQUID magnetometry and CEMS. According to the NRS results, we have observed the unidirectional anisotropy as the Fe spins freeze, making a certain angle with respect to the cooling field direction (which was at 45° relative to both AFM twin directions) close to the interface during FC. The Fe spins farther away from the interface align along the cooling field direction during field cooling. During reversal process the Fe spins rotate (from the saturation field direction) bidirectionally. By applying the reversal field, the Fe spins rotate continuously up to the easy axes of the MnF₂ twins ($\pm 45^\circ$), then switch by 180° to the opposite direction of the initial easy direction, and then continuously align towards the sweeping field direction for larger fields. This switch of the field is termed as "jump". This jump disappears above T_N ,

where the Fe spins rotate continuously. No indication of the Fe spin reversal via domain nucleation and propagation has been observed at any temperature. The Fe spin reversal field for different depths are different at 10 K ($T < T_N$), with the Fe spins near the interface reversing at a higher field than the Fe spins away from the interface. This is caused by the coupling of the Fe spins to the interfacial AFM moments. This effect is also reminiscent of the spiral-type of Fe spin arrangement in an applied magnetic field, in the exchange biases state, as predicted by Kiwi et al. [3–5]. All these phenomena (namely, the jump-type of magnetization reversal, the spin freezing, the influence of AFM anisotropy etc.) were found to vanish above T_N . From the NRS investigation we conclude that the contribution of the interfacial Fe spins to the coercivity and to the exchange bias is higher than that of the Fe spins far away from the interface.

Chapter 9

Summary

In this work, the ^{57}Fe probe layer technique is used in order to investigate the depth- and temperature-dependent Fe-layer spin structure of exchange biased Fe/MnF₂ and Fe/FeF₂ (pseudo-twinned) antiferromagnetic (AFM) systems by conversion electron Mössbauer spectroscopy (CEMS) and nuclear resonant scattering (NRS) of synchrotron radiation.

Two kinds of samples with a 10 Å ^{57}Fe probe layer directly at or 35 Å away from the interface, labeled as interface and center sample, respectively, were studied in this work. The spin structure was explained by considering two different models, unidirectional and step-shaped distribution (fanning) model. The results obtained by CEMS for Fe/MnF₂ suggests that, at 80 K, i.e., above $T_N = 67$ K of MnF₂, the remanent state Fe-layer spin structure of the two studied samples are slightly different due to their different microstructure. In the temperature range from 300 K to 80 K, the Fe-layer spin structure does not change just by zero-field cooling the sample in remanence. By zero-field cooling the samples in remanence to 18 K, i.e., below T_N , the Fe spins rotate towards the ($\pm 45^\circ$)- easy axes of MnF₂ twins. This rotation results in the same spin structure for both the interface and center samples at 18 K. By field cooling the interface sample in a field of 0.35 T to 18 K and measuring in remanence, a smaller rotation (or fanning angle) of the Fe-spins in comparison to the case of zero-field cooling in remanence from 300 K to 18 K was observed. When the interface sample was zero-field cooled or field cooled to 18 K, and subsequently zero-field heated to 80 K ($T > T_N$), the CEMS results indicate that the Fe-layer keeps the memory of its low temperature spin structure.

For Fe/FeF₂, a continuous non-monotonic change of the remanent-state Fe spin structure was observed by cooling from 300 K to 18 K. This effect can be related to the peculiar T-dependence of magnetic anisotropy of FeF₂ and short-range-ordered magnetic correlations in the AFM induced by Fe above $T_N = 78$ K. The high temperature Fe spin structure of the two different samples (interface and center) is different due to their different microstructure, but at 18 K ($T < T_N$) the spin structures of both samples are the same, and the Fe spins are oriented close to the easy axes of the FeF₂ twins, similar to the case of Fe/MnF₂ at 18 K.

NRS of synchrotron radiation was used to investigate the temperature- and depth-dependent Fe-layer spin structure during magnetization reversal in pseudo-twinned Fe/MnF₂. A ^{57}Fe -probe layer was embedded in the ^{56}Fe layer in a wedge-type manner, so that the distance of the ^{57}Fe layer from the Fe/MnF₂ interface varies when the synchrotron beam

is scanned from one end of the sample to the other end. A depth-dependent Fe spin structure in an applied magnetic field (applied along the bisector of the twin domains) was observed at 10 K, where the Fe spins closer to the interface are not aligned along the field direction. During magnetization reversal the spins of the top Fe layer rotate at a smaller field than the Fe spins closer to the interface. Upon decreasing the field from the fully aligned state in a strong positive magnetic field, the Fe spins coherently rotate up to the easy direction of MnF_2 (at $\pm 45^\circ$ from the applied field), then "jump" to the opposite direction of the easy axes (i.e., $\mp 45^\circ$), and then further rotate towards the negative applied field direction. The depth-dependence of the spin structure in an applied field and the rotation via the jump disappear at 150 K, i.e., above T_N of MnF_2 .

Bibliography

- [1] W. H. Meiklejohn, and C. P. Bean, Phys. Rev. **102**, 1413 (1956).
- [2] J. Nogués and I. K. Schuller, J. Magn. Magn. Mater. **192**, 203 (1999) and references there in.
- [3] M. Kiwi, J. M. López, R. D. Portugal, and R. Ramírez, Solid State Commun. **116**, 315 (2000).
- [4] M. Kiwi, J. Mejía-López, R. D. Portugal, and R. Ramírez, Appl. Phys. Lett. **75**, 3995 (1999).
- [5] M. Kiwi, J. Mejía-López, R. D. Portugal and R. Ramírez, Europhys. Lett., **48**, 573 (1999).
- [6] H. Ohldag, A. Scholl, F. Nolting, E. Arenholz, S. Maat, A. T. Young, M. Carey, and J. Stohr, Phys. Rev. Lett. **91**, 017203 (2003).
- [7] M. R. Fitzsimmons, P. Yashar, C. Leighton, Ivan K. Schuller, J. Nogués, C. F. Majkrzak, and J. A. Dura, Phys. Rev. Lett. **84**, 3986 (2000).
- [8] I. N. Krivorotov, C. Leighton, J. Nogués, Ivan K. Schuller, and E. Dan Dahlberg, Phys. Rev. B **65**, 100402 (2002).
- [9] F. Radu, M. Etzkorn, R. Siebrecht, T. Schmitte, K. Westerholt, and H. Zabel, Phys. Rev. B **67**, 134409 (2003).
- [10] B. Beckmann, K. D. Usadel, and U. Nowak, Phys. Rev. B **74**, 054431 (2006).
- [11] R. L. Mössbauer, Z. Physik **151**, 124 (1958).
- [12] R. L. Mössbauer, Naturwissenschaften **45**, 538 (1958).
- [13] R. L. Mössbauer, Z. Naturforsch. **14a**, 211 (1959).
- [14] V. I. Goldanskii and R. H. Herber, *Chemical applications of Mössbauer spectroscopy*, Academic press, New York (1968).
- [15] Leopold May, *An introduction to Mössbauer spectroscopy*, Adam Hilger, London (1971).
- [16] Ch. Sauer and W. Zinn, in: Magnetic Multilayers, Editor: L. H. Bennet and R. E. Watson, World Scientific, Singapore (1994).

-
- [17] G. K. Wertheim, *Mössbauer Effect: Principles and Applications* Academic Press, New York and London, 1964.
- [18] Mössbauer spectroscopy in 'Topics in applied physics' edited by U. Gonser, vol **5**, p. 139 (1975).
- [19] G. Schatz and A. Weidinger, *Nuclear condensed mater physics* John Wiley & sons, New York, 1992.
- [20] N. N. Greenwood and T. C. Gibb, Mössbauer spectroscopy, Chapman and Hall Ltd., (1971).
- [21] B. V. Thosar, P. K. Iyengar, J. K. Srivastava and S. C. Bhargava, *Advances in Mössbauer spectroscopy*, Elsevier scientific publishing company, (1983).
- [22] R. Ingalls, *Phys. Rev.* **128**, 1155 (1962).
- [23] R. Ingalls, *Phys. Rev.* **133**, A787 (1964).
- [24] J. Owen, *Proc. Roy. Soc. (London)* **A227**, 183 (1955).
- [25] W. Marshall and R. Stuart, *Phys. Rev.* **123**, 2048 (1961).
- [26] P. Gütlich, R. Link and A. Trautwein, *Mössbauer spectroscopy and transition metal chemistry*, Springer Verlag, (1978).
- [27] S. Chikazumi and S. H. Charap, *Physics of Magnetism*, Krieger Publishing Company, (1978).
- [28] R. A. Brand, *Nucl. Instrum. Methods B* **28**, 398 (1987).
- [29] R. A. Brand, *Nucl. Instrum. Methods B* **28**, 417 (1987).
- [30] C. Kittel, *Introduction to Solid State Physics* (1992).
- [31] T. Ruckert, Ph. D. Thesis, Gerhard-Mercator-Universität Duisburg, Germany (2001).
- [32] H. Wiedemann, *Particle Accelerator physics I + II*, Springer, Berlin (1993).
- [33] H. Winick, *Synchrotron Radiation Sources, a Primer*, World Scientific (1994).
- [34] J. D. Jackson, *Classical Electrodynamics*, Wiley, New York (1975).
- [35] R. Röhlberger, Habilitation Thesis, Universität Rostock, Germany (2002).
- [36] W. Brefeld and P. Gürtel, in: *Handbook on Synchrotron Radiation*, edited by S. Ebashi, M. Koch, and E. Rubinstein, Elsevier Science Publishers, Amsterdam (1991).
- [37] J. P. Hannon, G. T. Trammell, *Physica B* **159**, (1989) 161
- [38] Yu. V. Shvyd'ko, *Phys. Rev. B* **59**, (1999) 9132

-
- [39] U. van Brück, D. P. Siddons, J. B. Hastings, U. Bergmann and R. Hollatz, Phys. Rev. B **46**, (1992) 6207
- [40] G. V. Smirnov, Hyperfine Interact. **123/124**, (1999) 31.
- [41] W. Sturhahn, Hyperfine Interact. **125** (2000) 149.
- [42] R. Röhlberger, J. Bansmann, V. Senz, K. L. Jonas, A. Bettac, K. H. Meiwes-Broer, and O. Leupold, Phys. Rev. B **67**, 245412 (2003).
- [43] The counter was built and tested by U. von Hoersten at the Universität Duisburg-Essen, Duisburg, Germany.
- [44] U. von Hörsten, Program for evaluating Bragg reflexes and simulating the small angle XRD spectra, Universität Duisburg-Essen, Duisburg, Germany.
- [45] S. Steeb, G. Hildebrandt, L. Marosi, R. Lehnert, B. Scholtes and H. Schuon, Rontgen-und Elektronenbeugung, Expert Verlag, Sindelfingen (1985).
- [46] G. S. Cargill III, Mat. Res. Soc. Symp. Proc. 151 (1989) 231
- [47] P. F. Miceli, D. A. Neumann and H. Zabel, Appl. Phys. Lett. 48 (1986) 24
- [48] E. E. Fullerton, I. K. Schuller, H. Vanderstraeten and Y. Bruynseraede, Phys. Rev. B 45 (1992) 9292.
- [49] R. Röhlberger, Hyperfine Interact. 123/124, (1999) 301
- [50] S. W. Lovesey and S. P. Collins, *X-ray scattering and absorption by magnetic materials*, Claredon press, Oxford (1996).
- [51] R. Röhlberger, O. Leupold, J. Metge, H. D. Rüter, W. Sturhahn and E. Gerdau, Hyperfine Interact. **92**, (1994) 1107.
- [52] The samples were prepared by Dr. Waldemar A. A. Macedo at the university of California, San Diego (USA).
- [53] The X-ray characterization of the sample was performed by Dr. Waldemar A. A. Macedo at the university of California, San Diego (USA).
- [54] The SQUID measurements on this sample was performend by Dr. Waldemar A. A. Macedo at the university of California, San Diego (USA).
- [55] The sample was prepared by Dr. J. Eisenmenger at the University of California, San Diego (USA).
- [56] The X-ray characterization of the sample was performed by by Dr. J. Eisenmenger at the University of California, San Diego (USA).
- [57] The vector SQUID measurements on this sample was performend by Dr. J. Eisenmenger at the University of Ulm, Germany.
- [58] B. Aktas, Y. Öner, and H. Z. Durusoy, J. Magn. Magn. Mater. **119**, 339 (1993).

- [59] M. Ali, C. H. Marrows, M. Al Jawad, B. J. Hickey, A. Misra, U. Nowak, K. D. Usadel, *Phys. Rev. B* **68**, 214420 (2003).
- [60] O. Allegranza, and M. M. Chen, *J. Appl. Phys.* **73**, 6218 (1993).
- [61] T. Ambrose, R. L. Sommer, and C. L. Chien, *Phys. Rev. B* **56**, 83 (1997).
- [62] P. W. Anderson, *Phys. Rev.* **115**, 2 (1959).
- [63] W. J. Antel, Jr., F. Perjeru, and G. R. Harp, *Phys. Rev. Lett.* **83**, 1439 (1999).
- [64] A. R. Ball, A. J. G. Leenaers, P. J. van der Zaag, K. A. Shaw, B. Singer, D. M. Lind, H. Fredrikze, and M. T. Rekveldt, *Appl. Phys. Lett.* **69**, 583 (1996).
- [65] A. R. Ball, A. J. G. Leenaers, P. J. van der Zaag, K. A. Shaw, B. Singer, D. M. Lind, H. Fredrikze, and M. T. Rekveldt, *Appl. Phys. Lett.* **69**, 1489 (1996).
- [66] A. R. Ball, H. Fredrikze, D. M. Lind, R. M. Wolf, P. J. H. Bloemen, M. T. Rekveldt, and P. J. van der Zaag, *Physica B* **221**, 388 (1996).
- [67] A. Berger, and H. Hopster, *Phys. Rev. Lett.* **73**, 193 (1994).
- [68] B. Beckmann, U. Nowak, K. D. Usadel, *Phys. Rev. Lett.* **91**, 187201 (2003).
- [69] A. E. Berkowitz, and J. H. Greiner, *J. Appl. Phys.* **36**, 3330 (1965).
- [70] A. E. Berkowitz and K. Takano, *J. Magn. Magn. Mater.* **200**, 552 (1999).
- [71] S. D. Berry, D. M. Lind, G. Chern, and H. Mathias, *J. Magn. Magn. Mater.* **123**, 126 (1993).
- [72] C. Binek, A. Hochstrat, and W. Kleemann, *J. Magn. Magn. Mater.* **234**, 353 (2001).
- [73] C. Binek, B. Kagerer, S. Kainz, and W. Kleemann, *J. Magn. Magn. Mater.* **226-230**, 1814 (2001).
- [74] C. Binek, X. Chen, A. Hochstrat, and W. Kleemann, *J. Magn. Magn. Mater.* **240**, 257 (2002).
- [75] G. L. Bona, F. Meier, H. C. siegmann, and R. J. Gambino, *Appl. Phys. Lett.* **52**, 166 (1988).
- [76] J. W. Cai, Kai Liu, and C. L. Chien, *Phys. Rev. B* **60**, 72 (1999).
- [77] W. C. Cain, W. H. Meiklejohn, and M. H. Kryder, *J. Appl. Phys.* **61**, 4170 (1987).
- [78] I. A. Campbell, H. Hurdequint, and F. Hippert, *Phys. Rev. B* **33**, 3540 (1986).
- [79] M. J. Carey, and A. E. Berkowitz, *Appl. Phys. Lett.* **60**, 3060 (1992).
- [80] A. S. Carriço, R. E. Camley, and R. L. Stamps, *Phys. Rev. B* **50**, 13 453 (1994).
- [81] X. Chen, C. Binek, A. Hochstrat, and W. Kleemann, *Phys. Rev. B* **65**, 012415 (2002).

- [82] Y. J. Chen, D. K. Lottis, E. D. Dahlberg, J. N. Kuznia, A. M. Wowchak, and P. I. Cohen, *J. Appl. Phys.* **69**, 4523 (1991).
- [83] Y. Chen, D. K. Lottis, and E. D. Dahlberg, *J. Appl. Phys.* **70**, 5822 (1991).
- [84] Y. Chen, D. K. Lottis, and E. D. Dahlberg, *Mod. Phys. Lett.* **5**, 1781 (1991).
- [85] O. Cugat, D. Givord, J. P. Rebouillat, and Y. Souche, *J. Magn. Magn. Mater.* **104**, 397 (1992).
- [86] M. Chirwa, L. Lundgren, P. Nordblad, and O. Beckman, *J. Magn. Magn. Mater.* **15–18**, 457 (1980).
- [87] B. D. Cullity, *Introduction to Magnetic Materials*, Addison–Wesley, p. 165 (1972).
- [88] E. D. Dahlberg, K. T. Riggs, and G. A. Prinz, *J. Appl. Phys.* **63**, 4270 (1988).
- [89] E. D. Dahlberg, B. Miller, B. Hill, B. J. Jönsson, V. Ström, K. V. Rao, J. Nogués, and I. K. Schuller, *J. Appl. Phys.* **83**, 6893 (1998).
- [90] J. M. Daughton, A. V. Pohm, R. T. Fayfield, and C. H. Smith, *J. Phys. D* **32**, R169 (1999).
- [91] B. Dieny, V. S. Speriosu, S. S. P. Parkin, B. A. Gurney, D. R. Wilhoit, and D. Mauri, *Phys. Rev. B* **43**, 1297 (1991).
- [92] B. Dieny, *J. Magn. Magn. Mater.* **32**, 335 (1994).
- [93] D. V. Dimitrov, A. S. Murthy, G. C. Hadjipanayis, and C. P. Swann, *J. Appl. Phys.* **79**, 5106 (1996).
- [94] N. N. Efimova, S. R. Kufterina, Yu. A. Popkov, E. N. Khats'ko, and A. S. Chernyi, *Low Temp. Phys.* **22**, 824 (1996).
- [95] A. Ercole, T. Fujimoto, M. Patel, C. Daboo, R. J. Hicken, and J. A. C. Bland, *J. Magn. Magn. Mater.* **156**, 121 (1996).
- [96] R. A. Erickson, *Phys. Rev.* **90**, 779 (1953).
- [97] R. F. C. Farrow, R. F. Marks, S. Gider, A. C. Marley, S. S. P. Parkin, and D. Mauri, *J. Appl. Phys.* **81**, 4986 (1997).
- [98] G. P. Felcher, R. O. Hilleke, R. K. Crawford, J. Haumann, R. Kleb, and G. Ostrowski, *Rev. Sci. Instrum.* **58**, 609 (1987).
- [99] M. R. Fitzsimmons, C. Leighton, J. Nogués, A. Hoffmann, Kai Liu, C. F. Majkrzak, J. A. Dura, J. R. Groves, R. W. Springer, P. N. Arendt, V. Leiner, H. Lauter, and Ivan K. Schuller, *Phys. Rev. B* **65**, 134436 (2002).
- [100] M. R. Fitzsimmons, C. Leighton, A. Hoffmann, P. C. Yashar, J. Nogués, K. Liu, C. F. Majkrzak, J. A. Dura, H. Fritzsche, and Ivan K. Schuller, *Phys. Rev. B* **64**, 104415 (2001).
- [101] H. Fujiwara, K. Nishioka, C. Hou, M. R. Parker, S. Gangopadhyay, and R. Metzger, *J. Appl. Phys.* **79**, 6286 (1996).

- [102] E. Fulcomer and S. H. Charap, *J. Appl. Phys.* **43**, 4190 (1972).
- [103] E. E. Fullerton, J. S. Jiang, C. H. Sowers, J. E. Pearson, and S. D. Bader, *Appl. Phys. Lett.* **72**, 380 (1998).
- [104] E. E. Fullerton, I. K. Schuller, H. Vanderstraeten, and Y. Bruynseraede, **45**, 9292 (1992).
- [105] U. Gäfvert, L. Lundgren, P. Nordland, B. Westerstrandh, and O. Beckman, *Solid State Commun.* **23**, 9 (1977).
- [106] S. Gangopadhyay, G. C. Hadjipanayis, C. M. Sorensen, and K. J. Klabunde, *J. Appl. Phys.* **73**, 6964 (1993).
- [107] S. Gangopadhyay, G. C. Hadjipanayis, C. M. Sorensen, and K. J. Klabunde, *Nanostruct. Mater.* **1**, 449 (1992).
- [108] N. J. Gökemeijer and C. L. Chien, *J. Appl. Phys.* **85**, 5516 (1999).
- [109] N. J. Gökemeijer, T. Ambrose, C. L. Chien, N. Wang, and K. K. Fung, *J. Appl. Phys.* **81**, 4999 (1997).
- [110] N. J. Gökemeijer, T. Ambrose, and C. L. Chien, *Phys. Rev. Lett.* **79**, 4270 (1997).
- [111] R. B. Goldfarb, K. V. Rao, F. R. Fickett, H. S. Chen, *J. Appl. Phys.* **52**, 1744 (1981).
- [112] J. H. Greiner, *J. Appl. Phys.* **37**, 1474 (1966).
- [113] M. Grimsditch, A. Hoffmann, P. Vavassori, H. Shi, and D. Lederman, *Phys. Rev. Lett.* **90**, 257201 (2003).
- [114] D. H. Han, J. G. Zhu, and J. H. Judy, *J. Appl. Phys.* **81**, 4996 (1997).
- [115] H. Heffner, and G. Wade, *J. Appl. Phys.* **31**, 2316 (1960).
- [116] B. Heinrich, T. Monchesky, R. Urban, *J. Magn. Magn. Mater.* **236**, 339 (2001).
- [117] T. M. Hong, *Phys. Rev. B* **58**, 97 (1998).
- [118] C. Hou, H. Fujiwara, K. Zhang, A. Tanaka, and Y. Shimizu, *Phys. Rev. B* **63**, 024411 (2001).
- [119] C. Hou, H. Fujiwara, and K. Zhang, *Appl. Phys. Lett.* **76**, 3974 (2000).
- [120] C. M. Hsu, H. M. Lin, K. R. Tsai, and P. Y. Lee, *J. Appl. Phys.* **76**, 4793 (1994).
- [121] F. Huang, M. T. Kief, G. J. Mankey, and R. F. Willis, *Phys. Rev. B* **49**, 3962 (1994).
- [122] M. T. Hutchings, B. D. Rainford, and H. J. Guggenheim, *J. Phys. C* **3**, 307 (1970).
- [123] A. Hochstrat, C. Binek, and W. Kleemann, *Phys. Rev. B* **66**, 92409 (2002).

- [124] Y. Ijiri, J. A. Borchers, R. W. Erwin, P. J. van der Zaag, and R. M. Wolf, *Bull. Am. Phys. Soc.* **42**, 682 (1997).
- [125] Y. Ijiri, J. A. Borchers, R. W. Erwin, S.-H. Lee, P. J. van der Zaag, and R. M. Wolf, *Phys. Rev. Lett.* **80**, 608 (1998).
- [126] T. Iwata, K. Kai, T. Nakamichi, and M. Yamamoto, *J. Phys. Soc. Japan* **28**, 582 (1970).
- [127] Y. Imry and S. Ma, *Phys. Rev. Lett.* **35**, (1975) 1399.
- [128] V. Jaccarino, A. R. King, M. Motokawa, T. Sakakibara, M. Date, *J. Magn. Magn. Mater.* **31-34** 1117 (1983).
- [129] M. M. P. Janssen, *J. Appl. Phys.* **41**, 399 (1970).
- [130] R. Jungblut, R. Coehoorn, M. T. Johnson, C. Sauer, P. J. van der Zaag, A. R. Ball, T. G. S. M. Rijks, J. aan de Stegge, and A. Reinders, *J. Magn. Magn. Mater.* **148**, 300 (1995).
- [131] R. Jungblut, R. Coehoorn, M. T. Johnson, J. aan de Stegge, and A. Reinders, *J. Appl. Phys.* **75**, 6659 (1994).
- [132] B. Kagerer, C. Binek, and W. Kleemann, *J. Magn. Magn. Mater.* **217**, 139 (2000).
- [133] K. Liu, S. M. Baker, M. Tuominen, T. P. Russel, and I. K. Schuller, *Phys. Rev. B* **63**, 060403 (2001).
- [134] J. Keller, P. Miltenyi, B. Beschoten, G. Guntherodt, U. Nowak, and K. D. Usadel, *Phys. Rev. B* **66**, 014431 (2002).
- [135] W. Keune, V. E. Kuncser, M. Doi, M. Askin, H. Spies, B. Sahoo, E. Duman, M. Acet, J. S. Jiang, A. Inomata und S. D. Bader, *J. Phys. D* **35** 2352 (2002).
- [136] M. Kiwi, *J. Magn. Magn. Mater.* **234**, 584 (2001).
- [137] J. V. Kim, R. L. Stamps, B. V. McGrath, and R. E. Camley, *Phys. Rev. B* **61**, 8888 (2000).
- [138] R. H. Kodama, A. E. Berkowitz, E. J. McNiff, Jr., and S. Foner, *J. Appl. Phys.* **81**, 5552 (1997).
- [139] R. H. Kodama, S. A. Makhlof, and A. E. Berkowitz, *Phys. Rev. Lett.* **79**, 1393 (1997).
- [140] J. C. S. Kools, *IEEE Trans. Magn.* **32**, 3165 (1996).
- [141] N. C. Koon, *Phys. Rev. Lett.* **78**, 4865 (1997).
- [142] V. Korenivski, R. B. van Dover, Y. Suzuki, E. M. Gyorgy, J. M. Phillips, and R. J. Felder, *J. Appl. Phys.* **79**, 5926 (1996).
- [143] J. S. Kouvel, *J. Phys. Chem. sol.* **21**, 57 (1961).
- [144] J. S. Kouvel, and C. D. Graham Jr., *J. Phys. Chem. sol.* **11**, 220 (1959).

- [145] I. N. Krivorotov, C. Leighton, J. Nogués, I. K. Schuller, and E. D. Dahlberg, *Phys. Rev. B* **68**, 054430 (2002).
- [146] V. Kuncser, W. Keune, M. Vopsaroiu, and P. R. Bissel, *Nucl. Instrum. Meth. Phys. Res. B* **196**, 135 (2002).
- [147] V. Kuncser, W. Keune, B. Sahoo, E. Duman, M. Acet, F. Radu, M. Valeanu, O. Crisan, and G. Filoti, *J. Magn. Magn. Mater.* **272-276**, 348 (2004).
- [148] V. Kuncser, F. Stromberg, W. Keune, and K. Westerholt, *J. Appl. Phys.* **97**, 063513 (2005).
- [149] V. Kuncser, W. Keune, M. Vopsaroiu, and P. R. Bissel, *Nucl. Instrum. Meth. Phys. Res. B* **245**, 539 (2006).
- [150] J. Kushauer, C. Binek, and W. Kleeman, *J. Appl. Phys.* **75**, 5856 (1994).
- [151] C. H. Lai, W. E. Bailey, R. L. White, and T. C. Anthony, *J. Appl. Phys.* **81**, 4990 (1996).
- [152] D. Lederman, J. Nogués, and I. K. Schuller, *Phys. Rev. B* **56**, 2332 (1997).
- [153] C. Leighton, M. R. Fitzsimmons, A. Hoffmann, J. Dura, C. F. Majkrzak, M. S. Lund, and I. K. Schuller, *Phys. Rev. B* **65**, 064403 (2002).
- [154] C. Leighton, J. Nogués, B. J. Jönsson-Åkerman, and I. K. Schuller, *Phys. Rev. Lett.* **84**, 3466 (2000).
- [155] C. Leighton, H. Suhl, M. J. Pechan, R. Compton, J. Nogués, and I. K. Schuller, *J. Appl. Phys.* **92**, 1483 (2002).
- [156] C. Leighton, M. R. Fitzsimmons, P. Yashar, A. Hoffmann, J. Nogués, J. Dura, C. F. Majkrzak, and Ivan K. Schuller, *Phys. Rev. Lett.* **86**, 4394 (2001).
- [157] C. Leighton, J. Nogués, H. Suhl, and Ivan K. Schuller, *Phys. Rev. B* **60**, 12837 (1999).
- [158] Z. Li and S. Zhang, *Phys. Rev. B* **61**, R14 897 (2000).
- [159] M. H. Li, G. H. Yu, H. W. Jiang, J. W. Cai, W. Y. Lai, and F. W. Zhu, *J. Appl. Phys.* **92**, 2620 (2002).
- [160] H. M. Lin, C. M. Hsu, Y. D. Yao, Y. Y. Cben, T. T. Kuan, F. A. Yang, and C. Y. Tung, *Nanostruct. Mater.* **6**, 977 (1995).
- [161] X. Lin and G. C. Hadjipanayis, and S. I. Shah, *J. Appl. Phys.* **75**, 6676 (1994).
- [162] X. Lin, A. S. Murthy, G. C. Hadjipanayis, C. Swann, and S. I. Shah, *J. Appl. Phys.* **76**, 6543 (1994).
- [163] T. Lin, D. Mauri, N. Staud, C. Hwang, and J. K. Howard, *Appl. Phys. Lett.* **65**, 1183 (1994).
- [164] Kai Liu, Shenda M. Baker, Mark Tuominen, Thomas P. Russell, and Ivan K. Schuller, *Phys. Rev. B* **63**, 060403 (2001).

- [165] J. Löffler, H. Van Swygenhoven, W. Wagner, J. Meier, B. Doudin, and J. P. Ansermet, *Nanostruct. Mater.* **9**, 523 (1997).
- [166] M. S. Lund, W. A. A. Macedo, Kai Liu, J. Nogués, Ivan K. Schuller, and C. Leighton, *Phys. Rev. B* **66**, 054422 (2002).
- [167] W. A. A. Macedo, B. Sahoo, V. Kuncser, J. Eisenmenger, I. Felner, J. Nogués, K. Liu, W. Keune, and I. K. Schuller, *Phys. Rev. B* (2004) (in press).
- [168] A. P. Malozemoff, *Phys. Rev. B* **35**, 3679 (1987).
- [169] A. P. Malozemoff, *J. Appl. Phys.* **63**, 3874 (1988).
- [170] H. Matsuyama, C. Haginoya, and K. Koike, *Phys. Rev. Lett.* **85**, 646 (2000).
- [171] D. Mauri, H. C. Siegmann, P. S. Bagus, and E. Kay, *J. Appl. Phys.* **62**, 3047 (1987).
- [172] W. H. Meiklejohn, and C. P. Bean, *Phys. Rev.* **105**, 904 (1957).
- [173] W. H. Meiklejohn, *J. Appl. Phys.* **33**, 1328 (1962).
- [174] B. H. Miller and E. D. Dahlberg, *Appl. Phys. Lett.* **69**, 3932 (1996).
- [175] P. Miltényi, M. Gierlings, J. Keller, B. Beschoten, G. Güntherodt, U. Nowak, and K. D. Usadel, *Phys. Rev. Lett.* **84**, 4224 (2000).
- [176] P. Miltényi, M. Gierlings, M. Bammig, U. May, G. Güntherodt, J. Nogués, M. Gruyters, C. Leighton, and Ivan K. Schuller, *Appl. Phys. Lett.* **75**, 2304 (1999).
- [177] P. Miltényi, M. Gruyters, G. Güntherodt, J. Nogués, and I. K. Schuller, *Phys. Rev. B* **59**, 3333 (1999).
- [178] A. Misra, U. Nowak, K. D. Usadel, *J. Appl. Phys.* **93**, 6593 (2003).
- [179] A. Misra, U. Nowak, K. D. Usadel, *J. Appl. Phys.* **95**, 1357 (2004).
- [180] J. S. Moodera, T. H. Kim, C. Tanaka, C. H. De Groot, *Philos. Mag. B* **80**, 195 (2000).
- [181] T. J. Moran, J. M. Gallego, and I. K. Schuller, *J. Appl. Phys.* **78**, 1887 (1995).
- [182] T. J. Moran and I. K. Schuller, *J. Appl. Phys.* **79**, 5109 (1996).
- [183] T. J. Moran, J. Nogués, D. Lederman, and Ivan K. Schuller, *Appl. Phys. Lett.* **72**, 617 (1998).
- [184] H. Morita, H. Hiroyoshi, and K. Fukamichi, *J. Phys. F* **16**, 507 (1986).
- [185] V. I. Nikitenko, V. S. Gornakov, A. J. Shapiro, R. D. Shull, Kai Liu, S. M. Zhou, and C. L. Chien, *Phys. Rev. Lett.* **84**, 765 (2000).
- [186] O. Nikotin, P. A. Lindgard, and O. W. Dietrich, *J. Phys. C* **2**, 1168 (1969).

- [187] J. Nogués, D. Lederman, T. J. Moran, I. K. Schuller, and K. V. Rao, *Appl. Phys. Lett.* **68**, 3186 (1996).
- [188] J. Nogués, D. Lederman, T. J. Moran, and I. K. Schuller, *Phys. Rev. Lett.* **76**, 4624 (1996).
- [189] J. Nogués, T. J. Moran, D. Lederman, I. K. Schuller, and K. V. Rao, *Phys. Rev. B* **59**, 6984 (1999).
- [190] F. Nolting, A. Scholl, J. Stöhr, J. W. Seo, J. Fompeyrine, H. Siegart, J. P. Locquet, S. Anders, J. Lüning, E. E. Fullerton, M. F. Toney, M. R. Scheinfein, and H. A. Padmore, *Nature* **405**, 767 (2000).
- [191] U. Nowak, K. D. Usadel, J. Keller, P. Miltenyi, B. Beschoten, G. Guntherodt, *Phys. Rev. B* **66**, 014430 (2002).
- [192] U. Nowak, A. Misra, and K. D. Usadel, *J. Magn. Magn. Mater.* **240**, 243 (2002).
- [193] U. Nowak, A. Misra, and K. D. Usadel, *J. Appl. Phys.* **89**, 7269 (2001).
- [194] H. Ohldag, T. J. Regan, J. Stöhr, A. Scholl, F. Nolting, J. Lüning, C. Stamm, S. Anders, and R. L. White, *Phys. Rev. Lett.* **87**, 247201 (2001).
- [195] H. Ohldag, A. Scholl, F. Nolting, S. Anders, F. U. Hillebrecht, J. Stohr, *Phys. Rev. Lett.* **86**, 2878 (2001).
- [196] N. Ohshima, M. Nakada and Y. Tsukamoto, *Jpn. J. Appl. Phys.* **35**, L1585 (1996).
- [197] V. Papaefthymiou, A. Kostikas, A. Simopoulos, D. Niarchos, S. Gangopadyay, G. C. Hadjipanayis, C. M. Sorensen, and K. J. Klabunde, *J. Appl. Phys.* **67**, 4487 (1990).
- [198] A. S. Pavlovic, *Thermal Expansion*, edited by D. C. Larsen, Plenum, New York, p. 29 (1982).
- [199] M. J. Pechan, D. Bennett, N. Teng, C. Leighton, J. Nogués, and Ivan K. Schuller, *Phys. Rev. B* **65**, 064410 (2002).
- [200] E. Pina, C. Prados, and A. Hernando, *Phys. Rev. B* **69**, 052402 (2004).
- [201] F. Radu, M. Etzkorn, V. Leiner, T. Schmitte, A. Schreyer, K. Westerholt, and H. Zabel, *Appl. Phys. A* **A74**, S1570 (2002).
- [202] F. Radu, M. Etzkorn, T. Schmitte, R. Siebrecht, A. Schreyer, K. Westerholt, and H. Zabel, *J. Mag. Mag. Mater.* **240**, 251 (2002).
- [203] F. Radu, A. Vorobiev, J. Major, H. Humbolt, K. Westerholt, and H. Zabel, *Physica B* **335**, 63 (2003).
- [204] F. Radu, Ph. D. Thesis, Ruhr Universität Bochum, 2005.
- [205] C. A. Ramos, D. Lederman, A. R. Kind and V. Jaccarino, *Phys. Rev. Lett.* **65**, (1990) 2913.

- [206] A. S. Borovik-Romanov, *Sov. Phys. JETP* **11**, 786 (1960).
- [207] W. Abdul-Razzaq, and M. Wu, *J. Appl. Phys.* **69**, 5078 (1991).
- [208] B. Sahoo, W. A. A. Macedo, W. Keune, V. Kuncser, J. Eisenmenger, J. Nogues, I.K. Schuller, I. Felner, K. Liu and R. Röhlberger, *Hyperfine Interact.* (2006) (accepted).
- [209] N. Sakamoto, *J. Phys. Soc. Japan* **17**, 99 (1962).
- [210] C. Schlenker, and R. Buder, *Czech. J. Phys., Sect. B* **21**, 506 (1971).
- [211] C. Schlenker, S. S. P. Parkin, J. C. Scott, and K. Howard, *J. Magn. Magn. Mater.* **54-57**, 801 (1986).
- [212] C. Schlenker, and D. Paccard, *J. de Phys., (France)* **28**, 611 (1967).
- [213] A. Scholl, F. Nolting, J. Stöhr, T. Regan, J. Luning, J. W. Seo, J. P. Locquet, J. Fompeyrine, S. Anders, H. Ohldag, and H. A. Padmore, *J. Appl. Phys.* **89**, 7266 (2001).
- [214] A. Scholl, F. Nolting, J. Stöhr, J. Luning, J. W. Seo, J. P. Locquet, J. Fompeyrine, S. Anders, H. Ohldag, H. A. Padmore, *Synchrotron Radiat.* **8**, 101 (2001).
- [215] A. Scholl, J. Stöhr, J. Luning, J. W. Seo, J. Fompeyrine, H. Siegwart, J. P. Locquet, F. Nolting, S. Anders, E. E. Fullerton, M. R. Scheinfein, and H. A. Padmore, *Science* **287**, 1014 (2000).
- [216] I. K. Schuller, *Phys. Rev. Lett.* **44**, 1597 (1980).
- [217] T. C. Schulthess and W. H. Butler, *Phys. Rev. Lett.* **81**, 4516 (1998).
- [218] W. Sevenhans, M. Gijs, Y. Bruynseraede, H. Homma, and I. K. Schuller, *Phys. Rev. B* **34**, 5955 (1986).
- [219] H. Shi and D. Lederman, *Phys. Rev. B* **66**, 094426 (2002).
- [220] H. Shi, D. Lederman, and E. E. Fullerton, *J. Appl. Phys.* **91**, 7763 (2002).
- [221] E. V. Shipil, K. Y. Guslienko, and B. Szymynski, *IEEE Trans. Magn.* **30**, 797 (1994).
- [222] I. L. Siu, M. N. Islam, and J. C. Walker, *J. Appl. Phys.* **88**, 5293 (2000).
- [223] J. C. Slonczewski, *Phys. Rev. Lett.* **67**, 3172 (1991).
- [224] S. Soeya, S. Tadokoro, T. Imagawa, M. Fuyama, and S. Narishige, *J. Appl. Phys.* **74**, 6297 (1993).
- [225] S. Soeya, H. Hoshiya, and M. Fuyama, *J. Appl. Phys.* **80**, 1006 (1996).
- [226] S. Soeya, H. Hoshiya, R. Arai, and M. Fuyama, *J. Appl. Phys.* **81**, 6488 (1997).
- [227] S. Spagna, M. B. Maple, and R. E. Sager, *J. Appl. Phys.* **79**, 4926 (1996).

- [228] S. Spagna, R. E. Sager, and M. B. Maple, *Rev. Sci. Instr.* **66**, 5570 (1995).
- [229] R. L. Stamps, *J. Phys. D* **33**, R247 (2000).
- [230] M. B. Stearns, *J. Appl. Phys.* **55**, 1729 (1984).
- [231] M. D. Stiles and R. D. McMichael, *Phys. Rev. B* **59**, 3722 (1999).
- [232] M. D. Stiles and R. D. McMichael, *Phys. Rev. B* **60**, 12950 (1999).
- [233] M. D. Stiles and R. D. McMichael, *Phys. Rev. B* **63**, 064405 (2001).
- [234] J. W. Stout and S. A. Reed, *J. Am. Chem. Soc.* **76**, 5279 (1954).
- [235] W. Stoecklein, S. S. P. Parkin, and J. C. Scott, *Phys. Rev. B* **38**, 6847 (1988).
- [236] V. Ström, B. J. Jönsson, K. V. Rao, and E. D. Dahlberg, *J. Appl. Phys.* **81**, 5003 (1997).
- [237] H. Suhl and I. K. Schuller, *Phys. Rev. B* **58**, 258 (1998).
- [238] Y. Suzuki, R. B. van Dover, E. M. Gyorgy, Julia M. Phillips, V. Korenivski, D. J. Werder, C. H. Chen, R. J. Felder, R. J. Cava, J. J. Krajewski, and W. F. Peck, Jr., *J. Appl. Phys.* **79**, 5923 (1996).
- [239] Y. Suzuki, R. B. van Dover, E. M. Gyorgy, J. M. Phillips, and R. J. Felder, *Phys. Rev. B* **53**, 14016 (1996).
- [240] K. Takano, F. T. Parker, and A. E. Berkowitz, *J. Appl. Phys.* **81**, 5262 (1997).
- [241] M. Takahashi, A. Yanai, S. Taguchi, T. Suzuki, *Jpn. J. Appl. Phys.* **19** 1093 (1980).
- [242] M. Takahashi, A. Yanai, S. Taguchi, T. Suzuki, *Jpn. J. Appl. Phys.* **19** 1093 (1980).
- [243] Y. J. Tang, B. Roos, T. Mewes, S. O. Demokritov, B. Hillebrands, and Y. J. Wang, *Appl. Phys. Lett.* **75**, 707 (1999).
- [244] T. Tokunaga, M. Taguchi, T. Fukami, Y. Nakaki, and K. Tsutsumi, *J. Appl. Phys.* **67**, 4417 (1990).
- [245] M. F. Toney, C. Tsang, and J. K. Howard, *J. Appl. Phys.* **70**, 6227 (1991).
- [246] C. Tsang, and K. Lee, *J. Appl. Phys.* **53**, 2605 (1982).
- [247] M. Tsunoda, Y. Tsuchiya, M. Konoto, and M. Takahashi, *J. Magn. Magn. Mater.* **171**, 29 (1997).
- [248] Y. Tsuchiya, K. Kosuge, S. Yamaguchi, and N. Nakayama, *Mater. Trans. JIM* **38**, 91 (1997).
- [249] N. B. Weber, H. Ohldag, H. Gomonaj, and F. U. Hillebrecht, *Phys. Rev. Lett.* **91**, 237205 (2003).
- [250] M. Weissmann, A. M. Llois, and M. Kiwi, *J. Magn. Magn. Mater.* **234**, 19 (2001).

- [251] B. Y. Wong, C. Mitsumata, S. Prakash, D. E. Laughlin, and T. Kobayashi, *J. Appl. Phys.* **79**, 7896 (1996).
- [252] X. W. Wu, and C. L. Chien, *Phys. Rev. Lett.* **81**, 2795 (1998).
- [253] H. Xi, M. H. Kryder, and R. M. White, *Appl. Phys. Lett.* **74**, 2687 (1999).
- [254] Y. D. Yao, Y. Y. Chen, C. M. Hsu, H. M. Lin, C. Y. Tung, M. F. Tai, D. H. Wang, K. T. Wu, and C. T. Suo, *Nanostruct. Mater.* **6**, 933 (1995).
- [255] G. H. Yu, M. H. Li, F. W. Zhu, Q. K. Li, Y. Zhang, C. L. Chai, H. W. Jiang, and W. Y. Lai, *J. Appl. Phys.* **91**, 3759 (2002).
- [256] P. J. van der Zaag, Y. Ijiri, J. A. Borchers, L. F. Feiner, R. M. Wolf, J. M. Gaines, R. W. Erwin, and M. A. Verheijen, *Phys. Rev. Lett.* **84**, 6102 (2000).
- [257] P. J. van der Zaag, A. R. Ball, L. F. Feiner, R. M. Wolf, and P. A. A. van der Heijden, *J. Appl. Phys.* **79**, 5103 (1996).
- [258] H. Zabel, R. Siebrecht, and A. Schreyer, *Physica B* **276-278**, 17 (2000).
- [259] G. Champion, V. Escax, Ch. C. Moulin, A. Bleuzen, F. Villain, F. Baudalet, E. Dartyge, and M. Verdaguer, *J. Am. Chem. Soc.* **123**, 12544 (2001).
- [260] Ch. C. Moulin, P. Thuery, M. Verdaguer, J. Zarembowitch, and A. Michalowicz, *Journal de Physique* **C8-47**, 563 (1986).
- [261] P. Heller, and G. B. Benedek, *Phys. Rev. Lett.* **8**, 428 (1962).
- [262] M. J. M. Almeida, and P. J. Brown, *J. Phys. C* **21**, 1111 (1988).
- [263] R. A. Erickson, *Phys. Rev.* **90**, 779 (1953).
- [264] M. Lippert, Th. Brückel, Th. Köhler, and J. R. Schneider, *Europhys. Lett.* **27**, 537 (1994).
- [265] J. Stremper, U. Rütt, and W. Jauch, *Phys. Rev. Lett.* **86**, 3152 (2001).
- [266] J. W. Stout, and M. Griffel, *Phys. Rev.* **76**, 144 (1949).
- [267] J. W. Stout, and M. Griffel, *J. Chem. Phys.* **18**, 1455 (1950).
- [268] J. W. Stout, and L. M. Matarrese, *Rev. Mod. Phys.* **25**, 338 (1953).
- [269] M. Griffel and J. M. Stout, *J. Am. Chem. Soc.* **72**, 4351 (1950).
- [270] A. Ferrari, *Atti. Acad. Lincei* **3**, 324 (1926).
- [271] J. H. Van Vleck, *J. Chem. Phys.* **9**, 85 (1941).
- [272] G. K. Wertheim, and D. N. E. Buchanan, *Phys. Rev.* **161**, 161 (1967).
- [273] G. K. Wertheim, *Phys. Rev.* **121**, 63 (1961).
- [274] G. K. Wertheim, H. J. Guggenheim, and D. N. E. Buchanan, *Phys. Rev.* **169**, 465 (1968).

- [275] L. M. Levinson, *J. Phys. Chem. Solids* **29**, 1331 (1968).
- [276] D. S. Rimai, *Phys. Rev. B* **16**, 4069 (1977).
- [277] Y. Y. Zhou, and M. G. Zhao, *J. Phys. C: Solid State Phys.* **20**, 1827 (1987).
- [278] A. J. Devasahayam and M. H. Kryder, *J. Appl. Phys.* **85**, 5519 (1999).
- [279] S. Riedling, M. Bauer, C. Mathieu, B. Hillebrands, R. Jungblut, J. Kohlhepp, and A. Reinders, *J. Appl. Phys.* **85**, 6648 (1999).
- [280] J. van Driel, F. R. de Boer, K. M. H. Lenssen, and R. Coehoorn, *J. Appl. Phys.* **88**, 975 (2000).
- [281] T. J. Klemmer, V. R. Inturi, M. K. Minor, and J. A. Barnard, *Appl. Phys. Lett.* **70**, 2915 (1997).
- [282] H. Uyama, Y. Otani, K. Fukamichi, O. Kitakami, Y. Shimada, and J. Echigoya, *Appl. Phys. Lett.* **71**, 1258 (1997).
- [283] J. Satooka and A. Ito, *J. Phys. Soc. Japan* **66**, 784 (1997).
- [284] J. Satooka and A. Ito, *J. Phys: Condens. Matter* **10**, L711 (1998).
- [285] Z. P. Li, J. Eisenmenger, C. W. Miller, and I. K. Schuller, *Phys. Rev. Lett.* **96**, 137201 (2006).
- [286] I. V. Roshchin, O. Petravic, R. Morales, Z. P. Li, X. Battle, and I. K. Schuller, *Europhys. Lett.* **71**, 297 (2005).
- [287] S. Roy, M. R. Fitzsimmons, S. Park, M. Dorn, O. Petravic, I. V. Roshchin, Z. P. Li, X. Battle, R. Morales, A. Misra, X. Zhang, K. Chesnel, J. B. Kortright, S. K. Sinha, and I. K. Schuller, *Phys. Rev. Lett.* **95**, 047201 (2005).
- [288] J. Olamit, E. Arenholz, Z. P. Li, O. Petravic, I. V. Roshchin, R. Morales, X. Battle, I. K. Schuller and K. Liu, *Phys. Rev. B* **72**, 012408 (2005).
- [289] O. Petravic, Z. P. Li, I. V. Roshchin, M. Viret, R. Morales, X. Battle, and I. K. Schuller, *Appl. Phys. Lett.* **87**, 222509 (2005).

Chapter 10

Appendix

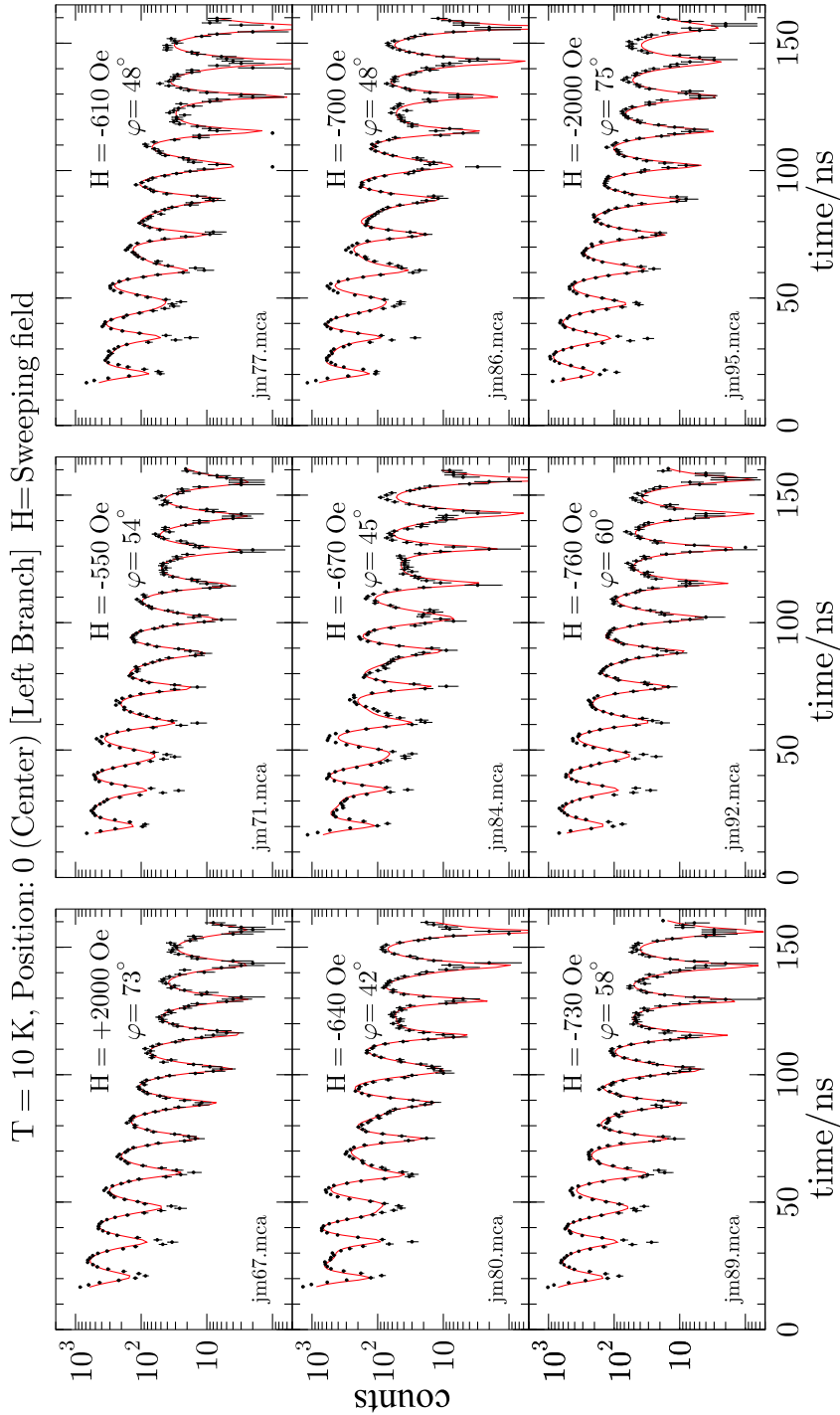


Figure 10.1: Time spectra measured at decreasing magnetic fields (from +2 kOe to -2kOe, left branch of the hysteresis loop) at 10 K and at position '0', of the Fe/MnF₂ sample having ⁵⁷Fe wedge. The red solid lines are the least-squares fitting to the data points. Prior to the measurements the sample was cooled from 150 K to 18 K at +2 kOe field applied along MgO[100] direction (between the easy axes of the MnF₂ twins). The sweeping field H was applied also along the MgO[100] direction. φ is the angle between the σ -polarization of the synchrotron beam and the Fe spin direction (assumed to be unidirectional) and the applied field direction.

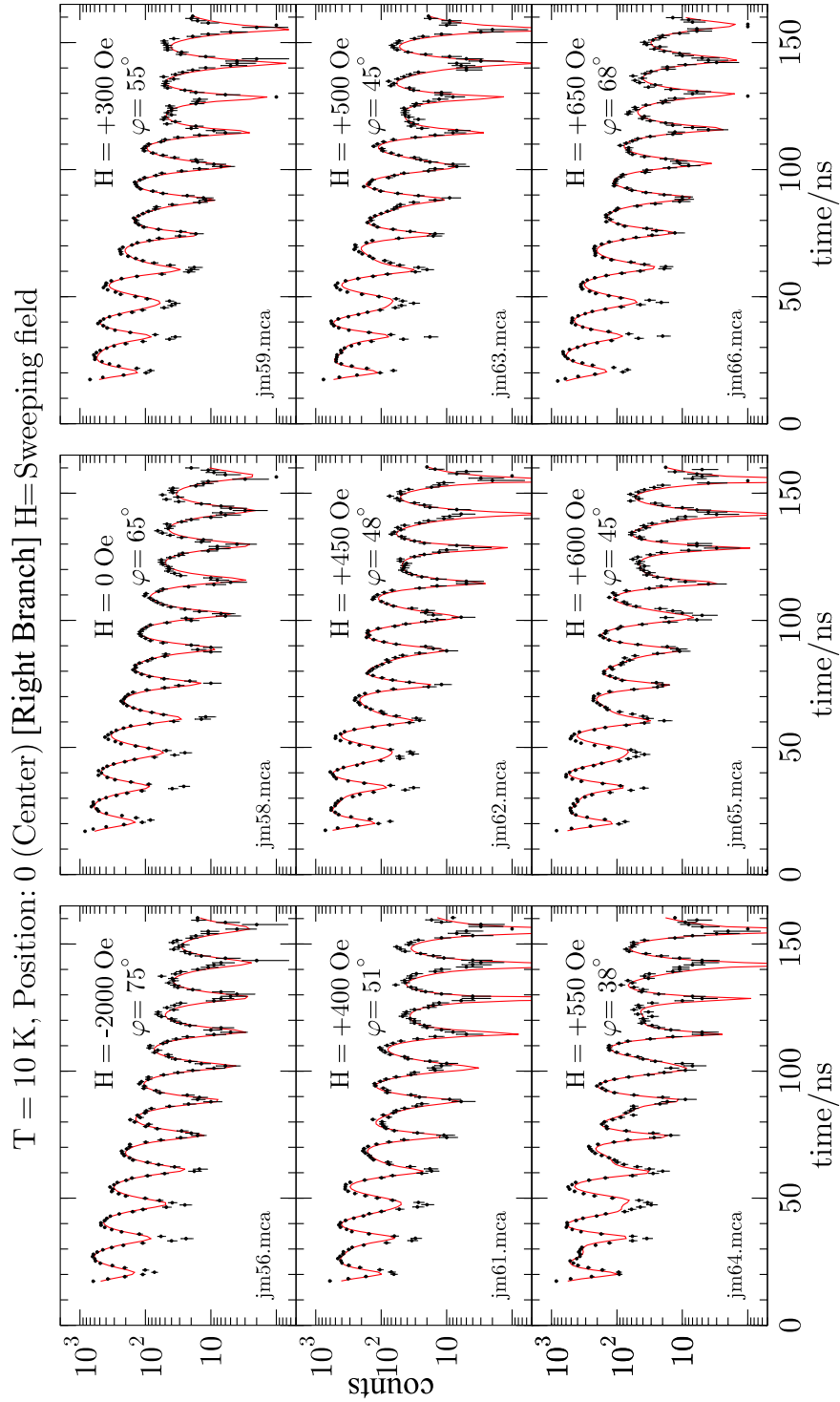


Figure 10.2: Time spectra measured at increasing magnetic fields (from -2 kOe to +2kOe, right branch of the hysteresis loop) at 10 K and at position '0', of the Fe/MnF₂ sample having ⁵⁷Fe wedge. The red solid lines are the least-squares fitting to the data points. The geometry of these measurements were similar to that of Fig. 10.1. φ is the angle between the σ -polarization of the synchrotron beam and the Fe spin direction (assumed to be unidirectional) and the applied field direction.

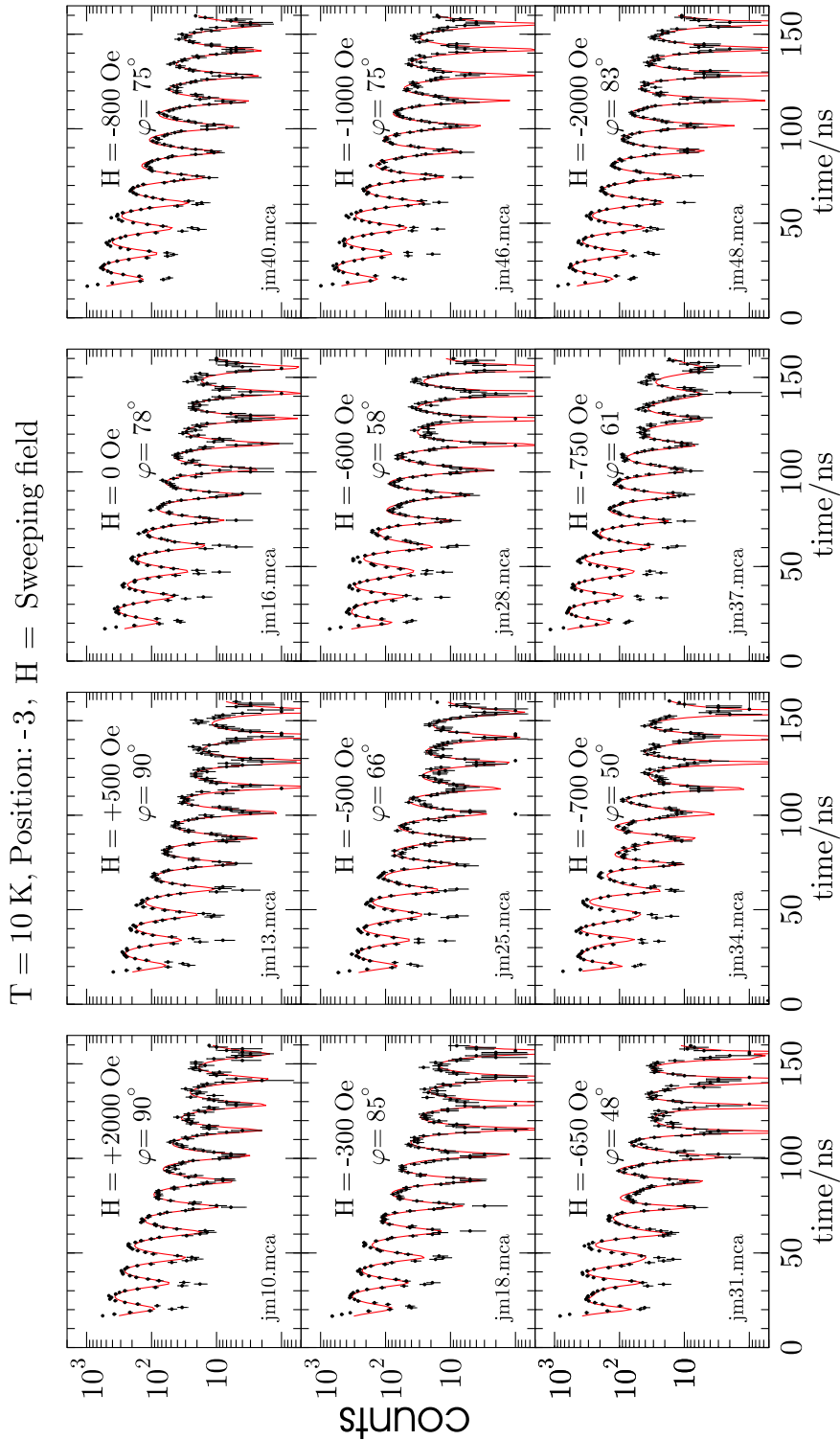


Figure 10.3: Time spectra measured at decreasing magnetic fields (from +2 kOe to -2kOe, left branch of the hysteresis loop) at 10 K and at position '-3', of the Fe/MnF₂ sample having ⁵⁷Fe wedge. The red solid lines are the least-squares fitting to the data points. The geometry of these measurements were similar to that of Fig. 10.1. φ is the angle between the σ -polarization of the synchrotron beam and the Fe spin direction (assumed to be unidirectional) and the applied field direction.

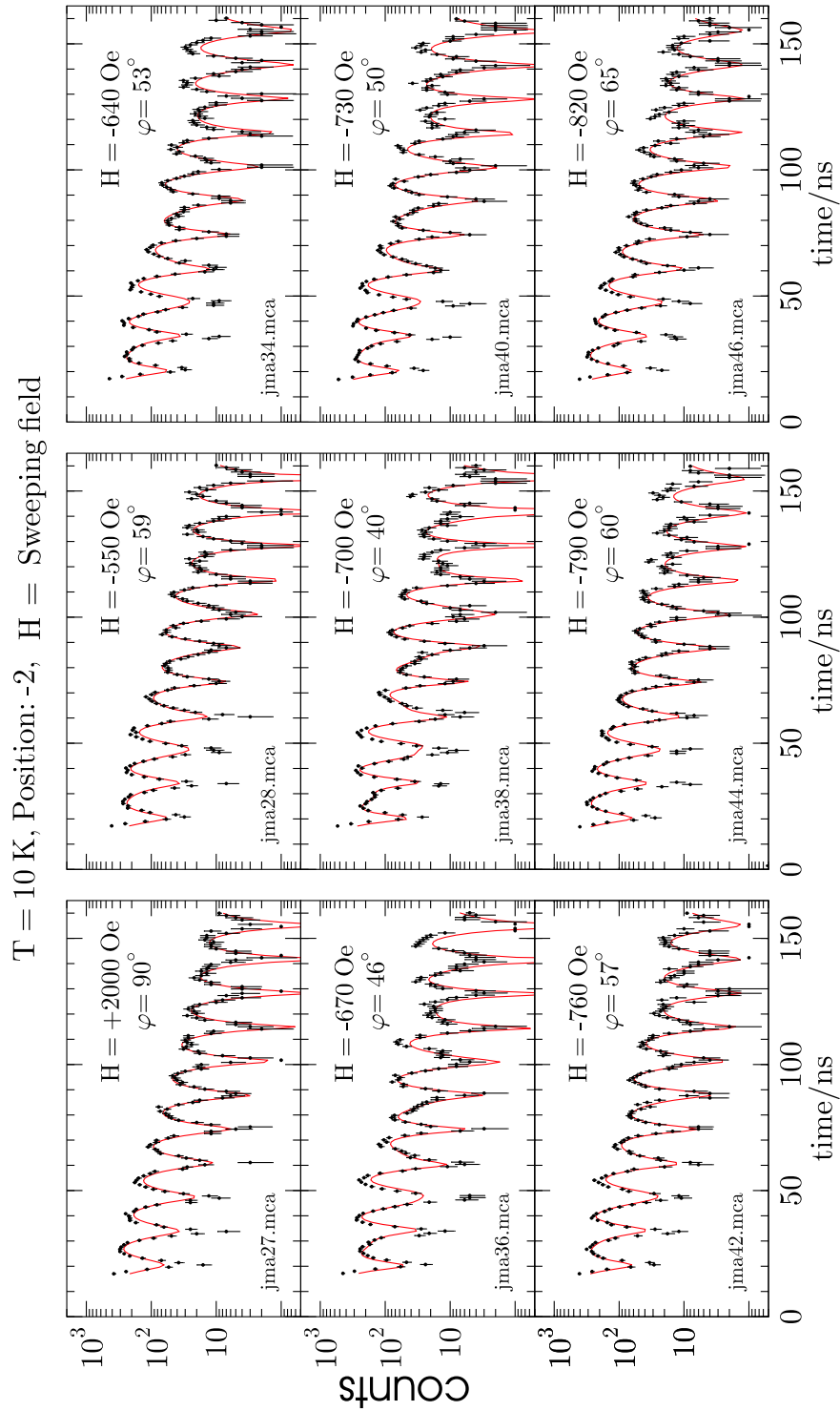


Figure 10.4: Time spectra measured at decreasing magnetic fields (from +2 kOe to -2 kOe, left branch of the hysteresis loop) at 10 K and at position '-2', of the Fe/MnF₂ sample having ⁵⁷Fe wedge. The red solid lines are the least-squares fitting to the data points. The geometry of these measurements were similar to that of Fig. 10.1. φ is the angle between the σ -polarization of the synchrotron beam and the Fe spin direction (assumed to be unidirectional) and the applied field direction.

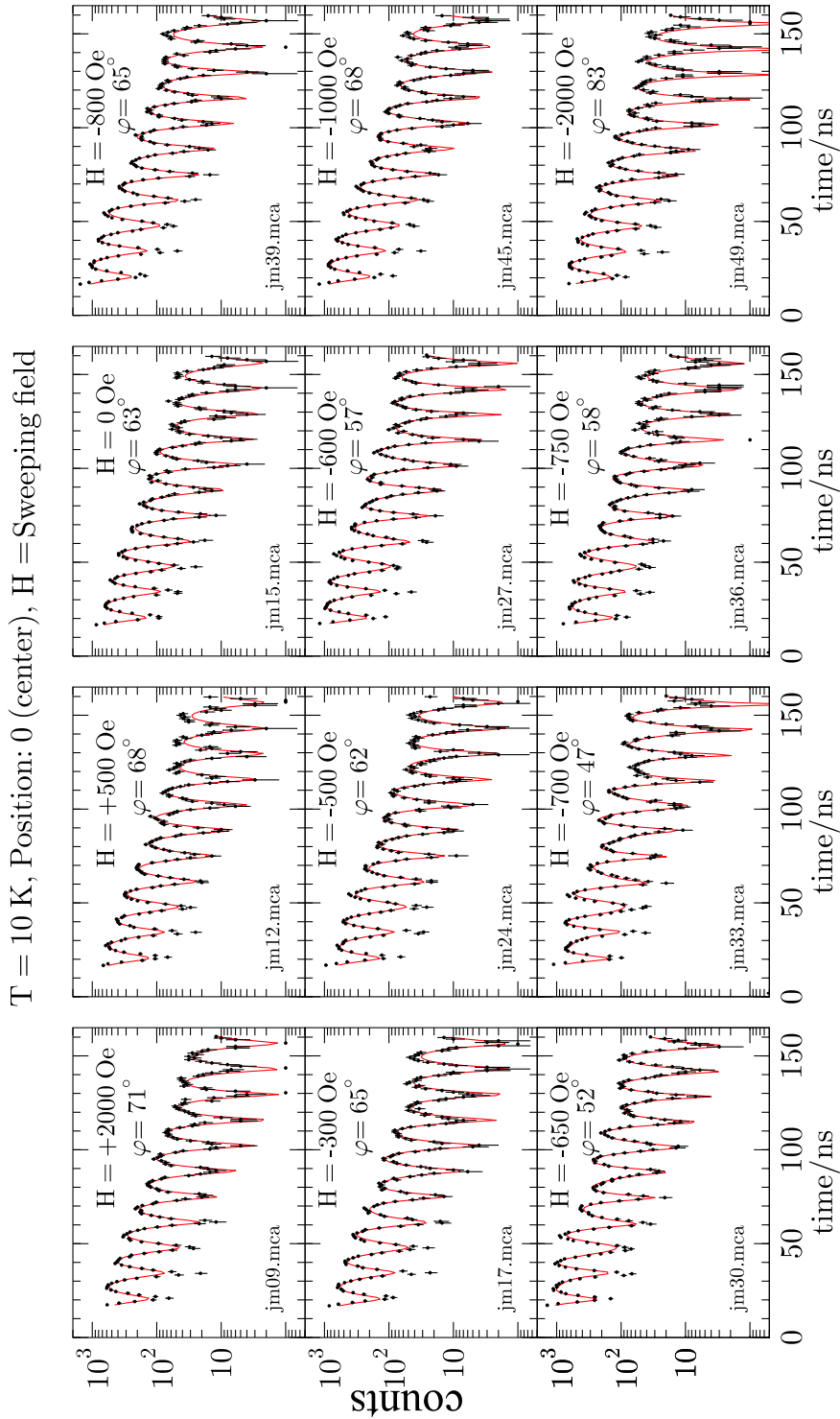


Figure 10.5: Time spectra measured at decreasing magnetic fields (from +2 kOe to -2 kOe, left branch of the hysteresis loop) at 10 K and at position '0', of the Fe/MnF₂ sample having ⁵⁷Fe wedge. The red solid lines are the least-squares fitting to the data points. The geometry of these measurements were similar to that of Fig. 10.1. φ is the angle between the σ -polarization of the synchrotron beam and the Fe spin direction (assumed to be unidirectional) and the applied field direction.

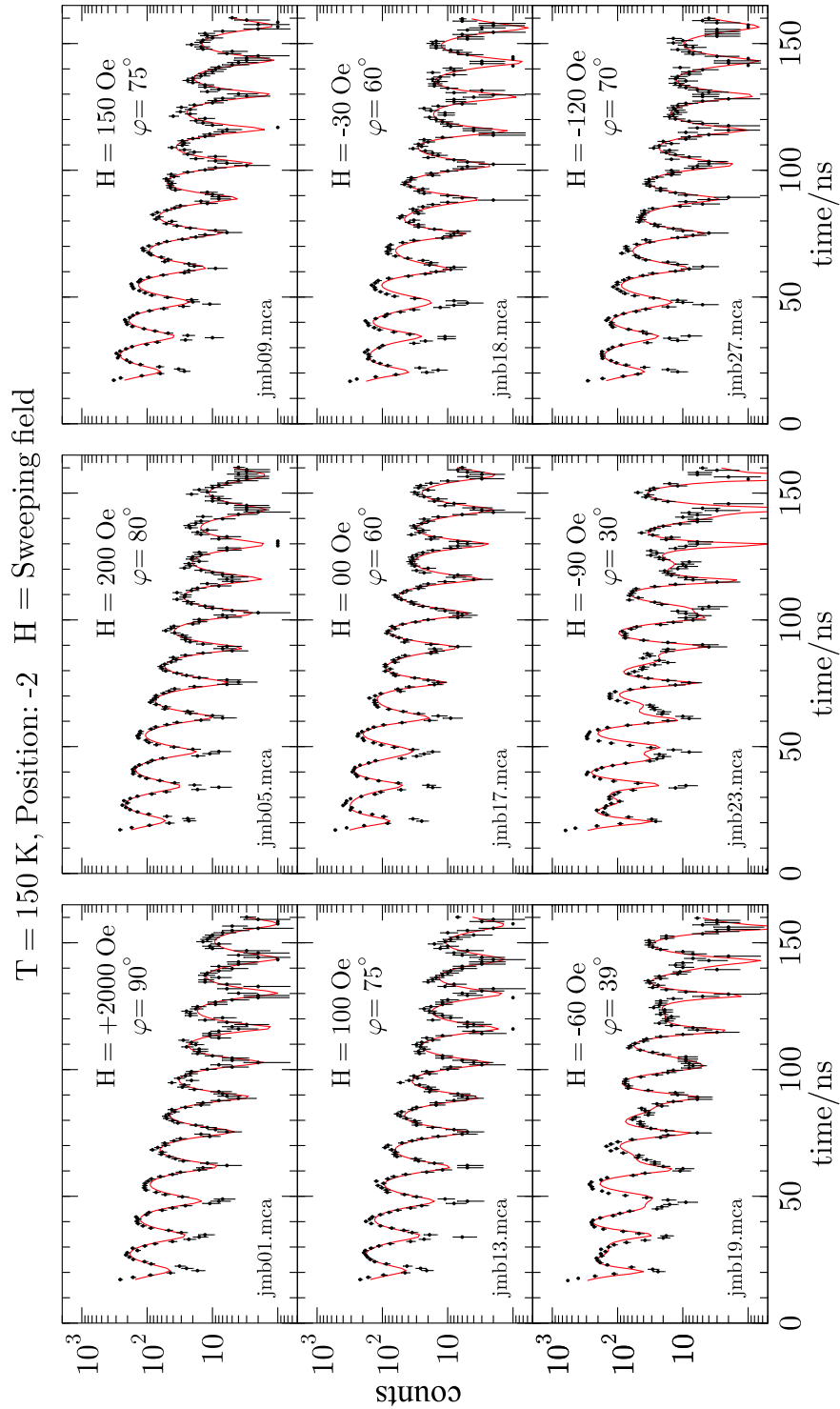


Figure 10.6: Time spectra measured at decreasing magnetic fields (from +2 kOe to -120 Oe, left branch of the hysteresis loop) at 150 K and at position '-2', of the Fe/MnF₂ sample having ⁵⁷Fe wedge. The red solid lines are the least-squares fitting to the data points. The geometry of these measurements were similar to that of Fig. 10.1. φ is the angle between the σ -polarization of the synchrotron beam and the Fe spin direction (assumed to be unidirectional) and the applied field direction.

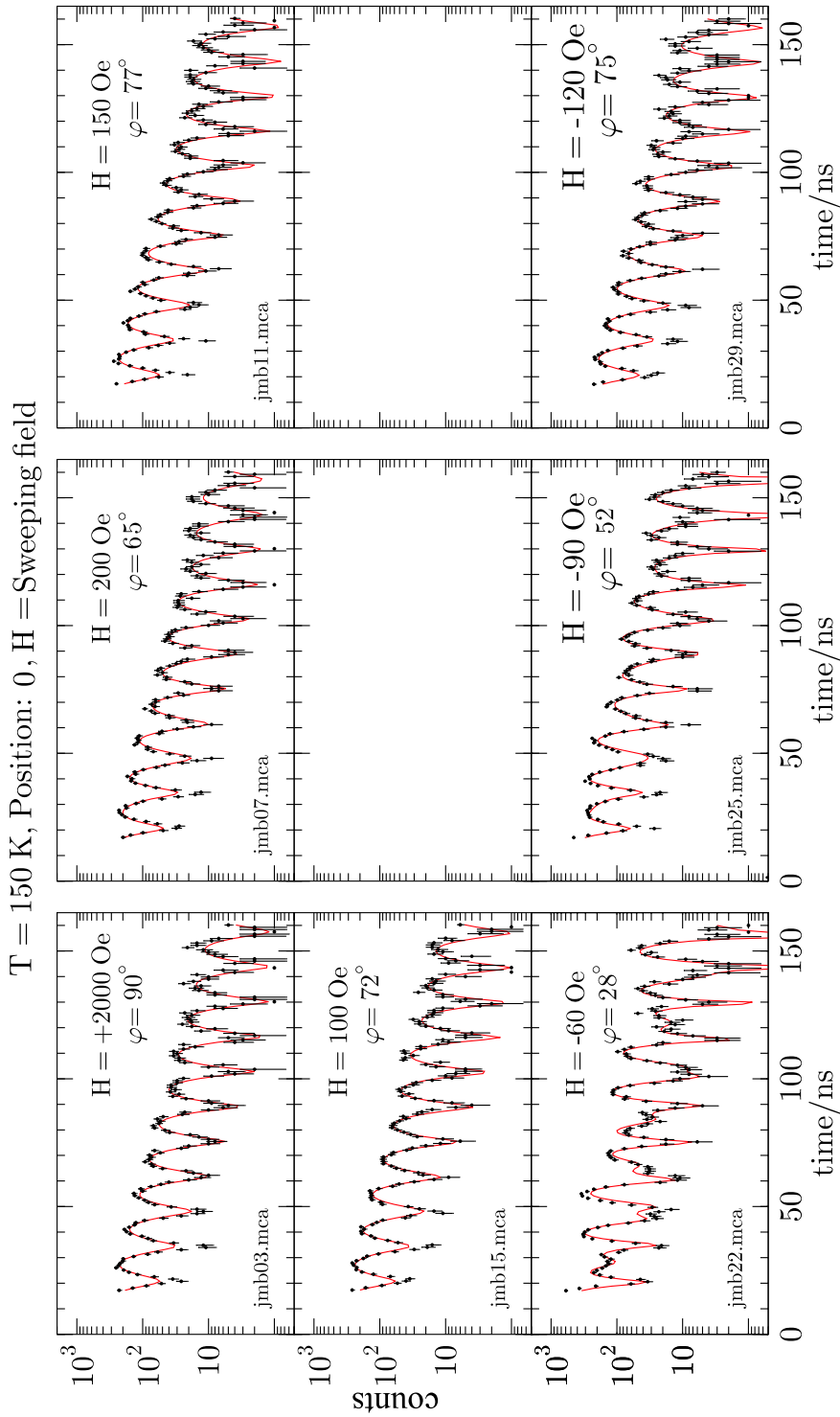


Figure 10.7: Time spectra measured at decreasing magnetic fields (from +2 kOe to -120 Oe, left branch of the hysteresis loop) at 150 K and at position '0', of the Fe/MnF₂ sample having ⁵⁷Fe wedge. The red solid lines are the least-squares fitting to the data points. The geometry of these measurements were similar to that of Fig. 10.1. φ is the angle between the σ -polarization of the synchrotron beam and the Fe spin direction (assumed to be unidirectional) and the applied field direction.

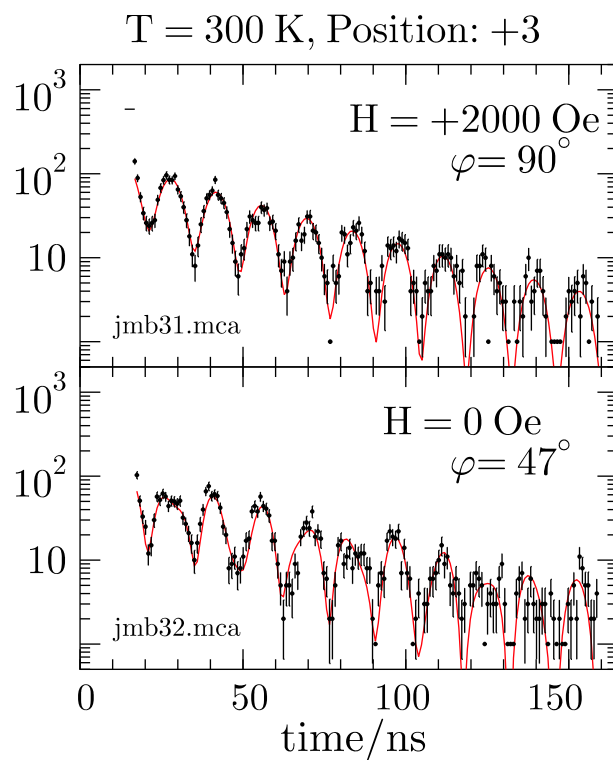


Figure 10.8: Time spectra measured at 300 K for the Fe/MnF₂ sample. top: H = 2000 Oe; bottom: H = 0 Oe.

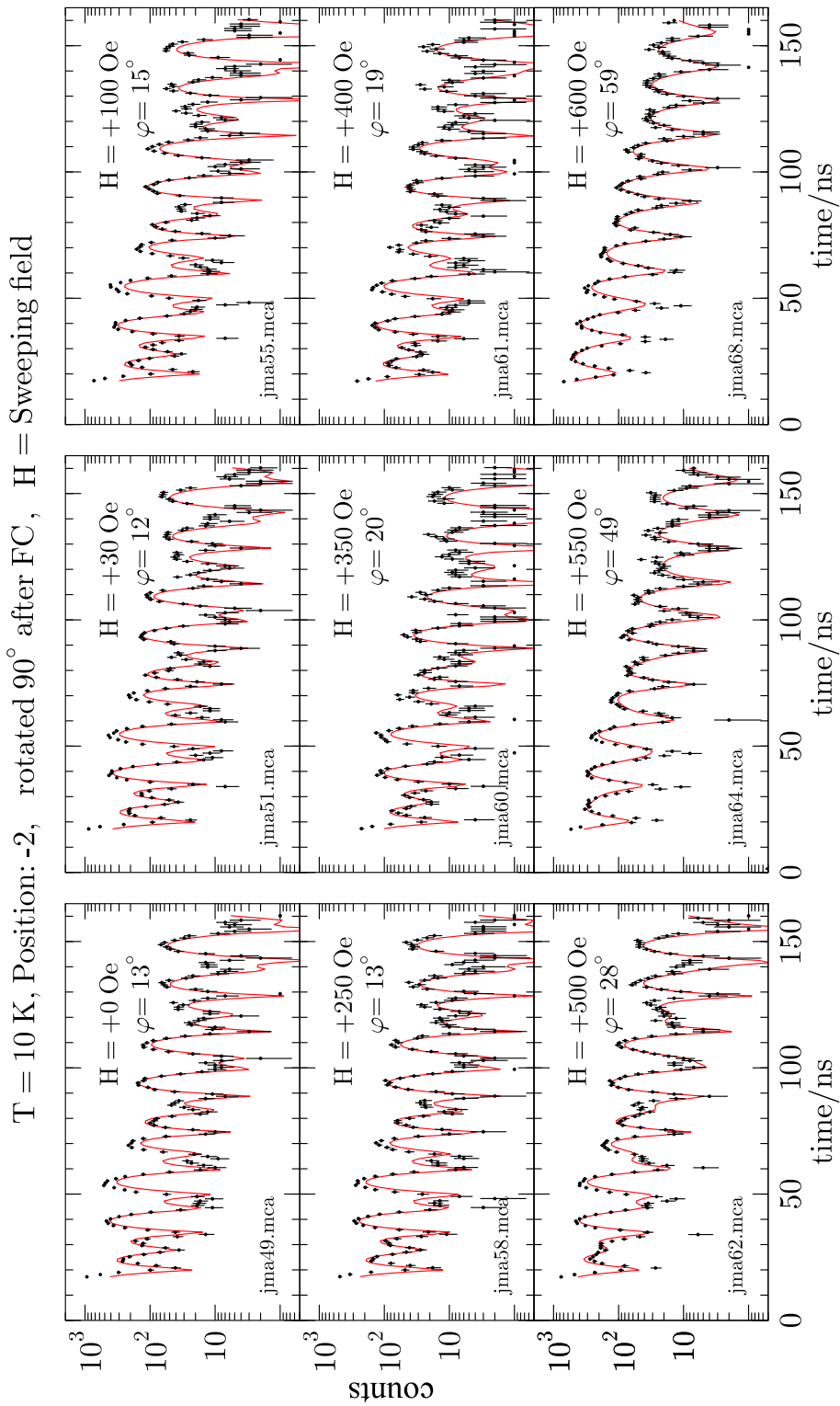


Figure 10.9: Time spectra taken at different sweeping fields for position '-2' of the Fe/MnF₂ wedge sample. The in-plane sweeping magnetic field was applied perpendicular to the cooling field (the cooling field was switched off at 10 K and the sample was rotated by 90°). The field was swept from 0 Oe to + 600 Oe.

Acknowledgments

First of all, I convey my sincere thanks to my thesis advisor Prof. Dr. Werner Keune, for his continuous encouragement and support during my Ph. D. period. I also convey my respect to him for his enthusiasm to teach me and make me motivated to learn and practise different subjects. Because of him I learned different ways to approach a research problem and the need to be persistent to accomplish any goal. Working with him I enjoyed my entire stay after joining the University of Duisburg-Essen (formerly, Gerhard-Mercator Universität). In addition, he also suggested and helped me to go to different places and learn different techniques useful in my future work. He accompanied me in many instances to my research work at various renowned institutions, like the APS (Advanced Photon Source, USA), ESRF (European Synchrotron Radiation Facility, France), and SPring-8 (Super Photon ring - 8 GeV, Japan). More importantly, due to him, I got the opportunity to meet many great researchers all over the world.

My special thanks also goes to our engineer, Ulrich von Hörsten, from whom I have learnt various pitfalls and the basics of an experiment and many other useful phrases like 'One learns from mistakes; if you don't do mistakes, you don't learn much', 'I will be a bird in my next birth' etc. He taught me how to perform X-ray diffraction, Mössbauer spectroscopy, how to prepare samples using molecular beam epitaxy and associated techniques like RHEED, LEED, and Auger electron spectrometer. I mostly like his punctuality and "do it now" approach.

I also specially thank Prof. Dr. Victor Eugen Kuncser from core of my heart for his invaluable friendly discussions and advices, starting from the basics of an instrument to the deeper level of the theories of a subject. I enjoyed my work more when he accompanied me. From him I have learned basic ideas and how to implicate them in necessary situations. I got the most benefits from him through numerous discussions.

I also convey my special thanks to PD Dr. Richard A. Brand, from whom I have learnt a lot. I had many useful scientific discussions with him about synchrotron radiation or neutron facilities. From him I have learnt various useful approaches in least-squares fitting Mössbauer spectra by using his computer program "NORMOS".

I convey my sincere thanks to Drs. Wolfgang Sturhahn, Tom Toellner, Ercan E. Alp, Jiang Zhao (from the Advanced Photon Source, Argonne National Laboratory, USA), Alexander Chumakov and Rudolf Rüffer (from the ESRF, Grenoble, France), Alfred Baron and John Sutter (from the SPring-8, Japan), for their help at their respective beamlines and many enlightening discussions. I gratefully acknowledge the advice from all these researchers, who exposed me to the new synchrotron-radiation based techniques, Nuclear Resonant Inelastic X-ray Scattering (NRIXS) for the study of atomic vibrational dynamics and Nuclear Resonant Scattering (NRS) for the study of spin structures at buried interfaces.

I am also grateful to Dr. Ralf Röhlsberger (DESY, Hamburg), for teaching me the computer programs PHOENIX (PHOnon Excitation by Nuclear Inelastic scattering of X-rays) and CONUSS (COherent NUclear resonant Scattering by Single crystals).

My special thanks also go to Prof. Dr. S. K. Date, from whom I have learned about chemical aspects of many materials, mainly various ferrites. I also thank him for his non-academical help.

My sincere thanks also goes to Prof. Dr. Wolfgang Kleemann for various discussions.

I would like to thank all my colleagues: Marco Walterfang, Frank Stromberg, Robert Peters, Ellen Schuster, Alexey Khrenov and many others for their direct or indirect help during my work and also for some valuable discussions.

Once again, I convey my gratitude to all our collaborators all over the world: Prof. Dr. Victor Eugen Kuncser, Prof. Dr. Waldemar A. A. Macedo, Dr. Johannes Eisenmenger, Prof. Dr. Ivan K. Schuller, Dr. Josep Nogués, Prof. Dr. Kai Liu, Dr. Wolfgang Sturhahn, Dr. Tom Toellner, Dr. Ercan E. Alp, Dr. Jiang Zhao, Dr. Alexander Chumakov (Shasa), Dr. Rudolf Ruffer, Dr. Alfred Baron, Dr. John Sutter, Prof. Dr. George Filoti, Mr. Gabriel Schinteie, Dr. Jörg Pieper, Prof. Dr. S. K. Date, Prof. Dr. M. Doi, Prof. Dr. Mehmet Acet, Prof. Dr. Peter Entel, Dr. Adeagbo A. Waheed, Dr. Alexei Zaiak and many others.

I am most thankful to my family, especially my parents, Mr. Somanath Sahoo and Mrs. Satyabhama Sahoo for their help and support from my childhood to educating me to follow the essence of everything. I am also thankful to my wife Mrs. Sonam Sahoo for her help, support and encouragement.

At last, but not the least, I acknowledge the financial support by the Deutsche Forschungsgemeinschaft, Graduierten Kolleg (GRK 277) (Duisburg) in the period from 2001 to 2003 and Sonderforschungsbereich (SFB 491) (Bochum-Duisburg) in the period from 2004 to 2006. Not all of the work I have done during my Ph. D. period of six years is included in this thesis, because it would have become too voluminous. However, the other parts of my work (importantly, the work on atomic vibrational dynamics) will be published in international journals in the near future.

Publications

Part of this work has been published in agreement with my supervisor, Prof. Dr. W. Keune:

- W. A. A. Macedo, B. Sahoo, V Kuncser, J. Eisenmenger, I. Felner, J. Nogués, Kai Liu, W. Keune and I. K. Schuller
Changes in Ferromagnetic spin structure Induced by Exchange bias in Fe/MnF₂ Films
Phys. Rev. B **70**, (2004) 224414.
- B. Sahoo, W. A. A. Macedo, V Kuncser, W. Keune, J. Eisenmenger, I. Felner, J. Nogués, Kai Liu and I. K. Schuller
Mössbauer spectroscopical investigation of exchange biased Fe/MnF₂ interfaces
Hyperfine Interact. (2006) (accepted).

Further publications

- W. Keune, V. E. Kuncser, M. Doi, M. Askin, H. Spies, B. Sahoo, E. Duman, M. Acet, J. S. Jiang, A. Inomata and S. D. Bader (invited paper)
Mössbauer Effect Study of the Fe Spin Structure in Exchange-Bias and Exchange-Spring Systems.
J. Phys. D: Applied Physics 35 (2002) 2352
- T. Ruckert, W. Keune, B. Sahoo, W. Sturhahn, T. Toellner, E. E. Alp and R. Röhlberger (invited)
Atomic Vibrational Dynamics of Thin Films Studied by Nuclear Resonant Inelastic X-Ray Scattering: Amorphous Tb_xFe_{1-x} Alloys.
Hyperfine Interactions 144/145 (2002) 65
- V. Kuncser, M. Vopsaroiu, B. Sahoo, P. R. Bissel and W. Keune
Advanced double coated metal particle tapes studied by Mössbauer spectroscopy and magnetic measurements.
Hyperfine Interactions (c) 5 (2002) 103
- S. K. Mohapatra, B. Sahoo, W. Keune and P. Selvam
Synthesis, characterization and catalytic properties of trivalent iron substituted hexagonal mesoporous aluminophosphates
Chem. Commun. (2002) 1466
- B. Sahoo, V. Kuncser, S. Kirsch and W. Keune
Superconductivity of MgB₂ Thin Films Prepared by Co-Evaporation and Magnetism of MgB₂/Fe Multilayers Studied by Mössbauer Spectroscopy
Phase Transitions 76 (2003) 423
- V. Kuncser, W. Keune, M. Vopsaroiu, P. R. Bissel, B. Sahoo and G. Filoti
Easy Axis Distribution in Modern Nanoparticle Storage Media: A New Methodological Approach
J. Optoelectronics and Advanced Mater. 5 (2003) 217

- V. Kuncser, M. Doi, B. Sahoo, F. Stromberg and W. Keune
Preparation and Structural Investigations of Epitaxially Grown Antiferromagnetic FeSn₂(001) Thin Films on InSb(001)
J. Appl. Phys. 94 (2003) 3573
- W. Keune, T. Ruckert, B. Sahoo, W. Sturhahn, T. S. Toellner, E. E. Alp and R. Röhlsberger
Atomic Vibrational Density of States in Crystalline and Amorphous Tb_{1-x}Fe_x Alloy Thin Films Studied by Nuclear Resonant Inelastic X-ray Scattering (NRIXS)
J. Phys.: Condens. Matter 16 (2004) S379
- V. Kuncser, W. Keune, B. Sahoo, E. Duman, M. Acet, F. Radu, M. Valeanu, O. Crisan and G. Filoti
Magnetic Interactions and Spin Configuration in FeRh and Fe/FeRh Systems
J. Magn. Magn. Mater. 272-276 (2004) 348
- D. Predoi, V. Kuncser, M. Zaharescu, W. Keune, B. Sahoo, M. Valeanu, M. Crisan, M. Raileanu, A. Jitianu and G. Filoti
Structural and Magnetic Properties of Iron Species//SiO₂ Nanocomposites Obtained by Sol-Gel Methods
Phys. Stat. Sol. (c) 1 (2004) 3507
- S. K. Date, P. A. Joy, P. S. Anil Kumar, B. Sahoo and W. Keune
Structural, Magnetic and Mössbauer Studies on Nickel-Zinc Ferrites Synthesized via a Precipitation Route
Phys. Stat. Sol. (c) 1 (2004) 3495
- V. Kuncser, C. P. Lungu, I. Mustata, A. M. Lungu, W. Keune, B. Sahoo, F. Stromberg, M. Walterfang, L. Ion and G. Filoti
Fe-Cu Granular Thin Films With Giant Magnetoresistance by Thermionic Vacuum Arc Method: Preparation and Structural Characterization
Surface and Coatings Technology 200 (2005) 980.
- B. Sahoo, W. Keune, W. Sturhahn, T. S. Toellner and E. E. Alp
Atomic Vibrational Dynamics of Amorphous Fe-Mg Alloy Thin Films
J. Phys. Chem. Solids 66 (2005) 2263.
- V. Kuncser, G. Schinteie, B. Sahoo, W. Keune, D. Bica, L. Vekas and G. Filoti
Complex Characterization of Magnetic Fluids by Mössbauer Spectroscopy
Romanian Reports in Physics 58 (2006) 235
- B. Sahoo, V. Kuncser, W. Keune and J. Pieper
Mössbauer Spectroscopical Investigation of Amorphous Fe-Y Alloy Ribbons Prepared by Melt Spinning
Hyperfine Interactions (2006) (accepted)

- B. Sahoo, W. Keune, W. Sturhahn, T.S. Toellner and E.E. Alp
Amorphous Fe-Mg Alloy Thin Films: Magnetic Properties and Atomic Vibrational Dynamics
Hyperfine Interactions (2006) (accepted)

- B. Sahoo, W. A. Adeagbo, F. Stromberg, W. Keune, E. Schuster, R. Peters, P. Entel, S. Lüttjohann, A. Gondorf, W. Sturhahn, J. Zhao, T. S. Toellner and E. E. Alp
Electronic Transport and Atomic Vibrational Properties of Semiconducting Mg₂¹¹⁹Sn Thin Film
Phase Transitions (2006) (accepted)

- B. Sahoo, W. Keune, E. Schuster, W. Sturhahn, J. Zhao, T. S. Toellner and E. E. Alp
Vibrational Dynamics of Fe in Amorphous Fe-Sc and Fe-Al Alloy Thin Films
Hyperfine Interactions (2006) (accepted)

- V. Kuncser, G. Schinteie, B. Sahoo, W. Keune, D. Bica, L. Vekas and G. Filoti
Magnetic interactions in water based ferrofluids studied by Mössbauer spectroscopy
J. Phys.: Condens. Matter (2006) (accepted).

CURRICULUM VITAE

Name:	Balaram Sahoo	
Date of Birth:	April 02, 1976	
Place of Birth:	Nayagarh, India	
Marital Status:	Married	
Matriculation:	1988 - 1991	Bahadajhola High School, Bahadajhola (Board of Secondary Education, Orissa, Cuttack)
Intermediate Science:	1991 – 1993	Nayagarh College, Nayagarh (Council of Higher Secondary Education, Orissa, Bhubaneswar)
Bachelor of Science:	1993 – 1996	Nayagarh College, Nayagarh (Utkal University, Orissa, Bhubaneswar) (Physics Hons.)
Master of Science:	1996 - 1998	Utkal University, Orissa, Bhubaneswar (Particle Physics Specialization)
Master of Technology:	1998 – 2000	Indian Institute of Technology Bombay, Mumbai, India (Metallurgical Engineering and Materials Science)
Doctor of Philosophy (Ph D): (Physics)	2001 – 2006	Fachbereich Physik, Universität Duisburg-Essen, Duisburg, Germany Thesis Title: Spin Structure of Exchange Biased Heterostructures: Fe/MnF ₂ and Fe/FeF ₂
Experience:	2001 – 2003	Research scholar (Graduiertenkolleg 277)
	2003 – 2006	Scientific assistant (Deutsche Forschungsgemeinschaft (DFG), Sonderforschungsbereich (SFB 491))